TURUN
YLIOPISTO
UNIVERSITY
OF TURKU

MONITORING CELLULAR GUANOSINE TRIPHOSPHATE (GTP) AND GTP ASSOCIATED PROTEINS

Randa Mahran

TURUN YLIOPISTON JULKAISUJA – ANNALES UNIVERSITATIS TURKUENSIS
SARJA – SER. AI OSA – TOM. 707 | ASTRONOMICA – CHEMICA – PHYSICA – MATHEMATICA | TURKU 2023

TURUN
YLIOPISTO
UNIVERSITY
OF TURKU

MONITORING CELLULAR GUANOSINE TRIPHOSPHATE (GTP) AND GTP ASSOCIATED PROTEINS

Randa Mahran

TURUN YLIOPISTON JULKAISUJA – ANNALES UNIVERSITATIS TURKUENSIS
SARJA – SER. AI OSA – TOM. 707 | ASTRONOMICA – CHEMICA – PHYSICA – MATHEMATICA | TURKU 2024

University of Turku

Faculty of Science
Department of Chemistry
Chemistry
Doctoral programme in Exact Sciences

Supervised by

Docent Harri Härmä, Ph.D.
University of Turku
Turku, Finland

Kari Kopra, Ph.D.
University of Turku
Turku, Finland

Morteza Malakoutikhah, Ph.D.
University of Turku
Turku, Finland

Reviewed by

Associate Professor, Matthew Smith
University of Montreal
Montreal, Quebec, Canada

Associate Professor, Joshua Jackman
Sungkyunkwan University
Seoul, South Korea

Opponent

Professor Paul Brennan
University of Oxford
Oxford, United Kingdom

ISBN 978-951-29-9614-8 (PRINT)
ISBN 978-951-29-9615-5 (PDF)
ISSN 0082-7002 (Print)
ISSN 2343-3175 (Online)
Painosalama, Turku, Finland 2024

To my husband and my two sons,
you are not only my family but also my dearest friends

UNIVERSITY OF TURKU
Faculty of Science
Department of Chemistry
Chemistry
RANDA MAHRAN: Monitoring cellular Guanosine triphosphate (GTP) and GTP associated proteins.
Doctoral Dissertation, 159 pp.
Doctoral Programme in Exact Sciences
March 2024

ABSTRACT

Guanosine-5'-triphosphate (GTP) is an essential molecule for cell survival and function. Although free GTP plays a crucial role in several cellular processes, most studies focus solely on the protein bound GTP and its association with cancer. Efficient methods for determining cellular GTP concentration are currently lacking. Chromatography or capillary electrophoresis (CE) are commonly utilized for separation and mass spectrometry (MS) for quantification of GTP in biological samples. For monitoring GTPases and their interactions with ligands, differential scanning fluorimetry, differential scanning calorimetry, or differential static light scattering are typically utilized. However, these methods either lack sensitivity or throughput.

In this PhD project, the Protein-Probe method, based on a Eu^{3+}-chelate peptide probe that interacts with the hydrophobic core of the protein, has been developed and applied for studying different factors that affect the thermal stability of small GTPases, such as inhibitors, buffer ions and nucleotides. Furthermore, the method was explored for a better understanding of the binding specificity of the recent Food and Drug Administration approved $KRAS^{G12C}$ covalent inhibitors to RAS GTPases.

Additionally, a novel dual-labeled Förster Resonance Energy Transfer (FRET)-based peptide probe was introduced and compared to the Protein-Probe method in the thermal stability assay. The FRET-Probe technique was also applied to determine the chemical stability of proteins with different chemical denaturants.

For measuring cellular GTP level, a homogenous high throughput assay was developed to measure the amount of GTP in cells utilizing a highly GTP-specific antibody. The assay yielded comparable results to those obtained with CE/MS, demonstrating a similar level of accuracy, while also exhibiting a substantial enhancement in throughput.

In conclusion, this thesis work aimed at developing novel and robust methods to address the current limitations in monitoring cellular GTP concentration and to study small GTPases. The focus of the study was free GTP, recognizing its essential role in various cellular processes.

KEYWORDS: Guanosine triphosphate, GTPases, thermal stability, chemical denaturation, lanthanide chemistry, time-resolved luminescence

TURUN YLIOPISTO
Matemaattis-luonnontieteellinen Tiedekunta
Kemian Laitos
Kemia
RANDA MAHRAN: Solun guanosiinitrifosfaatin (GTP) ja GTP-proteiinien monitorointi.
Väitöskirja,159 s.
Eksaktien tieteiden tohtoriohjelma
Maaliskuu 2024

TIIVISTELMÄ

Guanosiini-5'-trifosfaatti (GTP) on välttämätön molekyyli solujen selviytymiselle ja toiminnalle. Vaikka vapaalla GTP:llä on ratkaiseva rooli useissa soluprosesseissa, suurin osa tutkimuksista keskittyy vain GTPaaseihin sitoutuneeseen GTP:hen ja sen linkittymisessä syövän kehittymiseen. Tällä hetkellä solun GTP-konsentraation määrittämiseksi ei ole tehokkaita menetelmiä. Käyttämällä kromatografiaa tai kapillaarielektroforeesia (CE) erotukseen ja massaspektrometriaa (MS) kvantifiointiin voidaan biologisten näytteiden GTP-pitoisuutta seurata, mutta se on melko työlästä. GTPaasien ja niiden vuorovaikutusten seurantaan käytetään tyypillisesti differentiaalista pyyhkäisyfluorimetriaa, differentiaalista pyyhkäisykalorimetriaa tai differentiaalista staattista valonsirontaa. Kaikilta näistä menetelmistä puuttuu kuitenkin herkkyys tai suorituskyky. Tästä syystä tämän opinnäytetyön tavoitteena oli kehittää uusia herkkiä ja toimintavarmoja menetelmiä GTP-pitoisuuden seurantaan ja GTPaasien tutkimiseksi uudesta näkökulmasta.

Solujen GTP-tasojen mittaamiseksi kehitettiin homogeeninen tehoseulontaan yhteensopiva määritys käyttämällä GTP-spesifistä vasta-ainetta. Määritys tuotti samanlaisia tuloksia kuin vertailumenetelmänä käytetty CE/MS, mutta huomattavasti nopeammin ja helpommin. Tässä väitöskirjatyössä esiteltiin myös uusi kaksoisleimattu FRET-pohjainen peptidikoetin, jota käytettiin yhdessä aiemmin kehitetyn ”Protein-Probe” menetelmän kanssa. FRET-Probe tarjoaa saman korkean herkkyyden kuin Protein-Probe tekniikka, mutta se mahdollistaa proteiinin stabiilisuuden mittaamisen neutraalissa pH:ssa ja yhdessä vaiheessa. Protein-Probe menetelmää käytettiin pienten GTPaasien ja niiden lämpöstabiilisuuteen vaikuttavien tekijöiden tutkimiseen. Lisäksi kehitettyjä menetelmiä käytettiin FDA:n äskettäin hyväksymien kovalenttisten KRAS(G12C) inhibiittorien sitoutumisspesifisyyden, toiminnan ja resistenttiyden muodostumismekanismien tutkimiseen. FRET-Probe-tekniikkaa ei sovellettu ainoastaan proteiinien lämpöstabiilisuuden seurantaan, vaan sen osoitettiin soveltuvan myös proteiinien isotermaalisen kemiallisen stabiilisuuden seurantaan.

AVAINSANAT: Guanosiinitrifosfaatti, GTPaasit, lämpöstabiilisuus, kemiallinen denaturaatio, lantanidikemia, aikaresoluutioinen luminesenssi

Table of Contents

Abbreviations

ADP	Adenosine-5′-diphosphate
AELC	Anion exchange liquid chromatography
ATP	Adenosine-5′-triphosphate
AuNPs	Gold nanoparticles
BH4	Tetrahydrobiopterin
BL	Bioluminescence
BRET	Bioluminescence resonance energy transfer
CD	Circular Dichroism
CE	Capillary electrophoresis
CL	Chemiluminescence
cpYFP	Circular permutated yellow fluorescent protein
CTP	Cytidine-5'-triphosphate
dATP	2-deoxy adenosine triphosphate
dCTP	2-deoxy cytidine triphosphate
DETA	Diethylenetriamine
dGTP	2-deoxy guanosine triphosphate
DNA	Deoxyribonucleic acid
dNTP	2-deoxy nucleoside triphosphate
DSC	Differential Scanning Calorimetry
DSF	Differential Scanning Fluorimetry
dUTP	2-deoxy uridine triphosphate
EC_{50}	Half maximal effective concentration
ECL	Electrochemiluminescence
ERK	Extracellular signal-regulated kinase
ESI	Electron spray ionization
$FADH_2$	Flavin adenine dinucleotide
FDA	Food and Drug Administration
GAP	GTPases activating protein
GC	Gas chromatography
GDP	Guanosine-5′-diphosphate
GEF	Guanine nucleotide exchange factor

GMP	Guanosine-5´-monophosphate
GTP	Guanosine-5´-triphosphate
GTPase	Guanosine-tri-phosphatase
GTPγS	Guanosine-5'-(γ-thio)-triphosphate
HIDC	Hexamethylindodicarbocyanine
HILIC	Hydrophilic interaction liquid chromatography
HPRT	Hypoxanthine-guanine phosphoribosyl transferase
HPTS	8-hydroxy-1,3,6-pyrene trisulfonate
HRP	Horse radish peroxidase
IC	Internal conversion
IC_{50}	Half maximal Inhibitory concentration
ICS	Intersystem crossing
IMP	Inosine-5´-monophosphate
IPLC	Ion-pairing liquid chromatography
IP-RPLC	Ion-pairing reversed-phase liquid chromatography
IQGAP1	RAS GTPase-activating-like protein 1
LC	Liquid chromatography
MALDI	Matrix-assisted laser desorption ionization
MAPK	Mitogen-activated protein kinase
MAPK	Mitogen-activated protein kinase
MEK	Mitogen activated protein kinase
MPA	Mycophenolic acid
mTOR	Mammalian target of rapamycin
NTP	Ribonucleoside triphosphate
PBA	Phenylboronic acid group
PI3K	Phosphatidylinositol 3-kinase
RNA	Ribonucleic acid
SWNT	Single-walled carbon nanotube
TLC	Thin layer chromatography

List of Original Publications

This dissertation is based on the following original publications, which are referred to in the text by their Roman numerals:

I Kopra, K., Mahran, R., Yli-Hollo, T., Tabata, S., Vuorinen, E., Fujii, Y., Vuorinen, I., Ogawa-Iio, A., Hirayama, A., Soga, T., Sasaki, A.T., Härmä, H. Homogeneous luminescent quantitation of cellular guanosine and adenosine triphosphates (GTP and ATP) using QT-Luc$^{GTP\&ATP}$ assay. Analytical and Bioanalytical Chemistry, 2023; 415:6689–6700

II Kopra, K., Valtonen, S., Mahran, R., Kapp, J. N., Hassan, N., Gillette, W., Dennis, B., Li, L., Westover, K.D., Plückthun, A. & Härmä, H. Thermal Shift Assay for Small GTPase Stability Screening: Evaluation and Suitability. International journal of molecular sciences, 2022; 23(13):7095.

III Mahran, R., Vello, N., Komulainen, A., Malakoutikhah, M., Härmä, H., Kopra, K. Isothermal chemical denaturation assay for monitoring protein stability and inhibitors interactions. Scientific Reports, 2023.

IV Mahran, R., Kapp, J., Valtonen, S., Champagne, A., Ning, J., Gillette, W., Stephen, A. G., Hao, F., Plückthun, A., Härmä, H., Pantsar, T., Kopra, K. Beyond KRAS(G12C): biochemical and computational characterization of sotorasib and adagrasib binding specificity and the critical role of H95 and Y96.

1 Introduction

Nucleotides, also known as ribonucleoside triphosphates (NTPs), are essential molecules that exist in all mammalian cells. NTPs are composed of a pentose sugar, various nitrogenous bases, and triphosphate. Beside serving as precursor molecules for nucleic acids, NTPs play critical role in cellular functions. Purine nucleotides, namely adenosine-5′-triphosphate (ATP) and guanosine-5′-triphosphate (GTP), are extensively studied, and their roles as energy substrates and regulators of numerous cellular metabolic activities are well characterized.

Cellular concentrations of ATP and GTP are interdependent and strictly controlled within the cell. Impairment of GTP level in different body organs has been associated with multiple diseases such as blindness, gout arthritis, renal ischemia, muscle injury, and neurological diseases. The key players in regulating GTP levels are small guanosine triphosphatases (GTPases), which are monomeric, small guanine nucleotide-binding proteins (G-proteins) capable of catalyzing the hydrolysis of GTP into guanosine-5′-diphosphate (GDP) and inorganic phosphate (Pi). Small GTPases regulate downstream signaling pathways essential for cell proliferation and a multitude of other cellular processes. They act as key regulators in processes such as cell motility and membrane trafficking.

Additionally, it is crucial to recognize that GTPase activity is not limited to small GTPases alone. Another GTPase family includes the tubulin-GTPase, a critical protein for forming microtubules. It also binds guanine nucleotides and plays a fundamental role in cell proliferation, cell motility and intracellular transport.

Given the crucial role of GTP and its connection to various diseases, the accurate understanding of the functions and importance of GTP is essential. Existing methods for monitoring nucleotides fall in two categories: luminescence-based and separation-based methods. Separation-based methods operate with common principle for all nucleotides and detect nucleotides as a group. They separate nucleotides and nucleotide derivatives based on their chemical characteristics such as mass, charge, and polarity. Luminescence-based methods are typically designed specifically for individual target nucleotide and utilize the light emitted in enzymatic reactions or interactions withs fluorophores for detection. However, there is greater availability of techniques for measuring ATP compared to other nucleotides.

In separation-based techniques, also referred to as non-luminescent based methods, several approaches have been proposed for high-performance liquid chromatography (HPLC) separation of various nucleotides and their phosphate analogues (NMPs & NDPs). Ion-pairing and anion exchange LC are common HPLC methods for nucleotide separation, relying on varying polarity to separate different phosphate analogues. These methods require accurate optimization of the mobile phase buffer pH to provide optimal ionization of the target analytes. Mass spectrometry (MS) is a superior alternative to ultraviolet- visible detection for detection of the separated nucleotides due to its high sensitivity and ability to provide extensive information about nucleotide structure. Capillary electrophoresis (CE) is another valuable method for nucleotide monitoring, utilizing an electric current for separation based on charge and size. CE can be coupled with MS and offers several advantages over HPLC, including small sample volume and short run times. Despite the benefits, non-luminescent based methods for nucleotide detection often require trained personnel and specific equipment, with limited throughput capabilities. In contrast, luminescent based methods, such as chemiluminescent and fluorescent based sensors, offer higher throughput, but are predominantly developed for ATP detection, with relatively few methods specially designed for GTP analysis.

In conclusion, this thesis explores the monitoring of cellular GTP and conducts in-depth studying of small GTPases. The significance of this work lies in bridging the gap in methodologies for accurate and high throughput GTP detection. By enhancing our ability to monitor GTP levels, this research contributes to the advancement of diagnostics and therapeutic interventions, ultimately fostering a deeper comprehension of cellular processes and their impact on human health.

2 Literature Review

In the subsequent section of this thesis, I will give a versatile analysis of GTP regarding structural attributes, synthesis pathways, clinical relevance, and detection strategies. There are countless methods for nucleotides detection, yet not all of these are applicable in the complicated structure and composition of cells. Consequently, not all exhibit the sufficient level of sensitivity and selectivity. The most prevalent luminescence and non-luminescence-based detection methods that have demonstrated efficiency in nucleotides detection will be reviewed. A particular emphasis will be devoted to techniques that are designed for accurate detection and quantification of total GTP and are compatible with cell-based assays. Nevertheless, a brief reference to methods for GTPases bound GTP, will be presented in the relevant context.

2.1 Nucleotides

Given the context and objectives of this study, in the next review I will go through purine biosynthesis in brief and the physiological significance of nucleotides and related diseases. ATP and GTP have a more critical role in all cell types and have therefore been more extensively studied. Therefore, in the next chapter, their roles in cellular processes will be explored, with a particular focus on GTP, as it is the topic of this thesis. Additionally, I will discuss GTP in context of GTPases with only the RAS family as it is the main GTPase family studied in my PhD project.

2.1.1 Nucleotides' structure and intracellular synthesis pathways

Nucleotides are the primary building units for the biosynthesis of nucleic acids. They are formed of nitrogenous bases, a sugar molecule and phosphate (Pi) group. The nitrogenous bases are linked to the first carbon atom (C-1') of the sugar moiety via a glycosidic bond. In ribonucleic acid (RNA), the sugar molecule is a d-ribose, while in deoxyribonucleic acid (DNA), it is a 2-deoxy-d-ribose. In addition, nucleotides have one to three Pi groups bound at the (C-5') position. The base together with the sugar moiety are called 'nucleoside' (Figure 1), further linkage of α, β, and γ Pi

groups forms nucleosides mono, di- and tri- phosphates respectively. There are two types of nucleobases: pyrimidines and purines. Pyrimidines are a class of aromatic compounds that consist of a six-membered ring composed of four carbon and two nitrogen atoms at positions 1 and 3. There are three forms of pyrimidine bases: uracil (U), cytosine (C) and thymine (T). Purines on the other hand, are double ringed compounds, formed of a six-membered pyrimidine ring bound to a five-membered imidazole ring. Purine bases include guanine (G) and adenine (A), (Figure 1).[1,2] DNA is made of four nucleotides: A, G, C, and T, jointly known as 2-deoxy nucleoside triphosphates (dNTPs). In contrast, RNA is formed of the same nucleotides, except that thymine (T) is replaced by (U), and nucleotides are termed NTPs.[3]

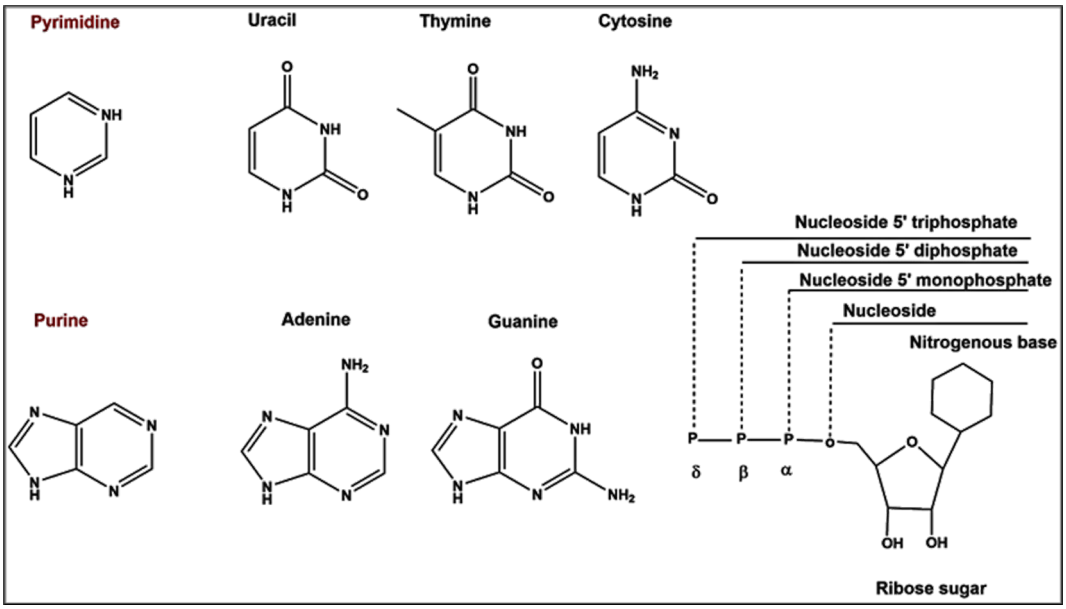

Figure 1. Nucleotide structures. Nucleosides are formed of a pentose sugar, a nitrogenous base which is either purine (double ring) or pyrimidine (single ring). Purines include adenine and guanine, and pyrimidines include uracil, cytosine and thymine. A nucleotide consists of nucleoside and one, two or three phosphate groups to form nucleoside monophosphate (NMP), nucleoside diphosphate (NDP), and NTP respectively.

There are two main ways for purine synthesis in mammalian cells: the salvage and the *de novo* pathways.[4] ATP is produced inside the mitochondria and during the process of glycolysis. The energy required for synthesis of adenosine-5′-diphosphate (ADP) and ATP is provided by other metabolic pathways, mainly oxidative phosphorylation, in which nicotinamide adenine dinucleotide (NADH) and flavin adenine dinucleotide ($FADH_2$) act as energy precursors for the reduction of oxygen

leading to the formation of ADP and ATP. ATP synthase catalyzes the production of ATP from ADP and inorganic Pi.[5] In the salvage pathway, intermediates produced during degradation of nucleotides are reused for synthesis of new nucleotides. This pathway utilizes enzymes such as adenine phosphoribosyl transferase to recycle adenine into adenosine-5′-monophosphate (AMP), and the Mg^{2+} dependent hypoxanthine-guanine phosphoribosyl transferase (HPRT) to recycle guanine and hypoxanthine bases to form guanosine-5′-monophosphate (GMP) and inosine-5′-monophosphate (IMP), respectively (Figure 2).[6,7]

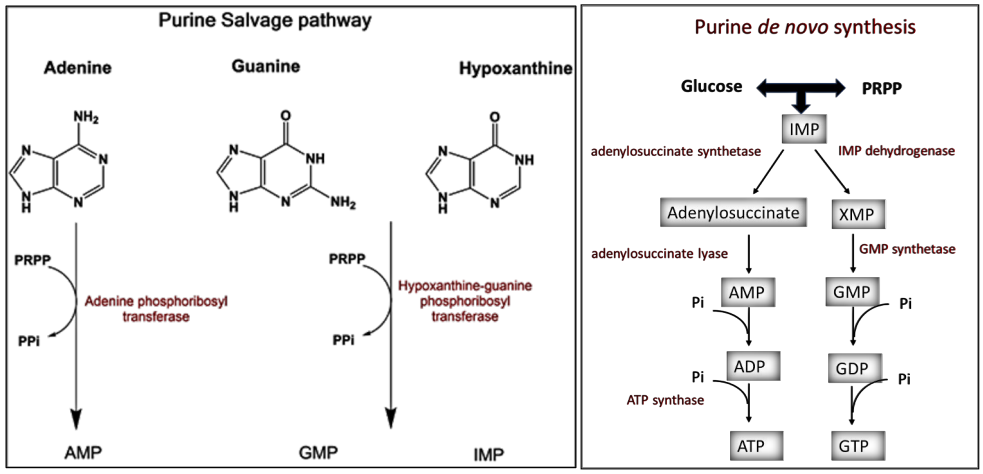

Figure 2. Purine nucleotides biosynthesis. Purines are either synthesized from free nucleotides by salvage pathway, or *de novo* from sugars. In the salvage pathway, adenine or guanine and hypoxanthine are turned into AMP or GMP and IMP by the action of adenine phosphoribosyl and hypoxanthine-guanine posphoribosyl transferase respectively. On the other hand, *de novo* synthesis utilizes phosphoribosylpyrophosphate and glucose to make IMP, which acts as a precursor compound to AMP and GMP. Lastly, AMP and GMP are phosphorylated into ATP and GTP respectively.

While the salvage pathway satisfies most of cellular demand for purines, the *de novo* pathway also plays a crucial role in the synthesis of purines. The *de novo* pathway relies on the production of nucleotides from simple sugars through utilizing six enzymes for the conversion of phosphoribosylpyrophosphate (PRPP) into IMP, or a ten-step pathway for metabolizing glucose into IMP. IMP is the key compound that is transformed in two steps pathway to either AMP or GMP.[8,9] IMP undergoes catabolic reactions where oxidation of C-2 of the purine ring of IMP into xanthosine-5′-monophosphate (XMP) by IMP dehydrogenase (IMPDH) occurs, this is then followed by adding an amide group to the new carbonyl group at C-2 of XMP. This reaction is catalyzed by GMP synthetase and the product is GMP. Finally, GMP is phosphorylated into GDP or GTP (Figure 2).[10]

The purine synthesis pathways, particularly the *de novo* pathway, are strictly regulated due to their high energy demand. Furthermore, the conversion of IMP into either GTP or ATP, and the requirement of GTP for ATP synthesis and ATP for GTP synthesis, highlights the mutual dependence of intracellular ATP and GTP levels.[11,12]

Under physiological conditions, nucleotides are primarily present inside cells, and their concentrations can vary among different cell types.[13] ATP stands out as the most abundant nucleotide in cells, with concentrations in healthy cells typically ranging from 2 to 8 millimolar (mM) under physiological conditions. Notably, cardiac muscle cells exhibit the highest levels of ATP, while brain cells have the lowest. Following ATP, GTP and uridine-5'-triphosphate (UTP) are the next most abundant nucleotides, with average intracellular concentrations of 0.2 to 0.5 mM, respectively.[14,15] Cytidine-5'-triphosphate (CTP) is present at comparatively low concentrations, typically ranging from 0.08 to 0.13 mM. In contrast, 2-deoxy adenosine triphosphate (dATP), 2-deoxy guanosine triphosphate (dGTP), 2-deoxy cytidine triphosphate (dCTP), and 2-deoxy uridine triphosphate (dUTP) are found in even lower concentrations, in the range of 0.001 to 0.005 mM. NDP analogues, such as ADP and GDP, are present in concentration of 0.1 and 0.03 mM, respectively, while cytidine-5'-diphosphate (CDP) and uridine-5'-diphosphate (UDP) exist in lower micromolar range.[16]

Cancer cells have significantly higher concentrations of NTPs and dNTPs compared to normal cells. The concentrations of NTPs and dNTPs in tumor cells are several folds higher than those found in normal cells, with CTP showing the most significant increase among all NTPs.[17] Among dNTPs, dATP, dCTP, and dUTP show an equal increase, while dGTP shows the least prominent increase. These observed changes are consequences of the altered metabolism during tumorigenesis, playing a crucial role in cancer cell proliferation and survival.[16,18] Moreover, ATP plays a key role in antitumor activity by enhancing the immune response through activation of the inflammatory pathways and inhibition of extracellular adenosine accumulation.[19]

2.1.2 Clinical relevance of nucleotides

2.1.2.1 Physiological significance of nucleotides in mammalian cells

Both NTPs and dNTPs are the building blocks of nucleic acids. They control cellular processes by carrying the genetic information required for encoding protein structure and function. Additionally, the balance in nucleotides pools is essential for accurate DNA replication and cell survival.[20,21] Beyond their primary role as constituents of nucleic acids, NTPs and their phosphate-containing analogues (NMPs & NDPs) play essential roles in various cellular functions. For instance, pyrimidine nucleotides like

UTP and UDP are required for glycosylation, while CDP is involved in synthesizing components of the plasma membrane.[22] Similarly, thymidine acts as a substrate in enzymatic reactions essential for DNA synthesis and cell replication.[23]

ATP plays multiple vital roles in diverse cellular activities, such as the contraction of muscles, vesicles transport, ions transport and intracellular communication between nucleus and cytoplasm.[24–27] Furthermore, ATP is essential for neuronal activity, serving as a neurotransmitter in the pre- and post-junctional sites of purinoceptors found nearly in all mammalian cell membranes.[28,29] Enzymes such as helicases, kinases and polymerases heavily rely on ATP for their activity. ATP kinases, for example, catalyze phosphorylation of lipids and proteins by transferring Pi from ATP. Additionally, during DNA replication, polymerases and helicases utilize ATP as an energy source.[30–32]

GTP plays a major role within the cell. Similar to ATP, GTP acts as an energy substrate through GTP hydrolysis, thus providing necessary energy for various cellular processes. For example, motor proteins utilize the energy produced from GTP hydrolysis for changing the shape of the cell and cell movement.[33] The energy of GTP is also consumed in the building and depolymerization of microtubules.[34,35] Additionally, the energy from GTP is required during the process of protein translation for the initiation and elongation steps of protein synthesis.[36]

Furthermore, GTP exerts a considerable impact on neuromodulation and neuroprotection in the brain and spinal cord, as supported by numerous findings.[37,38] Besides its direct functions within cells, the main role of GTP lies in the regulation of G-proteins.[39]G-proteins encompass both small GTPases and heterotrimeric G-proteins. Heteromeric G-proteins are formed of three subunits α, β, and γ with the Gα subunit possessing regulatory GTPases activity. Small GTPases are monomeric enzymes, typically single-chain 20-40 kDa proteins.[40] Large GTPases, such as the dynamin superfamily of proteins, constitute another distinct group of GTPases with a size of 100 kDa. They are characterized by their larger GTPase domain and the oligomerization dependent activity of GTPases. The oligomerization domain functions as GTPases activating proteins (GAP).[41–43]

Numerous small GTPases act as ON/OFF molecular switches for vital cellular activities, including vesicle transfer across the cell membrane for intercellular communication, cell survival, as well as cell division and migration.[44,445] They possess a unique characteristic of binding and hydrolysis of GTP.[46] The small GTPase superfamily is composed of more than 150 strains divided into five subfamilies, which are rat sarcoma virus (RAS), RAS related in brain (RAB), RAS homologous (Rho), RAS related nuclear protein (RAN), and ADP ribosylation factor (Arf), with variation in the degree of structural similarities.[47] RAS, the first small GTPase to be discovered, was identified as a protein product of the retrovirus oncogene. The Rho family plays a crucial role in regulating the actin cytoskeleton,

while RAN is essential for protein transport from the nucleus, and the RAB family is responsible for regulating vesicle trafficking within cells.[47]

RAS proteins, in this context, refer to members of the RAS subfamily, are formed of G-domain, which consists of six β-sheets and five-α-helices, forming the nucleotide binding pocket surrounded by five regions (phosphate-loop, two base binding loops, switch I and switch II regions).[48] GTP and GDP interact with the G-domain at the switch regions, with RAS and guanine nucleotide exchange factor (GEF) having equal affinity for both GTP and GDP, typically in the picomolar range. Therefore, the binding preference for the 10-fold more abundant cellular GTP is concentration- driven.[49] RAS proteins vary in the rate of nucleotide exchange, but generally, they all have a relatively low rate of intrinsic nucleotide exchange. Hence, GEFs such as SOS are required to amplify the exchange rate. The nucleotide exchange and, consequently, the activation of RAS signaling are regulated by the balance between the GEF induced nucleotide exchange and GAP mediated GTP hydrolysis.[50]

RAS proteins are in a state of a dynamic switch between the GDP and the GTP bound form. Upon binding of GTP to the nucleotide binding site, conformational changes occur due to the formation of hydrogen bonds between the γ phosphate and threonine 35 and glycine 60 of switch I and switch II regions, respectively.[51] GTP-bound RAS represents the active RAS form because effector proteins have higher affinity for the GTP-bound RAS than for the GDP-bound RAS. Upstream activation of RAS is regulated by various external stimuli, such as growth factors which bind to receptor tyrosine kinases (RTKs) on the cell membrane surface. This is followed by transmembrane signal transmission, causing dimerization of RTK and activation of RAS.[47]

RAS proteins play a vital role in the cell by activating various downstream signaling pathways (Figure 3), including RAF– mitogen activated protein kinase (MEK)– extracellular signal-regulated kinase (ERK)/ mitogen-activated protein kinase (MAPK). Additional downstream pathways involve phosphatidylinositol 3-kinase (PI3K)–AKT– mammalian target of rapamycin (mTOR) and RALGDS–RAL. These pathways collectively regulate vital cell processes such as the cell cycle, apoptosis, cell division and differentiation, and cell survival.[52]

KRAS, HRAS and NRAS genes encodes for the three major RAS isoforms: KRAS, HRAS and NRAS, respectively. The amino acid sequence 1-165 at the N-terminus of these three isoforms is approximately 92–98% conserved. Within this region, residues 1-86, representing the G-domain, is 100% identical. As a result, these three RAS isoforms share similar GTP binding and hydrolysis function.[53]

RAS mutations typically involve single base mutations, predominantly occurring at three positions: codons 12, 13 in the P-loop and codon 61 in switch II.[48,54] The replacement of the glycine amino acid at positions 12 (G12) and 13 (G13), or the

glutamine residue at position 61 (Q61), with other amino acids, except proline, interfere with the binding of GAP to the GTPase site of RAS, preventing the conversion of RAS from the GTP to the GDP-bound form.[55]

The most frequently mutated RAS isoform is KRAS, with codon G12 being the most affected. G12C, G12D and G12V mutations account for 90% of all KRAS mutations. In pancreatic ductal adenocarcinoma, 40% of cases have showed G12D, while G12C and G12V have been reported in 30-50% and 25% of cases in colorectal cancer and non-small cell lung cancer, respectively.[56,57] HRAS mutations are more prevalent in bladder carcinoma and squamous cell carcinoma especially G12V. While NRAS mutations are more have been linked to melanoma in the form of Q61R and Q61K, and to acute myeloid leukemia in the form of G13D and G12D.[58]

For more than a decade, RAS has been described as "undruggable" due to the lack of binding pocket that allow covalent binding of small molecule inhibitors to the RAS surface, except for the nucleotide binding pocket, which has a picomolar affinity for GTP/GDP. Recent studies have revealed a high mobility in switch II, particularly in $KRAS^{G12C}$ when in the GDP state.[59] Consequently, there has been extensive investigation of the Switch-II pocket (SII-P) for the development of $KRAS^{G12C}$ covalent inhibitors. Several generations of inhibitors have been developed, with the most notable among them being ARS853, ARS6120, AMG510, and MRTX849. ARS853 was the first $KRAS^{G12C}$ covalent inhibitor exhibiting high potency in *in vitro* studies. However, when evaluated *in vivo*, the drug did not replicate the same *in vitro* efficacy in mouse tumor models. It encountered challenges such as poor bioavailability and a short plasma half-life, ultimately leading to its discontinuation from pre-clinical experiments.[60] Later, ARS1620, another inhibitor targeting the Switch II pocket, was developed. ARS1620 has been the first inhibitor to demonstrate success *in vivo*.[61]

Similar to ARS1620, AMG510 was designed to target the cysteine residue in the Switch II pocket. Moreover, it exhibits the capability to occupy a cryptic pocket formed by the side chains of histidine 95 (H95), tyrosine 96 (Y96), and glutamine 99 (Q99), resulting in a 10 folds increase in potency.[62] Another inhibitor, related to ARS1620 and AMG510, has been developed and refined to yield MRTX849. This compound demonstrated exceptional results in clinical trials, which ultimately led to the approval of MRTX849 (adagrasib) and AMG510 (sotorasib) by the Food and Drug Administration (FDA). Ongoing research continue to explore combination therapies and investigate potential resistance mechanisms to further enhance the therapeutic efficacy of these inhibitors.[49,63-66]

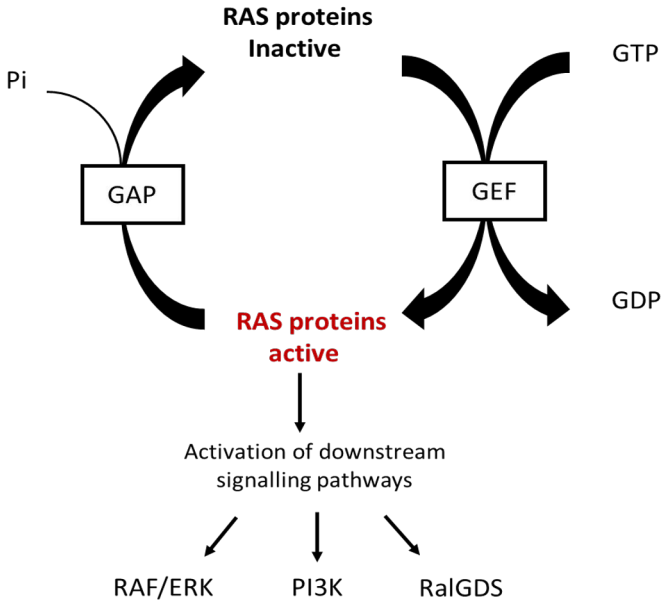

Figure 3. RAS proteins regulation by guanine nucleotide exchange. RAS proteins are activated by exchange of GDP with GTP by the action of GEF, then activated form induces the downstream effectors. Negative feedback occurs through GAP, which stimulates the GTPases mediated hydrolysis of GTP into GDP and Pi, thus restoring the inactive form of the protein.

2.1.2.2 Diseases related to GTP

The clinical effects of GTP are either related to abnormalities in GTP cellular level or dysfunction of GTP processing enzymes. Alteration of GTP level is associated with multiple congenital disorders affecting different body organs. Kelley-Seegmiller and Lesch-Nyhan syndromes are hereditary disorders characterized by an abnormal purine metabolism resulting from the partial or complete loss of HPRT1 function. This leads to the accumulation of uric acid in the blood, causing tissue damage.[67–70] Additionally, mutations in IMPDH were recently reported to cause autosomal dominant blindness and peripheral neuropathy, respectively.[71] The genetic autosomal dominant disease of GTP cyclohydrolase 1 (GCH1) deficiency is another inborn disease characterized by dystonia in early childhood and high risk of parkinsonism.[72] GCH1 is an enzyme that catalyzes the formation of 7,8-dihydroneopterin triphosphate from GTP, which is then converted into tetrahydrobiopterin (BH4). BH4 plays a key role in biosynthesis of neurotransmitters and nitric oxide.[73]

Furthermore, GTP depletion has beeen recognized as a triggering factor for cell death, which is the main pathogenesis and etiological factor for ischemic renal

injury.[74] This effect was reversed as early as 1 hour after supplementation of GTP.[75] Recent work has demonstrated that the imbalance of guanine nucleotide stimulates activation of replication stress signaling and leads to impaired cell division by prolongation of S phase of cell growth cycle.[76]

While free GTP has an essential role within the cell, GTP bound to RAS proteins also plays a critical role in regulation of cell functions. Harvey RAS (HRAS), Neuroblastoma RAS (NRAS), and KRAS isoforms of Ras family, are mutated in 30% of malignant tumors in humans, particularly at the codons of Gly12, Gly13 and Gln61.[77] These point mutations cause RAS to be locked in the GTP active form, resulting in uncontrolled cell division.[78] Consequently, RAS oncogenes generate uncontrolled cell division due to the persistent induction of RAS signaling pathways.[40,58,79,80] Especially in colorectal cancer, non-small cell lung cancer and pancreatic ductal carcinoma, KRAS mutations are predominant, whereas NRAS and HRAS are associated with malignant melanoma and bladder cancer, respectively.[81]

In addition to cancer, GTP-driven dysregulation of RAS signaling has been reported to cause various abnormalities.[82] Among these are several neurodegenerative diseases, such as diabetic neuropathy due to the downregulation of the RAS GTPase-activating-like protein 1 (IQGAP1), an effector of ERK pathways.[83] Neurofibromatosis is another condition resulting from RAS/ mitogen-activated protein kinase (MAPK) pathway dysregulation, along with Alzheimer's and schizophrenia.[84–86]Additionally, Noonan's syndrome, a developmental disease, is caused by exaggerated RAS/ ERK pathway due to hyper activation of the mutated GEF (SOS1).[87]

2.2 Methods for nucleotide monitoring

Before providing a comprehensive summary of methods for nucleotide detection, a concise overview of methods used for measuring protein stability will be introduced. This is particularly relevant due to the known interaction of GTP with small GTPases and inhibitors with RAS mutants, and the significant relevance of this ligand binding to the thermal stability of GTPases. This section will focus on common methods applied for measuring the thermal stability of small GTPases: Differential Scanning Calorimetry (DSC), Circular Dichroism (CD) spectroscopy, and Differential Scanning Fluorimetry (DSF).

DSC is widely recognized as the gold standard for measuring thermal shifts in proteins. It is considered an accurate tool for monitoring protein unfolding, providing direct data on thermodynamic parameters.[88] On the other hand, CD spectroscopy is another established method for monitoring thermal stability. It detects the thermal stability of proteins by measuring the temperature-dependent change in CD spectra. CD is highly valued for studying protein secondary structure and protein-ligand

interactions. However, both techniques are limited by their low sensitivity and low throughput.[89,90]Although CD instrument is more readily available and less complicated than DSC. [91]

On the contrary, DSF, a fluorescence-based method that employs a fluorescence dye, became highly adopted for determining protein thermal stability. [92] The binding mechanism of the DSF dye to target proteins is not yet fully understood, but it is hypothesized that SYPRO Orange, the most commonly used dye in DSF, interacts with the hydrophobic part of the protein exposed during protein unfolding. DSF is an affordable and high-throughput technique for measuring the melting temperature (T_m) of proteins, utilizing simple instrumentation and eliminating the need for labeling target proteins. [93] However, DSF does have certain limitations, including the use of environmentally sensitive dyes to monitor protein unfolding and being highly influenced by the assay buffer components, which may impact the accuracy and reliability of the method.[94] Another significant drawback of DSF is its low sensitivity, with a detection limit within the micromolar range.[95]

The binding of ligands can significantly influence protein stability. [96] In the case of RAS proteins, binding of covalent inhibitors with specific RAS mutants leads to an increase in the Tm values of these mutant proteins due to structural stability.[97] Similarly, guanine nucleotides play a stabilizing role, as it maintains the structural integrity of RAS proteins.[98] Additionally, RAS mutants have different intrinsic nucleotide exchange, consequently affecting their stability. Mutants with fast nucleotide exchange e.g., G13D are less thermally stable, whereas, mutants with slow exchange e.g., Q61R is more stable compared to the wild-type. [99]

NTPs exist mainly within the cells, alongside their phosphate analogues which are fairly similar in structure, therefore a highly sensitive and specific method is required for their analysis.[100] Most of the available methods require sample pre-treatment for nucleotide extraction and only few methods can be used for direct cell imaging. My review will primarily focus on the most commonly utilized methods for qualitative and quantitative analysis of free intracellular nucleotides, with special emphasis on purine NTPs especially GTP. The methods for nucleotide detection will be broadly divided into two categories: non-luminescent based methods and luminescent-based methods, although it can be argued that other methods are available for nucleotides detection. The non-luminescent based methods include colorimetry, chromatography, and CE, whereas the luminescent-based methods include chemiluminescence (CL), and fluorescence. Each of these methods has its own advantages and limitations, and the selection of method depends on the specific application and the needed sensitivity and specificity.

2.2.1 Non-luminescent based methods for nucleotide monitoring

2.2.1.1 Colorimetric assays

Colorimetric detection is a simple, rapid and inexpensive method that can be used for studying biological samples. The principle of colorimetry is based on measurement of light absorbance at specific wavelengths due to change in color, so that the quantity of light absorbed is directly proportional to the concentration of the target analyte.[101] Currently, the majority of available colorimetric assays are designed for ATP detection, while comparatively few assays have been developed for GTP detection. Most of the colorimetric assays have been designed for ATP and utilize gold nanoparticles (AuNPs). However, other methods, such as those utilizing supramolecule-based and hemin-G-quadruplex aptamers, have also been developed to improve the assay sensitivity.[102]

AuNPs are popular tools in ATP colorimetric sensors due to their unique optical and physical characteristics, such as high extinction coefficient and distance dependent color change.[103,104] AuNPs can also be coated with aptamers to form AuNPs aptasensors with high specificity and sensitivity to the target NTP.[105] Labeled aptamers might offer better assay sensitivity and specificity, but are more complex and expensive than non-labeled aptamers.[106] Additionally, DNA aptamers are more preferred than RNA aptamers because DNA aptamers are more stable.[107] The introduction of complex structures in the aptamer configuration such as stem-loop and bulge-loop structures, resulted in higher affinity, but it is not necessarily associated with higher specificity.[108,109] This emphasizes that the structure of the aptamer has a significant impact on both affinity and selectivity to GTP.

Typically, AuNPs remains separate and maintains the red color in absence of target ATP, however, in presence of ATP, binding to the aptamer results in salt-induced aggregation of nanoparticles manifested as a visible blue-shift change in color (Figure 4). The aptamer structure is designed to have a binding preference to ATP. The sequence is optimized to form a tertiary structure specifically with ATP, leading to formation of a stable folded complex upon binding.[110] The current AuNPs aptasensors can also be modified to amplify the signal. However, preparation of modified nanoparticles is a tedious and time-consuming process.[110,111] Initially, aptamer-modified AuNPs demonstrated a detection limit of 100 nM for the detection.[112] Subsequently, an enhanced sensitivity in the picomolar range was achieved by employing aptamer-based sensors that combine AuNPs with nanostructures, enabling an ultrahigh sensitivity.[113] A similar principle can be applied for GTP detection, although it is not yet available.

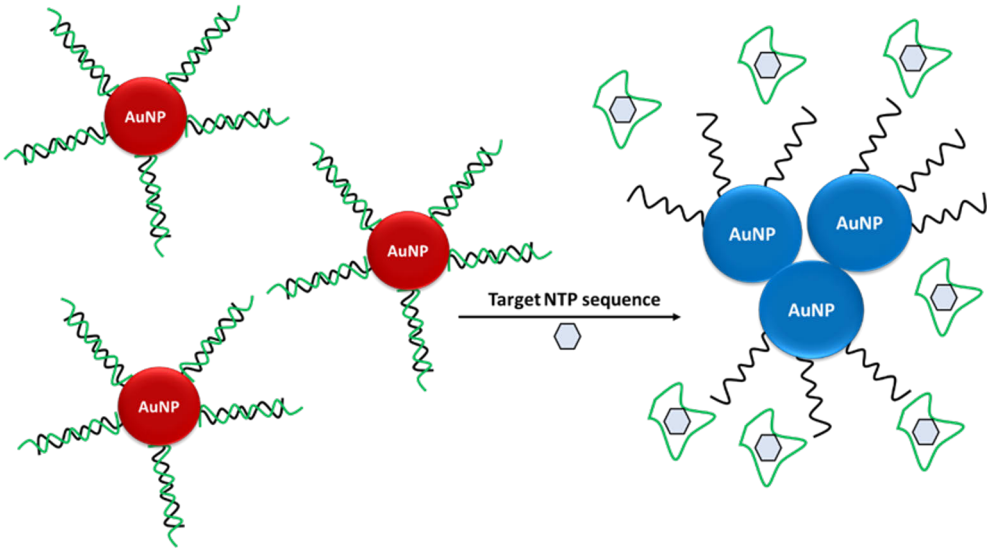

Figure 4. Basic principle of colorimetric detection of NTPs by AuNPs aptasensors. AuNPs with immobilized aptamers, designed to have a binding preference for the target NTP, are present in a stable form in absence of the target NTP, therefore a visible red color is shown. Upon dissociation of the aptamers from the AuNPs and their hybridization with the target nucleotides, AuNPs become unstable leading to an aggregation-induced change into blue color.

Another modification for improving AuNPs aptasensors sensitivity is based on enzymatic signal amplification. This approach relies on recognition of the specific DNA sequence within the DNA probe introduced to the reaction by the endonuclease enzyme. In absence of the target NTP, the DNA probe binds to the AuNPs aptamers resulting in aggregation induced blue color. In contrast, presence of target nucleotide allows the formation of AuNPs-target complex which triggers the endonuclease induced cleavage of the DNA probe into short fragments incapable of hybridizing to the AuNPs aptamers.[114] Several other colorimetric assays utilize DNAzymes, which typically consist of a high guanine content (G-quadruplex) aptamer of hemin. Hemin acts as a cofactor in numerous enzymatic reactions, resulting in formation of a colored product.[113,115]

Other colorimetric assays have been developed for the detection of GTP associated with GTPase activity. One strategy is measuring GTPase activity by monitoring Pi production associated with GTP hydrolysis. Another approach for Pi detection as an indicator of GTPase activity is an enzyme-linked spectrophotometric assay. The method relies on using 2-amino-6-mercapto-7-methylpurine ribonucleoside as a substrate for purine-nucleoside phosphorylase and measuring the change in absorbance at 360 nm.[116]

Colorimetric methods for nucleotide monitoring have multiple restrictions, including low sensitivity with a limited quantification range, liability to interference and challenging detection in complex biological matrices. These drawbacks can significantly limit the reliability and applicability of colorimetric assays.[117–119]

2.2.1.2 Chromatography

Chromatography is widely used for nucleotide detection. These methods provide efficient separation and simultaneous detection of nucleoside mono-, di- and tri-phosphate analogues as well as other smaller molecules such as nitrogen bases, xanthine, hypoxanthine moieties and nicotinamide adenine dinucleotide (NAD).[120]

Liquid chromatography (LC)

Here, some of the most promising LC methods for the separation of nucleotides will be discussed in detail. The following chromatographic techniques: anion exchange liquid chromatography (AELC), ion-pairing liquid chromatography (IPLC), and hydrophilic interaction liquid chromatography (HILIC) will be covered, to gain a deeper understanding of the strengths and shortcomings of each technique for the separation and analysis of nucleotides.

In liquid chromatography (LC), separation depends on the interaction of sample analytes present in a liquid mobile phase with the solid stationary phase. Typically, compounds bound to the stationary phase are eluted by changing solvents.[121] Recently, LC has become the most dominant method for separation of nucleotides. Nucleotides and their analogues vary in polarity based on the number of Pi groups with nucleosides di- and triphosphate being the most hydrophilic and are therefore commonly separated by AELC or IPLC.[122,123] However, nucleosides and nucleoside monophosphates, being less hydrophilic, require a combination of IPLC with reverse-phase liquid chromatography (RPLC) to achieve optimal separation.[124,125] Although AELC and IPLC techniques are widely used, they have some limitations which can affect the quality of the separation such as pH and buffer dependence, column instability, and ion suppression. To overcome these limitations, HILIC was proposed as a promising alternative. HILIC provides several advantages over AELC and IPLC, including more efficient separation, lower ion suppression, and compatibility with mass spectrometry (MS) detection.[126,127]

Beyond the selection of separation column, sensitivity and separation efficiency are profoundly influenced by sample preparation, column length and the detector used.[128] HPLC employs high pressure which makes it superior to low pressure liquid chromatography, as high pressure enhances separation efficiency, resolution, reproducibility, and the sensitivity of detection (Figure 5).[129]

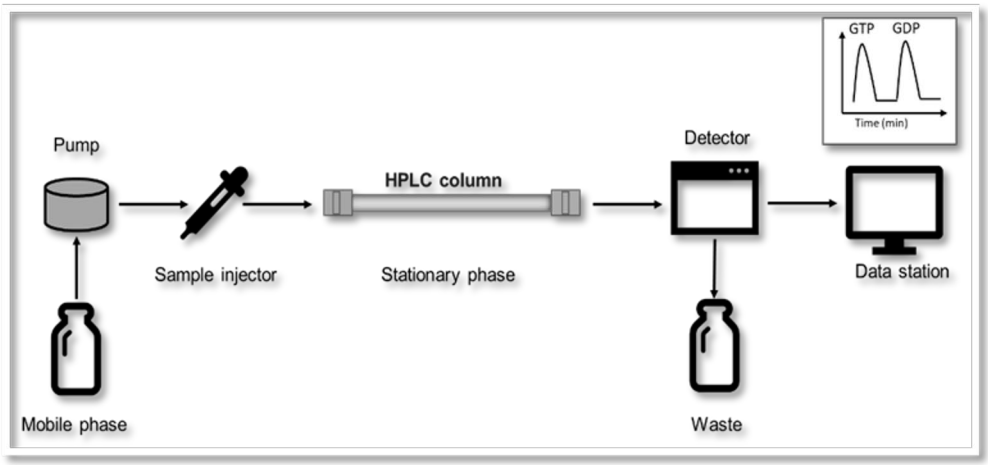

Figure 5. HPLC system. Eluent is pumped through high pressure tubes together with the sample, then travel through the column, where analytes interact with the stationary phase and then eluted and identified by the detector. The detector is connected to a computer for display of chromatogram which shows peaks of different analytes. Distinct retention times and intensity of the peaks are used to identify and quantify the products.

IPLC is performed using an ion pairing column and ion pairing reagents. To separate negatively charged nucleotides, pairing is achieved with cationic reagents, commonly alkylamines and tetrabutyl ammonium salt (Figure 6).[130] The pH of the mobile phase and the selection of ion pairing reagents are critical for optimization of nucleotide separation by IPLC, as they influence the solubility and stability of nucleotides.[131] The non-volatile mobile phase utilized in IPLC is incompatible with ESI/MS. Therefore, IPLC has typically been coupled with UV-vis or fluorescence detection after derivatization of nucleotides to increase its absorbance or confer fluorescent-like characteristics. This can be achieved by addition of a chromophore or a fluorophore, respectively.[132,133] Ion-pairing reversed-phase liquid chromatography (IP-RPLC) is a modified approach, developed to overcome this limitation.[134] IP-RPLC combines both IPLC and RPLP techniques. The method involves stationary and mobile phases similar to those used in RPLC. In addition, cationic pairing reagents e.g., alkyl amines, are introduced to the water/acetonitrile mobile phase. For separation of nucleotides, positively charged ion pairing molecules, retained on the stationary phase by their nonpolar ends, interact with the negatively charged nucleotides (Figure 6).[135] In RPLC, the order of compound elution depends on their hydrophobicity. Polar compounds elute first, followed by less polar analytes, such as nucleoside monophosphates, as the mobile phase polarity gradually decreases (Figure 7).[136,137]

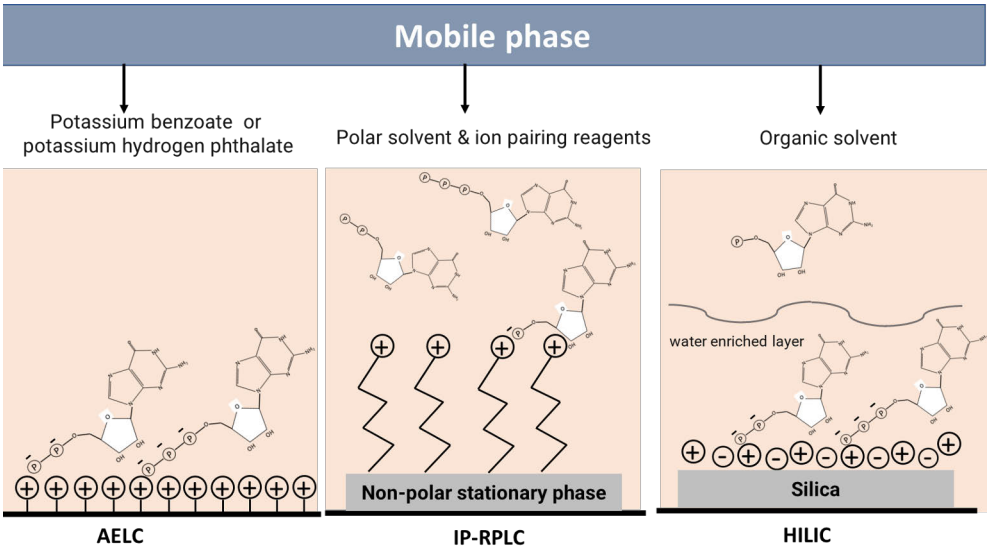

Figure 6. Principle of AELC, IP-RPLC and HILIC for nucleotide separation. In AELC, positively charged particles or resin is applied to attract the negatively charged nucleotides, mobile phase is supplied by potassium benzoate or potassium hydrogen phthalate to control pH and favour separation of highly charged anions. IP-RPLC method combines both IPLC and RPLP techniques. The method entails an aqueous buffer containing acetonitrile and ion pairing reagents which are anchored to the nonpolar stationary phase through their hydrophobic ends. Separation occurs when negatively charged nucleotides bind to the positively charged ion pairing molecules retained on the stationary phase. HILIC employs a polar stationary phase and an organic mobile phase, which allows the formation of a water rich layer through which the more hydrophilic analytes migrate towards the solid phase.

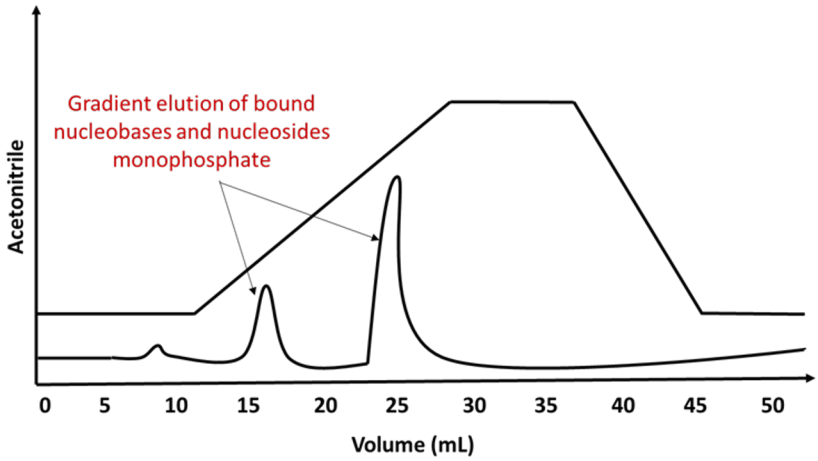

Figure 7. Reverse phase liquid chromatography. In RPLC, mobile phase is formed of polar solvents, typically a mixture of water and organic solvent e.g., acetonitrile. The more hydrophobic nucleotide species (NMP and nucleobases) bound to C8 or C18 column are eluted by decreasing polarity of mobile phase, which is achieved by increasing acetonitrile to water ratio.

Similar to IPLC, AELC is based on ion exchange by immobilizing negatively charged nucleotides on positively charged resin or particles under acidic pH conditions (Figure 6). However, AELC suffers from a reproducibility problem due to its high dependence on pH of the mobile phase, which might change retention times.[138] Other disadvantages of AELC are the high salt content of the solvent, which is not compatible with MS detection, and the poor selectivity of the method due to possible co-elution of closely related nucleotide species along with the target nucleotide.[139,140]

HILIC, on the other hand, is considered more compatible with MS, and is currently the second common LC mode coupled with MS after RPLC.[141] HILIC/MS has been utilized for nucleotide and nucleosides detection in various sample matrices such as meat products, yeast extracts, infant formula, and biological samples.[142–148] HILIC, occasionally referred to as aqueous normal phase chromatography, combines the polarity of the stationary phase from normal phase chromatography, the mobile phase composition of reverse phase chromatography, and the analyte selectivity seen in ion exchange chromatography.[149] In HILIC, the stationary phase is typically made of bare silica or silica modified with highly hydrophilic functional groups e.g., amide or imide groups to bind the ionic polar nucleotides. The mobile phase containing high organic solvent e.g., acetonitrile/low water mixture, allows better solubility of nucleotides and maximize retention of polar analytes on the column ((Figure 6, Table 1).[149] The separation of analyte occurs by partitioning between the mobile phase rich in organic solvent and the hydrophilic layer on the stationary phase.[149,150] However, HILIC requires optimization of mobile phase composition as well as proper column selection to obtain optimal separation and MS sensitivity.[151]

Table 1. Differences between IPLC, IP-RPLC and HILIC.

	IPLC	**IP-RPLC**	**HILIC**
Stationary phase	Ion-pairing column	Non-polar column e.g., C8 & C18	Polar e.g., silica or modified silica
Mobile phase	Ion pairing reagents	Polar solvent mixture (high water to acetonitrile ratio) with added ion pairing reagents	Polar organic solvent e.g., acetonitrile with low water content
Application	Separation of highly polar compounds e.g., NDP, dNDP, NTP & dNTP	Separation of less polar compounds e.g., NMP, dNMP & nucleobases	Separation of highly polar compounds e.g., NTPs, dNTPs, NDP & Dndp

LC/MS

UV-vis detection has been widely used in combination with chromatography. Nucleotides strongly absorb UV light at wavelength range 260–270 nanometers (nm) due to presence of conjugated double bonds in their structure.[152] However, UV

detection is limited by its low sensitivity and specificity.[153] In the context of nucleotide analysis in cells, the low detection limit of UV-vis detection is challenging as it necessitates a substantial amount of starting cellular material.[154,155]

MS is nowadays the most widely accepted alternative of UV-vis for nucleotide detection following chromatography. MS is considered 100–1000 folds more sensitive than UV-vis detection. It identifies nucleotides through the analysis of their mass-to-charge ratios (m/z) and identification of their molecular weights.[156] MS is a versatile analytical technique that can be combined with various separation methods including LC, thin layer chromatography (TLC), gas chromatography (GC) as well as non-chromatographic methods such as CE.[100] MS identifies and quantifies different molecules in a complex sample by ionization of molecules and identification of ions based on their mass-to-charge (m/z) ratio. Electron spray ionization (ESI) and matrix-assisted laser desorption ionization (MALDI) are two of the most prevalent ionization methods for nucleotide detection with MS.[157] ESI is a soft ionization method which relies on using unpaired electrons for protonation and deprotonation of the fragment ions. For nucleotide analysis, ESI negative ionization mode is often used, as it leads to deprotonation of the Pi group, and improves the signal level. It also provides better fragmentation and more information about nucleotide structure.[158–161] MALDI is another soft ionization technique widely utilized for nucleotide analysis with MS, it involves sample mixing with a specific matrix and ionization by laser beam.[157]

A common approach to improve the performance of LC/MS is precolumn derivatization, in which nucleotides are modified to improve their detection. Several derivatization methods have been proposed for LC/MS analysis of nucleotides in biological samples, including benzoyl acid anhydride and hexamethyleneimine.[162] Binding of these derivates to nucleotides increases their hydrophobicity which consequently improves retention on the nonpolar stationary phase in RPLC, even without using of ionic pairing reagents.[163,164]

After separation by LC, quantification of nucleotides is done by MS. Both direct and indirect methods have been developed for quantification. The direct quantification is the most widely used and is compatible with IP-LC or HILIC for separation of mono-, di- and trinucleotides into separate fractions followed by quantification of different nucleotide species by MS.[124] However, other LC methods such as IP-RPLC may not retain different phosphate analogues of nucleotides in separate fractions due to poor interaction with the column. In such cases, an indirect quantification is usually used. An indirect method involves dephosphorylation of nucleotides by acid or alkaline phosphatase. Nucleosides are then retained much better on the RP column compared to their triphosphates precursors and quantified by MS as surrogates to the parent compounds.[165]

To obtain higher sensitivity, more precise quantification and improved knowledge of nucleotide structure, liquid chromatography-tandem mass spectrometry (LC-MS/MS) has been applied for nucleotide analysis. It is nowadays considered as the gold standard method for the detection and quantification of nucleotides. The principle of tandem mass spectrometry (MS/MS) is based on using two mass analyzers. A specific product ion is selected from the mixture of ions generated by the first analyzer and directed towards the collision cell for further fragmentation. The product ions are then separated by the second mass analyzer based on m/z ratio.[166] Triple-quadrupole and ESI are commonly combined, for nucleotide analysis by MS/MS. These two techniques together offer high sensitivity and selectivity which enables accurate identification and quantification of each nucleotide variant. ESI provides soft ionization of large biomolecules without excessive fragmentation of intact nucleotides. Triple-quadrupole, on the other hand, provides information on the nucleotides structure by selection and further analysis of the specific precursor ion of each nucleotide which is crucial for differentiation of nucleotides.[124,167–170]

While HPLC/MS is a powerful technique, it comes with several limitations. One of the primary obstacles is the high cost of instrumentation and maintenance expenses, which can limit access in some laboratories. Additionally, the complexity of the technique requires well-trained personnel for development, optimization, and interpretation of data.[171,172] Another limitation is its low throughput as HPLC/MS tends to be time-consuming and less suitable for analyzing a large number of samples.[173] Moreover, nucleotide analysis using HPLC/MS requires large sample volume and extensive sample preparation including nucleotides extraction and derivatization.[174]

Gas chromatography

In comparison to LC, GC is a less useful technique for nucleotide analysis. The principle of GC is applied for separation of volatile and thermally stable compounds. Compounds are vaporized and carried by an inert gas mobile phase to interact with a solid or liquid stationary phase.[175] Efficient nucleotide analysis using GC faces two primary challenges: the thermal instability of nucleotides and their high polarity, which results in strong interactions with the stationary phase, leading to poor separation.[176–178] Consequently, this method necessitates the derivatization of nucleotides before analysis to enhance their volatility.[179]

2.2.1.3 Capillary electrophoresis

LC is a laborious and time-consuming process, where the sensitivity and quality of separation depends on a combination of multiple factors.[180] In addition to

chromatography, CE can be employed for nucleotide separation and coupled with MS for detection. However, it requires a specific interface method because most of CE buffers are not suitable for direct connection with MS.[181] The CE separation principle is based on migration of charged molecules under the effect of an electric field (Figure 8). CE/MS is a powerful tool with high-resolution for analysis of highly ionic molecules and has been extensively investigated for nucleotide analysis.[182–186] This method offers comparable sensitivity to HPLC but also provides additional benefits, including smaller sample volume and significantly shorter analysis time.[187,188] However, sample preparation must be optimized to reduce analysis time and improve recovery.[189,190] Additionally, CE/MS for anions has been associated by corona discharge formation, which interferes with reliability and reproducibility of the detection.[191] Other possible alternatives to MS, which have been coupled with CE for detection of nucleotides or nucleotides associated molecules, include UV-vis, CL, and fluorescence. However, these typically require modification of nucleotides for detection. MS, on the other hand, offers a higher sensitivity and provides more information about the matrix and other molecules present in the sample, therefore it is more widely applied in combination with CE.[189,192–194]

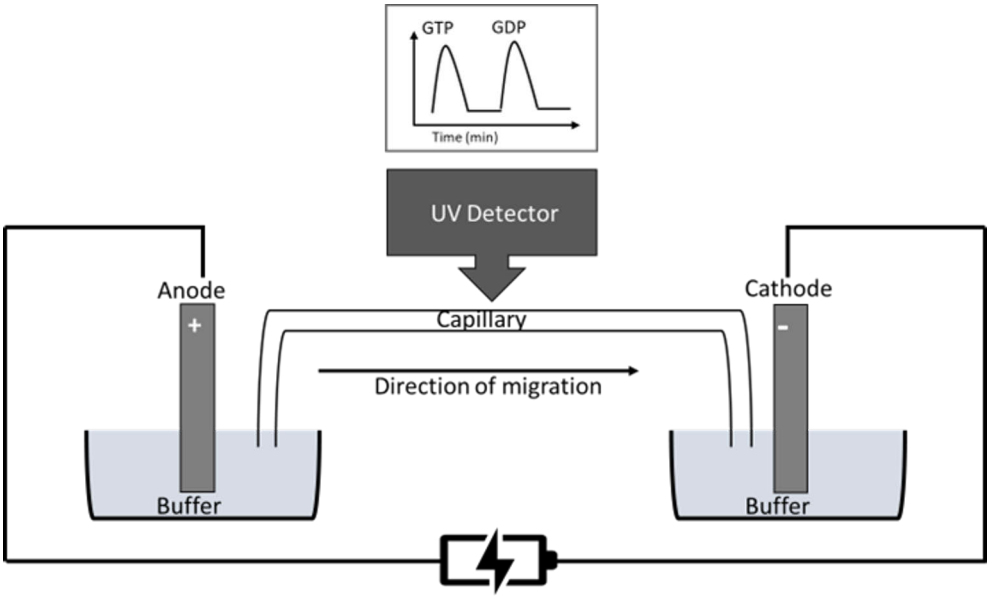

Figure 8. CE coupled with UV-vis detector. The principle of CE for separation of nucleotides relies on migration of negatively charged nucleotides in capillary tube, when an electric field is applied to the sample buffer. Speed of travel in the capillary depends on number of charges and size, so that smaller and more oppositely charged molecules migrate faster. The overall direction of migration is towards the cathode, nucleotides with more negative charges migrate slower than nucleotide analogues with less negative charges.

2.2.2 Luminescent-based methods for nucleotide monitoring

Luminescence is the release of energy from the excited state of a luminophore due to electron transfer from the ground state (S_0) to a higher energy level status. It can be classified according to excitation mechanism into photon and non-photon luminescence. Non-photon luminescence methods include CL and electrochemiluminescence (ECL), do not require an external light source for excitation. Conversely, photon luminescence methods, also known as photoluminescence, involves the excitation of a molecule by photons, so that an electron transfers from the ground state to the higher energy level state, subsequently relaxing to the ground state and emitting photons. Several forms of photoluminescence include fluorescence, delayed fluorescence, time-resolved luminescence (TRL) and phosphorescence.[195]

Jablonski diagram illustrates the energy transitions in fluorescence, phosphorescence and TRL, all of which share a common photon absorption phase followed by different relaxation mechanisms. In fluorescence, the relaxation of the excited electron from the first singlet state (S_1) to S_0 results in the emission of energy, typically occurring in a few nanoseconds. Occasionally, instead of the S_1 to S_0 transition, intersystem crossing (ICS) occurs, leading to electron transition from the S_1 state to the first triplet state (T_1). The S_1 to T_1 transition can result in various types of luminescence. Phosphorescence is formed by ICS and relaxation from T_1 to S_0, with photon emission. In phosphorescence, the process of electrons relaxation from T_1 to S_0, is forbidden due to different spin of the two electronic states. Therefore, phosphorescence has a prolonged emission time of 0.001-100 seconds.[195,197] In other cases, E-type delayed fluorescence arise from reversed ICS from T_1 to S_1 if the energy difference between S_1 and T_1 is small. Alternatively, P-type delayed fluorescence occurs due to transition from S_1 to S_0, as two excited T_1 electrons collide, producing energy that excites one electron back to S_1.[198]

On the other hand, in TRL, after the electron crosses to the T_1 state, intramolecular energy transfer from the excited ligand to the central ion occurs through relaxation from T_1 to ^5D. The lanthanide ion, after accepting energy from the excited chelate, undergoes an energy transition from ^5D to ^7F (Figure 9).[3] This emission typically occurs on a millisecond scale, therefore lanthanide chelates are characterized by having a long emission lifetime (Figure 9).[199]

Förster resonance energy transfer, also known as fluorescence resonance energy transfer (FRET), is a form of fluorescence in which two chromophores, one acting as a donor and the other as an acceptor, interact by exchanging energy.[200,201] The magnitude of FRET depends on multiple factors, with the most crucial being the donor-acceptor distance and their fluorescence spectra. FRET requires an overlap between donor emission and acceptor excitation, as well as a short intermolecular distance of approximately 10 nm between the donor and the acceptor.[201,202] In FRET,

the donor is fluorescent, while the acceptor can be either fluorescent or non-fluorescent. Excitation of the donor and the subsequent energy transfer to the acceptor is not accompanied by emission of donor fluorescence in case of non-fluorescent quencher.[203] Depending on the type of acceptor, FRET is detected by either an increase in the acceptor signal or a decrease in the donor fluorescence signal, or both.[204]

Bioluminescence resonance energy transfer (BRET) is a type of FRET that does not require an external light source to excite the donor fluorophore and stimulate the energy transfer. BRET is most often used for cellular protein studies with luciferase as a donor and a fluorescent protein or dye as an acceptor (Figure 9).[205]

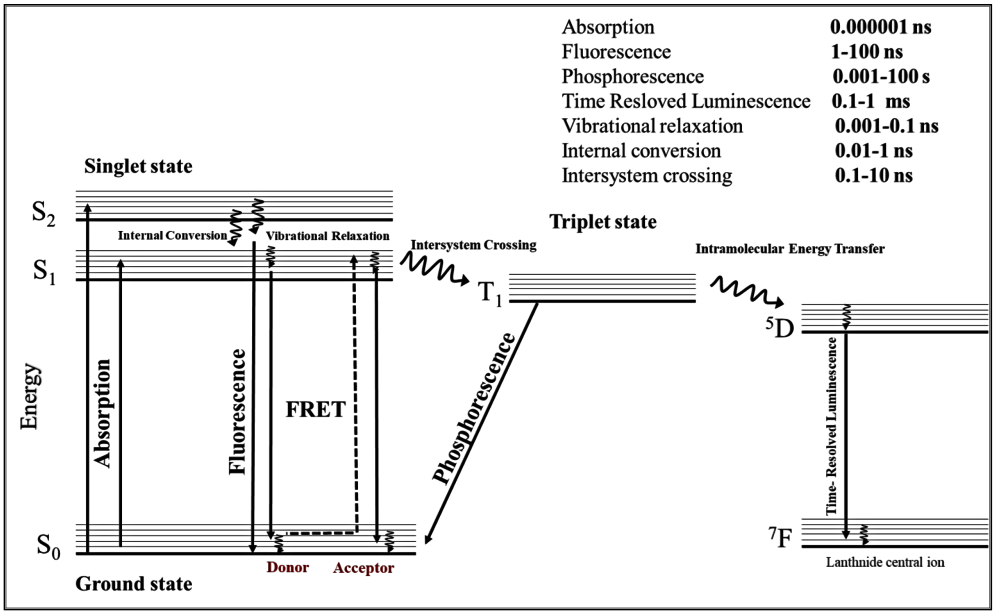

Figure 9. Jablonski diagram. Electron transfer from the ground state S_0 to the higher energy states S_1 or S_2. In fluorescence, after vibrational relaxations and internal conversions, the electron returns to S_0. If an acceptor molecule is within 10 nm from a donor molecule, energy is transferred to the acceptor without photon emission. In case of ICS, energy transition to T_1 takes place before returning to the ground state resulting in phosphorescence. Alternatively, in TRL, relaxation to ^5D state facilitates the energy transfer from the chelate to the central ion ultimately ending with relaxation to ^7F and subsequent photon emission.

In the forthcoming section, luminescent methods for the detection of nucleotides will be discussed. An efficient GTP sensor should recognize both the guanosine and the triphosphate to achieve high sensitivity and specificity. There are numerous methods designed for ATP detection and only a few are available for GTP detection, therefore, I will provide a general review of the methods used for NTPs with particular emphasis on GTP. These methods include chemiluminescent and

fluorescent based sensors. Not all luminescent techniques are applicable in real-time imaging of nucleotides, thus, a separate section will be dedicated for exploring probes specifically designed for live imaging.

2.2.2.1 Chemiluminescent based sensors

CL is a process in which a chemiluminescent enzyme reacts with a chemiluminescent substrate, producing light emission. Unlike other luminescence forms, CL does not require an external light source, making it advantageous in various fields such as biotechnology, molecular biology, and biochemistry.[196] This method can also be applied in biological settings, including biological fluids, cells and tissues.[206] Despite the high sensitivity of CL, the main drawback of this method is the weak signal level and substrate dependence.[207] One of the most common examples of chemiluminescent reactions is the oxidation of luminol- and acridan-based reagents catalyzed by horse radish peroxidase (HRP) in the presence of hydrogen peroxidase, resulting in 3-aminophthalate.This compound decays to ground state and emits photons to obtain stability.[195,208]

The most established chemiluminescent sensors have been developed for the detection of ATP. The chemical sensor's detection relies on the recognition of different structural components of ATP, including the negatively charged phosphate, the sugar moiety, and the adenine ring.[29] A typical example for an ATP chemiluminescent sensor consists of three structures: rhodamine, a xanthene derivative dye that binds to the adenine ring; a phenylboronic acid group (PBA) that binds to the pentose sugar and lastly a diethylenetriamine (DETA), which interacts with the phosphate. In the presence of ATP, these three interactions occur, leading to light emission from the rhodamine. The sensor exhibited a significant fluorescence enhancement upon addition of 0.1 mM ATP and has subsequently been successfully employed for the detection of intracellular ATP at a similar concentration. Nevertheless, the sensor demonstrated a high degree of selectivity for ATP, effectively distinguishing it from UTP, GTP, CTP, GMP, and AMP, although it lacked similar selectivity for ATP when ADP was present.[154,210]

In addition to CL sensors, several ECL techniques have been developed with picomolar sensitivity to ATP. ECL differs from CL in that it involves electrochemical reactions to provide the energy required for the excitation of luminophore in the vicinity of an electrode surface.[211] Due to its high sensitivity, this technique is widely used for detection of nucleotides.[212–214] One example of amplified ECL sensors involves the use of DNA sensors immobilized on a gold electrode. In the presence of ATP, the DNA complex is protected from digestion by exonucleases, because ATP binds to the DNA and stabilizes it, allowing the ECL reaction to occur at multiple positions, resulting in a significantly high signal.[215,216]

Bioluminescence (BL) is a biological phenomenon that takes place inside living organisms, involving a chemical reaction wherein luciferin is oxidized into a light-emitting form by the enzyme luciferase. This process results in the emission of visible light and is considered a form of CL. Importantly, this reaction consumes ATP as a source of energy, making the intensity of light emitted directly proportional to the concentration of ATP.[217] The most well-known luciferase is derived from fireflies, but luciferases from various sources such as jellyfish, bacteria, beetles, and several marine organisms also exhibit BL activity.[218] BL assays are characterized by their high sensitivity and low background.[219] It is also worth mentioning that the sensitivity of BL assays is dependent on sensitivity of the detection platform used. Advances in detection technology over the last decades, have contributed significantly to marked improvement in sensitivity level.[220]

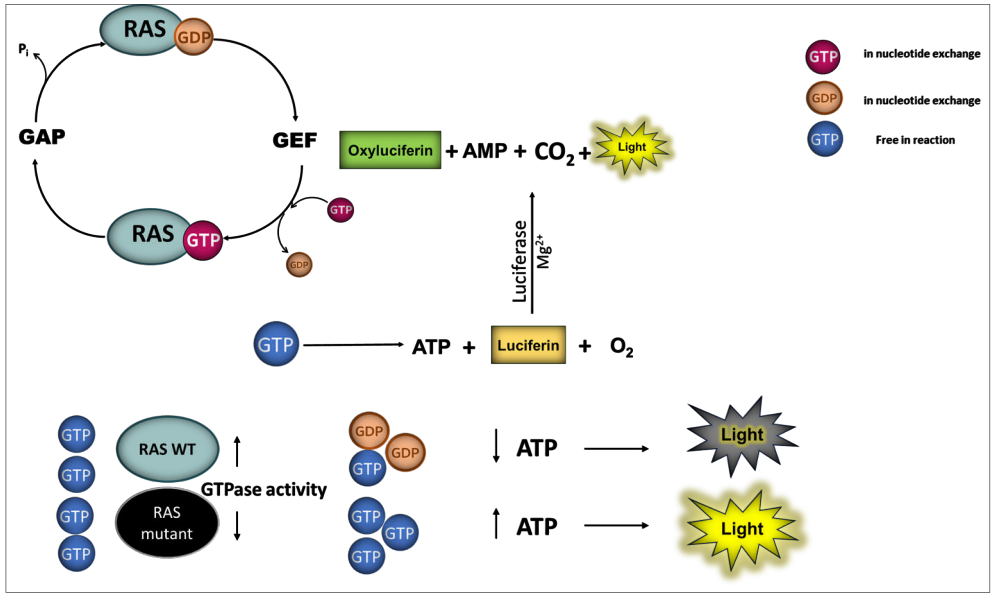

Figure 10. Bioluminescence for GTP detection. GTP remaining after GTPase nucleotide exchange is converted to ATP which is measured by BL. In a BL assay, ATP acts as an energy substrate for the luciferase catalyzed oxidation of luciferin resulting in the emission of photons.

Unlike ATP, which utilizes luciferase for detection, GTP lacks a comparable enzyme. Consequently, GTP detection by BL requires a combination of enzymes in a multi-enzyme system to convert GTP of nucleotide exchange into ATP and then measure ATP by BL (Figure 10), which makes BL a demanding and costly approach for GTP detection compared to methods targeting other nucleotides like ATP.[221,222] The BL-based assay is primarily developed for detection of GTP associated with

GTPase activity. This is because measuring free cellular GTP poses challenges in terms of control and accurate estimation. The challenge arises due to the conversion of GTP into ATP in cellular processes, making it difficult to distinguish between the two nucleotides in free form.

Several fluorescence-based approaches have been developed to detect anion compounds in neutral pH and in biological samples.[223] These sensors are commonly used for the accurate identification of NTPs. More than one approach is often combined to improve the affinity and selectivity of the method. In the context of GTP detection, many fluorescent sensors primarily rely on the recognition of triphosphate, achieved by hydrogen bond formation with pyridinium and imidazolium receptors. Additionally, recognition of guanosine occurs through electrostatic interactions with aromatic structures, resulting in quenching of fluorescence.[224]

Fluorescent aptamers have been widely investigated for nucleotide detection. Aptamers are not naturally fluorescent molecules; however, they can be conjugated with a fluorescent label to form a labeled fluorescent aptasensor. An alternative approach for utilizing fluorescent aptamers in NTPs detection is using unlabeled aptamers. In this method, a mechanism is developed to induce fluorescence emission based on the aptamer's inherent ability to recognize specific nucleotides. This strategy is markedly dependent on the aptamer's affinity to nucleotides, which manifests as a signal amplification, resulting in observable fluorescence.

Recently a promising label-free, fluorescent-based sensor for intracellular GTP detection was developed. This method involves using a DNAzyme, which is capable of self-phosphorylation at the 5' end by hydrolysis of GTP into GDP and Pi. The phosphorylation of the DNAzyme causes a conformational change which allows binding of the phosphorylated DNAzyme to the complementary DNA strand. The double stranded DNA will then be degraded by a specific A Lambda exonuclease, resulting in low signal upon binding of SYBR Green I fluorescent dye (Figure 11).[225] However, it is important to note that the specificity of this method is significantly dependent on the DNAzyme selectivity for GTP. For example, DK2 is highly specific for GTP,[226] while other DNAzymes can also dephosphorylate ATP, thus, cross reactivity with ATP is most likely to occur.[107]

Additionally, Ruthenium (II) intercalating dye is widely studied for development of label-free aptamers for ATP detection. $Ru(phen)2(dppz)]^{2+}$ is typically non-fluorescent in aqueous solution; however, it emits fluorescence when it binds with nucleotides. PicoGreen is another intercalating dye, utilized for development of ATP aptasensor, with metal-enhanced fluorescence (MEF) to amplify the signal and enhance the photostability of PicoGreen.[102,227]

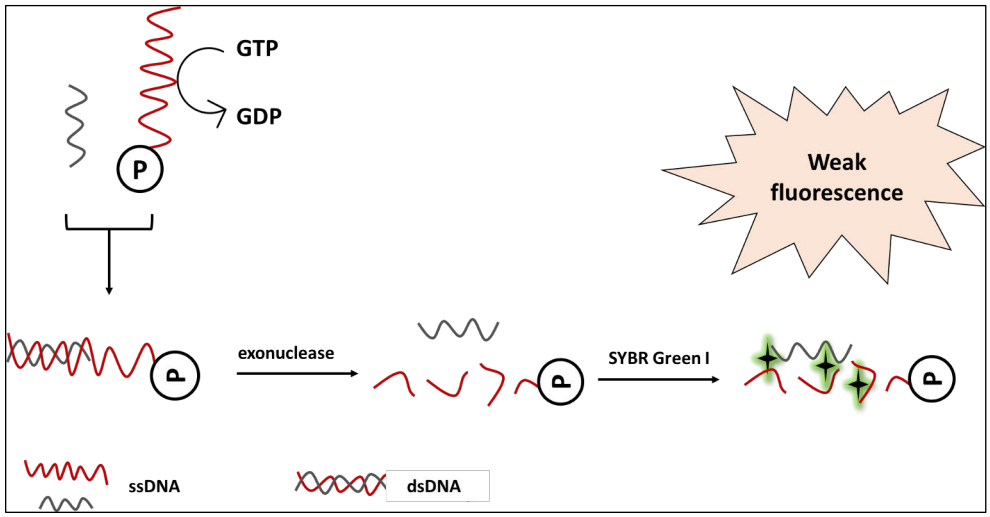

Figure 11. DNAzyme for detection of GTP. The DNAzyme used in this method recognizes only GTP as a substrate for DNAzyme phosphorylation at the 5'end. The phosphorylation causes a conformational change in the DNAzyme which allows the phosphorylated DNAzyme to hybridize with a complementary strand. The formed a double stranded DNA is then degraded by a specific A Lambda exonuclease. SYBR Green I fluorescent dye binds insufficiently to the digested DNA complex resulting in weak fluorescence. Figure is modified from the original.[225]

Other non-aptamer based fluorescent sensors for GTP detection in neutral pH include Metal-based Zn(II)-Dipicolylamine (Zn (II)-DPA) probe and imidazolium derivatives probes. Zn (II)-DPA is a metal ion that targets the ammonium-based anion receptors and interacts with guanine and the two phosphates (β and γ) bound to the nucleoside (Figure 12).[228,229] This metal ion recognition is combined with fluorescent reporter. Imidazolium derivatives probes have also been proven to bind to anion receptors and produce fluorescence quenching upon binding to GTP.[230–233] Conversely, BAB-PDI and Copper based fluorescent probes showed high potential in detecting GTP by exhibiting unique quenching patterns with minor interference from other NTPs and guanosine phosphate analogues.[234,235]

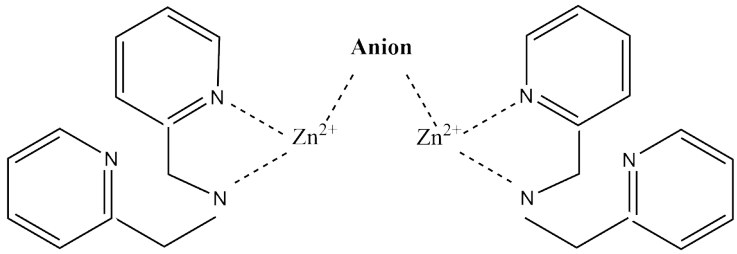

Figure 12. Zn (II)-DPA metal ion interaction with anions. Zn2+ has a high affinity to anions, especially with phosphate groups. Zn (II)-DPA is formed of a tridentate DPA bound to Zn2+ at two nitrogen atoms.

Among other strategies for GTP fluorescence-based detection, pyrene-based probes have been proposed. Examples of this probe include a fluorescent compound, 8-hydroxy-1,3,6-pyrene trisulfonate (HPTS) (Figure 13), and pyrene-modified ribonucleopeptide (RNP) probe.

The HPTS method for GTP detection is based on an indicator displacement strategy, in which HPTS fluorescence is quenched upon binding to a specific receptor and released in the presence of GTP due to HPTS displacement by the higher affinity nucleotide. The distinctive affinity of different nucleotides for that specific receptor, grants the differentiation of GTP from other nucleotides.[236]

On the other hand, the pyrene-modified RNP probe operates by synthesizing a RNP sensor derived from a GTP specific RNA library. This is followed by the modification of the peptide subunit to form a fluorescent labeled peptide that binds covalently to the RNA subunit. The intrinsic fluorescence of the RNP sensor is released from quenching upon binding to GTP. The approach combines the functionality of a fluorescent labeled peptide with the high sensitivity of aptamers. Both the HPTS and pyrene-based probes offer the additional benefit of being compatible with biological sample.[237,238]

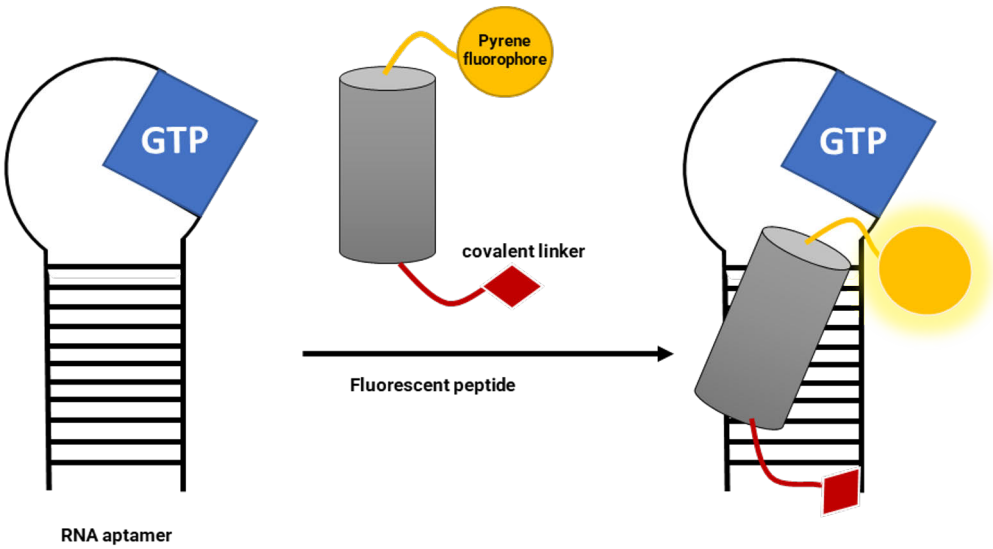

Figure 13. Fluorescent RNP probe for GTP detection. A pyrene-labeled peptide is modified with a linker that can bind covalently to the RNA aptamer forming a covalently bound fluorescent RNP probe to increase sensitivity and allow simultaneous detection of multiple targets. In absence of GTP, the probe fluorescence signal is quenched, however, binding of the target nucleotide stimulates emission of the intrinsic fluorescence. Figure is modified from the original.[237]

2.2.2.2 Live cell imaging

There are numerous well-established methods for measuring NTPs in cells, but only a few have the capability of real-time imaging of NTPs in living cells. The existing techniques are mostly developed for ATP detection.[122] In contrast, the techniques designed for measuring GTP primarily aim at measuring GTP bound to G-proteins.[239–241] Designing an optimal GTP probe is challenging, as it should have high temporal and spatial resolution.

Ratiometric probes have proven successful for live imaging of nucleotides. Ratiometric detection is based on measuring the ratio of two signals at two different wavelengths, one for the analyte of interest and the other for a reference compound with unchanging signal. The presence of the analyte induces a detectable change in the ratio of this dual excitation/emission system. Through signal comparison, the concentration of the analyte can be estimated.[242] Several ratiometric probes have been designed for ATP detection such as QUEEN and PercevalHR. In these probes, ATP binding, induces a change in the excitation wavelength of a circularly rearranged green and yellow fluorescent protein (YFP), respectively. Another ratiometric probe for real-time ATP visualization is ATeams, which measures the FRET signal between a donor cyan fluorescent protein (CFP) and an acceptor YFP.[243–245] A genetically encoded ratiometric probe has recently been developed for GTP detection by inserting a circular permutated YFP (cpYFP) into the bacterial FeoB. FeoB, is a transmembrane G-protein that binds to GTP, resulting in a ratiometric change in the fluorescence signal of cpYFP in presence of GTP.[246] On the other hand, fluorescent aptasensors offer a promising alternative for live imaging and direct quantification of nucleotides. Nano-flares aptasensors are formed of aptamers immobilized on AuNPs with fluorescent reporters. These aptasensors can be applied for imaging ATP in living cells after the cellular uptake of the nano-flares aptamer-modified nanoparticles. In the presence of the target molecules, aptamers bind to the analyte, leading to the release of the fluorescent reporters (Figure 14).[247]

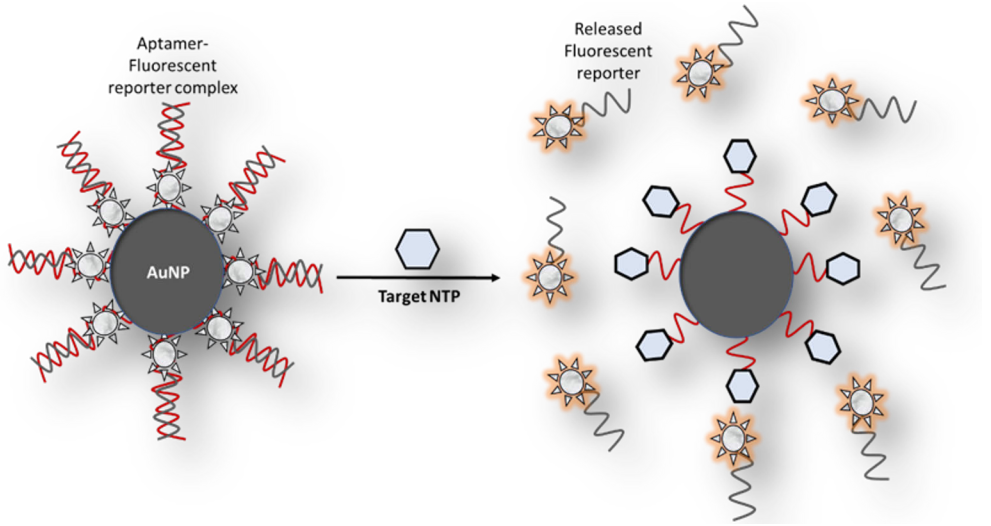

Figure 14. Nanoflare aptamer for ATP detection. A monolayer of aptamers is assembled on AuNP. The fluorescence signal of fluorescent reporters bound to aptamers is released when aptamers bind to the target nucleotides. Figure is modified from the original.[247]

Another aptamer with similar principle is ROX-aptamer, which undergoes active endocytosis after being incubated with the cells. This property makes it suitable for in vivo measurement of ATP. ATP specific ROX-tagged aptamers are assembled to titanium carbide nanosheets, which have a significant quenching efficiency for ROX. Upon binding of ATP, the ROX fluorescence is released (Figure 15).[248] The same principle can be adapted for GTP detection by utilizing GTP-specific aptamers.

Similarly, single-walled carbon nanotube (SWNT), which emits near-infrared fluorescence has been combined with the luciferase assay for live imaging of intracellular ATP. This method is based on BL recognition of ATP by luciferase, followed by the production of the light-emitting luciferin, which quenches the fluorescence of SWNT.[249]

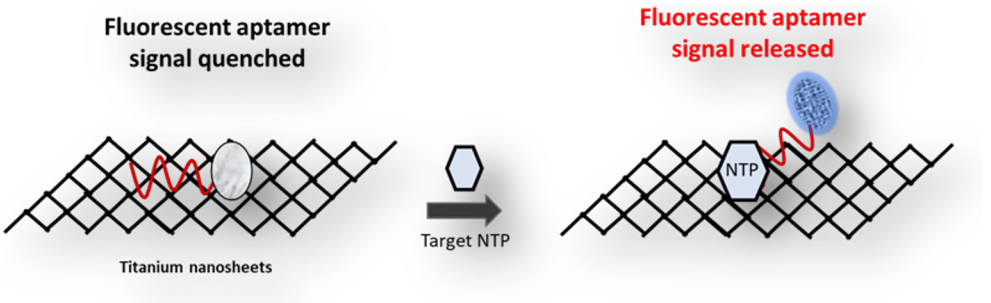

Figure 15. ROX-aptamer for NTP detection. A fluorescent aptamers signal is quenched by titanium nanosheets, however, when the aptamer is bound to NTP, the fluorescence signal is released. Figure is modified from the original.[248]

2.2.2.3 Indirect methods

In addition to direct measurement of intracellular GTP, the concentration can be estimated by measuring cellular GTP/GDP ratio. Various enzymes regulate the interconversion of GDP and GTP during glycolysis and oxidative phosphorylation. Change in GTP/GDP ratio indicates increased GTP hydrolysis due to high mitochondrial energy consumption. High Response of GTP/GDP Ratio Sensor (GRISerHR) is a genetically coded fluorescent sensor that was recently developed for monitoring GTP/GDP ratio in living cells.[250]

Table 2. Review of different methods for detection of nucleotides in cell-based assays.

Method	Principle	Through-put	Typical detection sensitivity	for GTP	Ref.
Colorimetry	Measures absorption and rely on change in color due to interaction of the target NTP with a specific reaction component	High	nM- µM	No not available for free GTP, measures only GTPase activity	104, 110, 114, 117, 251
HPLC + detection	Separates NTPs based on their interaction with the mobile and stationary phases	Low	µM -mM for UV nM-µM for MS	Yes	122, 123, 131, 137, 138, 140, 149, 150, 153, 169, 173, 252–260
CE + detection	Separates NTPs based on their size and charge in an electric field	Medium	µM -mM for UV nM-µM for MS	Yes	183, 184, 186, 187, 189–191, 261–266
CL	Measures light emission produced from a chemical reaction	High	pM-nM	Yes	194, 206, 212
ECL	Measures light emission produced from Electrochemical reaction	High	pM-nM	Yes	211, 213–216, 227, 267–273
BL	Measures light emission produced from Biological chemical reaction that uses ATP as an energy source, GTP is detected after conversion into ATP	High	pM-nM	No not available for cellular GTP, measures only GTP remaining from nucleotide exchange in RAS proteins	195, 205, 217, 218, 220, 221, 274
Fluorescence	Measures light emission of fluorophore labeled aptamers or Ruthenium based label free aptamers	High	nM-µM	Yes	102, 209, 224, 237–239, 242, 248, 275–279

2.3 Summary

There are a vast number of methods for measuring GTP and studying GTP-associated proteins. Methods for monitoring GTP associated with GTPases are more focused on evaluating the role of nucleotide exchange in cell biology context for understanding the dynamics of GTPases activity and its impact on cellular processes. This research aims to identify potential drug candidates for medical conditions with dysregulated GTPases activity. In addition to GTP associated with GTPases, GTP is involved in multiple cellular activities such as protein synthesis, energy currency and cell fate. Therefore, the estimation of free GTP concentration in cells is essential, as it reflects the metabolic activity and energy status of the cell. However, quantification of free GTP, whether by live imaging or by nucleotide extraction, is considered challenging. The cellular coexistence of other NTPs, especially ATP, and guanosine phosphate analogues (GDP and GMP), increases the risk of cross reactivity. Therefore, the selectivity and sensitivity of the detection method is crucial for accurate quantification.

Each of the luminescent and non-luminescent based methods for GTP quantification has its the strengths and weaknesses. The currently most established method for nucleotide detection is chromatographic separation followed by mass spectrometry for quantification. LC for GTP detection has many advantages, such as efficient separation of nucleotides and other metabolites simultaneously, high sensitivity, and compatibility with biological samples. Additionally, MS provides a vast amount of information about the nucleotide structural details. Despite all the benefits, this method is considered laborious and low throughput. In addition to the costly equipment, LC demands a high level of expertise. Furthermore, the selectivity and reproducibility of LC purification are drastically dependent on the column type and mobile phase components. Luminescent methods, on the other hand, maintain the sensitivity and have better throughput compared to LC. Moreover, some of the luminescent approaches can be adapted for live imaging for spatial detection of GTP. However, most of the currently available probes are developed for ATP detection. Therefore, development of novel probes for GTP determination is desperately needed.

The current methods for NTP detection are primarily designed for ATP detection, given its critical role for energy transfer and its abundance in cells. Methods exclusively dedicated to identifying and quantifying intracellular NTP levels typically begin with the laborious and time-consuming process of nucleotide extraction from cells. Efficient separation of various nucleotides and distinguishing the target NTP from NMP or NDP demands high selectivity to both the nitrogenous base and the triphosphate. Moreover, achieving a high sensitivity level is crucial for detecting trace amounts while minimizing the use of large sample volumes.

In contrast, real-time imaging within living cells bypasses the laborious nucleotide extraction process. However, it necessitates the creation of a probe with the ability to cross the cell membrane and exhibit high selectivity to GTP. This selectivity is crucial due to the simultaneous presence of other structurally related NTPs, such as ATP, which is found intracellularly at a higher concentration than GTP.

Luminescent biosensors currently rely predominantly on aptamer recognition, employing diverse detection techniques. Among these methods, colorimetric detection stands out for its cost-effectiveness and simplicity, while CL offers high sensitivity and minimal background interference. However, these approaches are typically tailored to identify a specific NTP through a corresponding aptamer, and their applicability is confined to specific matrices.

The introduction of a method capable of concurrently detecting both GTP and ATP would represent a significant advancement. Such a technique holds significant value for comprehending and investigating the ATP/GTP ratio, offering insights into how this ratio is influenced by various metabolic processes.

3 Aims of the Study

The main objective of this PhD was to develop innovative tools for monitoring free cellular GTP and GTP-associated proteins. The study aimed at developing a cell-based high throughput assay for combined GTP/ATP detection. Additionally, it aimed at investigating possible external luminescent probes to study GTPases and their interactions with potential inhibitors.

The specific objectives of the original publications were:

I To develop a novel homogenous high throughput assay for measuring GTP/ATP level in cells.

II To employ the Protein-Probe method for evaluating thermal shift assay as a tool for studying small GTPases stability.

III To Assess the new FRET-Probe method and its functionality in thermal and chemical stability monitoring of proteins.

IV To identify the chemical basis and binding specificity of KRASG12C covalent binders, AMG510 and MRTX849, and possible mechanisms of resistance.

4 Material and Methods

This chapter presents a collective description of all materials and methods used in the doctoral thesis. Separate and more detailed information is displayed in the related publications and their supplementary documents.

4.1 Luminescent Probes

Labeled reporter conjugates

The Eu^{3+}-Probe (**pub II-III**), Eu^{3+}–GTP and Eu^{3+}–GDP (**pub I, II & III**) were prepared by conjugating the target analyte to the 9-dentate chelate, {2,2',2",2'"-{[4'-(4'"-isothiocyanatophenyl)-2,2',6',2"-terpyridine-6,6"-diyl]bis(methylene-nitrilo)}tetrakisacetate)} europium(III). Additionally, Eu^{3+}–streptavidin (SA) was labeled by conjugating streptavidin to Heptadentate isothiocyanate (ITC)-TEKES-Eu(III)-chelate (**pub II**). For the Eu^{3+}-Probe, ITC Eu^{3+}–chelate is bound to peptide sequence (NH2-EYEEEEEVEEEVEEE) at the N terminus. Labeling procedure was described in previous work.[99,280,281] Then, the labeled compound was purified by reverse phase liquid chromatography. The product concentration was estimated based on the comparison of the TRL-signal of the Eu^{3+}–chelate conjugates to that of its appropriate commercial Eu^{3+} standard, according to Dissociation-Enhanced Lanthanide Fluorescent Immunoassay (DELFIA) principle, in which addition of DELFIA solution causes dissociation of Eu^{3+}, consequently the free Eu^{3+} emits much higher TRL-signal compared to the chelated Eu^{3+}.

FRET-Probe (**pub III**) is a short peptide sequence (H_2N-EYEEEEEVEEEVEEEVEEEVEEEK-Cy5), conjugated at the C-terminus to cyanine5 (Cy5) by the manufacturer, and at the N-terminus to 9-dentate chelate, {2,2',2",2'"-{[4'-(4'"-dichlorotriazine)-2,2',6',2"-terpyridine-6,6"-diyl] bis(methylene-nitrilo)}tetrakisacetate)} europium(III). Conjugation of Eu^{3+}– chelate was performed in the same way as described earlier for the single labeled conjugates.

AF647–GTP (**pub II**) was prepared by conjugating Alexa Fluor dye (AFDye) 647 Tetrafluorophenyl (TFP) to GTP according to the manufacturer's instructions.

The product concentration was estimated based on comparing the fluorescence of the AF647 conjugated GTP to that of a commercial standard.

4.2 Instrumentation and measurement parameters

TRL-signal was monitored with Tecan Spark 20M (Tecan, Switzerland). Eu^{3+}-Probe, Eu^{3+}–GTP, Eu^{3+}–GDP, Eu^{3+}–SA and AF647–GTP were purified by reverse-phase liquid chromatography, using Dionex Ultimate 3000 LC -system (Dionex, USA) and Ascentis RP-amide C18 column (Sigma-Aldrich, Supelco Analytical). Heating of protein samples for all thermal stability assays (TSA) (**pub II-IV**), was performed with PTC-100 Programmable Thermal cycler (MJ Research, Watertown, MA).

Black Framestar 96-well plate from (4titude) was used for all Protein-Probe TSA, SYPRO Orange, and ANS assays (**pub II–IV**). Black 384-well plates PCR (4titude) and black 384-well low volume plate (Corning) were used for FRET-Probe TSA and isochemical denaturation (ICD) assays, respectively (**pub III**). GTP-antibody and nucleotide exchange assays were performed in white 384-well low volume plate (Corning) (**pub I–IV**). In (**pub I**), 96-well Costar tissue culture treated plate was used for cell culturing (Corning) and 384-well cell black Optiplate (PerkinElmer, Netherlands) was utilized for sample preparation.

In all measurements, the plate-reader parameters were adjusted according to the specific method requirements. The delay time signifies the duration during which the measurement gate to the detector remains closed after excitation. Conversely, the decay time represents the duration during which the gate is reopened to monitor the emission of the fluorophore. In Protein-Probe, Eu^{3+} lanthanide chelate, exhibits a time-resolved luminescence with an emission decay that lasts for milliseconds.[282] To avoid autofluorescence and nonspecific signal, a delay of at least 400 µs is employed followed by the opening of the gate for an additional 400 µs to measure the emission decay. In our assays, a decay of 800 µs provides a better signal-to-background (S/B) ratio when the probe binds to the denatured protein, due to the lower background noise resulting from the interaction of the1',3,3,3',3'-Hexamethylindodicarbocyanine (HIDC) quencher with the probe. For the FRET-Probe, the Eu^{3+} acts as a donor transferring energy to the acceptor (Cy5). The energy transfer is observed as an accelerated emission decay of the Eu^{3+} when the Eu^{3+} and Cy5 are in close proximity.

Table 3. The Tecan plate reader measurement parameters.

Luminescent conjugates	Excitation wavelength (nM)	Emission wavelength (nM)	Delay (µs)	Decay (µs)	Publication
Eu^{3+}-Probe Eu^{3+}-GTP Eu^{3+}-GDP	340	620	800	400	I-IV
Eu^{3+}-SA /AF647-GTP	340	665	50	200	II
FRET-Probe	340	665	50	200	III
SYPRO Orange	485	590	0	40	II–IV

4.3 Assay reagents preparation

The detection solution and reagent dilutions for different methods were performed in different buffers. The buffer components in different assays are listed in Table 4.

Table 4. The buffer composition in different assays

Buffer	Application	Buffer components	Publication
1	QRET nucleotide exchange assay buffer	20mM HEPES (pH 7.5), 1 mM $MgCl_2$, 10 mM NaCl, 0.01% Triton-X 100, 0.005% γ-globulins	II–IV
2	QRET GTP-antibody buffer	25 mM HEPES, pH 7.5, 1 mM $MgCl_2$, 0.01% Triton X-100	I
3	FRET-Probe ICD sample buffer	10 mM Hepes pH 7.5, 10 mM NaCl, 0.01% Brij 30	III
4	FRET-Probe TSA	10 mM HEPES (pH 7.5), 0.001% Triton X-100	III
5	FRET-Probe pH 5 ICD	Citrate phosphate buffer (10.3 mM Na_2HPO_4, 4.85 mM citric acid pH 5, 0.01% (v/v) Brij 30)	III
6	FRET-Probe urea ICD	10 mM Hepes pH 7.5, 1 M urea, 10 mM NaCl, 0.01% Brij 30	III
7	FRET-Probe propanol ICD	10 mM Hepes pH 7.5, 10-50% propanol, 10 mM NaCl, 0.01% Brij 30	III
8	SYPRO and ANS buffer	10 mM HEPES (pH 7.5), 0.001% Triton X-100 and 20 mM NaCl	II–IV
9	Protein-Probe sample buffer	10 mM HEPES (pH 7.5), 0.001% Triton X-100, 20 mM NaCl with 0-10 mM $MgCl_2$, or 0-1 mM $CaCl_2$, or 0-1 mM EDTA	II–IV
10	Protein-Probe detection buffer	Citrate-phosphate buffer (7.7 mM Na_2HPO_4, 6.1 mM citric acid, pH 4) supplemented with 0.01% (v/v) Triton X-100, 3.5 µM HIDC, and 1 nM Eu^{3+}-Probe	II–IV

Cell culture and sample preparation for GTP antibody assay

In this study, cell lines Cell lines (A549, HEK293T, U87MG, QGP1, MDA-MB-468, HTC116, BT-474, and HeLa) were cultured and treated with either MPA and guanosine. U87MG, HTC116, A549, HeLa, MDA-MB-468 and HEK293T cells were cultured in DMEM, and QGP1 and BT-474 cells in RPMI 1640 media. All media were supplemented with 10% FBS, 1% penicillin/streptomycin, and 2mM L-glutamine. U87MG and HEK293T (10 000 cells) were cultivated in 96-well plate, followed by treatment and nucleotide extraction with 80% MeOH. For GTP and ATP detection in cell lysates, (~500 cells/well) in 384-well plate were performed in triplicates.

4.4 Assay proteins and ligands

$NRAS^{WT}$, $HRAS^{WT}$ and $KRAS^{WT}$ (**pub II & IV**), $KRAS^{G12C}$, $KRAS^{G13D}$, $KRAS^{Q61L}$ and $KRAS^{G12D}$ (**pub II-IV),** Ac-KRAS, iMet-KRAS, Gαi, RhoA, $KRAS^{Y96D}$, $KRAS^{H95L}$, $G12C^{H95L}$ and $G12C^{Y96D}$ (**pub IV**), $KRAS^{G12V}$ (**pub III & IV**), SOS^{cat}, Malate dehydrogenase (MDH) and trastuzumab (**pub III**) were tested.

The KRAS inhibitors utilized as ligands were GTP for $KRAS^{G12V}$, BI-2853, BAY-293, and BI-2852 for $KRAS^{WT}$, $KRAS^{G12C}$ and $KRAS^{G12D}$. DARPins K13 and K19 for $KRAS^{WT}$ and $KRAS^{G12C}$ and K27 for $KRAS^{WT}$, $KRAS^{G12D}$, $KRAS^{G12C}$, $KRAS^{Q61R}$ and $KRAS^{Q61L}$. AMG510, MRTX849, ARS1620 and ARS853 for $KRAS^{G12C}$, and NADH for MDH (**pub III & IV**).

4.5 Assays principles

4.5.1 QRET assays

A single-label GTP QRET technique is based on using a Eu^{3+}chelate labeled GTP. The binding of Eu^{3+}–GTP to its target protein protects the chelate from quenching by the soluble quencher (MT2) and is associated with high TRL-signal monitored at 620 nm. In this doctoral work, the QRET approach was applied for measuring GTP nucleotide exchange associated with small GTPases as well as cellular GTP level, using a unique GTP antibody, which is a Fragment antigen-binding (Fab) selected by phage display from a synthetic antibody fragment library (scFvM). This Fab fragment demonstrated exceptional specificity for GTP compared to GDP, ATP and CTP. [283,284] In the RAS nucleotide exchange reaction catalyzed by SOS, a high TRL-signal is monitored when Eu^{3+}–GTP is bound to RAS, indicating less GTP bound to RAS and high GTPase activity (Figure 16A). On the other hand, in the GTP antibody assay, a high signal is monitored when Eu^{3+}–GTP binds to the GTP specific antibody,

indicating a low level of free cellular GTP (Figure 16B). In the presence of GTP, the competition with Eu^{3+}–GTP for RAS or GTP antibody will result in a low TRL-signal due to the quenching of Eu^{3+}–GTP signal by MT2 (Figure 16).

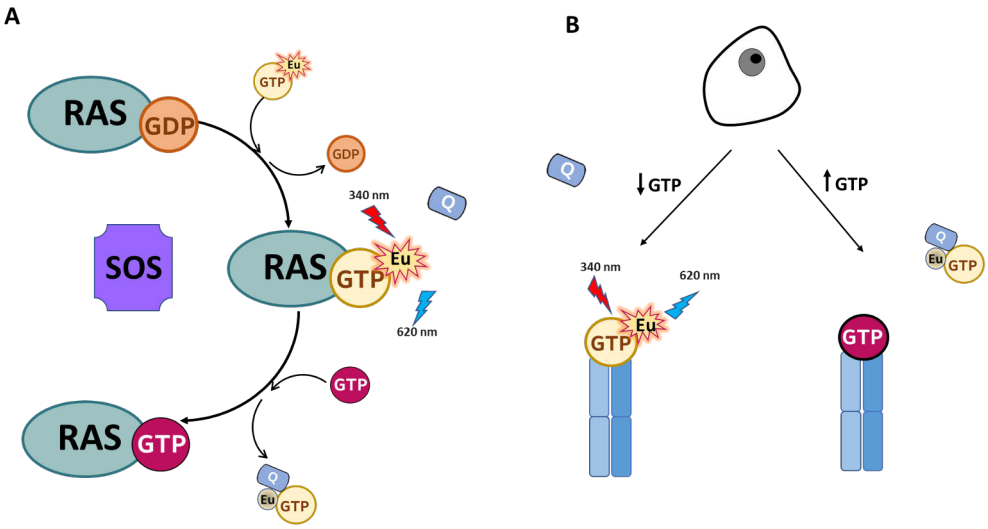

Figure 16. QRET assay principle for nucleotide exchange and GTP detection. QRET is based on competitive inhibition. In QRET assay, target GTP binds to (**A**) RAS protein or (**B**) GTP antibody, thus, TRL-signal of the free Eu^{3+}–labeled GTP is quenched by the soluble MT2 quencher molecule in solution. In absence of target GTP, Eu^{3+}–labeled GTP can bind efficiently to RAS or GTP antibody and high TRL-signal is monitored.

Nucleotide exchange QRET assay protocol: All QRET assays were implemented utilizing an endpoint protocol by monitoring the TRL-signal multiple times during 60 min incubation. $KRAS^{WT}$ (15-100 nM) (**pub II & IV**), $KRAS^{G12C}$ (50 nM) (**pub III**), HRAS, NRAS, $KRAS^{Q61L}$, $KRAS^{G12D}$, $KRAS^{G12V}$, $KRAS^{G13D}$, $KRAS^{Y96D}$, $KRAS^{H95L}$, $G12C^{H95L}$ and $G12C^{Y96D}$ (100 nM) (**pub IV**), were diluted in buffer 1 (Table 4). Eu^{3+}–GTP (10 nM) (**pub II**) or Eu^{3+}–GDP (10 or 50 nM) (**pub III & IV**), MT2 quencher (2.5–4.5 µM) and SOS^{cat} (5-10 nM) were added in the detection solution. Different KRAS inhibitors, AMG510, MRTX849 (**pub II–IV**), ARS853, ARS1620 (**pub II & III**), and BI-2852, BI-2853, BAY-293, and Designed Ankyrin Repeat Proteins (DARPins), K13, K19, and K27 (**pub II**), or nucleotides (ATP, GMP, guanosine-5'-(βγ)-imido] triphosphate (GMPPNP), guanosine-5'-[(βγ)-methyleno] triphosphate (GMPPCP), guanosine-5'-(γ-thio)-triphosphate (GTPγS), GDP, GTP) in buffer 1 (Table 4) were titrated after (5–30) min preincubation with the target protein. In a real-time TR-FRET assay conducted in a 10 µL assay volume, the ligands K13, K19, and K27 were incubated with the biotinylated Avi-KRAS (50 nM) for 10 minutes within a 6 µL solution.

Subsequently, 2 µL SOS^{cat} (0-10 nM) was introduced, followed by adding detection solution (2 µL) containing 50 nM AF647-GTP and 5 nM Eu^{3+}–SA. The kinetics of nucleotide exchange both in the presence and absence of SOS^{cat}, were monitored over a period of 90 minutes.

GTP antibody QRET assay protocol: All assays were performed in buffer 1 (Table 4), both GTP and ATP were detected simultaneously in final volumes of 10 µL detection solution for GTP and 20 µL for ATP assay. In addition to GTP and ATP, several other nucleotides (GMP, GDP, GTP, CTP, UTP, and ATP) were titrated (0–500 µM). All nucleotides were added in 5 µL, then mixed with 5 µL detection solution, Eu^{3+}–GTP (10 nM), GTP antibody $2A4^{GTP}$ (20 nM), and MT2 (2.7 µM). TRL signal was measured, then 10 µL of the ReadiUse™ Rapid Luminometric ATP detection kit was added to the 10 µL nucleotide samples, and luminescence signal for ATP was monitored for 5–60 min at several time points after 15 min incubation time. MeOH (2-28%) was added to GTP and ATP buffers to simulate MeOH level in cell lysates.

4.5.2 Stability assays

Protein-Probe is made of a short peptide labeled at its N-terminus with Eu^{3+}–chelate. The peptide binds to different proteins in the denatured form and interacts much less with the native protein form. Therefore, it is suggested that the binding mechanism of the probe depends mainly on interaction with the hydrophobic core of the protein which is accessible to the probe when the protein is thermally unfolded. Ligand binding increases protein stability and causes a shift in the T_m value. (Figure 17).

The Protein-Probe peptide is negatively charged at neutral pH. At lower pH, the binding efficiency to denatured proteins is markedly enhanced due to partial protonation. Protein-Probe detection solution is supplemented by HIDC quencher. The Eu^{3+}–chelate excitation/emission wavelengths (Table 2) and HIDC absorption (636 nm) is in the same emission range of Eu^{3+}–chelate. In absence of target protein, the signal of the free probe is quenched and thus background noise is significantly eliminated. On the other hand, when the probe binds to the denatured protein, it is protected from the quenching effect and high TRL-signal is monitored.

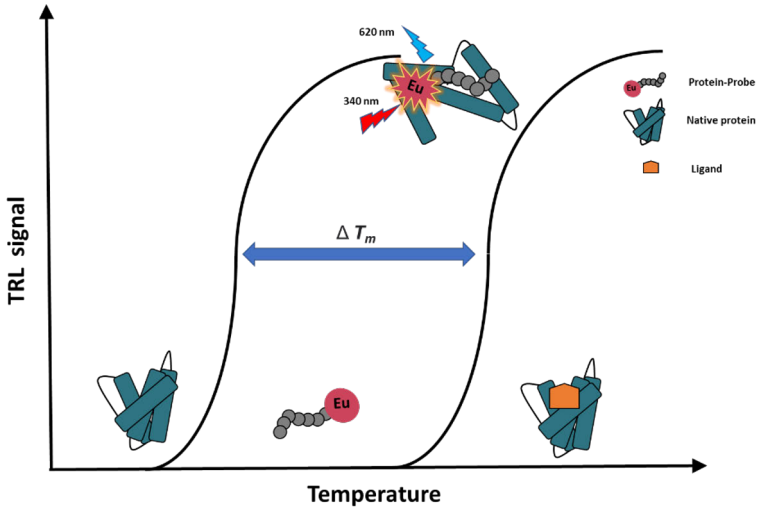

Figure 17. Protein-Probe principle for monitoring protein thermal stability. Protein-Probe is an Eu^{3+}–labeled peptide that interacts with the hydrophobic core of different proteins. The inner core is efficiently exposed to the probe when the protein is thermally denatured. This leads to sufficient binding and release from the quenching effect of the soluble modulator molecule in the reaction. TRL-signal monitored at different temperatures are indicative of the protein thermal curve and is used to calculate T_m value. Ligand induced stabilization of protein interferes with protein unfolding, therefore, results in weak binding with the probe and causes a T_m shift (ΔT_m).

The FRET-Probe is formed of a short peptide which is linked to Eu^{3+}–chelate at its N-terminus and to Cy5 dye at the C-terminus as donor and acceptor molecules, respectively. The probe detection mechanism is based on measuring the time-resolved FRET (TR-FRET) signal between the two fluorophores, which requires spectral overlap and close distance of the two molecules. In the FRET-Probe, Eu^{3+}–chelate is excited at a wavelength 340 nm and emits light at 620 nm, which overlaps with Cy5 excitation (635 nm) resulting in energy transfer and microsecond light emission at 665 nm.[285] In the absence of target protein, the distance between the two label molecules does not provide high energy transfer and low TR-FRET signal is monitored. In contrast, the two labels are in close proximity upon binding of the FRET-Probe to a target protein, resulting in a high TR-FRET signal. Similar to the Protein-Probe (**pub II**), the FRET-Probe is suggested to interact with the protein at its hydrophobic core, thus binding with denatured protein rather than the native form (Figure 18). In this thesis project, the FRET-Probe was applied to monitor protein thermal stability by measuring the T_m value in TSA (Figure 18A), and protein chemical stability by monitoring real-time kinetics of protein unfolding in the ICD assay (Figure 18B).

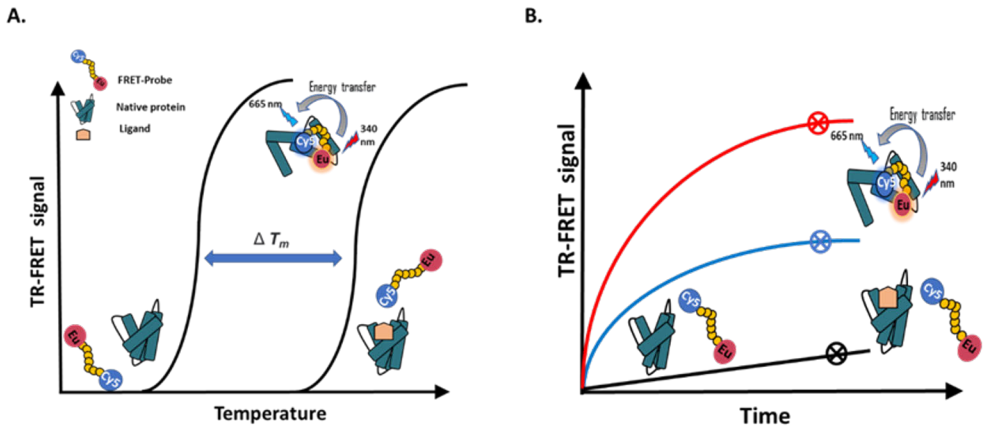

Figure 18. FRET-Probe principle for monitoring protein thermal and chemical stability. (**A**) Principle of FRET-Probe for thermal stability monitoring. FRET-Probe is a dual labeled peptide with Eu^{3+}chelate and Cy5 at the opposite ends. FRET-Probe binds to the hydrophobic core of the protein, which is exposed to the probe when the protein unfolds by heating. The binding reduces the distance between the donor (Eu^{3+}) and acceptor (Cy5) fluorescent molecules, resulting in energy transfer, which is monitored as high TR-FRET signal. In presence of ligand, the protein is more stable, and requires higher temperature to unfold, monitored as a T_m shift (Δ T_m). (**B**) Principle of FRET-Probe for chemical stability monitoring is based on monitoring real-time kinetics of protein stability over time.

Protein-Probe assay protocol: The Protein-Probe was conducted in a two-step protocol. $KRAS^{WT}$ and mutants (in 8 µL) at variable concentrations, were added in the sample buffer 9 (Table 4). Protein samples were heated for 3 min at each temperature, and 65 µL of the detection solution performed in buffer 10 was added (Table 4). Finally, TRL-signal was monitored.

FRET-Probe TSA protocol: TR-FRET signal TSA was measured in a 25 µL volume assay. 20 µL of FRET-Probe (0.5 nM) in buffer 4 was mixed with $KRAS^{WT}$, $KRAS^{G13D}$ and $KRAS^{Q61R}$ (150 µM), $KRAS^{G12V}$ and $KRAS^{G12C}$ (50 µM), trastuzumab (20 nM), MDH (25 nM), and SOS^{cat} (10 nM). NADH (5-50 µM), MRTX849 (250 nM) were incubated with proteins for 30 min before adding the detection solution. Next, the assay reaction was heated every 5 °C for 2 minutes before measuring the TR-FRET signal.

FRET-Probe ICD protocol: All FRET-Probe ICD experiments were implemented at room temperature in a 25 µL final volume. In all assays, proteins and ligands were prepared in buffer 3. KRAS ligands GTP (0-2 µM), AMG510 and MRTX849 (0-10 µM) or ARS853 and ARS1620 (0-50 µM), and MDH ligand NADH (0-50 µM) were preincubated for 30 min in a 5 µL volume with KRAS. Immediately after the addition of 0.5 nM FRET-Probe (20 µL) diluted in chemical denaturation buffers (5-7), real-time FRET signal is monitored.

SYPRO Orange and ANS TSA protocols: SYPRO Orange and ANS assays were carried out with 8 µL RAS (10 µM) and 12 µL inhibitors (20 µM) in buffer 8. After 30 min incubation, SYPRO Orange or ANS were added to achieve a final concentration of (5×) or (10 µM), respectively. The samples were then heated for 3 min at each temperature, and the fluorescence signal was measured.

5 Results and Discussion

The results and discussion section of this thesis offers a comprehensive overview of the findings. Detailed information is presented in the associated publications and their supplementary materials, where readers can have a more extensive insight into data and analytical discourse.

5.1 Cellular GTP studies

To continue with GTP studying, we aimed at single well detection of GTP in cell lysate (**pub I**). For that purpose, a QRET based assay using $2A4^{GTP}$ GTP antibody was utilized. The QRET assay was previously applied for studying RAS GTPase activity.[283,284] In this thesis project, the QRET method was employed for measuring the concentration of GTP extracted from cells with a short cell lysis protocol reducing preparation time and boosting overall throughput. Cellular GTP exists with other nucleotides and phosphate analogues, with high similarity in structure especially ATP which is 10-fold higher in concentration.[16] Therefore, it is essential for the GTP antibody to avoid cross reactivity with nucleotides. Methanol (MeOH) utilized for the extraction of nucleotides from cells, was first tested for its compatibility with the QRET method. Nucleotides' concentrations in both U87MG and A549 were measured before and after MeOH evaporation. GTP (Figure 19A) and ATP (Figure 19B) concentrations monitored directly from MeOH or after evaporation and reconstitution in Milli-Q water were the same, showing suitability of the QRET method for protocols that involve the use of MeOH.

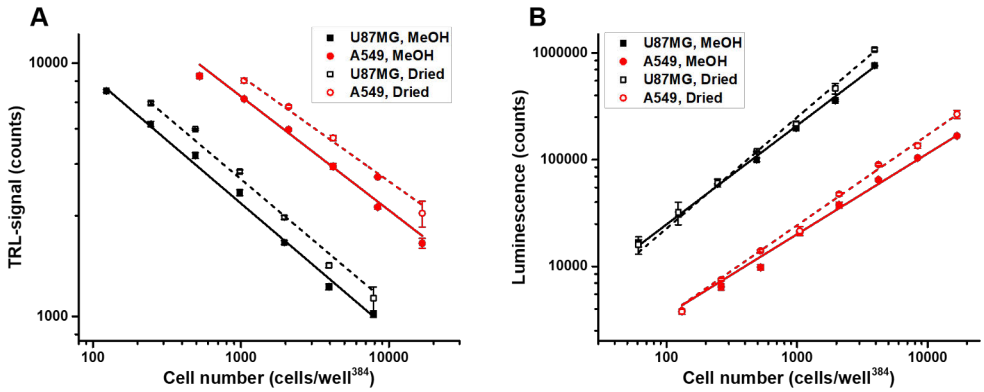

Figure 19. The effect of MeOH on the QRET method for monitoring GTP and ATP concentrations. GTP (**A**) and ATP (**B**) concentrations in U87MG (black) and A549 (red) were measured directly from samples in MeOH (solid) and after MeOH evaporation and samples reconstitution in Milli-Q water (dashed), data showed a similar linear response with both protocol suggesting that MeOH has no impact on the QRET method. Data represents mean ± SD (n=3).

Thereafter, the selectivity of the method was evaluated by titration of different nucleotides with the $2A4^{GTP}$ and measuring the separation among different nucleotides. Our data showed clear high selectivity for GTP compared to other nucleotides, with separation of > 1300 folds for GMP, 300 for ATP, 90 for UTP and CTP and 33 for GDP. These results show that the antibody is specific to both guanosine and triphosphate. For further method validation, the test was performed in different cell lines and results were compared to CE/MS technique (Figure 20).

First, GTP level in different cell lines was measured by the $2A4^{GTP}$ and CE/MS in parallel. Among the eight different cell lines tested, GTP concentrations measured by QRET and CE/MS were relatively similar. QGP1 (pancreatic cancer cell line) had the highest GTP level, whereas A549 (lung cancer cell line) had the lowest GTP concentration with 3-fold difference compared to QGP1 (Figure 20A). Next, GTP level was measured after treating U87MG (glioblastoma cell line) with different treatments that affect GTP concentration. Mycophenolic acid (MPA) was used to inhibit the function of IMPDH, an enzyme required for the *de novo* synthesis of GTP in cells under physiological conditions. On the other hand, cells treated with a combination of MPA and guanosine, were expected to have higher GTP due to biosynthesis of GTP by the alternative salvage pathway. U87MG was treated with DMSO as a negative control, MPA (10 µM) and MPA and guanosine (both 100 µM). GTP level was measured hourly for 8h, a clear change in the GTP level was observed overtime with both QRET and CE/MS with maximum decrease in concentration recorded at 4h. GTP concentrations with different treatments in both methods are in

line with each other, showing the correct functionality of the QRET assay (Figure 20B).

Similarly, simultaneous detection of ATP concentration was measured from single wells by measuring luminescence signal using a commercial ATP kit. The results were compared to that of CE/MS as a control. After validation of the combined ATP and anti-GTP $2A4^{GTP}$ QRET assay for measuring single well ATP/GTP, the test was applied in 384-well plate format for high throughput compatibility. For all the cell lines investigated, ATP concentrations with CE-MS and the combined GTP/ATP QRET assay, were 5.3–7.4 and 4.4–9.4 times higher than that of GTP.

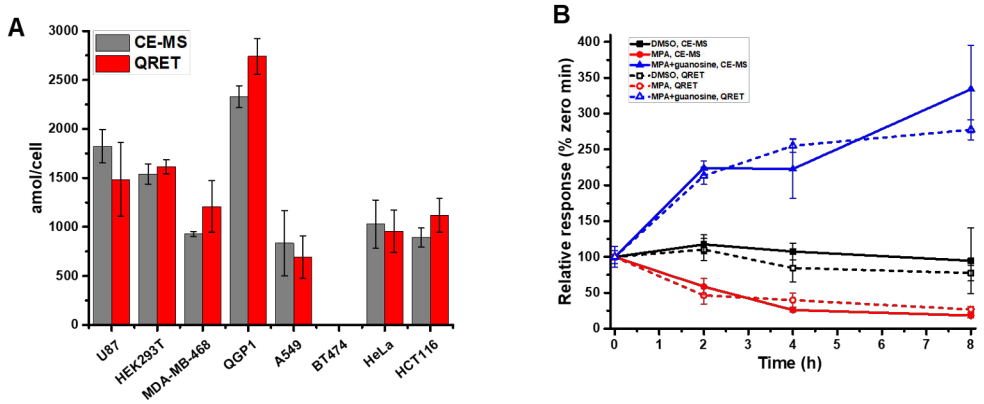

Figure 20. The luminescent GTP assay compared to reference method (CE/MS). (**A**) GTP level measured by QRET in multiple cell lines are relatively equal to that measured by CE/MS. (**B**) GTP concentration monitored overtime in U87MG cell line treated with MPA with and without added guanosine, indicated that QRET can detect GTP with the same accuracy as CE/MS. Data represent mean ± SD (n=3).

In conclusion, a QRET-based assay employing the 2A4 GTP antibody has been developed for single-well GTP detection in cell lysates. The assay demonstrated compatibility with MeOH and was optimized for measuring GTP concentrations with a brief cell lysis protocol, reducing preparation time and enhancing overall throughput. Selectivity tests revealed a clear preference for GTP over other nucleotides, with substantial separation among them. Comparative analysis with CE/MS validated the accuracy of the QRET assay in various cell lines and under different treatments affecting GTP levels. The assay, extended to simultaneously measure ATP concentrations, offering a valuable tool for high-throughput studies in diverse cellular contexts. Next, GTP is explored from the perspective of measuring GTPases. Novel bioanalytical methods have been developed to investigate small GTPases, focusing on aspects such as protein stability and ligand interactions.

5.2 Small GTPase stability studies

In this doctoral thesis, several aspects related to small GTPases were studied. Thermal and chemical stability of small GTPases were investigated and different parameters that affect thermal stability of small GTPases were evaluated (**II**–**IV**). In addition, the interaction of various inhibitors with different RAS proteins was assessed in detail with special emphasis on the two recently FDA approved $KRAS^{G12C}$ covalent inhibitors, AMG510 and MRTX849. The main aim of this part was to study GTP in the context of GTPase. TSA has been widely used to study GTPases, based on observing the change in T_m under different conditions e.g., protein ligand interactions (PLIs). In this PhD project, TSA was performed by two methods, Protein-Probe and FRET-Probe. Protein-Probe has already been introduced and validated for several applications.[95,286-288] FRET-Probe, on the other hand, is a novel technique that is introduced for the first time.

In this part of the thesis work, three luminescence-based methods were employed for studying GTPases. TRL-based Protein-Probe was applied for studying thermal stability, while the TR-FRET-based FRET-Probe was utilized for monitoring both thermal and chemical stability. These novel techniques bridge a notable gap in current approaches by enabling the detection of protein concentrations at the nanomolar level, a significant advancement beyond the micromolar sensitivity limitations of existing methods.

5.2.1 Evaluation of TSA for monitoring small GTPase stability

In **pub II**, Protein-Probe was applied in studying the suitability of TSA for measuring small GTPases thermal stability. To compare the thermal stability of $KRAS^{WT}$ to KRAS mutants, Protein-Probe T_m measurements were performed for $KRAS^{WT}$, $KRAS^{G13D}$ and $KRAS^{Q61R}$, these three mutants were deliberately chosen due to variation in their intrinsic nucleotide exchange rate.[289] Clear difference in T_m values were recorded, 57.2 ± 0.2, 49.9 ± 0.2 and 64.1 ± 0.2 °C respectively. This is related to different intrinsic nucleotide exchange, which plays a major role in stability, as the loss of nucleotide destabilizes KRAS. Among the three studied KRAS proteins, $KRAS^{G13D}$ has the fastest nucleotide exchange and $KRAS^{Q61R}$ has the slowest nucleotide exchange, which explains that $KRAS^{G13D}$ being the least stable and $KRAS^{Q61R}$ being the most stable.[50,290]

To study different buffer factors and inhibitory molecules that affect thermal shift of small GTPases, we first applied Protein-Probe for measuring T_m in presence of different buffer conditions. Mg^{2+} is known to stabilize the nucleotide loaded KRAS, thus increasing thermal stability. In contrast, EDTA is expected to destabilize nucleotide loaded KRAS due to its Mg^{2+} chelating effect. In the assays, $KRAS^{WT}$

was significantly stabilized with Mg^{2+}. T_m with 1 and 10 mM $MgCl_2$ were 60.1 ± 0.3 °C and 64.7 ± 0.5 °C respectively. On the other hand, addition of 1mM EDTA had a clear destabilizing effect, equivalent to that observed in absence of $MgCl_2$, T_m for $KRAS^{WT}$ with 1mM EDTA and without $MgCl_2$ were 48.9 ± 0.4 °C and 49.2 ± 0.4 °C respectively. The same effect was tested for KRAS mutants, $KRAS^{G13D}$ and $KRAS^{Q61R}$. The amount of stabilization or destabilization by Mg^{2+} and EDTA respectively, was found to be primarily dependent on the intrinsic nucleotide exchange activity. $KRAS^{G13D}$ having the fastest intrinsic nucleotide exchange showed similar destabilizing effect without Mg^{2+} and with adding 1mM EDTA, T_m were 43.4 ± 0.6 °C and 43.6 ± 0.8 °C respectively. However, for $KRAS^{Q61R}$, 1mM EDTA was not enough to achieve full unloading of nucleotide, T_m without Mg^{2+} and with addition of 1mM EDTA were 59.2 ± 0.7 °C and 50.6 ± 1.0 °C respectively.

Next, I moved to investigating the effect of different nucleotides on stabilization of KRAS and how it is linked to $Mg^{2+,}$ and whether it is equally manifested in different KRAS mutants. Small GTPases have very high affinity to GDP, which allow GTPases to constantly remain in the nucleotide loaded form. Therefore, excess GDP is typically added in storage buffer of GTPases to maintain its stability.

To test this effect, Protein-Probe was applied for measuring thermal stability of $KRAS^{WT}$ and mutants. $KRAS^{G13D}$, $KRAS^{Q61R}$ and $KRAS^{G12D}$ of different intrinsic nucleotide exchange rate, with and without GDP (10 μM). As expected, the GDP stabilizing effect on KRAS was mutant dependent, $KRAS^{G13D}$ had the largest thermal shift with and without GDP, (ΔT_m ~10 °C). On the contrary, $KRAS^{Q61R}$ did not show any shift in T_m. However, the GDP-induced stabilization was not Mg^{2+} or Ca^{2+} dependent, $KRAS^{WT}$ was efficiently stabilized with GDP in presence of 1mM EDTA, ΔT_m was 11.3 °C. In presence of $MgCl_2$ (1mM), $KRAS^{WT}$ was less stabilized with GDP, ΔT_m was 7.6 °C. On the other hand, $CaCl_2$ (1mM) did not have any additional stabilizing effect to that of GTP (Figure 21A). This outcome was anticipated, as introduction of 0.1 and 1mM $CaCl_2$ to assay buffer of $KRAS^{WT}$ had a negligible effect on stabilization, ΔT_m was 1.2 and 3.7 °C respectively. The same effect was observed with RhoA, with a more stabilizing effect for GTP than GDP. ATP on the other hand, had no notable effect on GTPases thermal stability.

The KRAS affinity to other nucleotides than GDP was also investigated by comparing $KRAS^{WT}$ thermal stability with Protein-Probe method in presence of GTP to that in presence of other non-hydrolysable analogues with lower affinity, GTPγS, in addition to GMP and GMP analogues GMP-PNP, and GMP-PCP. GTP and GTPγS at 10 μM concentration were the most stabilizing nucleotides. GMP-PNP showed similar stabilization only at 300 μM, whereas GMP and GMP-PCP had negligible effect even at very high concentrations, 300-1000 μM. This data shows that the nucleotide induced stabilization is affinity driven (Figure 21B).

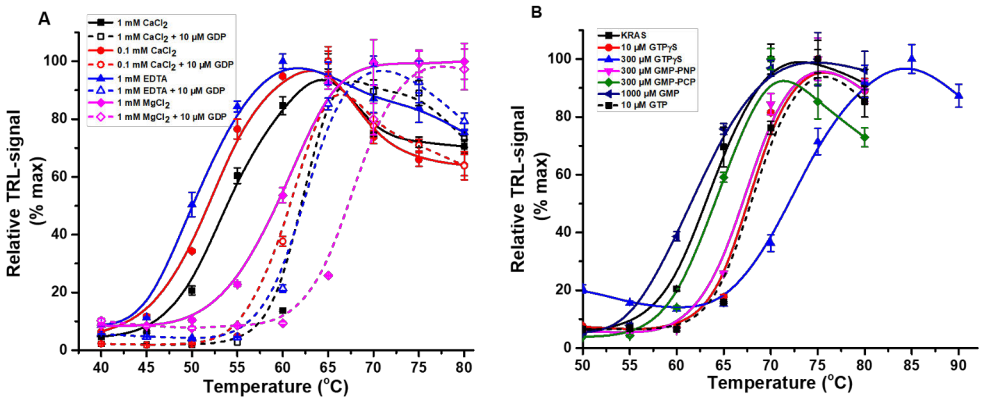

Figure 21. Nucleotides and cations stabilizing effect on KRAS. (**A**) Protein-Probe thermal stability assay for $KRAS^{WT}$ with (dashed) and without (solid) 10 µM GDP in presence of 0.1 (red) and 1mM (black) $CaCl_2$, 1 mM EDTA (blue) and 1 mM $MgCl_2$ (magenta), data showed that Mg^{2+} caused more stabilization than Ca^{2+} and GDP had an additional stabilizing effect in all cases. (**B**) Protein-Probe TSA for $KRAS^{WT}$ (solid black) in presence of 10 µM GTP (dashed), 10 µM GTPγS (red) showed equal effect, this effect is dose dependent as it increased with 300 µM GTPγS (blue), GMP-PNP (magenta) required much higher concentration, other nucleotides with lesser affinity GMP-PCP (green) and GMP (navy), did not show similar effect even at concentration of 300 and 1000 µM respectively. Data represents mean ± SD (n=3).

After that, binding specificity of the $KRAS^{G12C}$ binders was investigated further by Protein-Probe (**pub II** and **IV**). ARS853 and ARS1620 exhibited encouraging results in pre-clinical trials, however MRTX849 and AMG510 showed exceptionally notable results and were recently granted the FDA approval as inhibitors targeting $KRAS^{G12C}$.To confirm that ARS853 and ARS1620 binds specifically to $KRAS^{G12C}$, PLI was monitored by Protein-Probe in parallel with SYPRO Orange and ANS as reference methods. With Protein-Probe method, ARS853 and ARS1620 produced a thermal shift for $KRAS^{G12C}$ of 16 and 18 °C respectively, and with SYPRO Orange and ANS TSA, 20 µM ARS853 and ARS1620 produced double transitions with maximum shift of 13 °C for 10 µM $KRAS^{G12C}$. Due to the nanomolar sensitivity of Protein-Probe, 5 µM of inhibitors was already enough to provide saturation of the thermal stabilization for 50 nM $KRAS^{G12C}$.

Thereafter, MRTX849 and AMG510 were studied. Our data showed a significant ligand induced stabilization with Protein-Probe for MRTX849 and AMG510 for $KRAS^{G12C}$, ΔT_m was 15.6 and 24.8 °C respectively, even though Half maximal Inhibitory concentration (IC_{50}) calculated from the nucleotide exchange inhibition refers to higher binding with MRTX849 than AMG510. It was challenging to visualize the thermal shift for AMG510 with SYPRO Orange and ANS, because of signal quenching due to the micromolar sensitivity of this method which requires a high protein concentration. The quenching effect was not observed with $KRAS^{WT}$, which suggests that the quenching is indicative of binding. Similar quenching of

signal with KRAS^{G12C} was observed with the Protein-Probe method when AMG510 concentration was elevated to 20 µM, however, this challenge can be addressed due to the exceptional sensitivity of the method, eliminating the need to reach such high concentrations.

To confirm the MRTX849 and AMG510 binding to KRAS^{G12C}, a competitive TSA protocol was performed with Protein-Probe. KRAS specific DARPins are hypothesized to prevent inhibitors binding to the switch II pocket by either competition or changing the structure of KRAS. DARPin K13 has been tested for its effect on KRAS stability. In presence of K13, the inhibitors stabilizing effect on KRAS^{G12C} was lost or reduced, especially with AMG510 (Figure 22). The thermal shift of AMG510 on KRAS^{G12C} was detected only at AMG510 concentration > 100 nM with notable double transition in the thermal curve indicating competitive binding (Figure 22A). On the other hand, 900 nM MTRX849 in presence of K13, showed a smaller thermal shift (ΔT_m 3–7.4 °C) than that obtained by AMG510 at similar concentration (ΔT_m ~10 °C), which may indicate difference in binding (Figure 22B).

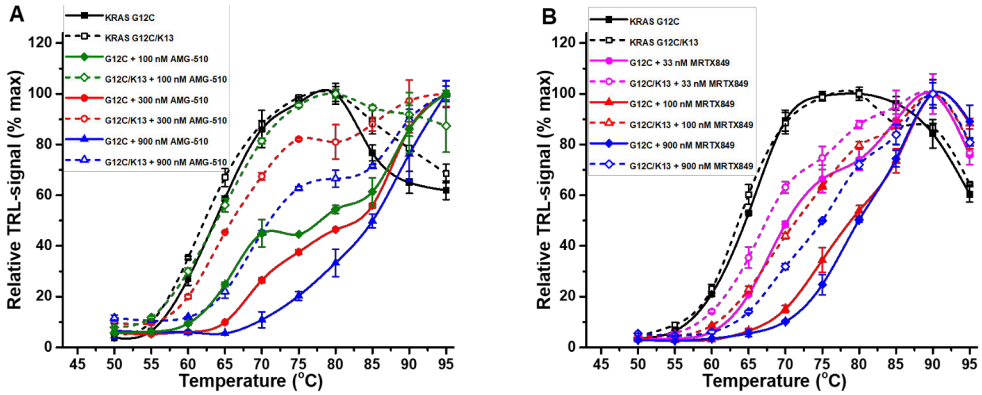

Figure 22. AMG510 and MRTX849 stabilizing effect on KRAS^{G12C} in a competitive TSA. The stabilizing effect of 100 nM (green), 300 nM (red) and 900 nM (blue) AMG510 (**A**) and (**B**) on KRAS^{G12C} (black) was monitored by Protein-Probe in presence (dashed) and absence of (solid) K13. The competition of K13 with the two covalent binders AMG510 and MRTX489 for binding with KRAS^{G12C} was visualized in the form of total or partial loss of the stabilizing effect. Data represent mean ± SD (n=3).

5.2.2 Small GTPases thermal and chemical stability monitoring by FRET-Probe

In **pub III**, FRET-Probe is introduced and applied for monitoring small GTPases in TSA and ICD format. For FRET-Probe proof of concept, melting curves of the same three KRAS proteins (KRAS^{WT}, KRAS^{G13D}, KRAS^{Q61R}) were measured and compared to that of Protein-Probe. We identified approximately 5 degrees down-

shifted T_m values with the FRET-Probe. T_m values of 53.6 ± 0.4, 44.7 ± 0.1 and 59.2 ± 0.3 °C were calculated for $KRAS^{WT}$, $KRAS^{G13D}$, $KRAS^{Q61R}$, respectively (Figure 23A). The difference in T_m values was anticipated due to the distinct assay conditions employed. Protein-Probe detection solution (65 µL) was performed in buffer 10 and was added to 8 µL of small GTPases in sample buffer 9 without additions of ions, on the other hand, FRET-Probe is carried out in buffer 4 supplemented with 1 mM $MgCl_2$ (Table 4). Moreover, the given protein concentration in the Protein-Probe method was calculated in 8µL volume, whereas in FRET-Probe technique, it is calculated in the total reaction volume (25 µL). Although there was minor difference in melting curves obtained by both methods, the rank order of the tested proteins was the same. The thermal shift of KRAS mutants compared to $KRAS^{WT}$ remained the same with both techniques, which shows that Protein-Probe and FRET-Probe are measuring the same properties of the studied protein. Similar ΔT_m were recorded by both methods, ΔT_m of $KRAS^{G13D}$ and $KRAS^{Q61R}$ compared to $KRAS^{WT}$ in the Protein-Probe (**pub II**) was 7.3 and 6.9 °C respectively. While ΔT_m of $KRAS^{G13D}$ and $KRAS^{Q61R}$ compared to $KRAS^{WT}$ in the FRET-Probe was 8.9 and 5.6 °C respectively (Figure 23A).

Next, FRET-Probe was applied to study the Mg^{2+} induced stabilization of $KRAS^{G12C}$ mutant in presence of $KRAS^{G12C}$ specific inhibitor MRTX849, with $KRAS^{G12V}$ as a control. MRTX849 binds to the GDP-loaded form of $KRAS^{G12C}$, thus, it was anticipated that the PLI will be lost in absence of Mg^{2+}. Data clearly showed that Mg^{2+} had a stabilizing effect on both mutants. Despite the absence of thermal shift by MRTX849 with $KRAS^{G12V}$, $KRAS^{G12C}$ was markedly stabilized with MRTX849, it was also noted that the thermal shift in absence of Mg^{2+} (ΔT_m 14.7°C) was more profound than that in presence (ΔT_m 8.7°C) of Mg^{2+}. This indicates that 1.25 µM Mg^{2+} in the protein storage buffer is sufficient to keep $KRAS^{G12C}$ in the GDP-loading state. On the other hand, $KRAS^{G12V}$ and $KRAS^{G12C}$ exhibited equal stabilization when treated with $MgCl_2$ (200 µM). Both mutants showed an approximate 15°C increase in T_m with Mg^{2+}. Without Mg^{2+}, T_m values for $KRAS^{G12V}$ and $KRAS^{G12C}$ were 38.3 ± 0.2 and 38.5 ± 0.4 °C respectively, and in presence of $Mg^{2+,}$ T_m for $KRAS^{G12V}$ and $KRAS^{G12C}$ were 53.2 ± 0.4 and 53.5 ± 0.4 °C respectively. Based on these results small GTPases are proven to be very sensitive to assay conditions.

Following the validation of FRET-Probe in the TSA, FRET-Probe has been applied for monitoring ICD of proteins. This application involved studying three distinct chemical denaturants with different denaturation mechanisms and employing $KRAS^{G12C}$ as a model protein.

Initially, FRET-Probe was utilized for exploring GTP stabilization of KRAS in the ICD assay. A dose-dependent stabilization of $KRAS^{G12V}$ was evidenced by the decrease of TR-FRET signal during the propanol and pH 5 ICD assays. Half

maximal effective concentration (EC_{50}) values calculated at 90 min were 5.2 ± 1.2 and 3.5 ± 0.1 nM, respectively, indicating a high affinity to GTP (Figure 23B).

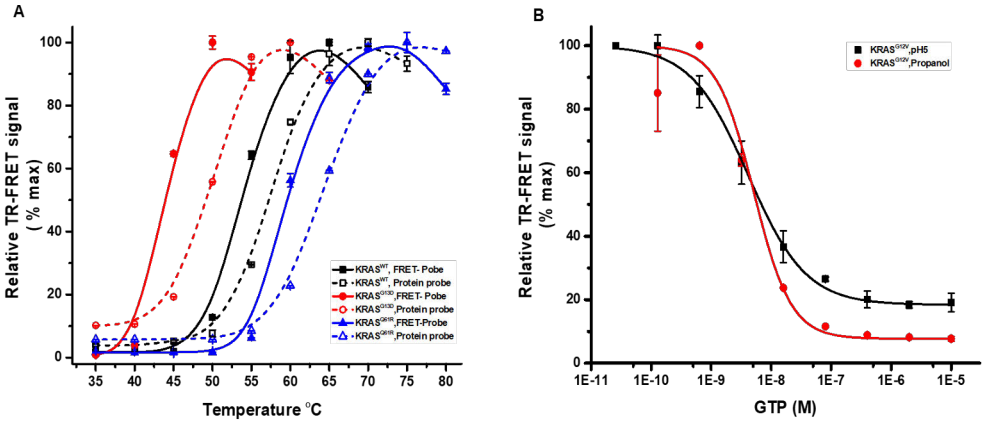

Figure 23. Effect of different cations and nucleotides on KRAS stability. (**A**) The thermal stability of three KRAS proteins with different intrinsic nucleotide exchange activity were compared with Protein-Probe (dashed) and FRET-Probe (solid) in parallel. The rank order of KRASWT (black), KRASG13D (red), and KRASQ61R (blue) is similar in both methods. Additionally, ΔT_m values calculated with both techniques for KRASG13D and KRASQ61R compared to KRASWT is the same. (**B**) Nucleotide titration with FRET-Probe from GTP titration (0-2 µM) with KRASG12V using pH5 (black) and propanol (red), E50 values show nanomolar affinity of KRASG12V to GTP and are equally measured in both denaturants. Data represents mean ± SD (n=3).

Next, FRET-Probe is utilized in studying PLIs of $KRAS^{G12C}$ with selected covalent and non-covalent inhibitors in ICD formats. The IC_{50} values reported for those inhibitors are mostly based on *in vitro* studies, therefore, we first confirmed the IC_{50} by nucleotide exchange assay using QRET technique. IC_{50} determined after 30 min incubation for ARS853 and ARS1620 were 1104 ± 126 and 289 ± 55 nM, and for MRTX849 and AMG510 were 18.9 ± 0.7 and 35 ± 7.1 nM, respectively (Figure 24). This data agrees well with the reported IC_{50} values and shows that the novel binders have much higher affinity compared to the previous generations.[49,60,291]

To test functionality of FRET-Probe in ICD assay, inhibition of ARS853 and ARS1620 was measured in urea, pH 5 and propanol ICD assays, IC_{50} of ARS853 and ARS1620 in pH 5 were 1017 ± 383 and 123 ± 35 nM, and in urea were 353 ± 50 and 240 ± 36 nM respectively (Figure 24A). In propanol, IC_{50} varied significantly according to alcohol concentration. IC_{50} values with 15, 20, and 25% propanol, for ARS1620 were 40.1 ± 1.3, 54.0 ± 2.7, and 414 ± 8 nM, and for ARS853 were 312 ± 23, 197 ± 62 and 1279 ± 98 nM respectively. Based on the combined results of the three denaturants, urea was found to be the most suitable denaturant for KRAS chemical denaturation due to fast kinetics and high S/B ratio. Similar conclusions

were observed with MRTX849 and AMG510 when tested in ICD assays with the same three chemical denaturants (Figure 24B), which indicates that selection of optimum denaturant is crucial for ICD assay.

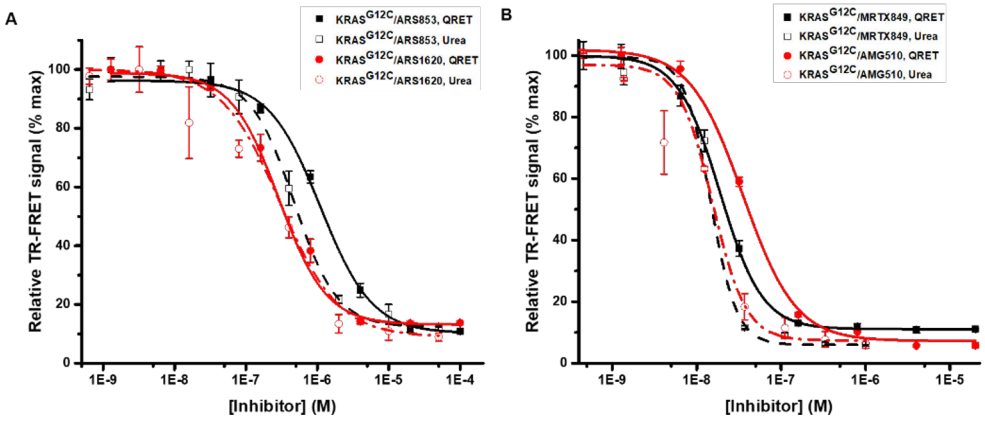

Figure 24. KRASG12C chemical stability with different covalent inhibitors. FRET-Probe was used to measure the binding induced stability by (**A**) ARS853 (black) and ARS1620 (red) and (**B**) MRTX849 (black) and AMG510 (red) for KRASG12C in urea (dashed), and nucleotide exchange (solid) as a control. In urea, the IC50 values obtained in the ICD assay was relatively similar to that estimated by nucleotide exchange. Data represents mean ± SD (n=3).

5.2.3 Investigation of the binding specificity and resistance mechanisms of the KRASG12C inhibitors, AMG510 and MRTX849

In **pub IV**, the interaction of AMG510 and MRTX849 to RAS proteins was investigated. To rule out binding of AMG510 and MRTX849 to the wild-type (WT), the affinity to $KRAS^{WT}$, $HRAS^{WT}$ and $NRAS^{WT}$ proteins was investigated. For that purpose, concentration dependent inhibition of the SOS^{cat} catalyzed nucleotide exchange was measured by QRET for $KRAS^{WT}$, $HRAS^{WT}$ and $NRAS^{WT}$. With all three RAS, both inhibitors showed low binding affinity. MRTX849 showed much lower binding to $HRAS^{WT}$ and $NRAS^{WT}$ (IC_{50} >15 µM) compared to $KRAS^{WT}$ (IC_{50} 200 ± 20 nM).[292] On the other hand, AMG510 had lower affinity to $KRAS^{WT}$ (IC_{50} 3.5 ± 0.8 µM) compared to $HRAS^{WT}$ and $NRAS^{WT}$ (1.3 ± 0.2 µM and 1.2 ± 0.2 µM respectively).[293] The low binding was similarly determined by Protein-Probe in TSA, in which 10 µM AMG510 and MRTX849 had nearly negligible effect on the thermal stability of 1µM KRAS, NRAS and HRAS.

At inhibitor concentration of 100 µM, Δ T_m with and without AMG510 for $KRAS^{WT}$, $NRAS^{WT}$ and $HRAS^{WT}$, was 10.4, 10.2 and 4.4 °C respectively. On the other hand, MRTX849 (100 µM) showed a shift with $KRAS^{WT}$ (Δ T_m 6.6 °C) and did

not have any measurable stabilizing effect on $NRAS^{WT}$ and $HRAS^{WT}$ (Figure 25). These results match the data determined earlier by QRET nucleotide exchange assay about MRTX849 higher affinity for KRAS compared to HRAS and NRAS.

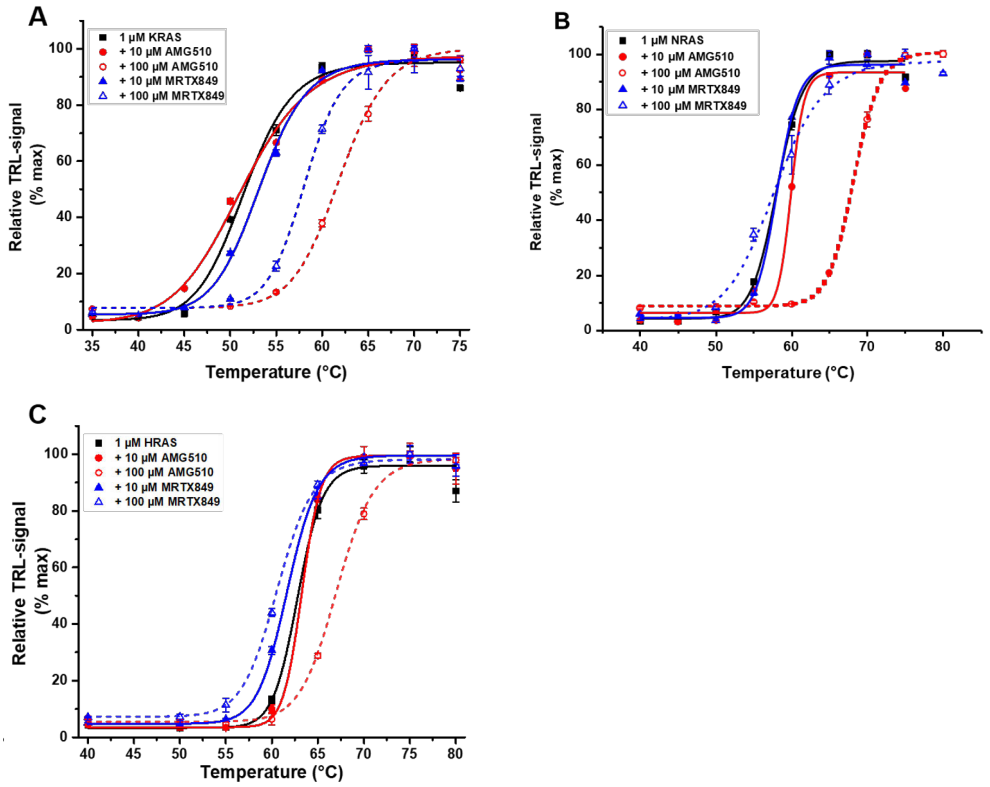

Figure 25. KRAS, NRAS and HRAS thermal stability with AMG510 and MRTX849. Protein - Probe technique applied for monitoring thermal stability of 1 µM (**A**) KRAS, (**B**) NRAS and (**C**) HRAS (black) with 10 µM (solid) and 100 µM (dashed) of AMG510 (red) and MRTX849 (blue), AMG510 showed a dose dependent stabilizing effect with KRAS and NRAS and a minor stabilization for HRAS. MRTX849 showed a dose dependent stabilizing effect only with KRAS, and no effect was observed with NRAS and HRAS, (mean ± SD, n = 3).

After confirmation that MRTX849 and AMG510 bind to $KRAS^{G12C}$ and not to WT, AMG510 and MRTX849 interaction with other KRAS mutants was next studied. Protein-Probe was applied to monitor PLI of the covalent binders with mutants ($KRAS^{G13D}$, $KRAS^{Q61L}$, $KRAS^{G12V}$, $KRAS^{G12D}$) in TSA. Interestingly, AMG510 showed micromolar affinity with all mutants. MRTX849 had also low affinity to all mutants, but it varied with different mutations, showing highest affinity

for $KRAS^{G13D}$ (IC_{50} = 401 ± 89 nM) and $KRAS^{Q61L}$ (IC_{50} = 432 ± 52 nM) and lowest for $KRAS^{G12V}$ and $KRAS^{G12D}$ (IC_{50} ~ 4µM).

Next, more in depth studying and comparative of AMG510 and MRTX849 binding mechanism was performed. The difference in the switch II pocket among these three RAS isoforms, KRAS, HRAS and NRAS lies only at position 95. To investigate the reason for MRTX849 higher affinity to $KRAS^{WT}$ and KRAS mutants, the binding affinity at position 95 was examined. The residues 95 in KRAS, HRAS and NRAS are His-95, Gln-95 and Leu-95 respectively. Y96D mutation was frequently reported in drug resistance studies, therefore, binding to position Y96 was also evaluated.[294] Based on computational simulations performed in the present study by co-authors, these two positions were selected to identify various interactions of the inhibitors at those positions. The data collected showed that MRTX849 had a remarkably high interaction with His-95 of KRAS compared to NRAS and HRAS. However, this same preference to His-95 was not seen with AMG510.

For further studying of the critical role of His-95 and Y96, these mutations were created in the $KRAS^{WT}$ and $KRAS^{G12C}$ constructs at position 95 and 96 to change histidine to leucine and tyrosine to aspartic acid. Both $KRAS^{H95L}$ and $KRAS^{Y96D}$ were stabilized with AMG510, Δ T_m 11.8 °C and 9.6 °C respectively. However, MRTX849 did not maintain the stabilizing effect that was previously monitored with $KRAS^{WT}$ at similar inhibitor concentration (100 µM) (Figure 26A). Similar results were obtained with double mutants ($G12C^{H95L}$ and $G12C^{Y96D}$), except that MRTX849 showed a small shift with $G12C^{H95L}$ (Δ T_m 4.1 °C), (Figure 26B), which indicates that AMG510 has weak interaction at these two residues. On the contrary, MRTX849 inhibition seems to be His-95 and Y96 dependent.

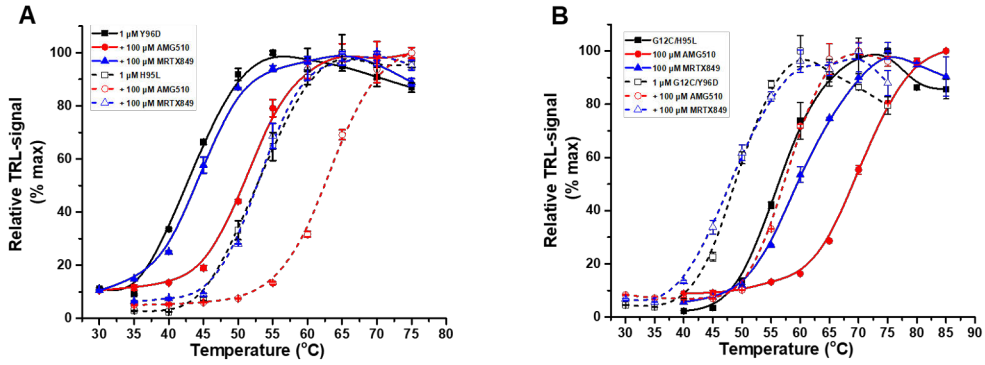

Figure 26. Role of His-95 and Y96 in AMG510 and MRTX849 binding specificity. Protein-Probe thermal stability of (**A**) KRASH95L (solid) and KRASY96D (dashed) or (**B**) G12CH95L (solid) and G12CY96D (dashed), in presence of AMG510 (red) and MRTX849 (blue) shows ligand induced stabilization with AMG510 and clear loss of the stabilizing effect with MRTX849, (mean ± SD, n = 3).

To examine these data further, the binding affinity of inhibitors to $KRAS^{WT}$, $KRAS^{H95L}$, $KRAS^{Y96D}$, $G12C^{H95L}$ and $G12C^{Y96D}$ was identified by QRET nucleotide exchange and compared to that with $KRAS^{G12C}$. AMG510 had weak binding to $KRAS^{WT}$, $KRAS^{H95L}$ and $KRAS^{Y96D}$. Interestingly, MRTX849 had better binding than AMG510 to $KRAS^{WT}$, but this effect was lost with H95L and Y96D mutations (Figure 27A). This data agrees with the previous observations with Protein-Probe in TSA and with the computational simulations.

As for nucleotide exchange data for the double mutants $G12C^{H95L}$ and $G12C^{Y96D}$, AMG510 inhibition of nucleotide exchange was markedly impaired in presence of H95L and Y96D, IC_{50} was 0.17 ± 0.04 and 1.6 ± 0.1 µM, respectively. Surprisingly, MRTX849 binding to $G12C^{Y96D}$ was lost, but this effect was partially rescued when H95L was introduced, IC_{50} with $G12C^{H95L}$ was 0.94 ± 0.07 µM (Figure 27B).

To achieve a definitive conclusion, the real-time kinetics of inhibitors nucleotide exchange with WT and double mutants was monitored by the QRET SOS^{cat} activated assay. $G12C^{H95L}$ nucleotide exchange was only inhibited with AMG510. On the other hand, only MRTX849 was able to initially block $KRAS^{WT}$ followed by an increase in signal due to the lack of covalent bond, as His-95 is KRAS specific and Y96 is conservative in all RAS isoforms. These combined results indicate that MRTX849 is intolerant to His-95 mutation, whereas AMG510 tolerates both His-95 and Y96 mutations, which indicates that MRTX849 is more KRAS specific than AMG510.

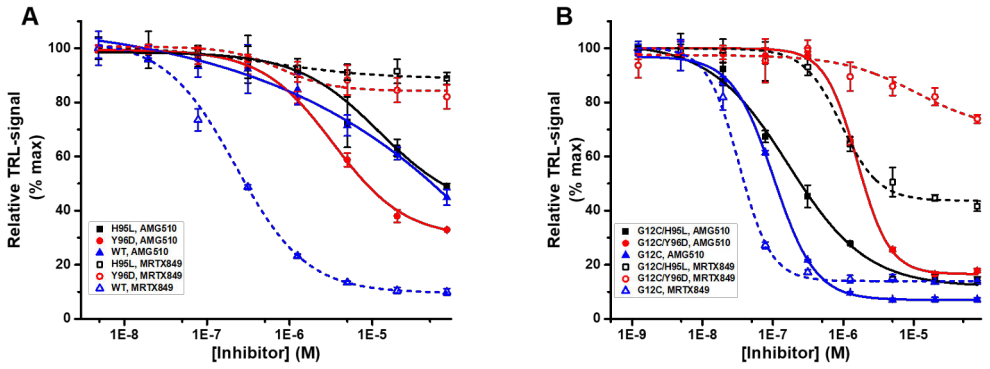

Figure 27. Interaction of AMG510 and MRTX849 to His-95 and Y96. SOS^{cat} activated QRET nucleotide exchange for (**A**) $KRAS^{WT}$ (blue), $KRAS^{H95L}$ (black) and $KRAS^{Y96D}$ (red), and (**B**) $KRAS^{G12C}$ (blue), $G12C^{H95L}$ (black) and $G12C^{Y96D}$ (red) in presence of AMG510 (solid) and MRTX849 (dashed), shows that MRTX849 affinity was compromised with $KRAS^{H95L}KRAS^{Y96D}$ and $G12C^{Y96D}$. On the other hand, AMG510 weak affinity to $KRAS^{WT}$ as well as its high affinity to $KRAS^{G12C}$ were not affected in presence of His-95 or Y96, (mean ± SD, n = 3).

6 Summary and Conclusions

GTP is an essential nucleotide that plays a critical role in building nucleic acids, regulating protein synthesis, and determining cell fate. One of its main functions is the regulation of downstream cell signaling pathways through the activation of small GTPases. Changes in cellular GTP concentration are linked to many diseases. Methods are needed to study small GTPases and GTP changes in different conditions and to develop novel therapeutic candidates for GTP-related diseases. However, current methods either lack sensitivity or throughput.

In this PhD project, robust, high throughput and label free techniques were developed to monitor GTP and small GTPases. A homogenous GTP antibody-based method was used for quantification of GTP from cell extracts. This technique is based on a competition between cellular GTP and Eu^{3+}–labeled GTP for the binding to GTP specific antibody. Moreover, two luminescent probes (Protein-Probe and FRET-Probe) were utilized to study small GTPases. Protein-Probe and FRET-Probe are designed as short peptide sequences that monitor TRL and TR-FRET signals, respectively. Protein-Probe is a Eu^{3+}–chelate labeled peptide probe that works in a two-step protocol and a low pH format. The FRET-Probe method, on the other hand, is labeled with Eu^{3+} and Cy5 at opposite ends. The probe is designed for single step protocol and works at a neutral pH. The principle of both luminescent probes is based on the increase in signal upon binding of the probe to the unfolded form of the protein due to interaction with the nonpolar protein core.

In publication **I**, QRET method was applied to detect GTP and ATP simultaneously from cell lysate. The method efficiently measured GTP and ATP concentrations in multiple cell lines, the results were validated by comparison to CE/MS as a control method. The detection of both GTP and ATP from the same well has great potential for diverse applications in many scientific fields. For example, in drug discovery, researchers can screen for compounds that affect cellular processes regulated by GTP and ATP. Additionally, in cancer research, the method can be employed to study the metabolic differences between normal and cancer cells, exploring the roles of GTP and ATP in cancer cell survival and proliferation.

GTP interacts with GTPases and affect their functions in cells, therefore, in the present study, the ligand interaction and thermal stability of small GTPases were

studied. In publications **II**, melting curves of different small GTPases were performed by Protein-Probe method in comparison with other commercial thermal stability methods. Additionally, different parameters that affect TSA were studied. The study showed that thermal stability is significantly affected by buffer ions as well as protein concentration. Therefore, T_m values are unlikely to be similar when performed with different methods or even with the same method if different assay conditions are applied. It was also determined that KRAS thermal stability by different nucleotides and nucleotides analogues is affinity and concentration dependent. PLI of $KRAS^{G12C}$ with different covalent inhibitors was monitored at low protein and inhibitor concentrations to avoid signal quenching which often occurs at high inhibitor concentrations.

In publication **III**, FRET-Probe was introduced and applied for measuring ICD. The study aimed at overcoming the limitations of TSA, such as irreversible denaturation, loss of protein activity and unpredictable protein stability at normal temperatures. The method was first compared to Protein-Probe in TSA and it was examined with KRAS mutants and their covalent inhibitors, with three common chemical denaturation systems (acid, alcohol, and urea). In TSA, FRET-Probe for $KRAS^{G13D}$, $KRAS^{Q61R}$ and $KRAS^{WT}$ showed the same stability order as obtained with Protein-Probe, which indicates that FRET-Probe can efficiently monitor thermal shifts at nanomolar concentration same as Protein-Probe. As for the real time signal monitoring in ICD assays, the method was successfully used to study the three denaturants in comparison with nucleotide exchange assay as a control. Among the three denaturants pH 5 was the slowest and had low S/B. As for propanol, it had dramatically variable effect when different alcohol concentrations were used. In contrast, urea was the most optimum denaturant for small GTPases, as it showed high S/B and fast kinetics. Moreover, PLI of covalent inhibitors and $KRAS^{G12C}$ studied with urea, showed very comparable IC_{50} to that obtained by nucleotide exchange assay.

In publication **IV**, Protein-Probe along with molecular dynamic simulations, were employed to thoroughly examine the binding specificity of the two FDA-approved drugs, AMG510 and MRTX849. The study concluded that while these two inhibitors bind to the same switch II pocket of the GDP-loaded $KRAS^{G12C}$, they interact in distinct ways. Among the three main RAS isoforms HRAS, NRAS and KRAS, MRTX849 showed significantly higher specificity to KRAS through His-95. However, binding to $KRAS^{G12C}$ is more affected by interaction with the Y96 residue, which might explain the frequent coexistence of the Y96 mutation with MRTX849 drug resistance.

In conclusion, in the current PhD thesis, novel methods were studied for GTP detection. A homogenous high throughput QRET based method was developed for monitoring GTP concentration in cells with the same sensitivity as in CE/MS and

with a shorter cell preparation protocol. On the other hand, the assay has room for improvement if the GTP-antibody was labeled to simplify the detection process and increase the sensitivity. In this scenario, the signal will be directly related to the GTP concentration, in contrast to the current competitive assay format. Nevertheless, the labeling of the GTP-specific Fab without impairing its efficacy, poses challenges. The binding site of the label may potentially disrupt GTP binding, thereby impacting GTP-Fab's affinity and specificity for GTP. The work with this project is ongoing and has provided promising preliminary results.

The Protein-Probe method addresses the need for a sensitive, label-free approach in protein stability and PLI studies. With nanomolar sensitivity, it surpasses several existing solution-based methods requiring higher concentrations. The method is versatile, easily applicable to various proteins and interactions with minimal assay modifications. The assay set up allows for significant sample dilution, reducing interference from protein storage buffer components.

However, the method has limitations. Protein-Probe works in a two-step protocol because the probe modulation solution is unstable at high temperatures. The need for a two-step protocol complicates the assay, demanding extra work and increasing sample requirements. Moreover, the probe function requires partial protonation of carboxylic groups at lowered pH, which may affect sensitive proteins, potentially denaturing them. Furthermore, the restriction of the probe's interaction with the hydrophobic core of the protein, predominantly exposed during heating, limits its application for detection of non-unfolded, native protein in room temperature assays. Currently, the main applications of Protein-Probe are monitoring protein thermal stability, ligand interactions and aggregation.

The FRET-Probe is dual-labeled with Eu^{3+} at the N-terminus and Cy5 at the C-terminus of the same peptide, unlike the Protein-Probe assay, that involves a separate Eu^{3+}-labeled peptide and a Cy5-containing quencher. Consequently, the FRET-Probe assay is performed in one step, using a qPCR instrument. It also has an additional advantage of working at neutral pH, which does not affect the protein structure. FRET-Probe has demonstrated efficiency not only in TSA but also in ICD assays. This eliminates the need for heating at high temperatures and allows real-time monitoring of protein unfolding kinetics, providing direct information about protein stability. Additionally, the FRET-Probe maintains the nanomolar sensitivity of the Protein-Probe.

The Protein-Probe and FRET-Probe have great potential for being utilized in a high throughput assay setup, due to the homogenous assay format and the simultaneous testing of numerous samples in a 384-well plate. In the present study, these methods have demonstrated significant applicability in the examination of small GTPases and their binding interactions with nucleotides and inhibitors. The

nanomolar sensitivity of these probes has enabled the exploration of novel aspects of RAS proteins.

However, it is important to note that Protein-Probe and FRET-Probe are not universal probes and are not applicable for all proteins. The probes must be tested first with the target protein to determine its interaction with the probes and the assay detection limit. Selecting the proper probe for a target protein is primarily dependent on the studied protein in terms of charge and structure. Protein-Probe and FRET-Probe work at different pH, which has a marked effect on the charge of the studied protein, consequently influencing its interaction and visualization with the probe. For these reasons, the same protein might exhibit a significantly different detection limit when tested with both probes.

The same applies to the FRET-Probe in ICD assays; each protein shows different tolerance to different chemical denaturants. Thus, each protein should be individually tested with several denaturants to select the optimum denaturant. Afterwards, the assay conditions should be further optimized in terms of denaturant concentration and buffer conditions to identify the best conditions that yield the fastest kinetics and the highest S/B ratio.

Acknowledgements

This doctoral thesis work was fulfilled in the Detection Technology group at the Department of Chemistry in the University of Turku during the years 2021–2023. I am grateful to the funding organizations of my PhD project: Academy of Finland, Otto A. Malm foundation and the Finnish Academy of Science and Letters (Vilho, Yrjö, and Kalle Väisälä) for their financial support, which played a crucial role in facilitating my research endeavors.

Furthermore, I extend my appreciation to the heads of the department, Prof. Pasi Virta, Prof. Juha-Pekka Salminen, and Prof. Carita Kvarnström, for giving me the opportunity to perform my doctoral studies at the Department of Chemistry.

My sincere gratitude goes to Prof. Matthew Smith and Prof. Joshua Jackman for reviewing my thesis and providing insightful comments on my work, and Prof. Paul Brennan for agreeing to be my opponent in the dissertation defense.

I would like to express my deepest gratitude to my PhD supervisors, Harri Härmä, Kari Kopra and Morteza Malakoutikhah, for their constant guidance, invaluable insights, and continuous support throughout the entire doctoral journey. Harri consistently guided me back on the right path when I sometimes lost my way, and he consistently encouraged me to reach my full potential. Thank you, Kari, for being so patient, and always having the answers to all my questions. Your passion for science, especially G-proteins, made this journey both educational and enjoyable. Morteza, without your mental support and encouragement, I would not have made it through some of the hard days in the lab. Thank you for consistently reminding me not to be too hard on myself.

I am also thankful for former members of the group, Emmiliisa Vuorinen, and Salla Valtonen, for their continuous help and sincere guidance. You shared your experiences and provided me with a shortcut to success. I hope we will stay friends forever, and Nazia Hassan, thank you for being there for me when I first joined the group, I am so happy for you for pursuing your career goals.

To Negin Gooran, our newest addition to the group, I wish you a fulfilling PhD journey. Given your responsible and hardworking nature, I am confident that you will excel in all your future endeavors.

I extend heartfelt appreciation to my colleagues at University of Turku/Department of Chemistry- Ashwini Jadhav, Sami Vuori, Sachin Kochrekar, Adefunke Koyejo and Majid Al-waeel-for their friendship, and shared enthusiasm. I am also grateful to the hardworking and ambitious students whom I had the pleasure to supervise during my time as a doctoral student, Niklas Vello, Anita Komulainen and Olivia Kuivala.

I thank Ahmadreza Masoumi for his dedicated work and polite nature, with your hard work and passion for science, you extended your research in our lab from 3 months to more than a year and you have done enough work for at least one publication. I wish you all the best in your future career.

I express my gratitude to Titta Yli-Hollo for not only being a brilliant master student but also a great person and a caring friend. I am aware of your high aspirations for the future, and with the wisdom that defines you, I am confident that you will succeed in fulfilling all your dreams.

I would like to extend my sincere appreciation to Jenni Vuorio, who has not only proven to be an exceptional student but has also evolved into a cherished friend. Thank you for supporting me during presentations and for the fun time we had during our shared courses.

I am very grateful to Susanna Virtanen for always being there for me and for all the international students to help us have a smooth start to our PhD journey.

Thank you, Kari Loikas, Mauri Nauma, and Kirsi Laaksonen for the technical and logistic support that made my life easier. A big thank you to everyone else at the Department of Chemistry for all the good time we had, such as decorating the Christmas tree, the department Christmas parties and summer trips.

My sincere thanks go to my mother and my father, who had no idea why I travelled to Finland and what exactly I am doing there, but they still supported my decision.

Yehia and Ismail, my dear sons, I have gone through this for you. Thank you for your understanding, even though you were quite young when this journey began. Thank you for all the fun times and the adventures we had together, whether here in Finland or during our travels.

Finally, to my dear husband, my soulmate, without you this research would not have been possible. Thank you for believing in me, even during moments when I doubted myself. Your unconditional emotional support made me able to survive through difficult times and challenges. I consider myself incredibly lucky to have you in my life. Thank you for simply being you.

11.01.2024
Randa Mahran

List of References

1. LeClair, R. J. Cell Biology, Genetics, and Biochemistry for Pre-Clinical Students. *Virginia Tech Carilion School of Medicine in association with Virginia Tech Publishing,* 2021. doi:10.21061/CELLBIO.
2. Alberts, B. *et al.* T Cells and MHC Proteins. *Mol Biol Cell* 1569–1588 (2008).
3. Stillman, B. Deoxynucleoside triphosphate (dNTP) synthesis and destruction regulate the replication of both cell and virus genomes. *Proc Natl Acad Sci U S A* **110**, 14120–14121 (2013).
4. Moffatt, B. A. & Ashihara, H. Purine and pyrimidine nucleotide synthesis and metabolism. *Arabidopsis Book* **1**, e0018 (2002).
5. Cooper, G. M., & Adams, K. W. *The cell: a molecular approach*. Oxford University Press (2023).
6. Yin, J. *et al.* Potential Mechanisms Connecting Purine Metabolism and Cancer Therapy. *Front Immunol* **9**, 1697 (2018).
7. Ansari, M. Y. *et al.* Establishment of correlation between in-silico and in-vitro test analysis against Leishmania HGPRT to inhibitors. *Int J Biol Macromol* **83**, 78–96 (2016).
8. Ali, E. S. *et al.* ERK2 Phosphorylates PFAS to Mediate Posttranslational Control of De Novo Purine Synthesis. *Mol Cell* **78**, 1178-1191 (2020).
9. Villa, E., Ali, E. S., Sahu, U. & Ben-Sahra, I. Cancer Cells Tune the Signaling Pathways to Empower de Novo Synthesis of Nucleotides. *Cancers* **11**, 688 (2019).
10. Kofuji, S. & Sasaki, A. T. GTP metabolic reprogramming by IMPDH2: Unlocking cancer cells' fuelling mechanism. *Journal of Biochemistry* **168**, 319–328 (2020). doi.org/10.1093/jb/mvaa085
11. Meshkini, A., Yazdanparast, R., & Nouri, K. Intracellular GTP level determines cell's fate toward differentiation and apoptosis. *Toxicol Appl Pharmacol* **253**, 188–196 (2011).
12. Sumita, K. *et al.* The Lipid Kinase PI5P4Kβ Is an Intracellular GTP Sensor for Metabolism and Tumorigenesis. *Mol Cell* **61**, 187–198 (2016).
13. Jansen, R. S., Rosing, H., Schellens, J. H. M. & Beijnen, J. H. Mass spectrometry in the quantitative analysis of therapeutic intracellular nucleotide analogs. *Mass Spectrom Rev* **30**, 321–343 (2011).
14. Ferraro, P., Franzolin, E., Pontarin, G., Reichard, P. & Bianchi, V. Quantitation of cellular deoxynucleoside triphosphates. *Nucleic Acids Res* **38**, e85–e85 (2010).
15. Díaz-Talavera, A. *et al.* A cancer-associated point mutation disables the steric gate of human PrimPol. *Scientific Reports 2019 9:1* **9**, 1–13 (2019).
16. Traut, T. W. Physiological concentrations of purines and pyrimidines. *Mol Cell Biochem* **140**, 1–22 (1994).
17. Aird, K. M. & Zhang, R. Nucleotide metabolism, oncogene-induced senescence and cancer. *Cancer Lett* **356**, 204–210 (2015).
18. Rogne, P. *et al.* Molecular mechanism of ATP versus GTP selectivity of adenylate kinase. *Proc Natl Acad Sci U S A* **115**, 3012–3017 (2018).
19. Qian, Y. *et al.* Extracellular ATP is internalized by macropinocytosis and induces intracellular ATP increase and drug resistance in cancer cells. *Cancer Lett* **351**, 242–251 (2014).
20. Patel, J. A. & Kim, H. The TIMELESS effort for timely DNA replication and protection. *Cell Mol Life Sci* **80,** 84 (2023).

21. Moretton, A. & Loizou, J. I. cancers Interplay between Cellular Metabolism and the DNA Damage Response in Cancer. *Cancers* **12,** 2051 (2020). doi:10.3390/cancers12082051.
22. Lecca, D. & Ceruti, S. Uracil nucleotides: From metabolic intermediates to neuroprotection and neuroinflammation. *Biochem Pharmacol* **75**, 1869–1881 (2008).
23. Bitter, E. E., Townsend, M. H., Erickson, R., Allen, C. & O'Neill, K. L. Thymidine kinase 1 through the ages: a comprehensive review. *Cell & Bioscience* **10**, 1–16 (2020).
24. Dzeja, P. P., Bortolon, R., Perez-Terzic, C., Holmuhamedov, E. L. & Terzic, A. Energetic communication between mitochondria and nucleus directed by catalyzed phosphotransfer. *Proc Natl Acad Sci U S A* **99**, 10156–10161 (2002).
25. Aprille, J. R. Mechanism and regulation of the mitochondrial ATP-Mg/Pi carrier. *J Bioenerg Biomembr* **25**, 473–481 (1993).
26. Zala, D. *et al.* Vesicular glycolysis provides on-board energy for fast axonal transport. *Cell* **152**, 479–491 (2013).
27. Rivas, L., Stathis, C. G., Johnson, T. A., Jinnah, H. A. & Kamatani, N. Shortage of Cellular ATP as a Cause of Diseases and Strategies to Enhance ATP. *Frontiers in pharmacology, 10, 98* (2019).
28. Fields, R. D. & Burnstock, G. Purinergic signalling in neuron-glia interactions. *Nat Rev Neurosci* **7**, 423 (2006).
29. Magistretti, P. J. & Allaman, I. A. Cellular Perspective on Brain Energy Metabolism and Functional Imaging. *Neuron* **86**, 883–901 (2015).
30. Hauk, G. & Berger, J. M. The role of ATP-dependent machines in regulating genome topology. *Curr Opin Struct Biol* **36**, 85–96 (2016).
31. Nagata, R., Fujihashi, M., Sato, T., Atomi, H. & Miki, K. Identification of a pyrophosphate-dependent kinase and its donor selectivity determinants. *Nat Commun* **9**, 1765 (2018).
32. Frick, D. N. & Lam, A. M. I. Understanding Helicases as a Means of Virus Control. *Current pharmaceutical design* **12**, 1315-1338 (2006).
33. Pyeritz, R. E. The Genetics of Cardiac Electrophysiology in Humans. Emery and Rimoin's Principles and Practice of Medical Genetics. *Academic press* (2018)
34. Dogterom, M. & Yurke, B. Measurement of the force-velocity relation for growing microtubules. *Science* **278,** 856–860 (1997).
35. Mitchison, T. & Kirschner, M. Dynamic instability of microtubule growth. *Nature* **312,** 237–242 (1984).
36. Jewett, M. C., Miller, M. L., Chen, Y. & Swartz, J. R. Continued protein synthesis at low [ATP] and [GTP] enables cell adaptation during energy limitation. *J Bacteriol* **191,** 1083–1091 (2009).
37. Chojnowski, K., Opielka, M., Nazar, W., Kowianski, P. & Smolenski, R. T. Neuroprotective Effects of Guanosine in Ischemic Stroke—Small Steps towards Effective Therapy. *International Journal of Molecular Sciences* **22**, 6898 (2021).
38. Schmidt, A. P., Lara, D. R. & Souza, D. O. Proposal of a guanine-based purinergic system in the mammalian central nervous system. *Pharmacol Ther* **116**, 401–416 (2007).
39. Zala, D. *et al.*The advantage of channeling nucleotides for very processive. *F1000Research* **6**, (2017).
40. Takai, Y., Sasaki, T. & Matozaki, T. Small GTP-Binding Proteins. *Physiological reviews* **81,** 153-208 (2001).
41. Praefcke, G. J., & McMahon, H. T. The dynamin superfamily: universal membrane tubulation and fission molecules?. *Nature reviews Molecular cell biology* 5, 133-147 (2004).
42. Vestal, D. J. The guanylate-binding proteins (GBPs): Proinflammatory cytokine-induced members of the dynamin superfamily with unique GTPase activity. *Journal of Interferon and Cytokine Research* **25**, 435–443 (2005).
43. Sever, S., Muhlberg, A. B. & Schmid, S. L. Impairment of dynamin's GAP domain stimulates receptor-mediated endocytosis. *Nature* **398**, (1999).
44. Etienne-Manneville, S. Cdc42 - the centre of polarity. *J Cell Sci* **117**, 1291–1300 (2004).

45. Park, H.-O. & Bi, E. Central Roles of Small GTPases in the Development of Cell Polarity in Yeast and Beyond. *Microbiology and Molecular Biology Reviews* **71**, 48–96 (2007).
46. He, H. *et al.* The roles of GTPase-activating proteins in regulated cell death and tumor immunity. *J Hematol Oncol* **14**, (2021).
47. Cox, A. D. & Der, C. J. Ras history: The saga continues. *Small GTPases* **1**, 2–27 (2010).
48. L Ostrem, J. M. & Shokat, K. M. Direct small-molecule inhibitors of KRAS: from structural insights to mechanism-based design. Nat. Rev. Drug Discov **15,** 771-785 (2016).
49. Kwan, A. K., Piazza, G. A., Keeton, A. B. & Leite, C. A. The path to the clinic: a comprehensive review on direct KRAS G12C inhibitors. *J. Exp. Clin. Cancer Res.* **41,** 27 (2021).
50. Hunter, J. C. et al. Oncogenes and Tumor Suppressors Biochemical and Structural Analysis of Common Cancer-Associated KRAS Mutations. Mol. Cancer Res. **13,** 1325-1335(2015).
51. Ann Boriack-Sjodin, P., Margarit, S. M., Bar-Sagi, D. & Kuriyan, J. The structural basis of the activation of Ras by Sos. Nature **394,** 337-343 (1998).
52. Li, L. et al. The Ras/Raf/MEK/ERK signaling pathway and its role in the occurrence and development of HCC (Review). *Oncol Lett* **12,** 3045–3050 (2016).
53. Hobbs, G. A., Der, C. J. & Rossman, K. L. RAS isoforms and mutations in cancer at a glance. *J Cell Sci* **129,** 1287–1292 (2016).
54. Lampson, B. L. et al. Report Rare Codons Regulate KRas Oncogenesis. *Current Biology* **23,** 70–75.
55. Scheffzek, K. et al. The Ras-RasGAP complex: Structural basis for GTPase activation and its loss in oncogenic ras mutants. Science **277,** 333–338 (1997).
56. Haigis, K. M. KRAS Alleles: The devil is in the detail. *Trends Cancer* **3,** 686–697 (2017).
57. Shen, H. et al. KRAS G12D Mutation Subtype in Pancreatic Ductal Adenocarcinoma: Does It Influence Prognosis or Stage of Disease at Presentation? *Cells* **11,** 3175 (2022).
58. Prior, I. A., Lewis, P. D. & Mattos, C. A Comprehensive Survey of Ras Mutations in Cancer. *Cancer Res* **72,** 2457–2467 (2012).
59. Cox, A. D., Fesik, S. W., Kimmelman, A. C., Luo, J. & Der, C. J. Drugging the undruggable RAS: Mission Possible? *Nat Rev Drug Discov* **13,** 828–851 (2014).
60. Janes, M. R. et al. Targeting KRAS Mutant Cancers with a Covalent G12C-Specific Inhibitor. *Cell* **172,** 578-589 (2018).
61. Huang, L., Guo, Z., Wang, F. & Fu, L. KRAS mutation: from undruggable to druggable in cancer. *Signal Transduct. Target. Ther.* **6,** 386 (2021).
62. Lanman, B. A. et al. Discovery of a Covalent Inhibitor of KRASG12C (AMG 510) for the Treatment of Solid Tumors. *J Med Chem* **63,** 52–65 (2019).
63. Liu, J., Kang, R. & Tang, D. The KRAS-G12C inhibitor: activity and resistance. Cancer Gene Therapy *Cancer Gene Therapy* **29,** 875-878 (2022).
64. Awad, M. M. et al. Acquired Resistance to KRAS G12C Inhibition in Cancer . New England *J Med* **384,** 2382–2393 (2021).
65. Addeo, A., Banna, G. L. & Friedlaender, A. KRAS G12C Mutations in NSCLC: From Target to Resistance. *Cancers* **13,** 2541(2021).
66. Blaquier, J. B., Cardona, A. F. & Recondo, G. Resistance to KRASG12C Inhibitors in Non-Small Cell Lung Cancer. *Front Oncol* **11,** 5551 (2021).
67. Mateos, F. A. & Puig, J. G. Purine metabolism in Lesch-Nyhan syndrome versus Kelley-Seegmiller syndrome. *J Inherit Metab Dis* **17**, 138–142 (1994).
68. Nyhan, W. L. The recognition of Lesch-Nyhan syndrome as an inborn error of purine metabolism. *J Inherit Metab Dis* **20**, 171–178 (1997).
69. Torres, R. J. & Puig, J. G. Hypoxanthine-guanine phosophoribosyltransferase (HPRT) deficiency: Lesch-Nyhan syndrome. *Orphanet J Rare Dis* **2**, 1–10 (2007).
70. Zoref-Shani, E., Feinstein, S., Frishberg, Y., Bromberg, Y. & Sperling, O. Kelley-Seegmiller syndrome due to a unique variant of hypoxanthine-guanine phosphoribosyltransferase: reduced

affinity for 5-phosphoribosyl-1-pyrophosphate manifested only at low, physiological substrate concentrations. *Biochim Biophys Acta* **1500**, 197–203 (2000).
71. Burrell, A. L. & Kollman, J. M. IMPDH dysregulation in disease: a mini review. *Biochem. Soc. Trans.* **50,** 71–82. (2022).
72. Mencacci, N. E. *et al.* Parkinson's disease in GTP cyclohydrolase 1 mutation carriers. *Brain* **137**, 2480–2492 (2014).
73. Fanet, H., Capuron, L., Castanon, N., Calon, F. & Vancassel, S. Tetrahydrobioterin (BH4) Pathway: From Metabolism to Neuropsychiatry. *Curr Neuropharmacol* **19**, 591–609 (2020).
74. Dagher, P. C. Apoptosis in ischemic renal injury: roles of GTP depletion and p53. *Kidney Int* **66**, 506–509 (2004).
75. Kelly, K. J., Plotkin, Z. & Dagher, P. C. Guanosine supplementation reduces apoptosis and protects renal function in the setting of ischemic injury. *J Clin Invest* **108**, 1291–1298 (2001).
76. Diehl, F. F. *et al.* Nucleotide imbalance decouples cell growth from cell proliferation. *Nature Cell Biology* **24**, 1252–1264 (2022).
77. Stalnecker, C. A. & Der, C. J. RAS, wanted dead or alive: Advances in targeting RAS-mutant cancers. *Sci Signal* **13**, (2020).
78. Rajasekharan, S. K. & Raman, T. Ras and Ras mutations in cancer. *Cent Eur J Biol* **8**, 609–624 (2013).
79. Takashima, A. & Faller, D. V. Targeting the RAS oncogene. *Expert opinion on therapeutic targets* **17**, 507–531 (2013).
80. Buhrman, G., Kumar, V. S. S., Cirit, M., Haugh, J. M. & Mattos, C. Allosteric modulation of Ras-GTP is linked to signal transduction through RAF kinase. *J Biol Chem* **286**, 3323–3331 (2011).
81. Fernández-Medarde, A. and S. E. Ras in Cancer and Developmental Diseases. *Genes Cancer* **2**, 344–358 (2011).
82. Sastre, A. A. *et al.* Small GTPases of the Ras and Rho Families Switch on/off Signaling Pathways in Neurodegenerative Diseases. *Int. J. Mol. Sci.* **21**, 6312 (2020).
83. Zhou, H. *et al.* The Ras GTPase-activating-like protein IQGAP1 is downregulated in human diabetic nephropathy and associated with ERK1/2 pathway activation. *Mol Cell Biochem* **391**, 21–25 (2014).
84. Wang, Y. *et al.* Oligomer β-amyloid Induces Hyperactivation of Ras to Impede NMDA Receptor-Dependent Long-Term Potentiation in Hippocampal CA1 of Mice. *Front Pharmacol* **11**, 1894 (2020).
85. Gamache, T. R., Araki, Y. & Huganir, R. L. Twenty Years of SynGAP Research: From Synapses to Cognition. *J Neurosci* **40**, 1596–1605 (2020).
86. Anastasaki, C., Orozco, P. & Gutmann, D. H. RAS and beyond: the many faces of the neurofibromatosis type 1 protein. *Disease Models and Mechanisms* **15**, dmm049362 (2022).
87. Roberts, A. E. *et al.* Germline gain-of-function mutations in SOS1 cause Noonan syndrome. *Nature genetics* **39,** 70-74 (2007).
88. Jelesarov, I. & Bosshard, H. R. Isothermal titration calorimetry and differential scanning calorimetry as complementary tools to investigate the energetics of biomolecular recognition. *J. Mol. Recognit.* **12,** 3-18 (1999).
89. Johnson, C. M. Differential scanning calorimetry as a tool for protein folding and stability. *Arch Biochem Biophys* **531,** 100–109 (2013).
90. Fiedler, S., Cole, L. & Keller, S. Automated circular dichroism spectroscopy for medium-throughput analysis of protein conformation. *Anal Chem* **85,** 1868–1872 (2013).
91. Alexander Harrison, J., Pruška, A., Oganesyan, I., Bittner, P. & Zenobi, R. Temperature-Controlled Electrospray Ionization: Recent Progress and Applications. *Chem. - Eur. J* **27,** 18015–18028 (2021).
92. Senisterra, G., Chau, I. & Vedadi, M. Thermal Denaturation Assays in Chemical Biology. Assay Drug Dev Technol **10,** 128-136 (2012).

93. McClure, S. M., Ahl, P. L. & Blue, J. T. High Throughput Differential Scanning Fluorimetry (DSF) Formulation Screening with Complementary Dyes to Assess Protein Unfolding and Aggregation in Presence of Surfactants. *Pharm Res* **35,** 1–10 (2018).
94. Gao, K., Oerlemans, R. & Groves, M. R. Theory and applications of differential scanning fluorimetry in early-stage drug discovery. *Biophys. Rev.* **12,** 85–104 (2020).
95. Valtonen, S. et al. Sensitive, homogeneous, and label-free protein-probe assay for antibody aggregation and thermal stability studies. *MAbs* **13,** 1955810 (2021).
96. Cimmperman, P. et al. A Quantitative Model of Thermal Stabilization and Destabilization of Proteins by Ligands. *Biophys J* **95,** 3222–3231 (2008).
97. Zeng, M. et al. Potent and Selective Covalent Quinazoline Inhibitors of KRAS G12C. *Cell Chem Biol* **24,** 1005-1016 (2017).
98. Kopra, K. et al. Thermal Shift Assay for Small GTPase Stability Screening: Evaluation and Suitability. *Int J Mol Sci* **23,** 7095 (2022).
99. Kopra, K. et al. Homogeneous Dual-Parametric-Coupled Assay for Simultaneous Nucleotide Exchange and KRAS/RAF-RBD Interaction Monitoring. *Anal Chem* **92,** 4971 (2020).
100. Mičová, K. *et al.* Mass Spectrometry for the Sensitive Analysis of Intracellular Nucleotides and Analogues. *Mass Spectrometry* (2017). doi:10.5772/68073.
101. Gosling, J. P. Enzyme Immunoassay. *Immunoassay* 287–308 (1996). doi:10.1016/B978-012214730-2/50014-5.
102. Ng, S., Lim, H. S., Ma, Q. & Gao, Z. Optical Aptasensors for Adenosine Triphosphate. *Theranostics* **6**, 1683–1702 (2016).
103. Chang, C. C. *et al.* Gold Nanoparticle-Based Colorimetric Strategies for Chemical and Biological Sensing Applications. *Nanomaterials* **9**, 861 (2019).
104. Liu, G., Lu, M., Huang, X., Li, T. & Xu, D. Application of Gold-Nanoparticle Colorimetric Sensing to Rapid Food Safety Screening. *Sensors* **18**, 4166 (2018).
105. Deng, G., Zha, H., Luo, H. & Zhou, Y. Aptamer-conjugated gold nanoparticles and their diagnostic and therapeutic roles in cancer. *Front Bioeng Biotechnol* **11**, (2023).
106. Nutiu, R. & Li, Y. Aptamers with fluorescence-signaling properties. *Methods* **37**, 16–25 (2005).
107. Li, Y. & Liu, J. Sensing guanine and its derivatives: From molecular recognition to applications. *Sensors and Actuators Reports* **2**, 100020 (2020).
108. Davis, J. H. & Szostak, J. W. Isolation of high-affinity GTP aptamers from partially structured RNA libraries. *Proceedings of the National Academy of Sciences* **99**, 11616–11621 (2002).
109. Carothers, J. M., Oestreich, S. C. & Szostak, J. W. Aptamers Selected for Higher-Affinity Binding Are Not More Specific for the Target Ligand. *Journal of the American Chemical Society* **128,** 7929-7937 (2006). doi:10.1021/ja060952q.
110. Zhao, W., Chiuman, W., Brook, M. A. & Li, Y. Simple and Rapid Colorimetric Biosensors Based on DNA Aptamer and Noncrosslinking Gold Nanoparticle Aggregation. *ChemBioChem* **8,** 727-731(2007). doi:10.1002/cbic.200700014.
111. Wang, J. *et al.* A Gold Nanoparticle-Based Aptamer Target Binding Readout for ATP Assay. *Advanced Materials* **19,** 3943-3946 (2007). doi:10.1002/adma.200602256.
112. Chen, Y. T., Hsu, C. L. & Hou, S. Y. Detection of single-nucleotide polymorphisms using gold nanoparticles and single-strand-specific nucleases. *Anal Biochem* **375**, 299–305 (2008).
113. Li, S. *et al.* An ultrasensitive colorimetric aptasensor for ATP based on peptide/Au nanocomposites and hemin-G-quadruplex DNAzyme. *RSC Advances* **4,** 23185-23190 (2014). doi:10.1039/c4ra02823f.
114. Li, J. *et al.* General Colorimetric Detection of Proteins and Small Molecules Based on Cyclic Enzymatic Signal Amplification and Hairpin Aptamer Probe. *Analytical chemistry* **84,** 5309-5315 (2012). doi:10.1021/ac3006186.
115. Elbaz, J., Moshe, M., Shlyahovsky, B. & Willner, I. Cooperative multicomponent self-assembly of nucleic acid structures for the activation of DNAzyme cascades: A paradigm for DNA sensors and aptasensors. *Chemistry - A European Journal* **15**, 3411–3418 (2009).

116. Webb, M. R. A continuous spectrophotometric assay for inorganic phosphate and for measuring phosphate release kinetics in biological systems. *Proc Natl Acad Sci U S A* **89**, 4884–4887 (1992).
117. Xia, F. *et al.* Colorimetric detection of DNA, small molecules, proteins, and ions using unmodified gold nanoparticles and conjugated polyelectrolytes. *Proc Natl Acad Sci U S A* **107**, 10837–10841 (2010).
118. Gao, L., Wang, Y. & Li, Y. Biomimetic biodegradable Ag@Au nanoparticle-emb e dde d ureteral stent with a constantly renewable contact-killing antimicrobial surface and antibiofilm and extraction-free properties. *Acta Biomater* **114**, 117–132 (2020).
119. Giacomini, M. *et al.* A novel and innovative quantitative kinetic software for virological colorimetric assays. *J Virol Methods* **73**, 201–209 (1998).
120. Khlyntseva, S. V., Bazel', Y. R., Vishnikin, A. B. & Andruch, V. Methods for the determination of adenosine triphosphate and other adenine nucleotides. *Journal of Analytical Chemistry* **64**, 657–673 (2009).
121. Fiorelia, N. E., Wibowo, A. D., Lae, N. L., Ang, A. & Krisbianto, O. Types of High-Performance Liquid Chromatography (HPLC) Columns: A Review. *FoodTech: Jurnal Teknologi Pangan* **5**, 1–16 (2022).
122. Jansen, R. S., Rosing, H., De Wolf, C. J. F. & Beijnen, J. H. Development and validation of an assay for the quantitative determination of cladribine nucleotides in MDCKII cells and culture medium using weak anion-exchange liquid chromatography coupled with tandem mass spectrometry. *Rapid Communications in Mass Spectrometry* **21**, 4049–4059 (2007).
123. Veltkamp, S. A. *et al.* Quantitative analysis of gemcitabine triphosphate in human peripheral blood mononuclear cells using weak anion-exchange liquid chromatography coupled with tandem mass spectrometry. *Journal of Mass Spectrometry* **41**, 1633–1642 (2006).
124. Jimmerson, L. C., Bushman, L. R., Ray, M. L., Anderson, P. L. & Kiser, J. J. A LC-MS/MS Method for Quantifying Adenosine, Guanosine and Inosine Nucleotides in Human Cells. *Pharmaceutical research* **34**, 73-83 (2017).
125. Bushman, L. R. *et al.* Determination of nucleoside analog mono-, di-, and tri-phosphates in cellular matrix by solid phase extraction and ultra-sensitive LC–MS/MS detection. *J Pharm Biomed Anal* **56**, 390–401 (2011).
126. Strezsak, S. R., Beuning, P. J. & Skizim, N. J. Versatile separation of nucleotides from bacterial cell lysates using strong anion exchange chromatography. *Journal of Chromatography B* **1188**, 123044 (2022).
127. Pesek, J. J., Matyska, M. T., Hearn, M. T. W. & Boysen, R. I. Aqueous normal-phase retention of nucleotides on silica hydride columns. *J Chromatogr A* **1216**, 1140–1146 (2009).
128. Barth, H. Chromatography Fundamentals, Part VII: Influence of Peak Broadening on Detection Sensitivity, Solute Dilution, and Efficiency of Coupled Columns. *LCGC North America* **37,** 478-480 (2019).
129. Vaishnavi, J., Reddy, S., Narmadha, S. & Osborne, W. J. Detection and purification of microbial volatile organic compounds. *Volatiles and Metabolites of Microbes* 51–64 (2021) doi:10.1016/B978-0-12-824523-1.00021-3.
130. Fornstedt, T. & Enmark, M. Separation of therapeutic oligonucleotides using ion-pair reversed-phase chromatography based on fundamental separation science. *Journal of Chromatography Open* **3,** 100079 (2023) doi:10.1016/J.JCOA.2023.100079.
131. Guimaraes, G. J., & Bartlett, M. G. The critical role of mobile phase pH in the performance of oligonucleotide ion-pair liquid chromatography–mass spectrometry methods. *Future Science OA* **7,** FSO753 (2021).
132. Cardinael, P., Casabianca, H., Peulon-Agasse, V., & Berthod, A. (2015). Sample derivatization in separation science. *Analytical separation science* **5,** 1725-1756 (2015). doi:10.1002/9783527678129.assep063.

133. Bhatt, D. P., Chen, X., Geiger, J. D. & Rosenberger, T. A. A sensitive HPLC-based method to quantify adenine nucleotides in primary astrocyte cell cultures. *J Chromatogr B Analyt Technol Biomed Life Sci* **889**, 110–115 (2012).
134. Wei, B. *et al.* Development of an ion pairing reversed-phase liquid chromatography-mass spectrometry method for characterization of clustered regularly interspaced short palindromic repeats guide ribonucleic acid. *J Chromatogr A* **1665**, 462839 (2022).
135. Mateos-Vivas, M., Rodríguez-Gonzalo, E., Domínguez-Álvarez, J., García-Gómez, D. & Carabias-Martínez, R. Determination of nucleosides and nucleotides in baby foods by hydrophilic interaction chromatography coupled to tandem mass spectrometry in the presence of hydrophilic ion-pairing reagents. *Food Chem* **211**, 827–835 (2016).
136. Dudley, E. & Bond, L. Mass spectrometry analysis of nucleosides and nucleotides. *Mass Spectrometry Reviews* **33,** 302-331 (2014) doi:10.1002/mas.21388.
137. Klimek-Turek, A., Misiołek, B., Dzido, T. H., Wojciak-Kosior, M. & Buszewski, B. molecules Comparison of the Retention and Separation Selectivity of Aromatic Hydrocarbons with Polar Groups in RP-HPLC Systems with Different Stationary Phases and Eluents. doi:10.3390/molecules25215070.
138. Edelson, E. H., Lawless, J. G., Timothy Wehr, C. & Abbott, S. R. Ion-exchange separation of nucleic acid constituents by high-performance liquid chromatography. *J Chromatogr* **174**, 409–419 (1979).
139. Ranogajec, A., Beluhan, S. & Šmit, Z. Analysis of nucleosides and monophosphate nucleotides from mushrooms with reversed-phase HPLC. *J Sep Sci* **33**, 1024–1033 (2010).
140. Studzińska, S. & Buszewski, B. Effect of mobile phase pH on the retention of nucleotides on different stationary phases for high-performance liquid chromatography. *Anal Bioanal Chem* **405**, 1663–1672 (2013).
141. Periat, A., Kohler, I., Veuthey, J. L., & Guillarme, D. Advances in hydrophilic interaction liquid chromatography for pharmaceutical analysis. *LCGC Supplements* **31,** (2013).
142. Tang, D. Q., Zou, L., Yin, X. X. & Ong, C. N. HILIC-MS for metabolomics: An attractive and complementary approach to RPLC-MS. *Mass Spectrom Rev* **35**, 574–600 (2016).
143. Medina, J., van Der Velpen, V., Teav, T., Guitton, Y., Gallart-Ayala, H., & Ivanisevic, J. Single-step extraction coupled with targeted HILIC-MS/MS approach for comprehensive analysis of human plasma lipidome and polar metabolome. *Metabolites* **10,** 495 (2020).
144. Nguyen, H. P., Tippens, H. D. & Schug, K. A. HILIC-MS for Targeted Metabolomics and Small Molecule Bioanalysis. *Hydrophilic Interaction Chromatography: A Guide for Practitioners* 219–238 (2013) doi:10.1002/9781118495247.CH7.
145. Medina, J. et al. Single-Step Extraction Coupled with Targeted HILIC-MS/MS Approach for Comprehensive Analysis of Human Plasma Lipidome and Polar Metabolome. *Metabolites* **10,** 495 (2020).
146. Subbaraj, A. K., Kim, Y. H. B., Fraser, K. & Farouk, M. M. A hydrophilic interaction liquid chromatography-mass spectrometry (HILIC-MS) based metabolomics study on colour stability of ovine meat. *Meat Sci* **117**, 163–172 (2016).
147. Vieira, E., Brandão, T. & Ferreira, I. M. P. L. V. O. Evaluation of Brewer's spent yeast to produce flavor enhancer nucleotides: Influence of serial repitching. *J Agric Food Chem* **61**, 8724–8729 (2013).
148. Inoue, K., Obara, R., Hino, T. & Oka, H. Development and application of an HILIC-MS/MS method for the quantitation of nucleotides in infant formula. *J Agric Food Chem* **58**, 9918–9924 (2010).
149. Buszewski, B. & Noga, S. Hydrophilic interaction liquid chromatography (HILIC)-a powerful separation technique. *Anal Bioanal Chem* **402**, 231–247 (2012).
150. Gong, L. & McCullagh, J. S. O. Analysis of oligonucleotides by hydrophilic interaction liquid chromatography coupled to negative ion electrospray ionization mass spectrometry. *J Chromatogr A* **1218**, 5480–5486 (2011).

151. Hosseinkhani, F. *et al.* Systematic Evaluation of HILIC Stationary Phases for Global Metabolomics of Human Plasma. *Metabolites* **12**, 165 (2022).
152. Yin, R. *et al.* Light based anti-infectives: ultraviolet C irradiation, photodynamic therapy, blue light, and beyond. *Current opinion in pharmacology* **13,** 731-762. doi:10.1016/j.coph.2013.08.009.
153. Cohen, S., Jordheim, L. P., Megherbi, M., Dumontet, C. & Guitton, J. Liquid chromatographic methods for the determination of endogenous nucleotides and nucleotide analogs used in cancer therapy: A review. *Journal of Chromatography B* **878**, 1912–1928 (2010).
154. Ley-Ngardigal, S. & Bertolin, G. Approaches to monitor ATP levels in living cells: where do we stand? *FEBS J* **289**, 7940–7969 (2022).
155. Menegollo, M., Tessari, I., Bubacco, L. & Szabadkai, G. Determination of ATP, ADP, and AMP levels by reversed-phase high-performance liquid chromatography in cultured cells. *Methods in Molecular Biology* **1925**, 223–232 (2019).
156. Narayan, V. S. HPLC analysis of nucleotides. (2017). (Doctoral dissertation, Queensland University of Technology).
157. Lin, C. H., Lee, C., Wu, Y. C. & Lu, I. C. New Strategy to Preserve Phosphate by Ionic Liquid Matrices in Matrix-Assisted Laser Desorption/Ionization: A Case of Adenosine Nucleotides. *Molecules* **25**, 1217 (2020).
158. Curtis, M. *et al.* Direct analysis in real time (DART) mass spectrometry of nucleotides and nucleosides: elucidation of a novel fragment [C5H5O]+ and its in-source adducts. *J Am Soc Mass Spectrom* **21**, 1371–1381 (2010).
159. Rozenski, J. Analysis of nucleosides using the atmospheric-pressure solids analysis probe for ionization. *Int J Mass Spectrom* **304**, 204–208 (2011).
160. Frańska, M. Cytidine-Ag+-purine base complexes as studied by electrospray ionization mass spectrometry. *Eur J Mass Spectrom (Chichester)* **16**, 587–594 (2010).
161. Strzelecka, D., Chmielinski, S., Bednarek, S., Jemielity, J. & Kowalska, J. Analysis of mononucleotides by tandem mass spectrometry: investigation of fragmentation pathways for phosphate- and ribose-modified nucleotide analogues. *Scientific Reports* **7**, 1–12 (2017).
162. Zhang, H. *et al.* MTBSTFA derivatization-LC-MS/MS approach for the quantitative analysis of endogenous nucleotides in human colorectal carcinoma cells. *J Pharm Anal* **12**, 77–86 (2022).
163. Nordstro, A. *et al.* Derivatization for LC-electrospray ionization-MS: a tool for improving reversed-phase separation and ESI responses of bases, ribosides, and intact nucleotides. *ACS Publications* **17**, 2869–2877 (1999).
164. Flarakos, J., Xiong, W., Glick, J. & Vouros, P. A deoxynucleotide derivatization methodology for improving LC-ESI-MS detection. *Anal Chem* **77**, 2373–2380 (2005).
165. Gautam, N., Alamoudi, J. A., Kumar, S. & Alnouti, Y. Direct and indirect quantification of phosphate metabolites of nucleoside analogs in biological samples. *J Pharm Biomed Anal* **178**, (2020).
166. Kaklamanos, G., Aprea, E. & Theodoridis, G. Mass spectrometry: principles and instrumentation. *Chemical Analysis of Food* 525–552 (2020) doi:10.1016/B978-0-12-813266-1.00011-5.
167. Bartoli, J., Citerne, S., Mouille, G., Bouveret, E. & Field, B. Quantification of guanosine triphosphate and tetraphosphate in plants and algae using stable isotope-labelled internal standards. *Talanta* **219**, 121261 (2020).
168. Gill, B. D., Indyk, H. E. & Manley-Harris, M. Analysis of nucleosides and nucleotides in infant formula by liquid chromatography-tandem mass spectrometry. *Anal Bioanal Chem* **405**, 5311–5319 (2013).
169. Ge, Y. *et al.* Comparative Analysis of Amino Acids, Nucleosides, and Nucleobases in Thais clavigera from Different Distribution Regions by Using Hydrophilic Interaction Ultra-Performance Liquid Chromatography Coupled with Triple Quadrupole Tandem Mass Spectrometry. *International Journal of Analytical Chemistry* (2015). doi:10.1155/2015/394526.

170. Quinn, R., Basanta-Sanchez, M., Rose, R. E. & Fabris, D. Direct infusion analysis of nucleotide mixtures of very similar or identical elemental composition. *Wiley Online Library* **48**, 703–712 (2013).
171. Stone, J. A., & Fitzgerald, R. L. Liquid chromatography–mass spectrometry education for clinical laboratory scientists. *Clinics in laboratory medicine* **38,** 527-537 (2018). doi:10.1016/j.cll.2018.04.002.
172. Menger, F., Gago-Ferrero, P., Wiberg, K., & Ahrens, L. Wide-scope screening of polar contaminants of concern in water: A critical review of liquid chromatography-high resolution mass spectrometry-based strategies. *Trends in Environmental Analytical Chemistry* **28,** e00102 (2020).
173. Da Silva Bezerra, K. Perspective Chapter: High-Performance Liquid Chromatography Coupled to Mass Spectrometry – The Advance in Chemical Analysis. *High Performance Liquid Chromatography - Recent Advances and Applications* (2023) doi:10.5772/INTECHOPEN.110880.
174. Gago-Ferrero, P., Gros, M., Ahrens, L. & Wiberg, K. Impact of on-site, small and large scale wastewater treatment facilities on levels and fate of pharmaceuticals, personal care products, artificial sweeteners, pesticides, and perfluoroalkyl substances in recipient waters. *Science of The Total Environment* **601**, 1289–1297 (2017).
175. Azzouz, A., Jurado-S Anchez, B., Souhail, B. & Ballesteros, E. Simultaneous Determination of 20 Pharmacologically Active Substances in Cow's Milk, Goat's Milk, and Human Breast Milk by Gas ChromatographyÀMass Spectrometry. *J. Agric. Food Chem* **59**, 5125–5132 (2011).
176. Miles, H. T. & Fales, H. M. Application of Gas Chromatography to Analysis of Nucleosides. *Anal. Chem* **34**, 860–861 (1962).
177. Schram, K. H., Taniguchi, Y. & McCloskey, J. A. Gas chromatography of nucleotides and nucleosides of cytosine. *J Chromatogr A* **155**, 355–361 (1978).
178. Castro-Cerritos, K. V., Torres-Elguera, J. C., Capataz-Tafur, J., Juarez-Arellano, E. A. & Lopez-Torres, A. Microwave Assisted DNA Hydrolysis for Global Methylation Analysis by Gas Chromatography/Tandem Mass Spectrometry. *J Mex Chem Soc* **62**, (2018).
179. Moldoveanu, S. C. & David, V. Derivatization Methods in GC and GC/MS. *Gas Chromatography-Derivatization, Sample Preparation, Application* **9,** (2018). doi:10.5772/intechopen.81954.
180. Malachová, A. *et al.* Advanced LC-MS-based methods to study the co-occurrence and metabolization of multiple mycotoxins in cereals and cereal-based food. *Analytical and Bioanalytical Chemistry* **410,** 801-825 (2018). doi:10.1007/s00216-017-0750-7.
181. Niessen, W. M. A., Tjaden, U. R. & van der Greef, J. Capillary electrophoresis—mass spectrometry. *J Chromatogr A* **636**, 3–19 (1993).
182. Liu, C. C., Huang, J. S., Tyrrell, D. L. J. & Dovichi, N. J. Capillary electrophoresis-electrospray-mass spectrometry of nucleosides and nucleotides: Application to phosphorylation studies of anti-human immunodeficiency virus nucleosides in a human hepatoma cell line. *Electrophoresis* **26**, 1424–1431 (2005).
183. Soga, T. *et al.* Analysis of nucleotides by pressure-assisted capillary electrophoresis–mass spectrometry using silanol mask technique. *J Chromatogr A* **1159**, 125–133 (2007).
184. Friedecký, D. *et al.* Capillary electrophoretic method for nucleotide analysis in cells: Application on inherited metabolic disorders. *Electrophoresis* **28**, 373–380 (2007).
185. Bezy, V. *et al.* Analysis and validation of the phosphorylated metabolites of two anti-human immunodeficiency virus nucleotides (stavudine and didanosine) by pressure-assisted CE-ESI-MS/MS in cell extracts: Sensitivity enhancement by the use of perfluorinated acids and alcohols as coaxial sheath-liquid make-up constituents. *Electrophoresis* **27**, 2464–2476 (2006).
186. Geldart, S. E., & Brown, P. R. Analysis of nucleotides by capillary electrophoresis. *Journal of Chromatography A* **828,** 317-336 (1998).
187. Ng, M., Blaschke, T. F., Arias, A. A. & Zare, R. N. Analysis of Free Intracellular Nucleotides Using High-Performance Capillary Electrophoresis. *Anal. Chem* **64**, 1682–1684 (1992).

188. Buel, E., Schwartz, M. B., & LaFountain, M. J. Capillary electrophoresis STR analysis: comparison to gel-based systems. Journal of forensic sciences **43,** 164-170(1998).
189. Bucsella, B., Fornage, A., Le Denmat, C. & Kálmán, F. Nucleotide and Nucleotide Sugar Analysis in Cell Extracts by Capillary Electrophoresis. *Chimia (Aarau)* **70**, 732–735 (2016).
190. Feng, H. T., Wong, N., Wee, S. & Lee, M. M. Simultaneous determination of 19 intracellular nucleotides and nucleotide sugars in Chinese Hamster ovary cells by capillary electrophoresis. *Journal of Chromatography B* **870**, 131–134 (2008).
191. Liu, J. X., Aerts, J. T., Rubakhin, S. S., Zhang, X. X., & Sweedler, J. V. (2014). Analysis of endogenous nucleotides by single cell capillary electrophoresis-mass spectrometry. *Analyst* **139,** 5835-5842 (2014) doi:10.1039/c4an01133c.
192. de Kort, B. J., de Jong, G. J. & Somsen, G. W. Native fluorescence detection of biomolecular and pharmaceutical compounds in capillary electrophoresis: Detector designs, performance and applications: A review. *Anal Chim Acta* **766**, 13–33 (2013).
193. Zhao, C. *et al.* Simultaneous determination of intracellular nucleotides and coenzymes in Yarrowia lipolytica producing lipid and lycopene by capillary zone electrophoresis. *J Chromatogr A* **1514**, 120–126 (2017).
194. Dadoo, R., Seto, A. G., Colón, L. A. & Zare, R. N. End-Column Chemiluminescence Detector for Capillary Electrophoresis. *Anal Chem* **66**, 303–306 (1994).
195. Yan, Y., Shi, P., Song, W. & Bi, S. Chemiluminescence and Bioluminescence Imaging for Biosensing and Therapy: *In Vitro* and *In Vivo* Perspectives. *Theranostics* **9**, 4047–4065 (2019).
196. Lakowicz, J. R. Principles of Fluorescence Spectroscopy, Third Edition. *J Biomed Opt* **13**, (2009).
197. Lichtman, J. W. & Conchello, J. A. Fluorescence microscopy. *Nat Methods* **2**, 910–919 (2005).
198. Data, P. & Takeda, Y. Recent Advancements in and the Future of Organic Emitters: TADF- and RTP-Active Multifunctional Organic Materials. *Chem Asian J* **14**, 1613–1636 (2019).
199. Vuojola, J., Syrjä Npä Ä, M., Lamminmä, U. & Soukka, T. Genetically Encoded Protease Substrate Based on Lanthanide-Binding Peptide for Time-Gated Fluorescence Detection. *Anal. Chem* **85**, 55 (2013).
200. Schneckenburger, H. Förster resonance energy transfer–what can we learn and how can we use it? *Methods Appl Fluoresc* **8**, 013001 (2019).
201. Pawley, J. B. Handbook of biological confocal microscopy: Third edition. *Handbook of Biological Confocal Microscopy: Third Edition* 1–985 (2006). doi:10.1007/978-0-387-45524-2/COVER.
202. Ahmed, A., Schoberer, J., Cooke, E. & Botchway, S. W. Multicolor FRET-FLIM Microscopy to Analyze Multiprotein Interactions in Live Cells. *Methods in Molecular Biology* **2247**, 287–301 (2021).
203. Tsien, R. Y. The green fluorescent protein. *https://doi.org/10.1146/annurev.biochem.67.1.509* **67**, 509–544 (2003).
204. Förster, T. Energy migration and fluorescence. *J Biomed Opt* **17**, 011002 (2012).
205. Xia, Z. & Rao, J. Biosensing and imaging based on bioluminescence resonance energy transfer. *Curr Opin Biotechnol* **20**, 37–44 (2009).
206. Roda, A., Pasini, P., Guardigli, M., Baraldini, M., Musiani, M., & Mirasoli, M. Bio-and chemiluminescence in bioanalysis. Fresenius' journal of analytical chemistry **366,** 752-759 (2000).
207. Calabretta, M. M. *et al.* Paper-Based Immunosensors with Bio-Chemiluminescence Detection. *Sensors* **21**, 4309 (2021).
208. Kim, B. B., Pisarev, V. V. & Egorov, A. M. A comparative study of peroxidases from horse radish and Arthromyces ramosus as labels in luminol-mediated chemiluminescent assays. *Anal Biochem* **199**, 1–6 (1991).
209. Wu, Y., Wen, J., Li, H., Sun, S. & Xu, Y. Fluorescent probes for recognition of ATP. *Chinese Chemical Letters* **28**, 1916–1924 (2017).
210. Xu, Z. *et al.* Monitoring mitochondrial ATP in live cells: An ATP multisite-binding fluorescence turn-on probe. *Dyes and Pigments* **163**, 559–563 (2019).

211. Richter, M. M. Electrochemiluminescence. *Optical Biosensors,* 317–384 (2008) doi:10.1016/B978-044453125-4.50009-7.
212. Kai, M., Ohkura, Y., Yonekura, S. & Iwasaki, M. Chemiluminescence determination of guanine its nucleosides and nucleotides using phenylglyoxal. *Analyrica Chimica Acta* **287**, 75–81 (1994).
213. Ortolani, T. S. *et al.* Electrochemical sensing of purines guanine and adenine using single-walled carbon nanohorns and nanocellulose. *In Optical biosensors,* 317-384 (2018).
214. Ensafi, A. A., Gorgabi-Khorzoughi, M., Rezaei, B. & Jafari-Asl, M. Electrochemical behavior of polyoxometalates decorated on poly diallyl dimethyl ammonium chloride-MWCNTs: A highly selective electrochemical sensor for determination of guanine and adenine. *J Taiwan Inst Chem Eng* **78**, 56–64 (2017).
215. Zhao, T., Lin, C., Yao, Q. & Chen, X. A label-free electrochemiluminescent sensor for ATP detection based on ATP-dependent ligation. *Talanta* **154**, 492–497 (2016).
216. Liu, Y., Lei, J., Huang, Y. & Ju, H. 'Off-on' electrochemiluminescence system for sensitive detection of ATP via target-induced structure switching. *Anal Chem* **86**, 8735–8741 (2014).
217. Engel, L., Alves, J., Hennek, J., Goueli, S. A., & Zegzouti, H. (2021). Utility of bioluminescent homogeneous nucleotide detection assays in measuring activities of nucleotide-sugar dependent glycosyltransferases and studying their inhibitors. *Molecules* **26,** 6230 (2021). doi:10.3390/molecules26206230.
218. Vysotski, E. S. Bioluminescent and Fluorescent Proteins: Molecular Mechanisms and Modern Applications. *Int J Mol Sci* **24**, 281 (2022).
219. Ihssen, J., Jovanovic, N., Sirec, T., & Spitz, U. Real-time monitoring of extracellular ATP in bacterial cultures using thermostable luciferase. PLoS One **16**, e0244200 (2021). doi:10.1371/journal.pone.0244200.
220. Wilson, T. & Hastings, J. W. Bioluminescence. *Annu Rev Cell Dev Biol* **14**, 197–230 (1998).
221. Mondal, S., Hsiao, K. & Goueli, S. A. A Homogenous Bioluminescent System for Measuring GTPase, GTPase Activating Protein, and Guanine Nucleotide Exchange Factor Activities. *Assay Drug Dev Technol* **13**, 444–455 (2015).
222. Anderson, E. L. & Hamann, M. J. Detection of Rho GEF and GAP activity through a sensitive split luciferase assay system. *Biochem. J* **441**, 869–879 (2012).
223. Beer, P. D., & Gale, P. A. Anion recognition and sensing: the state of the art and future perspectives. *Angewandte Chemie International Edition*, 40(3), 486-516 (2001).
224. Li, W., Gong, X., Fan, X., Yin, S., Su, D., Zhang, X., & Yuan, L. Recent advances in molecular fluorescent probes for organic phosphate biomolecules recognition. *Chinese Chemical Letters* **30,** 1775-1790 (2019). doi:10.1016/j.cclet.2019.07.056.
225. Hu, C., Jiang, K., Shao, Z., Shi, M. & Meng, H.-M. A DNAzyme-based label-free fluorescent probe for guanosine-5'-triphosphate detection. *Analyst* **145**, 6948 (2020).
226. Mcmanus, S. A. & Li, Y. Multiple Occurrences of an Efficient Self-Phosphorylating Deoxyribozyme Motif. *Biochemistry* **46**, 2198–2204 (2007).
227. Fahnrich, K. A. *et al.* [Ru(bpy) 2 dppz] 2+ Electrochemiluminescence Switch and Its Applications for DNA Interaction Study and Label-free ATP Aptasensor. *TrAC, Trends Anal. Chem* **54**, 9807–9811 (2001).
228. Ojida, A., Park, S. K., Mito-Oka, Y. & Hamachi, I. Efficient fluorescent ATP-sensing based on coordination chemistry under aqueous neutral conditions. *Tetrahedron Lett* **43**, 6193–6195 (2002).
229. Bazany-Rodríguez, I. J., Salomón-Flores, M. K., Bautista-Renedo, J. M., González-Rivas, N., & Dorazco-González, A. Chemosensing of guanosine triphosphate based on a fluorescent Dinuclear Zn (II)-Dipicolylamine complex in water. Inorganic Chemistry **59,** 7739-7751 (2020). doi:10.1021/acs.inorgchem.0c00777.
230. Wu, N., Lan, J., Yan, L., & You, J. A sensitive colorimetric and fluorescent sensor based on imidazolium-functionalized squaraines for the detection of GTP and alkaline phosphatase in aqueous solution. *Chemical Communications* **50,** 4438-4441(2014).

231. Kwon, J. Y. *et al.* Fluorescent GTP-sensing in aqueous solution of physiological pH. *J Am Chem Soc* **126**, 8892–8893 (2004).
232. Ahmed, N., Shirinfar, B., Youn, I. S., Yousuf, M. & Kim, K. S. Selective detection of guanosine-5′-triphosphate and iodide by fluorescent benzimidazolium-based cyclophanes. *Org Biomol Chem* **11**, 6407–6413 (2013).
233. Ahmed, N., Shirinfar, B., Youn, I. S., Bist, A., Suresh, V., & Kim, K. S. A highly selective fluorescent chemosensor for guanosine-5′-triphosphate via excimer formation in aqueous solution of physiological pH. *Chemical Communications* **48,** 2662-2664 (2012).
234. Juan Zhao ab, X. & Zhi Huang, C. Water-soluble luminescent copper nanoclusters reduced and protected by histidine for sensing of guanosine 5 0-triphosphate †. *New J. Chem* **38**, 3673 (2014).
235. Mittal, L. S., Sharma, P., Kaur, N., & Singh, P. (2019). A perylenediimide based 'on-off'chemosensor for the detection of nucleoside triphosphates: an efficient ensemble for monitoring alkaline phosphatase activity. *Analytical Methods* **11,** 5320-5327 (2019) doi:10.1039/c9ay01608b.
236. Hargrove, A. E., Nieto, S., Zhang, T., Sessler, J. L. & Anslyn, E. V. Artificial receptors for the recognition of phosphorylated molecules. *Chem Rev* **111**, 6603–6782 (2011).
237. Nakano, S. *et al.* Simultaneous Detection of ATP and GTP by Covalently Linked Fluorescent Ribonucleopeptide Sensors. *J. Am. Chem. Soc* **135**, (2013).
238. Neelakandan, P. P., Hariharan, M. & Ramaiah, D. A Supramolecular ON-OFF-ON Fluorescence Assay for Selective Recognition of GTP. *J. AM. CHEM. SOC* **128**, 11334–11335 (2006).
239. Kunzelmann, S. & Webb, M. R. Fluorescence detection of GDP in real time with the reagentless biosensor rhodamine-ParM. *Biochem. J* **440**, 43–49 (2011).
240. Jameson, E. E. *et al.* Real-time detection of basal and stimulated G protein GTPase activity using fluorescent GTP analogues. *Journal of Biological Chemistry* **280**, 7712–7719 (2005).
241. Voss, S., Krüger, D. M., Koch, O., Wu, Y. W. & Lippincott-Schwartz, J. Spatiotemporal imaging of small GTPases activity in live cells. *Proc Natl Acad Sci U S A* **113**, 14348–14353 (2016).
242. Aderinto, S. O. Fluorescent, colourimetric, and ratiometric probes based on diverse fluorophore motifs for mercuric(II) ion (Hg2+) sensing: highlights from 2011 to 2019. *Chemical Papers* **74**, 3195–3232 (2020).
243. Tantama, M. & Yellen, G. Imaging Changes in the Cytosolic ATP-to-ADP Ratio. *Methods Enzymol* **547**, 355–371 (2014).
244. Yaginuma, H. *et al.* Diversity in ATP concentrations in a single bacterial cell population revealed by quantitative single-cell imaging. *Scientific Reports* **4**, 1–7 (2014).
245. Imamura, H. *et al.* Visualization of ATP levels inside single living cells with fluorescence resonance energy transfer-based genetically encoded indicators. *Proc Natl Acad Sci U S A* **106**, 15651–15656 (2009).
246. Bianchi-Smiraglia, A. *et al.* internally ratiometric fluorescent sensors for evaluation of intracellular GtP levels and distribution. *Nature methods* **14,** 1003-1009 (2017).
247. Zheng, D., Seferos, D. S., Giljohann, D. A., Patel, P. C., & Mirkin, C. A. Aptamer nano-flares for molecular detection in living cells. *Nano letters* **9,** 3258-3261(2009). doi:10.1021/nl901517b.
248. Chu, B. *et al.* Ex vivo and in vivo fluorescence detection and imaging of adenosine triphosphate. *J Nanobiotechnology* **19**, 1–12 (2021).
249. Kim, J. H., Ahn, J. H., Barone, P. W., Jin, H., Zhang, J., Heller, D. A., & Strano, M. S. A luciferase/single-walled carbon nanotube conjugate for near-infrared fluorescent detection of cellular ATP. Angewandte Chemie **122,** 1498-1501(2010). doi:10.1002/anie.200906251.
250. Zhang, M. *et al.* Monitoring the Dynamic Regulation of the Mitochondrial GTP-to-GDP Ratio with a Genetically Encoded Fluorescent Biosensor. *Angewandte Chemie International Edition* **61**, e202201266 (2022).
251. Veloria, J. *et al.* Developing Colorimetric and Luminescence-Based High-Throughput Screening Platforms for Monitoring the GTPase Activity of Ferrous Iron Transport Protein B (FeoB). *SLAS Discov* **24**, 597–605 (2019).

252. Pesek, J. J., Matyska, M. T., Fischer, S. M. & Sana, T. R. Analysis of hydrophilic metabolites by high-performance liquid chromatography–mass spectrometry using a silica hydride-based stationary phase. *J Chromatogr A* **1204**, 48–55 (2008).
253. Goyon, A., Yehl, P. & Zhang, K. Characterization of therapeutic oligonucleotides by liquid chromatography. *J Pharm Biomed Anal* **182**, 113105 (2020).
254. Ryll, T. & Wagner, R. Improved ion-pair high-performance liquid chromatographic method for the quantification of a wide variety of nucleotides and sugar—nucleotides in animal cells. *J Chromatogr B Biomed Sci Appl* **570**, 77–88 (1991).
255. Gilar, M. *et al.* Characterization of therapeutic oligonucleotides using liquid chromatography with on-line mass spectrometry detection. *Oligonucleotides* **13**, 229–243 (2003).
256. Domínguez-Álvarez, J. *et al.* Determination of nucleosides and nucleotides in food samples by using liquid chromatography and capillary electrophoresis. *TrAC Trends in Analytical Chemistry* **92**, 12–31 (2017).
257. Holdšvendová, P., Suchánková, J., Bunček, M., Bačkovská, V. & Coufal, P. Hydroxymethyl methacrylate-based monolithic columns designed for separation of oligonucleotides in hydrophilic-interaction capillary liquid chromatography. *J Biochem Biophys Methods* **70**, 23–29 (2007).
258. RL, C., SJ, H., CA, O. & DA, B. Quantitative profiling of nucleotides and related phosphate-containing metabolites in cultured mammalian cells by liquid chromatography tandem electrospray mass spectrometry. *J Chromatogr B Analyt Technol Biomed Life Sci* **871**, 115–124 (2008).
259. Czarnecka, J., Cieślak, M. & Michał, K. Application of solid phase extraction and high-performance liquid chromatography to qualitative and quantitative analysis of nucleotides and nucleosides in human cerebrospinal fluid. *J Chromatogr B Analyt Technol Biomed Life Sci* **822**, 85–90 (2005).
260. Contreras-Sanz, A. *et al.* Simultaneous quantification of 12 different nucleotides and nucleosides released from renal epithelium and in human urine samples using ion-pair reversed-phase HPLC. *Purinergic Signal* **8**, 741–751 (2012).
261. Rowena Monton, M. N. & Soga, T. Metabolome analysis by capillary electrophoresis-mass spectrometry. *J Chromatogr A* **1168**, 237–246 (2007).
262. Soga, T., Ohashi, Y., Ueno, Y., Naraoka, H., Tomita, M., & Nishioka, T. Quantitative metabolome analysis using capillary electrophoresis mass spectrometry. *Journal of proteome research* **2,** 488-494 (2003). doi:10.1021/pr034020m.
263. Dam, H. V *et al.* Simultaneous Determination of Anionic Intermediates for Bacillus subtilis Metabolic Pathways by Capillary Electrophoresis Electrospray Ionization Mass Spectrometry. *Proc. Natl. Acad. Sci. U.S.A* **19**, 2233–2239 (2001).
264. Sugimoto, M., Wong, D. T., Hirayama, A., Soga, T., & Tomita, M. Capillary electrophoresis mass spectrometry-based saliva metabolomics identified oral, breast and pancreatic cancer-specific profiles. Metabolomics **6,** 78-95 (2010). doi:10.1007/s11306-009-0178-y.
265. Hirayama, A. *et al.* Quantitative metabolome profiling of colon and stomach cancer microenvironment by capillary electrophoresis time-of-flight mass spectrometry. *Cancer Res* **69**, 4918–4925 (2009).
266. Rodríguez-Gonzalo, E., Domínguez-Álvarez, J., Mateos-Vivas, M., García-Gómez, D. & Carabias-Martínez, R. A validated method for the determination of nucleotides in infant formulas by capillary electrophoresis coupled to mass spectrometry. *Electrophoresis* **35**, 1677–1684 (2014).
267. Liu, B., Cui, Y., Tang, D., Yang, H. & Chen, G. Au(III)-assisted core-shell iron oxide@poly(o-phenylenediamine) nanostructures for ultrasensitive electrochemical aptasensors based on DNase I-catalyzed target recycling. *Chemical Communications* **48**, 2624–2626 (2012).

268. Li, J. *et al.* Highly selective electrochemiluminescence aptasensor coupled with mesoporous Fe3O4@Cu@Cu2O as co-reaction accelerator for ATP assay based on target-triggered emitter release. *Sens Actuators B Chem* **346**, 130581 (2021).
269. T, B., H, S., W, W., X, Z. & S, W. A sensitive electrochemical aptasensor for ATP detection based on exonuclease III-assisted signal amplification strategy. *Anal Chim Acta* **862**, 64–69 (2015).
270. Yin, B.-C., Guanz, Y.-M. & Ye, B.-C. An ultrasensitive electrochemical DNA sensor based on the ssDNA-assisted cascade of hybridization reactionw ChemComm. *This journal is Cite this: Chem. Commun* **48**, 51 (2012).
271. Chen, H. *et al.* Electrochemiluminescence aptasensor for adenosine triphosphate detection using host-guest recognition between metallocyclodextrin complex and aptamer. *Talanta* **121**, 229–233 (2014).
272. Huang, Y., Lei, J., Cheng, Y. & Ju, H. Target-assistant Zn 2+-dependent DNAzyme for signal-on electrochemiluminescent biosensing. *Electrochimica Acta* **155,** 341-347 (2015). doi:10.1016/j.electacta.2014.12.165.
273. Yao, W., Wang, L., Wang, H., Zhang, X. & Li, L. An aptamer-based electrochemiluminescent biosensor for ATP detection. *Biosens Bioelectron* **24**, 3269–3274 (2009).
274. Dart, M. L. *et al.* Homogeneous Assay for Target Engagement Utilizing Bioluminescent Thermal Shift. *ACS Med Chem Lett* **9**, 546–551 (2018).
275. Vancraenenbroeck, R. & Webb, M. R. A Fluorescent, Reagentless Biosensor for ATP, Based on Malonyl-Coenzyme A Synthetase. *ACS Chem Biol* **10**, 2650–2657 (2015).
276. Jun, Y. W., Sarkar, S., Kim, K. H. & Ahn, K. H. Molecular Probes for Fluorescence Imaging of ATP in Cells and Tissues. *ChemPhotoChem* **3**, 214–219 (2019).
277. M, Z., WJ, M., CT, H., L, J. & TB, L. Highly selective recognition and fluorescence imaging of adenosine polyphosphates in aqueous solution. *Inorg Chem* **52**, 4873–4879 (2013).
278. Bianchi-Smiraglia, A. & Nikiforov, M. A. Assessment of Intracellular GTP Levels Using Genetically Encoded Fluorescent Sensors. *Methods in Molecular Biology* **2394**, 163–169 (2022).
279. Tsuyama, T. *et al.* In vivo fluorescent adenosine 5′-triphosphate (ATP) imaging of Drosophila melanogaster and Caenorhabditis elegans by using a genetically encoded fluorescent ATP Biosensor optimized for low temperatures. *Anal Chem* **85**, 7889–7896 (2013).
280. Kopra, K. *et al.* A homogeneous quenching resonance energy transfer assay for the kinetic analysis of the GTPase nucleotide exchange reaction. *Anal Bioanal Chem* **406**, 4147–4156 (2014).
281. Syrjänpää, M. *et al.* QTR-FRET: Efficient background reduction technology in time-resolved förster resonance energy transfer assays. *Anal Chim Acta* **1092**, 93–101 (2019).
282. Cho, U. & Chen, J. K. Lanthanide-Based Optical Probes of Biological Systems. *Cell Chem. Biol* **27,** 921–936 (2020).
283. Kopra, K. et al. High-Throughput Dual Screening Method for Ras Activities and Inhibitors. Anal Chem 89, 4508–4516 (2017).
284. Kopra, K. et al. GTP-Specific Fab Fragment-Based GTPase Activity Assay. Anal Chem 87, 3527–3534 (2015).
285. Paul, R., Suklabaidya, S. & Arshad Hussain, S. Fluorescence resonance energy transfer (FRET) as biomarkers. Mater Today Proc 46, 6301–6303 (2021).
286. Valtonen, S. *et al.* Nanomolar Protein–Protein Interaction Monitoring with a Label-Free Protein-Probe Technique. *Anal Chem* **92**, 15781–15788 (2020).
287. Vuorinen, E. *et al.* Sensitive Label-Free Thermal Stability Assay for Protein Denaturation and Protein-Ligand Interaction Studies. *Anal Chem* **92**, 3512–3516 (2020).
288. Vuorinen, E. *et al.* Protease substrate-independent universal assay for monitoring digestion of native unmodified proteins. *Int J Mol Sci* **22**, 6362 (2021).
289. Muñoz-Maldonado, C., Zimmer, Y. & Medová, M. A comparative analysis of individual ras mutations in cancer biology. *Front Oncol* **9**, 1088 (2019).
290. Buhrman, G., Holzapfel, G., Fetics, S. & Mattos, C. Allosteric modulation of Ras positions Q61 for a direct role in catalysis. *Proc Natl Acad Sci U S A* **107**, 4931–4936 (2010).

291. Lito, P., Solomon, M., Li, L. S., Hansen, R. & Rosen, N. Cancer therapeutics: Allele-specific inhibitors inactivate mutant KRAS G12C by a trapping mechanism. *Science* **351**, 604–608 (2016).
292. Vasta, J. D. *et al.* KRAS is vulnerable to reversible switch-II pocket engagement in cells. *Nature chemical biology* **18,** 596-604 (2020).
293. Ryan, M. B. *et al.* KRASG12C-independent feedback activation of wild-type RAS constrains KRASG12C inhibitor efficacy.*Cell reports* **39**, 110993 (2022).
294. Tanaka, N. *et al.* Clinical Acquired Resistance to KRASG12C Inhibition through a Novel KRAS Switch-II Pocket Mutation and Polyclonal Alterations Converging on RAS–MAPK Reactivation. *Cancer Discov* **11**, 1913–1922 (2021).

Original Publications

Mahran, R., Kopra, K., Yli-Hollo, T., Vuorinen, E., Vuorinen, I., Tabata, S., Sasaki, A. and Härmä, H. (2023)
Homogeneous luminescent quantitation of cellular guanosine and adenosine triphosphates (GTP and ATP) using QT-Luc$^{GTP\&ATP}$ assay.
Analytical and Bioanalytical Chemistry 415:6689–6700

I

Analytical and Bioanalytical Chemistry (2023) 415:6689–6700
https://doi.org/10.1007/s00216-023-04944-9

RESEARCH PAPER

Homogeneous luminescent quantitation of cellular guanosine and adenosine triphosphates (GTP and ATP) using QT-Luc$^{GTP\&ATP}$ assay

Kari Kopra[1] · Randa Mahran[1] · Titta Yli-Hollo[1] · Sho Tabata[2] · Emmiliisa Vuorinen[1] · Yuki Fujii[3] · Iida Vuorinen[1] · Aki Ogawa-Iio[3] · Akiyoshi Hirayama[2] · Tomoyoshi Soga[2] · Atsuo T. Sasaki[2,3,4] · Harri Härmä[1]

Received: 2 August 2023 / Revised: 4 September 2023 / Accepted: 7 September 2023 / Published online: 16 September 2023

Abstract
Guanosine triphosphate (GTP) and adenosine triphosphate (ATP) are essential nucleic acid building blocks and serve as energy molecules for a wide range of cellular reactions. Cellular GTP concentration fluctuates independently of ATP and is significantly elevated in numerous cancers, contributing to malignancy. Quantitative measurement of ATP and GTP has become increasingly important to elucidate how concentration changes regulate cell function. Liquid chromatography–coupled mass spectrometry (LC–MS) and capillary electrophoresis-coupled MS (CE–MS) are powerful methods widely used for the identification and quantification of biological metabolites. However, these methods have limitations related to specialized instrumentation and expertise, low throughput, and high costs. Here, we introduce a novel quantitative method for GTP concentration monitoring (GTP-quenching resonance energy transfer (QRET)) in homogenous cellular extracts. CE–MS analysis along with pharmacological control of cellular GTP levels shows that GTP-QRET possesses high dynamic range and accuracy. Furthermore, we combined GTP-QRET with luciferase-based ATP detection, leading to a new technology, termed QT-Luc$^{GTP\&ATP}$, enabling high-throughput compatible dual monitoring of cellular GTP and ATP in a homogenous fashion. Collectively, GTP-QRET and QT-Luc$^{GTP\&ATP}$ offer a unique, high-throughput opportunity to explore cellular energy metabolism, serving as a powerful platform for the development of novel therapeutics and extending its usability across a range of disciplines.

Keywords Adenosine triphosphate (ATP) · Capillary electrophoresis (CE) · Guanosine triphosphate (GTP) · Immunoassay · Mass spectrometry (MS) · Time-resolved luminescence (TRL)

Introduction

Nucleotides are organic molecules composed of pentose sugar, phosphate ester, and varying nitrogenous base moieties (see Electronic Supplementary Material Fig. S1). Apart from serving as building blocks for RNA synthesis, the triphosphate forms of adenine and guanine nucleotides, ATP and GTP, function as energy molecules that drive a multitude of cellular processes. However, their roles exhibit a clear distinction [1, 2]. ATP is involved in nearly all cellular metabolic reactions and is necessary also for GTP synthesis [3, 4]. In mammalian cells, cellular ATP concentrations are consistently high, typically maintained at levels of 1–5 mM [5]. In contrast, GTP primarily drives protein synthesis and regulation, cytoskeleton organization, membrane transport, and signal transduction. The cellular GTP concentrations are more variable than those for ATP, fluctuating between 0.1 and 1 mM. GTP levels are regulated differently depending

Atsuo T. Sasaki and Harri Härmä are co-senior authors.

✉ Kari Kopra
kari.kopra@utu.fi

[1] Department of Chemistry, University of Turku, Henrikinkatu 2, 20500 Turku, Finland

[2] Institute for Advanced Biosciences, Keio University, Tsuruoka, Yamagata 997-0052, Japan

[3] Department of Internal Medicine, University of Cincinnati College of Medicine, 3125 Eden Ave, Cincinnati, OH 45267-0508, USA

[4] Department of Clinical and Molecular Genetics, Hiroshima University Hospital, Hiroshima 734-8551, Japan

on tissue and cell type, and the GTP-to-ATP ratio varies significantly [5, 6]. GTP concentration is generally increased in cells undergoing proliferation, as documented by a wide range of organisms [6, 7].

Dysregulation of GTP synthesis has been linked to several inherited diseases. The range of phenotypes highlights the importance of GTP metabolism regulation in vivo for brain function, vision, and the immune system. For instance, deletion mutations in HPRT1 (hypoxanthine-phosphoribosyltransferase-1) can cause hyperuricemia, resulting in severe gout and acute renal failure (Kelley–Seegmiller syndrome) [8–10]. Also, a substantial loss of HPRT1 activity contributes to self-injurious behaviors and motor and cognitive dysfunction (Lesch–Nyhan syndrome) [11–13]. The retina has particularly high GTP concentrations [5, 14], and it relies on photoreceptor cells in converting GTP to cGMP upon light stimulation, triggering input signals to the optic nerve. Loss-of-function mutations in IMPDH1 (inosine monophosphate dehydrogenase 1), the rate-limiting enzyme for de novo GTP synthesis [15], cause retinitis pigmentosa. IMPDH1 dysfunction results in retinal degeneration, accelerated visual aging, and blindness [16–18]. IMPDH inhibitors, including mycophenolic acid (MPA), exhibit immunosuppressive effects and are employed to suppress rejection in organ transplantation and treat autoimmune diseases like systemic lupus erythematosus (SLE). This indicates GTP's vital role in immune system operation [15, 19]. GTP metabolic reprogramming occurs in cancer cells, where high GTP concentrations promote cellular anabolism, potentially making the GTP metabolic system a target for cancer therapy. However, despite considerable research, our understanding of the comprehensive and precise roles of nucleotides under physiological and pathological conditions remains limited. Furthermore, the implications of alterations in nucleotide levels in relation to various diseases have yet to be fully elucidated. While the mechanism translating changes in GTP concentrations into cellular and biological functions remains elusive, evidently, it is crucial to monitor cellular GTP levels and define its ratio against ATP. This would give us a better understanding on the role of cellular energy metabolism and might enable development of novel therapeutics for diseases associated with dysregulated GTP metabolism [20].

The biological relevance of nucleotides and their involvement in various diseases underscores the necessity for a straightforward and precise intracellular-nucleotide-level monitoring tool. Numerous methods have been developed to specifically measure adenosine- and guanosine-related nucleotides using high-performance liquid chromatography (HPLC) coupled with ultraviolet–visible light detection [21–23]. More recent approaches employ mass spectrometry (MS) as a highly selective and sensitive detection method. In these techniques, quantification has been performed across various matrices and for multiple nucleotides [24–28]. However, most of these methods rely on direct analysis, in which phosphate fractions are separated on an HPLC column using ion-pairing-based mobile phases. This separation approach may induce ion suppression from the mobile phase and may consequently impact the measurement of other molecules using HPLC. To address these limitations, a capillary electrophoresis–MS (CE-MS) method has been developed [29–31]. CE is first used to separate metabolites based on their charge and size, followed by selective detection through MS. The major advantages of CE–MS include its high resolution and the capability to analyze nearly any charged species, encompassing both cationic and anionic analytes [32–34]. These methods possess significant advantages in terms of accuracy, specificity, sensitivity, and dynamic range. However, all separation-based techniques require expertise and specialized equipment, such as HPLC and MS apparatus. As a result, only a limited number of researchers can perform these assays. Furthermore, these methods generally require relatively large amounts of biological samples, typically over 10,000 cells for each run, which limits the use of multi-well plate cultures and increases costs. Consequently, it has been challenging to perform high-throughput analysis for GTP and ATP concentrations, which hampers our understanding of their precise roles in cellular functions, disease progression, and drug screenings. Currently, there are high-throughput screening methods available enabling luminescence-based ATP detection, but the same is not true for GTP [35–37]. In addition to luminescence, there have been several attempts to develop fluorescent probes for live cell monitoring of ATP and GTP, but none of these methods for GTP has reached higher popularity, because of the complexity, low sensitivity and selectivity, and the need for specialized expertise and equipment [38]. However, especially aptamer-based detection strategies have already shown promises for also intracellular nucleotide monitoring [39–41].

In our previous work, we identified GTP-specific single-chain variable fragments (scFv) from the synthetic antibody fragment library by phage display screening, and converted that to the first GTP-specific antigen-binding fragment (Fab) [42, 43]. The anti-GTP Fab clone 2A4 (hereafter $2A4^{GTP}$ Fab) has shown superior specificity to GTP over GDP and ATP in vitro, which we have utilized to measure the rate of GTP hydrolysis activity by $2A4^{GTP}$ Fab and Eu^{3+}-GTP in a homogenous assay format. The principle underlying the monitoring of GTP consumption is based on the $2A4^{GTP}$ Fab competition between GTP and Eu^{3+}-GTP, which is detected using the single-label quenching resonance energy transfer (QRET) principle and time-resolved luminescence (TRL) readout [42]. While the $2A4^{GTP}$ Fab-based GTP detection with QRET enables nanomolar sensitivity using pure solutions and proteins, it has remained untested whether it can still selectively react with GTP in the presence of cellular extracts that contain

thousands of metabolites and proteins. Cellular extracts have a high ATP concentration, typically five- to tenfold higher than that of GTP [5]. Likewise, cellular concentrations of the other nucleotides (e.g., UTP, CTP) and nucleotide derivatives (e.g., nicotinamide adenine dinucleotide, NAD^+, and S-adenosyl methionine, SAM) have comparable ranges to GTP [44, 45]. Thus, $2A4^{GTP}$ Fab may cross-react with many of these metabolites in the presence of homogenous cellular extract or possess a polyvalent feature binding some other cellular components [46]. To answer these concerns, here, we studied a series of key parameters of the GTP-QRET system and conducted a rigorous validation using CE-MS as a reference method. We were able to verify the functionality of $2A4^{GTP}$ Fab under homogenous conditions. Moreover, we successfully developed a QT-$Luc^{GTP\&ATP}$ platform to monitor both GTP and ATP from the same sample in the same well by combining the GTP-QRET platform with direct luminescence–based ATP monitoring. This technique, termed QT-$Luc^{GTP\&ATP}$, can be applied to 6- to 384-well-plate formats, and results can be obtained in less than an hour with as few as 100 cells/well. Given the current extensive applicability of ATP detection, the simultaneous detection of GTP and ATP in a multi-well plate format presents significant potential for establishing a new QT-$Luc^{GTP\&ATP}$ cost-effective technological platform with broad application across numerous fields, encompassing medicine, pharmacology, agriculture, and life, food, and analytical sciences.

Experimental section

Materials and apparatus

Nonadentate europium-chelate-9d, {2,2′,2″,2‴-{[4′-(4‴-isothiocyanatophenyl)-2,2′,6′,2″-terpyridine-6,6″-diyl]bis(methylene-nitrilo)} tetrakis(acetate)}europium(III), used for Eu^{3+}-GTP conjugation, and the soluble quencher molecule, named MT2, were obtained from QRET Technologies (Turku, Finland). Labels were used according to the manufacturer's instructions, and purification and concentration determination was performed as previously described [47–49]. A ReadiUse™ Rapid Luminometric ATP Assay Kit was obtained from AAT Bioquest. White Corning 384-well low-volume assay plates were used in all GTP-QRET and QT-$Luc^{GTP\&ATP}$ assays for the detection of GTP and ATP. The 96-well Costar tissue culture plates (Corning, NY, USA) and black 384-well Optiplates (PerkinElmer, Netherlands) were used in cell sample preparation. Cell lines (U87MG, HEK293T, A549, MDA-MB-468, QGP1, BT-474, HeLa, and HTC116) were obtained from the American Type Culture Collection (ATCC, Manassas, VA, USA), and all larger cultures were performed in a 6-well plate or a T75 culture flask (Corning). Dulbecco's modified Eagle medium (DMEM), Roswell Park Memorial Institute (RPMI) 1640 medium, fetal bovine serum, trypsin/EDTA, L-glutamine, and penicillin/streptomycin were purchased from (Gibco, Thermo Fisher Scientific, Waltham, MA, USA). Phosphate-buffered saline (PBS) without calcium and magnesium was from Lonza (Walkersville, USA). Normocin was from InvivoGen (USA). All nucleotide phosphates, GTP, ATP, guanosine-5′-diphosphate (GDP), guanosine-5′-monophosphate (GMP), cytidine-5′-triphosphate (CTP), and uridine-5′-triphosphate (UTP) were from Jena Bioscience (Jena, Germany) and Sigma-Aldrich (St. Louis, MO, USA). All other reagents, including analytical-grade solvents, buffer components, guanosine, mannitol, methionine sulfone, ethane sulfonic acid, d-camphor-10-sulfonic acid, chloroform, 1,3,5-benzene tricarboxylic acid, 3-aminopyrrolidine, and MPA were from Sigma-Aldrich.

A reverse-phase liquid chromatography Dionex ultimate 3000 LC system (Dionex Corporation, Sunnyvale, CA, USA) and an Ascentis RP-amide C18 column (Sigma-Aldrich, Supelco Analytical) were used for Eu^{3+}-GTP purification [47–49]. All measurements were performed using a Spark 20 M from Tecan Life Sciences (Männedorf, Switzerland). Time-resolved luminescence (TRL) measurements for GTP were performed at 620 nm, using a 340-nm excitation wavelength (800 µs delay and 400 µs decay). Total luminescence for ATP measurement was monitored using 1000 ms of integration time. CE-MS analysis was performed using an Agilent G7100 CE system (Santa Clara, CA, USA), with an Agilent 6210 time-of-flight mass spectrometer (TOFMS), Agilent1200 series isocratic HPLC pump, and Agilent G1607A CE-ESI–MS sprayer kit. For ATP and GTP analysis, the original Agilent SST316Ti stainless steel ESI needle was replaced with platinum [50].

Cell culturing and sample preparation

The cell lines used were all cultured in a humidified atmosphere of 5% CO_2 at 37 °C. Culturing of U87MG, HEK293T, A549, MDA-MB-468, HeLa, and HTC116 was performed in DMEM and QGP1 and BT-474 in RPMI 1640 media supplemented with 10% fetal bovine serum (FBS), 1% penicillin/streptomycin, and 2 mM L-glutamine.

For comparison of QT-$Luc^{GTP\&ATP}$ and CE-MS, subconfluent cells in a 6-well plate were washed with 5% (w/v) mannitol and dissolved in 2 mL of methanol (MeOH) containing internal standards for CE-MS (25 µM each of methionine sulfone, ethane sulfonic acid, and d-camphor-10-sulfonic acid). This solution was directly used for QT-$Luc^{GTP\&ATP}$ or dried and used after reconstitution. For CE-MS, 400 µL of this homogenate, 200 µL of Milli-Q water, and 400 µL of chloroform were mixed. After centrifugation (12,000 g for 15 min at 4 °C), the separated

upper aqueous layer was filtered through a Millipore 5-kDa cutoff filter (Millipore, Bedford, MA, USA) to exclude proteins. The filtrate was freeze-dried and resolved in 25 µL of Milli-Q water containing internal standards (200 µM each of 1,3,5-benzene tricarboxylic acid and 3-aminopyrrolidine) prior to the analysis using CE-MS.

For the 96-well plate test, 10,000 cells (U87MG and HEK293T) were transferred to each well in a 96-well plate and cultured to 60–80% confluence. For MPA (1–100 µM) and guanosine (100 µM) testing, cells were further treated for 4 h by adding these compounds in a fresh media. Thereafter, the medium was aspirated, and cells were washed with PBS before 80% MeOH was added (100 µL). Plates were centrifuged at 1600 g for 10 min at room temperature (RT), and 2 µL of MeOH solution containing the nucleotide extracts was directly used for GTP-QRET or QT-Luc$^{GTP\&ATP}$ in a 384-well plate (100–1000 cells/well).

Luminescence-based GTP and ATP monitoring

GTP-QRET assay optimization was performed using pure GTP and ATP samples (0–10 µM) and detection components in varying concentrations, Eu^{3+}-GTP (2–20 nM), anti-GTP 2A4^{GTP} Fab (5–50 nM), and MT2 modulator (1.5–5 µM). Tests were performed in a preselected GTP buffer (25 mM HEPES, pH 7.5, 1 mM $MgCl_2$, 0.01% Triton X-100). All assays were performed in 10 µL final volume in a white 384-well plate. ATP assay was separately optimized in the same plate using 10–25 µL final volumes. Nucleotides were in all cases added in 5 µL and ATP detection in 5–20 µL volume. In both assays, TRL- and luminescence signals were monitored at multiple time points between 5 and 60 min. Optimized conditions for each assay were used for specificity analysis and assayed separately. Titrated (0–500 µM) nucleotides (GTP, GDP, GMP, ATP, UTP, and CTP) were added in 5 µL and pre-made and optimized detection solution, Eu^{3+}-GTP (10 nM), anti-GTP 2A4^{GTP} Fab (20 nM), and MT2 quencher (2.7 µM), in 5 µL. Concentrations are reported in final 10 µL volume. Nucleotides were similarly titrated with the ReadiUse™ Rapid Luminometric ATP Assay Kit using 10-µL nucleotide samples and 10 µL of the ATP detection reagent in a total of 20-µL final volumes. In both assays, signals were monitored after 15 min of incubation at RT.

Two individual assays were combined by testing nucleotide (GTP, ATP, and ATP + GTP) addition in Milli-Q water, GTP buffer, and GTP buffer supplemented with MeOH (2–28%). In all assays, the nucleotide sample was added in 5 µL followed by GTP detection solution addition (5 µL), and TRL-signal detection (15 min). ATP detection solution was added in 10 µL on top of GTP assay components, and the luminescence signal was monitored (15 min). Nucleotides extracted from the cells were measured using the same protocol, with the exception that standard buffer's MeOH concentration was adjusted to match with the cell samples. Typically, MeOH concentration was below 8%. Cells cultured in a 96-well plate were monitored similarly to other samples except that nucleotides were added in 2 µL and GTP detection in 8 µL. GTP detection solution concentrations in the final 10-µL volume were the same in all assays.

Quantifications of ATP and GTP using CE-TOFMS

Cellular ATP and GTP were detected and quantified using time-of-flight CE–TOFMS (Agilent Technologies) as previously reported [31, 51, 52]. The raw data were processed with MasterHands [53]. ATP and GTP were identified by matching their m/z values and migration times to standard compounds. A series of other metabolites were analyzed in a similar manner.

Data analysis

In all assays, the signal-to-background ratio (S/B) was calculated as μ_{max}/μ_{min} either by using the true minimum and maximum or from the linear range of the assay. The coefficient of variation (CV%) was calculated as $(\sigma/\mu)*100$. In both formulas, μ is the mean value and σ is the standard deviation (SD). Data were analyzed using Origin 8 software (OriginLab, Northampton, MA) and basic linear and sigmoidal fitting functions. The half-maximal effective concentration (EC_{50}) values were obtained from sigmoidal fitting, and ATP and GTP concentrations were determined based on the linear part of the appropriate standards.

Results and discussion

2A4^{GTP} Fab preferentially binds GTP over GDP, GMP, ATP, CTP, and UTP

In the previous study, we monitored GTP consumption in vitro with the 2A4^{GTP}, using purified recombinant GTPases [42, 43]. While 2A4^{GTP} Fab displayed remarkable sensitivity and specificity toward GTP over GDP in vitro, whether 2A4^{GTP} Fab can discriminate GTP from cellular extracts remains untested. Given that a cell contains thousands of metabolites and proteins, it is possible that these cellular components may interfere with the reactivity of 2A4^{GTP} Fab toward GTP. Nucleotide structures are highly similar, and thus, for the 2A4^{GTP} Fab, it is important to recognize not only the triphosphate ester, but also the varying nucleotide base (see Electronic Supplementary Material Fig. S1).

Thus, we set out to test 2A4^{GTP} Fab for its guanine base recognition by comparing the reactivity to three other major

ribonucleotides, ATP, UTP, and CTP. On the other hand, we compared the detectability of GTP over GDP and GMP to estimate phosphate recognition. Based on the initial tests, 10 nM Eu^{3+}-GTP and 20 nM $2A4^{GTP}$ Fab were selected for these titrations to enable better tolerability of the cellular extracts without significantly sacrificing the sensitivity and selectivity. Under these conditions, $2A4^{GTP}$ Fab detects GTP 86-, 90-, and over 300-fold better than CTP, UTP, and ATP, respectively (see Electronic Supplementary Material Fig. S2). Similarly, GTP was detected at a 33-fold lower concentration than GDP and the difference was over 1300-fold with GMP (see Electronic Supplementary Material Fig. S2). Even though cellular ATP levels are typically 5- to 10-folds higher than GTP, the results suggest that $2A4^{GTP}$ Fab is highly likely to distinguish GTP signal from ATP in a cellular extract. Likewise, since GTP levels are typically comparable or even higher than those of CTP and UTP, and significantly higher in comparison to that of GDP (10- to 50-fold) and GMP, $2A4^{GTP}$ Fab is expected to detect GTP specifically in cellular extracts [5]. As the ultimate goal of the present study is to develop $2A4^{GTP}$ Fab-based GTP detection using cellular extract, we also tested the effect of MeOH used in nucleotide extract preparation. This method is widely used for metabolomics analysis, including CE-MS for assessing polar metabolites [53–56]. While MeOH extraction for metabolomics is typically followed by evaporation and reconstitution with water or solvent, to increase simplicity and throughput, we omitted this step, and instead, used diluted cellular extract. As shown in Fig. S3 (see Electronic Supplementary Material), $2A4^{GTP}$ Fab can detect GTP up to 14% MeOH without a major difference in dynamic range.

GTP-QRET by $2A4^{GTP}$ Fab detects exogenously added GTP in the presence of cellular extracts

Cellular extracts contain thousands of metabolites, which may interfere with the $2A4^{GTP}$ Fab recognition of GTP. To test this possibility, we measured exogenously added GTP in the presence and absence of serially diluted cellular extracts to evaluate the effect of these extracts on GTP concentration measurements. Throughout the study, we employed both 96-well and 384-well microplates for our experiments. To clearly delineate the cell number in a well of these two plates, we will henceforth utilize the notations "$well^{96}$" and "$well^{384}$" to represent a single well within the respective 96-well and 384-well microplates. We performed the assay using typical cell numbers in 96-well plates, simultaneously studying the high-throughput compatibility of our assay. Widely used glioblastoma U87MG cells were studied to design an experiment under culture conditions in a 96-well plate. U87MG cells proliferate in 96-well plates to a density of approximately 10,000 to 50,000 cells/$well^{96}$, and metabolites can be extracted from the 96-well plates using 100 µL of 80% MeOH. A threefold dilution was performed to simplify the pipetting, and 2 µL of this diluted sample was subsequently analyzed in a 384-well plate using the optimized GTP-QRET. The amount of metabolite in the assay solution was estimated to be around 1.2% of the total, equating to extracts of approximately 100 cells in a $well^{384}$. The results demonstrated that the accuracy of the GTP-QRET assay was well preserved for cell contents ranging from 100 to 500 cells/$well^{384}$, corresponding to typical cell numbers from 12,000 to 60,000 cells/$well^{96}$ (Fig. 1). In contrast, when cellular extracts reached 1000 cells/$well^{384}$ (roughly 120,000 cells/$well^{96}$), which are uncommon densities used for the biological assay, the GTP concentration measured by GTP-QRET appeared higher than expected. Our data suggest that, using this protocol, the GTP–QRET assay exhibits high accuracy within the standard cell count range typically employed in conventional experiments. However, as the cell size and content composition can vary between cell types, it is crucial to optimize the cell number and dilution factor for each cell line.

Development of QT-$Luc^{GTP\&ATP}$ detecting cellular GTP and ATP down to 100 cells

The dual-detection method of GTP and ATP in a multi-well plate format has a high potential to provide a new technological platform applicable for many fields including, life, analytical, and food science as well as agriculture. Having validated the GTP-QRET applicability for cellular GTP detection, we set out to explore if GTP-QRET can equip additional functions to measure both GTP and ATP from the same sample. Towards this end, we adapted a commercial luminescence-based ATP assay from ATT Bioquest, since this ATP assay performed with only a single component addition is expected to work in a similar cell number (up to ~ 5000 cells/$well^{384}$) to GTP-QRET. While GTP-QRET and ATP assay use luminescence-based detection, the readout is very different. GTP-QRET is monitored utilizing a TRL-signal readout using 620-nm and 340-nm excitation wavelengths (800 µs delay and 400 µs decay). On the other hand, in ATP assay, the total luminescence is monitored, and thus, no interference was expected when GTP detection was performed prior to the ATP measurement. We individually optimized the use of the ATP assay to enable simultaneous detection with GTP. For this, the added amount of ATP detection reagent was lowered from 25 to 10 µL, without any effect on the ATP detection in the concentration area of interest (data not shown). Under this condition, ATP detection also had a good MeOH tolerability and had no cross-reactivity to other nucleotides than ATP (see Electronic Supplementary Material Fig. S2 and S3).

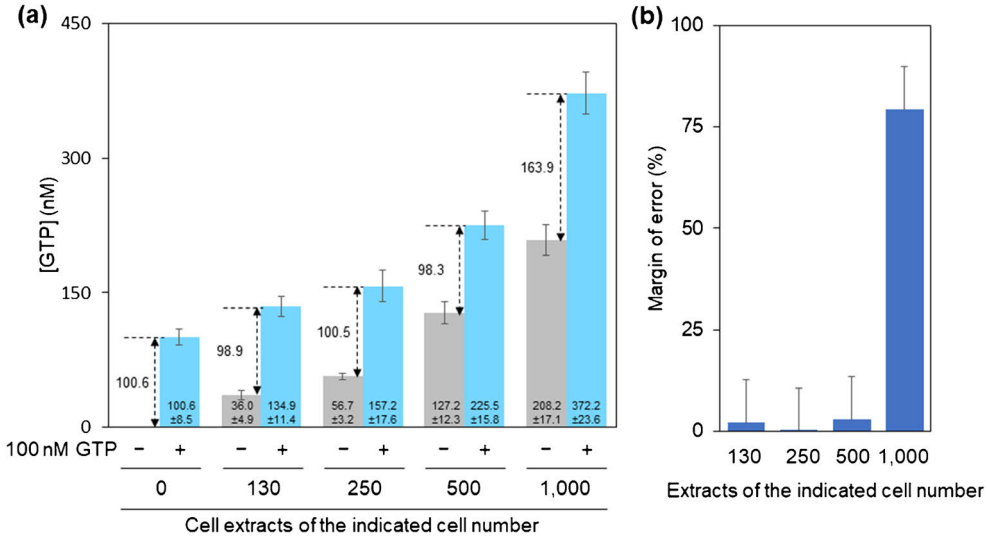

Fig. 1 The effect of the cellular extract on the measurement of GTP concentration. **a** GTP concentration was measured in the presence or absence of diluted cellular extracts, and in the presence or absence of 100 nM GTP used as a standard. The cellular extract of U87MG cells was prepared in 80% MeOH and diluted to GTP buffer to obtain cell contents ranging from 100 to 1000 cells/well[384]. Data represent mean ± SD ($n = 3$). **b** The perturbation effect of cellular extracts on GTP-QRET is shown as a margin of error based on the result of **a**

As GTP-QRET and ATP detection methods showed the expected functionality individually, next, we combined the assays by detecting GTP and ATP from the same well. We selected a three-step protocol for the detection: addition of (1) nucleotide sample, (2) detection solution and TRL-signal monitoring, and (3) ATP detection solution and luminescence readout (see Electronic Supplementary Material Fig. S4). The first dual-readout tests were performed by adding GTP and ATP individually or together in Milli-Q water or GTP assay buffer. Based on these results, no change in GTP and ATP detection was seen in either case, when different addition were compared to each other (see Electronic Supplementary Material Fig. S5). For the GTP-QRET detection, the linear range in the presence of GTP with or without ATP was from 10 to 1000 nM, as ATP alone was not detected at these concentrations. Also, in the luciferase-based ATP assay, linear range was up to 1000 nM ATP without any GTP-related interferences (see Electronic Supplementary Material Fig. S5). The optimization showed good functionality using the dual-parametric single-well assay platform, and the obtained sensitivity is expected to be sufficient for GTP and ATP detection from cells. We named this new dual GTP and ATP detection system as QT-Luc$^{GTP\&ATP}$. The assay functionality was deemed satisfactory when using pure GTP and ATP solutions, as well as during the initial tests conducted with GTP-QRET alone. Good assay performance was observed when the cell number exceeded 100 cells per well in a 384-well plate, depending on the specific cell line and its nucleotide concentration (Fig. 1 and S5 see Electronic Supplementary Material).

For metabolomic analysis, MeOH-based extraction is a widely used method. However, protocol often requires MeOH evaporation and sample reconstitution in water before metabolomic analysis. Technically and ideally, the direct use of MeOH simplifies the protocol and will be the preferred option especially when multi-well plate cultures are used. To determine if QT-Luc$^{GTP\&ATP}$ is applicable for samples prepared by MeOH extraction, we used U87MG and A549 cell lines and two sample preparations, (1) direct dilution and detection from the 80% MeOH or (2) samples in Milli-Q water after MeOH evaporation. The cell titration analysis suggested that sample preparation by MeOH or reconstitution with water after MeOH extraction did not impact GTP or ATP detection (Fig. 2). In addition, both cell lines gave a linear response for GTP and ATP, with U87MG being detectable at lower cell numbers than A549. This is likely due to the higher nucleotide concentration in U87MG. Based on these results, the optimal cell number for the upcoming assays for U87MG is 200–2000 cells/well[384] and 500–5000 cells/well[384] in the case of A549. When these results were used to estimate the ratio between GTP and ATP, ATP concentration was shown to be five- to tenfold higher in comparison to GTP, A549 cells having the higher ratio. These results are in accordance with the ones reported previously [5]. Importantly, no similar interference with the extracts from higher cell number was detected as with

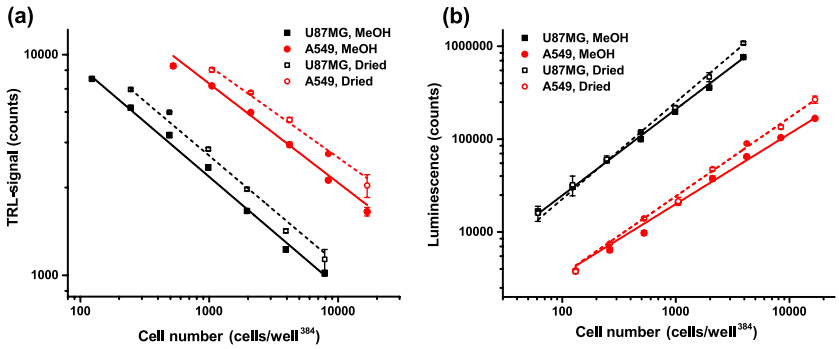

Fig. 2 Linearity of the GTP and ATP concentration measurement from the cellular extract. Cell (U87MG, black, and A549, red) extract titration for GTP (**a**) and ATP (**b**) using MeOH solution samples (solid) and samples after MeOH evaporation and reconstitution in Milli-Q water (dashed). Data represents mean ± SD ($n = 3$)

GTP-QRET with 96-well cultures. Together, these results show that QT-Luc$^{GTP\&ATP}$ retains high assay functionality with samples prepared with the MeOH extraction.

QT-Luc$^{GTP\&ATP}$ detects dynamic changes in cellular GTP concentrations

To assess the detection fidelity of QT-Luc$^{GTP\&ATP}$, we used pharmacological perturbation of cellular GTP levels using MPA, an inhibitor of the GTP-biosynthetic enzyme IMPDH [15–19]. Previous studies have shown that treatment of MPA decreases cellular GTP levels within 4 h, while ATP levels are transiently increased due to the reflux towards the ATP synthesis pathway. A previous study also showed significant growth suppression of U87MG cells by 10 µM MPA while the effect was moderate at 1 µM MPA [54]. U87MG cells (2000 cell/well^{384}) were first treated with or without MPA for 8 h and subjected to QT-Luc$^{GTP\&ATP}$ assay. Consistent with the previous data detected by CE-MS by others [15], the QT-Luc$^{GTP\&ATP}$ assay shows that GTP concentrations were decreased approx. 50% and 30% to that of control (no MPA) by 1 µM and 10 µM MPA treatment, respectively (Fig. 3a). To further verify the functionality of QT-Luc$^{GTP\&ATP}$ assay, we next tested if the assay can detect the cellular GTP elevation induced by guanosine supplement, which increases cellular GTP concentration via HPRT1 in a time-dependent manner. For this, we also included A549 cells in addition to U87MG. Consistent with the Fig. 3a result, QT-Luc$^{GTP\&ATP}$ assay detected MPA-induced decrease in cellular GTP concentrations also in A549 cells, and importantly, QT-Luc$^{GTP\&ATP}$ assay detected the increase in cellular GTP concentration treatment with 100 µM guanosine (Fig. 3b). This is consistent with the previous CE–MS-based quantification [57]. Furthermore, we spiked a cell sample after lysis as a second control, and confirmed that a theoretically correct approximately twofold increase in GTP concentration was detected (data not shown).

Detection fidelity of QT-Luc$^{GTP\&ATP}$ is comparable to CE-MS

To further verify the accuracy of the QT-Luc$^{GTP\&ATP}$ method, we employed CE–MS-based quantification technology as a reference method [31, 58–61], First, we assayed the U87MG cells cultured in 6-well plates and modulated with MPA (10 µM) or guanosine (100 µM) (Fig. 4a). Cells designated for both assays were cultured and treated at the same time and manner before division

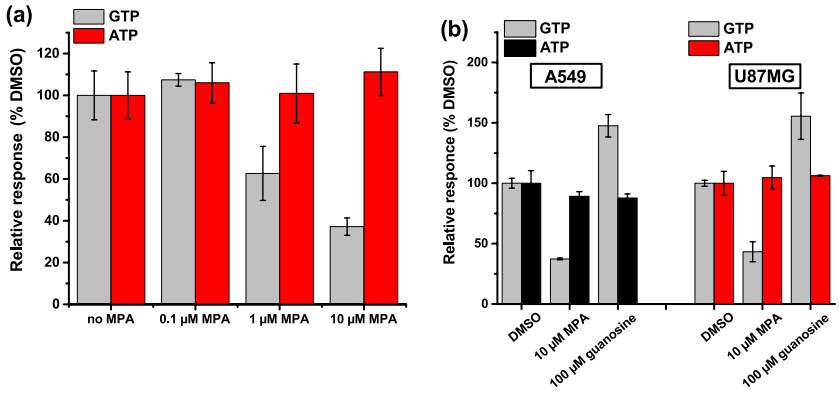

Fig. 3 MPA and guanosine effect on GTP and ATP concentration in cellular extracts. **a** Concentration-dependent (0–10 µM) effect of MPA for GTP and ATP concentrations derived from U87MG cells, 2000 cells/well.^{384}. **b** Single time-point and concentration effect of MPA (10 µM) with or without guanosine (100 µM) detected from U87MG and A549 cellular extract. Data represent mean ± SD ($n = 3$)

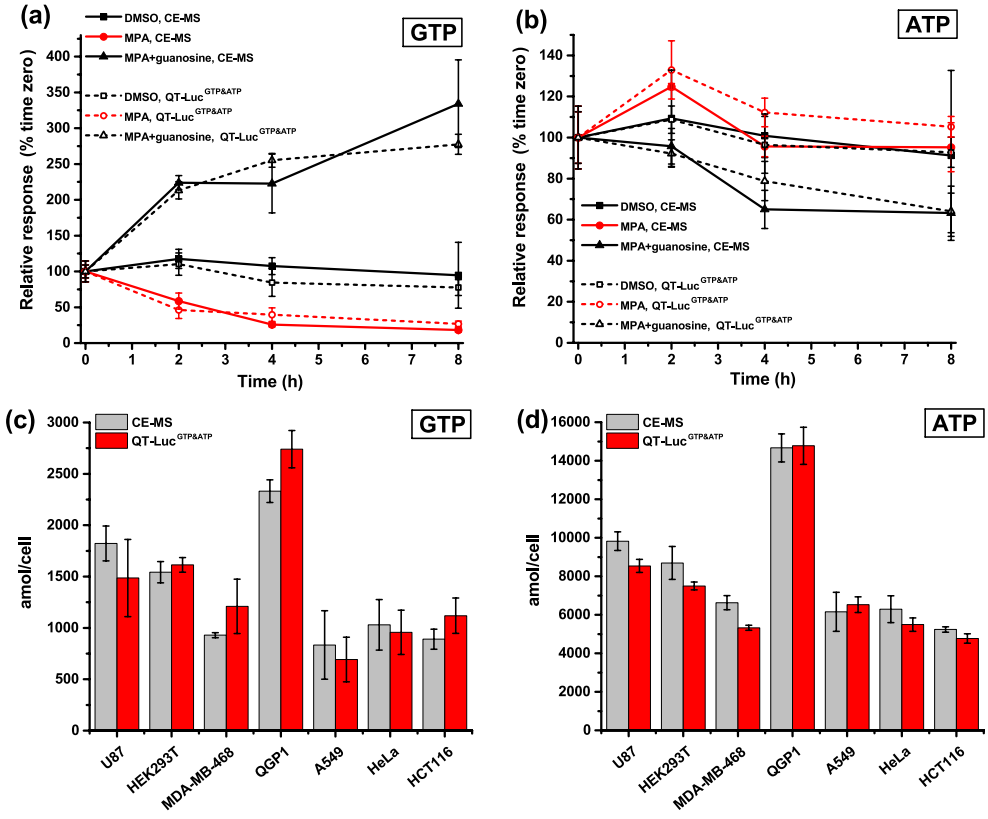

Fig. 4 Comparison of the QT-Luc$^{GTP\&ATP}$ assay to the CE–MS reference method. Time-dependent effect of MPA (10 μM) with or without guanosine (100 μM) for GTP (**a**) and ATP (**b**) levels in U87MG cells detected using either QT-Luc$^{GTP\&ATP}$ or CE-MS. GTP (**c**) and ATP (**d**) levels in multiple different cell lines detected with QT-Luc.$^{GTP\&ATP}$ or CE-MS. Data represent mean ± SD ($n = 3$)

for either assay (see Electronic Supplementary Material Fig. S6). In the presence of MPA, a near-maximal decrease in GTP concentration was achieved after 4 h of the treatment, while guanosine continued to elevate GTP levels even after 8 h. These trends were consistently observed with both GTP–QRET and CE–MS methods (Fig. 4a). As expected, ATP measurements displayed a less profound effect (Fig. 4b). We also determined CTP and UTP concentrations with CE-MS to estimate potential interferences for the GTP detection (see Electronic Supplementary Material Fig. S7a). In the case of untreated cells, GTP concentration was approximately 1800 amol/cell, whereas CTP and UTP concentrations were 1100 and 2200 amol/cell when monitored with CE-MS, respectively. Together, these data suggest that the QT-Luc$^{GTP\&ATP}$ method can detect cellular GTP concentration with accuracy comparable to CE-MS in U87MG cells, and without interferences occurring from nucleotide triphosphates or other cellular components.

To widen our analysis, we employed a diverse panel of cell lines, including SV40-transformed human embryonic kidney HEK293T, human lung adenocarcinoma A549, human breast adenocarcinoma MDA-MB-468, human pancreatic neuroendocrine cancer QGP1, human cervical adenocarcinoma HeLa, and human colorectal adenocarcinoma HTC116 cells. Across all cell lines examined, ATP concentrations were 5.3–7.4 (CE-MS) or 4.4–9.4 (QT-Luc$^{GTP\&ATP}$) times higher than to GTP. Despite the similar nucleotide ratios, greater variation was observed in their concentrations (Fig. 4). Notably, QGP1 cells had significantly higher GTP and ATP level compared to all other cell lines, with ATP and GTP concentrations approximately threefold higher than those in HCT116 for ATP and A549 for GTP, having the lowest concentrations.

From these cell lines, we also analyzed the CTP and UTP content using CE–MS (see Electronic Supplementary Material Fig. S7b). In all cell lines, CTP concentration (550–1400

amol/cell) was similar or lower in comparison to the GTP (830–2400 amol/cell) concentration. On the other hand, UTP concentrations (1500–4100 amol/cell) were slightly higher than those of GTP in all cell lines, which is typical for common cell lines [5]. In all cases, even the highest UTP concentrations are not anticipated to impact on GTP detection, as the $2A4^{GTP}$ Fab specificity against GTP is nearly 100-fold greater than for UTP (see Electronic Supplementary Material Fig. S2a). In addition, GDP interference is not expected, as its concentration was generally approx. 10 times lower in comparison to GTP, and in all cases, GDP was not even detected with CE-MS, falling below the detection limit (data not shown). Based on the CE–MS data, not only were the nucleotide triphosphate concentrations of interest changed from cell to cell and condition to condition, but also some other metabolites like NAD^+ and UDP-glucose showed significant change in their concentration, indicating changes in the whole-cell metabolism (see Electronic Supplementary Material Fig. S8).

QT-Luc$^{GTP\&ATP}$ increases the throughput of GTP and ATP detection

The commonly used nucleotide extraction protocol consists of multiple steps such as (1) cell washing and collection, (2) MeOH extraction, (3) centrifugation, (4) drying, and (5) dissolution to selected buffer [62]. We showed already with GTP-QRET that GTP is detectable from cellular extract from the 96-well plates, and that QT-Luc$^{GTP\&ATP}$ assay is not MeOH sensitive (Fig. 1 and S3 see Electronic Supplementary Material). However, as the dynamic range of the GTP-QRET and QT-Luc$^{GTP\&ATP}$ did not match when the nucleotide extraction was performed either in 96-well plates or higher-volume cultures, we decided to study QT-Luc$^{GTP\&ATP}$ further. U87MG and HEK293T cells were assayed, using 96-well plate cultures and 500 cells/well^{384} in the detection. Under these conditions, no interferences were detected, and calculated ATP and GTP concentrations correlated to those detected earlier from the cellular extracts (Fig. 4 and S9 see Electronic Supplementary Material). Five hundred cells/well^{384} were previously found optimal for GTP-QRET, and the observed interferences at higher cell number indicate that the protocol using extracts directly from the 96-well plate prefers a low cell number in the detection. This might be due to the high MeOH concentration, over the assay detection capacity (Fig. 2), caused by limited maximum cell capacity in the 96-well plates. Alternatively, centrifugation and sampling from the 96-well plate might be more prone to error. This needs to be considered if the nucleotide concentration of 500 cells/well^{384} is not sufficient, and it is expected to be fixed using alternative protocol in a 48-well plate. Overall, these results demonstrate the high-throughput potential of the QT-Luc$^{GTP\&ATP}$ method.

Conclusions

The intrinsic roles of ATP and GTP in fueling cellular processes make them crucial in understanding disease mechanisms and discovering new therapeutic approaches. While existing technologies like HPLC and MS-based analysis have facilitated insightful investigations into cellular energy metabolism, their limitations in throughput, cost, and accessibility highlight the pressing need for alternative, high-throughput solutions. Recognizing this, we have developed and validated the novel GTP-QRET and QT-Luc$^{GTP\&ATP}$ technologies. By simultaneous monitoring of ATP and GTP levels in standard multi-well formats, we achieved results in a time- and cost-effective manner with a minimal number of cells. By surpassing the barriers presented by current methods, our GTP-QRET and QT-Luc$^{GTP\&ATP}$ platforms hold the potential to greatly enhance our understanding of the roles of nucleotides in cellular function and disease progression. Moreover, these methods are highly suited for drug screening, opening new avenues for therapeutic development, particularly for diseases linked with dysregulated GTP metabolism. However, despite our advancements, we recognize that the cell number, especially in the case of high-throughput 96-well plate cultures, is of high importance and in the current format, maximal cell number in high-throughput format is limited to approx. 500 cells/well^{384}. Nonetheless, with the technological strides made in this study, we are one step closer to unraveling the complexities of cellular energy metabolism. We anticipate that our platforms will serve as the cornerstone for future studies in various fields, from medicine to food science, catalyzing the discovery of novel findings and advancements. While the full understanding of nucleotide functions remains a complex endeavor, our novel tools provide a significant stride forward, simplifying and expediting the journey toward this goal.

Supplementary Information The online version contains supplementary material available at https://doi.org/10.1007/s00216-023-04944-9.

Acknowledgements The authors gratefully acknowledge the financial contribution of Academy of Finland grants 323433, 329012, and 353324 (K.K.) and 296093 (H.H.). R.M. was supported by the Otto. A. Malm Foundation and Finnish Academy of Science and Letters Vilho, Yrjö, and Kalle Väisälä. This work was also supported in part by the Project for Promotion of Cancer Research and Therapeutic Evolution (P-PROMOTE; 22ama221112h0001) from Japan Agency for Medical Research and Development (AMED), Creation of Fundamental Technologies by Interdisciplinary Research to Coexist with Infectious Diseases including COVID-19 from Japan Science and Technology Agency (JST), CREST program (JP20356709), KAKENHI (20H03165) from Japan Society for the Promotion of Science (JSPS), Human Frontier Science Program (HFSP) (RGP0028/2022) and NIH grants (R01NS089815, R01CA255331, and R01GM144426) (A.T.S). Y.F. was supported in part by the Uehara Memorial Foundation, and A.I.O. was in part supported by a JSPS research fellow (22J12765). A.H. was supported in part by the JST FOREST Program (JPMJFR2052). The research conducted at Keio University was supported

by grants from the Yamagata prefectural government and the city of Tsuruoka. We extend our thanks to Drs. Eric P. Smith, Danielle Tapp, and Shun Kageyama for their diligent proofreading and editing of our work.

Author contribution K. Kopra: conceptualization, methodology, investigation, validation, supervision, writing—original draft, writing—review and editing, project administration, funding acquisition. R. Mahran: investigation, validation, writing—original draft, writing—review and editing. T. Yli-Hollo: investigation. S. Tabata: investigation. E. Vuorinen: methodology, investigation, validation. Y. Fujii: investigation. I. Vuorinen: investigation. A. Ogawa-Iio: investigation. A. Hirayama: investigation. T. Soga: supervision, investigation. A. Sasaki: supervision, writing—review and editing, project administration, funding acquisition. H. Härmä: supervision, writing—review and editing, project administration, funding acquisition.

Funding Open Access funding provided by University of Turku (UTU) including Turku University Central Hospital.

Declarations

Competing interests The authors declare the following competing financial interest(s): Kari Kopra and Harri Härmä have commercial interest through QRET Technologies Ltd. Randa Mahran, Titta Yli-Hollo, Sho Tabata, Emmiliisa Vuorinen, Yuki Fujii, Iida Vuorinen, Aki Ogawa-Iio, Akiyoshi Hirayama, Tomoyoshi Soga, and Atsuo T. Sasaki declare that they have no relevant financial or non-financial interests to disclose.

References

1. Yegutkin GG. Nucleotide- and nucleoside-converting ectoenzymes: important modulators of purinergic signalling cascade. Biochim Biophys Acta Mol Cell Res. 2008;1783:673–94.
2. Alberts B, Johnson A, Lewis J, Raff M, Roberts K, Walter P. Molecular biology of the cell. T cells and MHC proteins, fourth ed., Garland Science. New York, 2002.
3. Sumita K, Lo YH, Takeuchi K, Senda M, Kofuji S, Ikeda Y, Terakawa J, Sasaki M, Yoshino H, Majd N, Zheng Y, Kahoud ER, Yokota T, Emerling BM, Asara JM, Ishida T, Locasale JW, Daikoku T, Anastasiou D, Senda T, Sasaki AT. The lipid kinase PI5P4Kβ is an intracellular GTP sensor for metabolism and tumorigenesis. Mol Cell. 2016;61(2):187–98.
4. Schultheisz HL, Szymczyna BR, Scott LG, Williamson JR. Pathway engineered enzymatic de novo purine nucleotide synthesis. ACS Chem Biol. 2008;3(8):499–511.
5. Traut TW. Physiological concentrations of purines and pyrimidines. Mol Cell Biochem. 1994;140(1):1–22.
6. Zala D, Schlattner U, Desvignes T, Bobe J, Roux A, Chavrier P, Boissan M. The advantage of channeling nucleotides for very processive functions. F1000Res. 2017;6:724.
7. Porporato PE, Dhup S, Dadhich RK, Copetti T, Sonveaux P. Anticancer targets in the glycolytic metabolism of tumors: a comprehensive review. Front Pharmacol. 2011;2:49.
8. Mateos FA, Puig JG. Purine metabolism in Lesch-Nyhan syndrome versus Kelley-Seegmiller syndrome. J Inherit Metab Dis. 1994;17(1):138–42.
9. Zoref-Shani E, Feinstein S, Frishberg Y, Bromberg Y, Sperling O. Kelley-Seegmiller syndrome due to a unique variant of hypoxanthine-guanine phosphoribosyltransferase: reduced affinity for 5-phosphoribosyl-1-pyrophosphate manifested only at low, physiological substrate concentrations. Biochim Biophys Acta. 2000;1500(2):197–203.
10. Puig JG, Torres JR, Mateos FA, Ramos TH, Arcas JM, Buno AS, O'NEILL P. The spectrum of hypoxanthine-guanine phosphoribosyltransferase (HPRT) deficiency. Clinical experience based on 22 patients from 18 Spanish families. Medicine. 2001;80(2):102–12.
11. Nyhan WL. Lesch-Nyhan disease. J Hist Neurosci. 2005;14(1):1–10.
12. Nyhan WL. The recognition of Lesch-Nyhan syndrome as an inborn error of purine metabolism. J Inherit Metab Dis. 1997;20(2):171–8.
13. Torres RJ, Puig JG. Hypoxanthine-guanine phosophoribosyltransferase (HPRT) deficiency: Lesch-Nyhan syndrome. Orphanet J Rare Dis. 2007;2(1):1–10.
14. Plana-Bonamaisó A, López-Begines S, Fernández-Justel D, Junza A, Soler-Tapia A, Andilla J, Loza-Alvarez P, Rosa JL, Miralles E, Casals I, Yanes O, De la villa P, Buey RM, Mendez A. Post-translational regulation of retinal IMPDH1 in vivo to adjust GTP synthesis to illumination conditions. Elife. 2020;9:e56418.
15. Kofuji S, Sasaki AT. GTP metabolic reprogramming by IMPDH2: unlocking cancer cells' fuelling mechanism. J Biochem. 2020;168(4):319–28.
16. Bowne SJ, Sullivan LS, Mortimer SE, Hedstrom L, Zhu J, Spellicy CJ, Gire AI, Hughbanks-Wheaton D, Birch DG, Lewis RA, Heckenlively JR, Daiger SP. Spectrum and frequency of mutations in IMPDH1 associated with autosomal dominant retinitis pigmentosa and Leber bongenital amaurosis. Invest Ophthalmol Vis Sci. 2006;47(1):34–42.
17. Kennan A, Aherne A, Palfi A, Humphries M, McKee A, Stitt A, Simpson DA, Demtroder K, Orntoft T, Ayuso C, Kenna PF, Farrar GJ, Humphries P. Identification of an IMPDH1 mutation in autosomal dominant retinitis pigmentosa (RP10) revealed following comparative microarray analysis of transcripts derived from retinas of wild-type and Rho–/– mice. Hum Mol Genet. 2002;11(5):547–58.
18. Bowne SJ, Sullivan LS, Blanton SH, Cepko CL, Blackshaw S, Birch DG, Hughbanks-Wheaton D, Heckenlively JR, Daiger SP. Mutations in the inosine monophosphate dehydrogenase 1 gene (IMPDH1) cause the RP10 form of autosomal dominant retinitis pigmentosa. Hum Mol Genet. 2002;11(5):559–68.
19. Naffouje R, Grover P, Yu H, Sendilnathan A, Wolfe K, Majd N, Smith EP, Takeuchi K, Senda T, Kofuji S, Sasaki AT. Anti-tumor potential of IMP dehydrogenase inhibitors: a century-long story. Cancers. 2009;11(9):1346.
20. Sasaki AT. Dynamic role of the GTP energy metabolism in cancers. Keio J Med. 2016;65(1):21.
21. Ryll T, Wagner R. Improved ion-pair high-performance liquid chromatographic method for the quantification of a wide variety of nucleotides and sugar—nucleotides in animal cells. J Chromatogr B Biomed Sci Appl. 1991;570(1):77–88.
22. Strezsak SR, Beuning PJ, Skizim NJ. Versatile separation of nucleotides from bacterial cell lysates using strong anion exchange chromatography. J Chromatogr B. 2022;1188:123044.

23. Kochanowski N, Blanchard F, Cacan R, Chirat F, Guedon E, Marc A, Goergen JL. Intracellular nucleotide and nucleotide sugar contents of cultured CHO cells determined by a fast, sensitive, and high-resolution ion-pair RP-HPLC. Anal Biochem. 2006;348(2):243–51.
24. Matsuda S, Kasahara T. Simultaneous and absolute quantification of nucleoside triphosphates using liquid chromatography–triple quadrupole tandem mass spectrometry. Genes Environ. 2018;40(1):1–9.
25. Cordell RL, Hill SJ, Ortori CA, Barrett DA. Quantitative profiling of nucleotides and related phosphate-containing metabolites in cultured mammalian cells by liquid chromatography tandem electrospray mass spectrometry. J Chromatogr B Analyt Technol Biomed Life Sci. 2008;871(1):115–24.
26. He L, Wei X, Ma X, Yin X, Song M, Donninger H, Yaddanapudi K, McClain CJ, Zhang X. Simultaneous quantification of nucleosides and nucleotides from biological samples. J Am Soc Mass Spectrom. 2019;30(6):987–1000.
27. Liu CC, Huang JS, Tyrrell DLJ, Dovichi NJ. Capillary electrophoresis-electrospray-mass spectrometry of nucleosides and nucleotides: application to phosphorylation studies of anti-human immunodeficiency virus nucleosides in a human hepatoma cell line. Electrophoresis. 2005;26(7–8):1424–31.
28. Mičová K, Friedecký D, Adam T. Mass spectrometry for the sensitive analysis of intracellular nucleotides and analogues. Mass Spectrometry, InTech, 2017. Available from: https://doi.org/10.5772/65165.
29. Friedecký D, Tomková J, Maier V, Janoštḱová A, Procházka M, Adam T. Capillary electrophoretic method for nucleotide analysis in cells: application on inherited metabolic disorders. Electrophoresis. 2007;28(3):373–80.
30. Zhang W, Guled F, Hankemeier T, Ramautar R. Profiling nucleotides in low numbers of mammalian cells by sheathless CE–MS in positive ion mode: circumventing corona discharge. Electrophoresis. 2020;41(5–6):360–9.
31. Soga T, Ohashi Y, Ueno Y, Naraoka H, Tomita M, Nishioka T. Quantitative metabolome analysis using capillary electrophoresis mass spectrometry. J Proteome Res. 2003;2(5):488–94.
32. Hirayama A, Wakayama M, Soga T. Metabolome analysis based on capillary electrophoresis-mass spectrometry. TrAC, Trends Anal Chem. 2014;61:215–22.
33. Rowena Monton MN, Soga T. Metabolome analysis by capillary electrophoresis-mass spectrometry. J Chromatogr A. 2007;1168:237–46.
34. Soga T. Capillary electrophoresis-mass spectrometry for metabolomics. Methods Mol Biol. 2007;358:129–37.
35. Fang W, Liu C, Yu F, Liu Y, Li Z, Chen L, Bao X, Tu T. Macroscopic and fluorescent discrimination of adenosine triphosphate via selective metallo-hydrogel formation: a visual, practical, and reliable rehearsal toward cellular imaging. ACS Appl Mater Interfaces. 2016;8(32):20583–90.
36. Jun YW, Sarkar S, Kim KH, Ahn KH. Molecular probes for fluorescence imaging of ATP in cells and tissues. ChemPhotoChem. 2019;3(5):214–9.
37. Zheng D, Seferos DS, Giljohann DA, Patel PC, Mirkin CA. Aptamer nano-flares for molecular detection in living cells. Nano Lett. 2009;9(9):3258–61.
38. Bianchi-Smiraglia A, Nikiforov MA. Assessment of intracellular GTP levels using genetically encoded fluorescent sensors. Methods Mol Biol. 2022;2:163–9.
39. Wang Y, Tang L, Li Z, Lin Y, Li J. In situ simultaneous monitoring of ATP and GTP using a graphene oxide nanosheet–based sensing platform in living cells. Nat Protoc. 2014;9:1944–55.
40. Ratajczak K, Lukasiak A, Grel H, Dworakowska B, Jakiela S, Stobiecka M. Monitoring of dynamic ATP level changes by oligomycin-modulated ATP synthase inhibition in SW480 cancer cells using fluorescent "on-off" switching DNA aptamer. Anal Bioanal Chem. 2019;411:6899–911.
41. Ratajczak K, Stobiecka M. DNA Aptamer beacon probe (ABP) for monitoring of adenosine triphosphate level in SW480 cancer cells treated with glycolysis inhibitor 2-deoxyglucose. Int J Mol Sci. 2023;24:9295.
42. Kopra K, van Adrichem AJ, Salo-Ahen O, Peltonen J, Wennerberg K, Härmä H. High-throughput dual screening method for Ras activities and inhibitors. Anal Chem. 2017;89(8):4508–16.
43. Kopra K, Rozwandowicz-Jansen A, Syrjänpää M, Blaževitš O, Ligabue A, Veltel S, Lamminmäki U, Abankwa D, Härmä H. GTP-specific Fab fragment-based GTPase activity assay. Anal Chem. 2015;87(6):3527–34.
44. Witte C-P, Herde M. Nucleotide metabolism in plants. Plant Physiol. 2020;182(1):63–78.
45. Moffatt BA, Ashihara H. Purine and pyrimidine nucleotide synthesis and metabolism. The Arabidopsis Book / American Society of Plant Biologists. 2002;1:e0018
46. Frutiger A, Tanno A, Hwu S, Tiefenauer RF, Vörös J, Nakatsuka N. Nonspecific binding - fundamental concepts and consequences for biosensing applications. Chem Rev. 2021;121(13):8095–160.
47. Kopra K, Ligabue A, Wang Q, Syrjänpää M, Blaževitš O, Veltel S, van Adrichem AJ, Hänninen P, Abankwa D, Härmä H. A homogeneous quenching resonance energy transfer assay for the kinetic analysis of the GTPase nucleotide exchange reaction. Anal Bioanal Chem. 2014;406(17):4147–56.
48. Kopra K, Vuorinen E, Abreu-Blanco M, Wang Q, Eskonen V, Gillette W, Pulliainen AT, Holderfield M, Härmä H. Homogeneous dual-parametric-coupled assay for simultaneous nucleotide exchange and KRAS/RAF-RBD interaction monitoring. Anal Chem. 2020;92:4971–79.
49. Syrjänpää M, Vuorinen E, Kulmala S, Wang Q, Härmä H, Kopra K. QTR-FRET: Efficient background reduction technology in time-resolved Förster resonance energy transfer assays. Anal Chim Acta. 2019;1092:93–101.
50. Soga T, Igarash K, Ito C, Mizobuchi K, Zimmermann HP, Tomita M. Metabolomic profiling of anionic metabolites by capillary electrophoresis mass spectrometry. Anal Chem. 2009;81(15):6165–74.
51. Tabata S, Yamamoto M, Goto H, Hirayama A, Ohishi M, Kuramoto T, Mitsuhashi A, Ikeda R, Haraguchi M, Kawahara K, Shinsato Y. Thymidine catabolism as a metabolic strategy for cancer survival. Cell Rep. 2017;19(7):1313–21.
52. Soga T, Baran R, Suematsu M, Ueno Y, Ikeda S, Sakurakawa T, Kakazu Y, Ishikawa T, Robert M, Nishioka T, Tomita M. Differential metabolomics reveals ophthalmic acid as an oxidative stress biomarker indicating hepatic glutathione consumption. J Biol Chem. 2006;281(24):16768–76.
53. Sugimoto M, Wong DT, Hirayama A, Soga T, Tomita M. Capillary electrophoresis mass spectrometry-based saliva metabolomics identified oral, breast and pancreatic cancer-specific profiles. Metabolomics. 2010;6:78–95.
54. Shryock JC, Rubio R, Berne RM. Extraction of adenine nucleotides from cultured endothelial cells. Anal Biochem. 1986;159(1):73–81.
55. Beltran A, Suarez M, Rodríguez MA, Vinaixa M, Samino S, Arola L, Correig X, Yanes O. Assessment of compatibility between extraction methods for NMR- and LC/MS-based metabolomics. Anal Chem. 2012;84(14):5838–44.
56. Römisch-Margl W, Prehn C, Bogumil R, Röhring C, Suhre K, Adamski J. Procedure for tissue sample preparation and metabolite extraction for high-throughput targeted metabolomics. Metabolomics. 2012;8(1):133–42.
57. Kofuji S, Hirayama A, Eberhardt AO, Kawaguchi R, Sugiura Y, Sampetrean O, Ikeda Y, Warren M, Sakamoto N, Kitahara S, Yoshino H, Yamashita D, Sumita K, Wolfe K, Lange L, Ikeda S,

Shimada H, Minami N, Malhotra A, Morioka S, Ban Y, Asano M, Flanary VL, Ramkissoon A, Sasaki AT. IMP dehydrogenase-2 drives aberrant nucleolar activity and promotes tumorigenesis in glioblastoma. Nat Cell Biol. 2019;21(8):1003–14.
58. Hirayama A, Kami K, Sugimoto M, Sugawara M, Toki N, Onozuka H, Kinoshita T, Saito N, Ochiai A, Tomita M, Esumi H, Soga T. Quantitative metabolome profiling of colon and stomach cancer microenvironment by capillary electrophoresis time-of-flight mass spectrometry. Cancer Res. 2009;69(11):4918–25.
59. Soga T, Heiger DN. Amino acid analysis by capillary electrophoresis electrospray ionization mass spectrometry. Anal Chem. 2000;72(6):1236–41.
60. Ishii N, Nakahigashi K, Baba T, Robert M, Soga T, Kanai A, Hirasawa T, Naba M, Hirai K, Hoque A, Ho PY, Kakazu Y, Sugawara K, Igarashi S, Harada S, Masuda T, Sugiyama N, Togashi T, Hasegawa M, Takai Y, Yugi K, Arakawa K, Iwata N, Toya Y, Nakayama Y, Nishioka T, Shimizu K, Mori H, Tomita M. Multiple high-throughput analyses monitor the response of E. coli to perturbations. Science. 2007;316(5824):593–7.
61. Soga T, Ueno Y, Naraoka H, Ohashi Y, Tomita M, Nishioka T. Simultaneous determination of anionic intermediates for bacillus subtilis metabolic pathways by capillary electrophoresis electrospray ionization mass spectrometry. Anal Chem. 2002;74(10):2233–9.
62. Ser Z, Liu X, Tang NN, Locasale JW. Extraction parameters for metabolomics from cultured cells. Anal Biochem. 2015;475:22–8.

Kopra, K., Valtonen, S., Mahran, R., Kapp, J. N., Hassan, N., Gillette, W., Dennis, B.; Li, L.; Westover, K.D.; Plückthun, A. & Härmä, H. (2022)
Thermal Shift Assay for Small GTPase Stability Screening: Evaluation and Suitability. International
Journal of molecular sciences 23:7095.

II

International Journal of
Molecular Sciences

MDPI

Article

Thermal Shift Assay for Small GTPase Stability Screening: Evaluation and Suitability

Kari Kopra [1,*], Salla Valtonen [1], Randa Mahran [1], Jonas N. Kapp [2], Nazia Hassan [1], William Gillette [3], Bryce Dennis [4], Lianbo Li [4], Kenneth D. Westover [4], Andreas Plückthun [2] and Harri Härmä [1]

[1] Department of Chemistry, University of Turku, Henrikinkatu 2, 20500 Turku, Finland; sallamaria.valtonen@gmail.com (S.V.); randa.r.mahran@utu.fi (R.M.); nazia.n.hassan@utu.fi (N.H.); harri.harma@utu.fi (H.H.)
[2] Department of Biochemistry, University of Zurich, Winterthurerstrasse 190, 8057 Zurich, Switzerland; j.kapp@bioc.uzh.ch (J.N.K.); plueckthun@bioc.uzh.ch (A.P.)
[3] Leidos Biomedical Research, Inc., Frederick National Laboratory for Cancer Research, 8560 Progress Dr., Frederick, MD 21702, USA; gillettew@mail.nih.gov
[4] Departments of Biochemistry and Radiation Oncology, University of Texas Southwestern Medical Center at Dallas, 5323 Harry Hines Blvd, L4.270, Dallas, TX 75390, USA; brycedennis@gmail.com (B.D.); lianbo.li@utsouthwestern.edu (L.L.); kenneth.westover@utsouthwestern.edu (K.D.W.)
* Correspondence: kari.kopra@utu.fi; Tel.: +358-456339259

Abstract: Thermal unfolding methods are commonly used as a predictive technique by tracking the protein's physical properties. Inherent protein thermal stability and unfolding profiles of biotherapeutics can help to screen or study potential drugs and to find stabilizing or destabilizing conditions. Differential scanning calorimetry (DSC) is a 'Gold Standard' for thermal stability assays (TSA), but there are also a multitude of other methodologies, such as differential scanning fluorimetry (DSF). The use of an external probe increases the assay throughput, making it more suitable for screening studies, but the current methodologies suffer from relatively low sensitivity. While DSF is an effective tool for screening, interpretation and comparison of the results is often complicated. To overcome these challenges, we compared three thermal stability probes in small GTPase stability studies: SYPRO Orange, 8-anilino-1-naphthalenesulfonic acid (ANS), and the Protein-Probe. We studied mainly KRAS, as a proof of principle to obtain biochemical knowledge through TSA profiles. We showed that the Protein-Probe can work at lower concentration than the other dyes, and its sensitivity enables effective studies with non-covalent and covalent drugs at the nanomolar level. Using examples, we describe the parameters, which must be taken into account when characterizing the effect of drug candidates, of both small molecules and Designed Ankyrin Repeat Proteins.

Keywords: differential scanning fluorimetry (DSF); thermal stability assay (TSA); GTPase; KRAS; Protein-Probe; SYPRO Orange

Citation: Kopra, K.; Valtonen, S.; Mahran, R.; Kapp, J.N.; Hassan, N.; Gillette, W.; Dennis, B.; Li, L.; Westover, K.D.; Plückthun, A.; et al. Thermal Shift Assay for Small GTPase Stability Screening: Evaluation and Suitability. *Int. J. Mol. Sci.* **2022**, *23*, 7095. https://doi.org/10.3390/ijms23137095

Academic Editor: Francisco Ciruela

Received: 19 May 2022
Accepted: 22 June 2022
Published: 26 June 2022

1. Introduction

In recent years, thermal shift assays (TSAs) have become a popular tool, especially for early drug screening and development, but also for determining optimal buffer compositions [1–3]. Differential scanning calorimetry (DSC), the TSA 'Gold Standard', has limited potential for these higher throughput purposes, and thus other biophysical techniques, such as differential scanning fluorimetry (DSF), have become increasingly practical and popular options [3–5]. DSF offers a cost-effective alternative, as it can be performed in parallel; DSC experiments are typically run sequentially. DSC is considered to be the most precise method for protein unfolding measurements and can in some cases lead to the direct measurement of thermodynamic parameters (ΔH, $T\Delta S$, ΔG) in addition to melting temperature (T_m). These factors are outweighed by the benefit afforded by a higher throughput method such as DSF [4,6,7]. Another consideration is that T_m values may vary between approaches [3,4].

Within the DSF technique, scan rate and dye selection affect the accuracy and values gathered. There is limited knowledge regarding the exact mechanisms of how each dye interacts with the target protein, and thus the suitability of each DSF dye also varies from case to case [2,4,8–10]. There are several types of external fluorescent DSF dyes that function through different mechanisms, and they are often used for different types of applications. Rotational dyes sense the viscosity changes in their vicinity and produce higher signals when the environment becomes more viscous. [2,11]. Thus, these dyes, e.g., Proteostat® and thioflavin T, are most often used to monitor aggregation but also surfactant and other buffer composition-related aspects [2,11,12]. On the other hand, environmental polarity sensing dyes, e.g., SYPRO Orange and 8-anilino-1-naphthalenesulfonic acid (ANS), are useful for protein thermal stability and interaction monitoring. These dyes are quenched in an aqueous environment, but upon protein denaturation, where the inner hydrophobic amino acids are exposed, the non-polar binding environment intensifies the fluorescence of these dyes [2,4,12]. Unlike rotational dyes, which are used for fibrillation and aggregation monitoring, polarity-sensing dyes have broader applicability [2,4,13]. These dyes can detect aggregation but are mainly used for protein thermal stability monitoring. SYPRO Orange, in particular, has gained popularity, as it is directly compatible with most common qPCR equipment [1,2,4].

While the robustness of DSF enables broad applicability in drug discovery, there are some limitations related to this technique. One comes from the non-specific nature of the extrinsic DSF dyes, which mainly utilize weak non-covalent interactions for binding to their target [1–4,8]. However, by monitoring the intrinsic tryptophan fluorescence at 330 nm and 350 nm, the use of extrinsic dyes can be overcome. This technique enables not only the detection of protein unfolding, but also the refolding, which is not usually measurable using conventional DSF [2,14,15]. In addition, denaturation monitoring from red-shifted tryptophan fluorescence is more compatible with detergents compared to extrinsic dyes like SYPRO Orange [2,16,17]. However, tryptophan is a relatively rare amino acid and can vary in number and position from protein to protein. In addition, fluorescence at low wavelengths (250–350 nm), as with tryptophan or ANS, is subject to background fluorescence noise related to assay materials or experimental compounds [18]. Thus, the dye selection and knowledge about assayed materials has become even more important. Careful attention to these details might alleviate problems related to the thermal profile and reduce the occurrence of incorrect conclusions by lowering background fluorescence.

We previously developed a novel DSF-like method called the Protein-Probe [19–22]. The method is based on a Eu^{3+}-labeled peptide probe, where a negatively charged peptide has minimal interaction with a folded protein, and the time-resolved luminescence (TRL) signal is low in the modulation solution containing a cyanine dye as quencher. The TRL signal increases upon unfolding of the protein because of an increased interaction of the hydrophobic core with the peptide and greater distance of the Eu^{3+}-label from the quencher. This technique can avoid many of the problems related to conventional DSF dyes. The Protein-Probe enables similar stability, interaction, and buffer solution composition studies as conventional external thermal dyes, but with significantly improved sensitivity [19–22]. In addition, we have extensively studied KRAS and other GTPase proteins to enable monitoring of their functional properties [23–26]. KRAS has gained high interest as a drug target, and multiple inhibitors applicable as tool compounds have been developed. Due to the enzymatic nature of KRAS, it is a structurally flexible protein [27–29]. Activating mutations in all RAS proteins are clustered around the nucleotide binding pocket, at amino acids 12, 13, 61, 117, and 146. The hotspot mutation positions of G12 and G13 are located on the P-loop, have a nucleotide-stabilizing role, and in the case of G13, a significant effect on RAS activity [25,30]. On the other hand, Q61, located at the switch II region, participates in the conformational changes crucial for RAS inactivation, having the lowest hydrolysis rates among all KRAS alleles [25,30]. Lately, KRAS G12C has been in the spotlight and KRAS G12C-targeted molecules have been developed as potential cancer treatments [31–33].

Thus we selected the KRAS of other GTPase proteins as our models to address how point mutations, protein and nucleotide concentration, buffer components, and inhibitors affect target protein stability. Here, we show that the improved sensitivity of the Protein-Probe method allows more differentiating studies of KRAS mutants, in comparison to existing TSA dyes. We also highlight the potential problems and shortcomings of DSF approaches, which emphasize the need for careful assay optimization and the significance of small details in data collection, interpretation, and comparison.

2. Results and Discussion

2.1. Thermal Stability Is Buffer and Target GTPase Concentration Dependent

DSF is a widely used technique due to its simplicity. However, results obtained in various studies are rarely comparable, even when the assays use the same DSF probe, usually SYPRO Orange. Previously, we demonstrated a new and highly sensitive method for TSA, the Protein-Probe technique. The Protein-Probe senses the protein stability and factors affecting its stability, but with significantly improved sensitivity compared to dyes like SYPRO Orange [19,20]. Partly due to improved sensitivity, we found it nearly impossible to evaluate and compare it with previously published results. Nevertheless, by using KRAS and other GTPases as model systems, we were able to address critical factors that were not clearly addressed in previous publications. Mutation positions of the studied KRAS constructs are marked in Figure S1.

It is widely known that buffer composition drastically affects protein stability. This is especially true with proteins like KRAS, in which Mg^{2+} maintains the protein in its stable nucleotide-bound form. Thus, we first studied the KRAS WT thermal stability in the presence or absence of $MgCl_2$ and the effect of EDTA as a chelating agent (Figure 1A, Table S1). With 1 mM Mg^{2+}, KRAS WT showed the expected stability (T_m = 60.1 ± 0.3 °C) within the broad range of previously reported values (53.3–74.4 °C) [34–37]. Next, we repeated the assay with 10 mM $MgCl_2$ and observed a further KRAS-stabilizing effect (T_m = 64.7 ± 0.5 °C). EDTA addition resulted in no change to observed T_m values with KRAS WT in comparison to the assay performed without $MgCl_2$. In both cases, T_m values of 48.9 ± 0.4 °C and 49.2 ± 0.4 °C were significantly lower in comparison to those detected with $MgCl_2$ (Figure 1A).

Next, we tested if the same was true for the KRAS mutants G13D and Q61R and if assays could be performed with or without 1 mM $MgCl_2$, referring to nucleotide-loaded and nucleotide-free KRAS, respectively (Figure 1B, Table S1). These mutants were selected, as G13D is known to have an exceptionally fast intrinsic nucleotide exchange rate, while the intrinsic exchange of Q61R is very low [25,27,30,38]. The observed thermal stability inversely correlated with the rate of intrinsic nucleotide exchange, as the fast exchange G13D (T_m = 47.7 ± 0.4 °C) showed lower stability, and the slow exchange Q61R (T_m = 66.5 ± 0.5 °C) displayed higher stability compared to the KRAS WT in the same conditions (Figure 1B). While we observed similar T_m for G13D without Mg^{2+} and with EDTA (T_m = 43.4 ± 0.6 °C and 43.6 ± 0.8 °C), we observed a pronounced difference between Mg^{2+} and EDTA for Q61R (T_m = 59.2 ± 0.7 °C and 50.6 ± 1.0 °C). Clearly, Q61R needed an additional 1 mM EDTA to reach the partially nucleotide-free state. These results indicate a clear link between KRAS thermal stability and the intrinsic nucleotide exchange related to Mg^{2+} binding.

We tested this hypothesis with other KRAS hotspot mutants, G12D, G12C, and Q61L, in the presence of 1 mM $MgCl_2$ (Figure S1). All of these displayed similar thermal stability as KRAS WT and thus were between the stability of G13D and Q61R (Figure 1C, Table S1). These mutants are reported to have a similar rate of intrinsic nucleotide exchange activity as KRAS WT; this suggests that the intrinsic nucleotide exchange activity linked to Mg^{2+} coordination might be the main factor determining thermal stability [27]. Thus, the Mg^{2+} concentration, even when present in great excess, used in each assay might cause significant variations in T_m values reported.

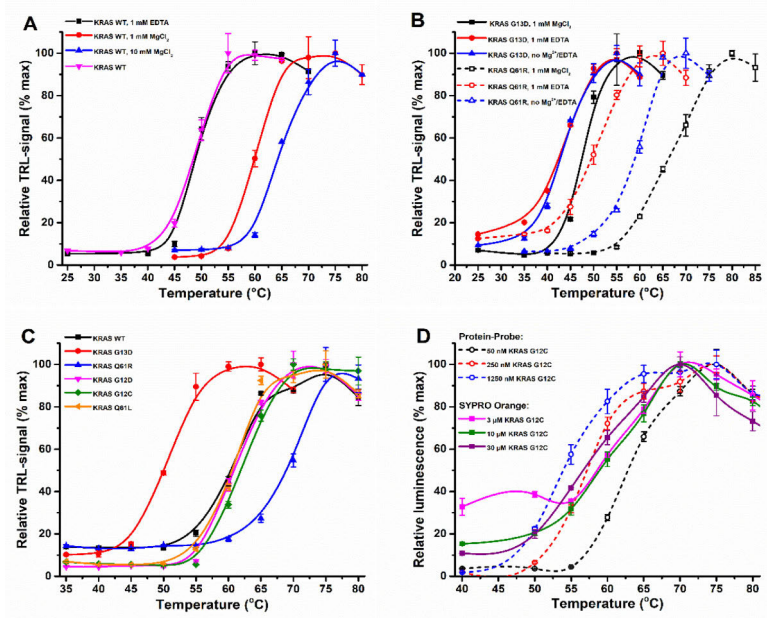

Figure 1. Buffer, mutational status, and concentration effects on KRAS thermal stability. (**A**) KRAS WT (100 nM) showed clear $MgCl_2$-dependent thermal stabilization when assayed using the Protein-Probe. The presence of 1 (red) or 10 mM (blue) $MgCl_2$ increased KRAS WT thermal stability by approximately 10 °C over that without $MgCl_2$ (black) and with additional 1 mM EDTA (magenta). (**B**) KRAS (100 nM) mutational status affects the $MgCl_2$ dependence. KRAS G13D (solid line) and Q61R (dashed line) responded differently in the absence of $MgCl_2$ (blue) or presence of 1 mM $MgCl_2$ (black) or 1 mM EDTA (red). While KRAS G13D is thermally unstable in all conditions, Q61R showed significantly compromised stability in the presence of 1 mM EDTA. (**C**) KRAS (50 nM) thermal stability is dependent on its mutational status. From the hotspot KRAS mutants tested, G13D (red) and Q61R (blue) significantly differ from the other tested KRAS proteins: WT (black), G12D (magenta), G12C (green), and Q61L (orange). (**D**) Increase in KRAS G12C concentration decreased its stability in Protein-Probe (dashed line) and SYPRO Orange (solid line) assays. Using the Protein-Probe, a significant decrease in KRAS G12C thermal stability was obtained when protein concentration was increased from 50 nM (black) to 250 nM (red) or 1250 nM (blue). Using the SYPRO Orange, the decrease in KRAS G12C T_m was less pronounced at the assayed concentrations of 3 µM (magenta), 10 µM (green) or 30 µM (violet). Data represent mean ± SD (n = 3).

The assays of KRAS mutants were performed at a lower protein concentration than that used in the $MgCl_2$ assays (Figure 1A), and we saw a slight shift in T_m values when these two assays were compared. When the results obtained with the Protein-Probe were further compared to those with SYPRO Orange, we saw consistently slightly higher T_m values using the Protein-Probe. As in these assays, the KRAS concentration was the main determinant for these changes; we titrated KRAS G12C using the Protein-Probe (0.01–1.25 µM) and SYPRO Orange (1–30 µM). The concentration-related shift in T_m was observed with SYPRO Orange (55.7–60.3 °C) but especially with the Protein-Probe (Figures 1D and S2A). When the KRAS G12C concentration was increased 25-fold, from 50 to 1250 nM, T_m values shifted from 61.8 ± 0.5 °C to 53.4 ± 0.6 °C, respectively. We confirmed this result using the Protein-Probe with the Q61R and Q61L mutants, and in these cases the thermal stability decreased by 11.3 °C and 11.8 °C upon KRAS concentration increase from 50 to 1250 nM, respectively (data not shown). These results indicate that care should be taken when comparing T_m values from different studies.

When testing various RAS constructs, we found that the sensitivity of the Protein-Probe is related to the exact type of KRAS construct. Even though KRAS is a small protein, it is often studied using only the so-called G-domain, a truncated form that does not contain the *C*-terminal hypervariable region of residues 170–188. Two G-domain constructs were assessed here using Ac-KRAS and iMet-KRAS [39]. In Ac-KRAS, the *N*-terminal initiator methionine (iMet) was cleaved off, and threonine was *N*-acetylated. On the other hand, iMet-KRAS contained an additional non-native glycine as the second amino acid in its *N*-terminus. With the Protein-Probe, 50-fold (Ac-KRAS) and 10-fold (iMet-KRAS) higher concentrations were needed for comparable signal strength to full-length KRAS (Figure S2B). However, not only the length but also *N*-terminal processing affected the detectability, as there is a clear difference between Ac-KRAS and iMet-KRAS (Figure S2B). This indicates the increase in flexibility of iMet-KRAS in comparison to Ac-KRAS, even though there is no clear difference in T_m values, suggesting no changes in nucleotide and Mg^{2+} coordination [39]. In addition, the assays performed with the full-length HRAS and NRAS indicate that the size of the construct is not the main determinant of protein detectability using the Protein-Probe, as both of these constructs were less visible compared to full-length KRAS. Interestingly, the T_m values were all higher in comparison to KRAS (54.4 $\pm$ 0.6 °C) when assayed at the same conditions using 1 μM KRAS concentration. Detected values for iMet-KRAS, Ac-KRAS, HRAS, and NRAS were 66.9 $\pm$ 0.2, 66.0 $\pm$ 1.0, 59.0 $\pm$ 0.3, and 64.0 $\pm$ 0.1 °C, respectively (Table S1).

In conclusion, not only the length of the RAS construct but also mutations and flexibility might affect protein detectability, especially at nM concentrations. SYPRO Orange could not be used at nM KRAS concentrations, but its optimal signal-to-background (S/B) ratio was found at the very high KRAS concentration of 10 μM (data not shown). In addition, the second dye tested, 8-anilinonaphthalene-1-sulfonic acid (ANS), requires KRAS concentration levels of 2–10 μM. With μM KRAS used in SYPRO Orange and ANS assays, the relatively high concentration seems to equalize differences, which were visible using the Protein-Probe assays at nM concentrations.

2.2. Increased Nucleotide Concentration Increases GTPase Stability

Many of the commercially available GTPases are stored in buffers with an excess of GDP to increase their stability. In addition, an excess of GMP (guanosine-5′-monophosphate) is often used to thermally and enzymatically stabilize the nucleotide-free form of RAS, as its effect on biochemical RAS activity assays can be considered negligible due to the low binding affinity of GMP [40]. Results obtained with or without Mg^{2+} indicate that the stabilizing effect is mediated through intrinsic nucleotide exchange or through Mg^{2+}-independent nucleotide binding, occurring with lowered affinity [41–43]. These processes have been reported to be linked but to occur with different rates, as Mg^{2+} is in very rapid equilibrium with the solvent. Processes are also found to vary between different GTPases and their mutants, and the degree to which stabilization occurs should vary as well [41–43].

To test this, we first performed a GDP (guanosine-5′-diphosphate) titration (0–0.9 mM) using KRAS G13D, a highly unstable mutant due to A59 placement in the Mg^{2+} binding site (Figure 2A) [27,44]. As anticipated, a significant increase in KRAS G13D stability was observed with the Protein-Probe as a response to increased GDP concentration, saturating at approximately 300 μM GDP. We confirmed this stability increase with SYPRO Orange using the minimally possible KRAS concentration for this assay (3 μM), but the saturation could not be reached with the used concentrations (Figure S3). The control (1 mM ATP) showed no KRAS G13D stabilization. As the stability increase was saturated in the Protein-Probe assay, the intrinsic nucleotide exchange or another factor affecting nucleotide binding was most likely responsible. The high nucleotide concentration in solution and the high nucleotide binding affinity of KRAS together change the equilibrium and drive RAS to stay constantly in a nucleotide-loaded and thus stable form. As the stabilization is RAS concentration-dependent, with the used nucleotide concentrations, it was detected only with the Protein-Probe, using 50 nM KRAS.

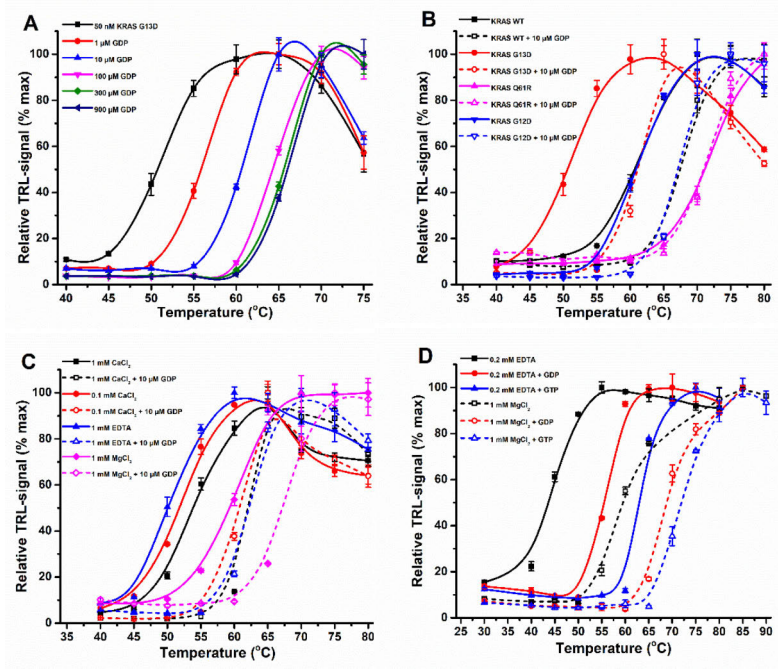

Figure 2. KRAS and other small GTPases were stabilized by GDP/GTP in the Protein-Probe assay. (**A**) KRAS G13D (50 nM) stability was determined in the presence of free GDP (0–900 μM). KRAS G13D (black) was significantly thermally stabilized with 1 μM GDP (red). GDP-induced stabilization of KRAS G13D further increased with 10 (blue) and 100 μM (magenta) GDP and was saturated at approximately 300 μM (green) concentration, without further change with 900 μM GDP (navy). (**B**) KRAS (50 nM) thermal stabilization in the absence (solid line) or presence (dashed line) of additional GDP (10 μM) was dependent on its mutational status. KRAS G13D (red) was more responsive to GDP addition in comparison to KRAS WT (black) or G12D (blue). KRAS Q61R (magenta) was not stabilized by the addition of GDP. (**C**) GDP-induced KRAS WT (50 nM) stabilization was not dependent on divalent cations. Both 0.1 (red) and 1 mM (black) Ca^{2+} stabilized KRAS, but to a lesser extent than 1 mM Mg^{2+} (magenta), when compared to KRAS with 1 mM EDTA (blue). In all buffers, 10 μM GDP (dashed line) addition stabilized KRAS in comparison to buffer without additional nucleotide (solid line). (**D**) RhoA WT (2 μM) nucleotide-specific stabilization was more significant in the presence of 0.2 mM EDTA (solid) than with 1 mM Mg^{2+} (dashed). RhoA (black) stability increased significantly more with 100 μM GTP (blue) than GDP (red). Difference in GTP preferred stability increase was more significant in the absence of Mg^{2+}. Data represent mean ± SD (n = 3).

To further test nucleotide-induced KRAS stabilization, we next performed single or dual (10 or 100 μM) concentration stability assays using GDP, GTP (guanosine-5′-triphosphate), and ATP (adenosine-5′-triphosphate). Assays were performed not only with the G13D mutant but also several other KRAS mutants. With KRAS G13D, the addition of 10 μM GDP shifted the observed T_m value by over 10 °C, which was more than with KRAS WT or G12D (Figure 2B, Table S1). More significantly, no change in T_m was observed with Q61R. These stabilizing concentrations of GDP are several-fold higher compared to the reported affinity to KRAS, which indicates stabilization potentially in a Mg^{2+}-independent fashion. Indeed, GDP stabilized KRAS WT both in the presence and absence of Mg^{2+}, and the effect was more pronounced in the presence of 1 mM EDTA, resulting in a ΔT_m of 11.3 °C compared with a ΔT_m of only 7.6 °C in 1 mM $MgCl_2$ (Figure 2C, Table S1) [40,43,45]. Another divalent cation, Ca^{2+}, stabilized KRAS WT both with and without GDP [45,46].

When KRAS WT assayed with 1 mM EDTA (T_m 50.8 ± 0.6) was compared to the samples with 0.1 or 1 mM $CaCl_2$ or 1 mM $MgCl_2$, the stability increase was 1.2, 3.7, and 9.1 °C, respectively. On the other hand, GDP addition brought the T_m with both 0.1 and 1 mM Ca^{2+} to the same value, 61.2 ± 0.9 and 61.8 ± 0.6, respectively (Figure 2C). This indicates that Ca^{2+} cannot be used as a replacement for Mg^{2+} but that stability increase is most probably due to an additional weak affinity binding pocket for Ca^{2+} [46,47]. However, the Ca^{2+} binding affinity to this pocket is expected to be biochemically too weak to play a role, especially considering the low Ca^{2+} concentrations in the cytoplasm.

In addition to KRAS, we tested the additional small GTPases NRAS, HRAS, and RhoA, as well as Gαi, an α-subunit from the heterotrimeric G protein, to see if similar behavior in the presence or absence of Mg^{2+} and GDP/GTP occurred. Again, ATP showed no stabilization at any tested condition or protein (data not shown). On the other hand, all the tested small GTPases were stabilized by GDP and GTP both with and without Mg^{2+}, as shown with RhoA and the Protein-Probe technique (Figures 2D and S4). RhoA was significantly more stabilized with GTP than GDP, and the preference further increased in the absence of Mg^{2+}, as also confirmed with SYPRO Orange and ANS dyes (Figure S4) [48]. In the presence of EDTA, NRAS and potentially also HRAS showed preference for GTP over GDP, indicating higher binding affinity of GTP in the absence of Mg^{2+}, but the effect was less pronounced than with RhoA (Figure S4) [40,43,48].

To further confirm that KRAS stability is linked to its intrinsic enzymatic activities and affinity for the nucleotide, we performed an assay with KRAS V14I located in a P-loop [49]. In addition to increased binding to SOS, it also had increased intrinsic nucleotide dissociation properties. As expected, KRAS V14I had a relatively low thermal stability (T_m ~48 °C), and it was stabilized with both nucleotides but showed a clear preference for GTP over GDP (Figure S5A). On the other hand, Gαi showed no clear stabilization with Mg^{2+} (max ΔT_m = 1.0 °C) or without Mg^{2+} (max ΔT_m = 3.3 °C) when 100 μM GDP or GTP was tested (Figure S5B). In addition, the effect of Mg^{2+} with Gαi was lower (~4.2 °C) compared to, e.g., KRAS assayed in the same conditions.

In biochemical and enzymatic studies with KRAS, non-hydrolysable GTP analogs are often used, as GTP-loaded RAS has a limited shelf-life. These analogs, however, have a lower affinity compared to the natural GTP ligand, and they also affect RAS conformation. We hypothesized that the use of different GTP analogs change the KRAS stability differently, which needs to be considered when these results are interpreted. Initially, we performed a nucleotide titration using a SOS^{cat} catalyzed nucleotide exchange assay with KRAS (Figure 3A). The assay was performed with 15 nM KRAS, which limits us in monitoring the binding affinity of the highest affinity nucleotides, GDP (EC_{50} = 11.9 ± 0.7 nM), GTP (EC_{50} = 7.9 ± 0.6 nM), and GTPγS (guanosine-5′-(γ-thio)-triphosphate) (EC_{50} = 11.7 ± 0.8 nM) (Table S2). In contrast, GMP-PNP (guanosine-5′-[(β,γ)-imido]triphosphate), GMP-PCP (guanosine-5′-[(β,γ)-methyleno]triphosphate), and especially GMP had significantly lower affinity for KRAS, with EC_{50} values of 71.2 ± 9.3 nM, 542 ± 38 nM, and 101 ± 8 μM, respectively (Figure 3A, Table S2). Protein-Probe analysis with the same analogs and KRAS WT showed a similar pattern as nucleotide exchange (Figure 3B). The high affinity nucleotides GDP, GTP, and GTPγS stabilized KRAS already at 10 μM concentration, while for GMP-PNP, 300 μM concentration was needed for stabilization. The 300 μM GMP-PCP showed minor effects, but GMP, often used to stabilize the nucleotide-free form of RAS, had no KRAS stabilizing effect even at 1 mM concentration. Because we clearly observed stability increasing effects with GTP analogs in solution, we next loaded KRAS with GMP-PNP, the most widely used GTP analog due to its resistance to hydrolysis. As shown previously, a significantly reduced T_m value, 53.2 ± 0.3, was detected with GMPPNP-loaded KRAS in comparison to GDP-KRAS, 60.4 ± 0.2 (Figure 3C) [20]. Thus, we can conclude that not only assay conditions, but also mutations, activation state, and nucleotides/analogs affect the observed T_m and must be considered when comparing the results obtained using any TSA method.

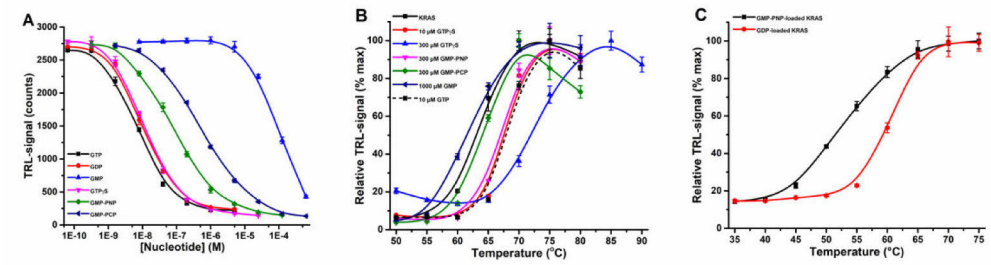

Figure 3. KRAS stabilization by additional nucleotides is affinity dependent. (**A**) The binding affinity order for nucleotide binding to KRAS (15 nM) was determined by QRET nucleotide exchange assay in a SOS^{cat} (10 nM) induced reaction. KRAS binding for GTP (black), GDP (red), and GTPγS (magenta) was <15 nM, while GMP-PNP (green) and GMP-PCP (navy) bound at micromolar and GMP (blue) only at millimolar levels. (**B**) KRAS (50 nM) nucleotide-dependent thermal stabilization was affinity- and concentration-dependent as assayed with the Protein-Probe. KRAS WT (solid black) was similarly stabilized by 10 µM GTP (dashed black) and 10 µM GTPγS (red). At 300 µM concentration, GTPγS (blue) showed the highest stabilization, followed by GMP-PNP (magenta) and GMP-PCP (green). GMP (navy) showed no KRAS stabilization. (**C**) Thermal stability using preloaded KRAS (50 nM) was in agreement with solution-based binding using an excess of nucleotides. KRAS-GDP WT (red) was thermally significantly more stable than KRAS-GMP-PNP WT (black). Data represent mean ± SD (n = 3).

2.3. Small Molecular Covalent Inhibitors Are Overrepresented in TSA over Non-Covalent Inhibitors

TSA is not only used as a tool for protein stability but also for protein–ligand interaction (PLI) studies utilizing the thermal shift that occurs upon binding. KRAS is a high-priority drug target, but the modulation of its functionality has been difficult [50,51]. This is due to the lack of an obvious targetable binding pocket, except for the nucleotide binding one. However, drugging KRAS G12C has shown promise, as this mutant enables covalent intervention by small molecular inhibitors [50,51]. As multiple parameters related to assay conditions might affect RAS stability, we next studied KRAS with multiple known covalent or non-covalent inhibitors to address their function side by side under the same conditions.

Selected inhibitors were first assayed with a conventional nucleotide exchange assay utilizing KRAS WT and its G12C mutant [23,25]. This was done to ensure the correct functionality and concentration range for the inhibitors. Two selected covalent binders, ARS-853 and ARS-1620, were used with KRAS G12C, and a non-covalent inhibitor, BI-2852, with KRAS WT. As a control for both assays, we used the KRAS/SOS interaction inhibitor BAY-293 and the non-binding control BI-2853. All inhibitors were tested in a nucleotide exchange assay using 100 nM KRAS (WT or G12C) and 10 nM SOS^{cat}. Importantly, the individual inhibitors were preincubated with KRAS for 20 min before assay initiation by addition of SOS^{cat}. In the selected conditions, BAY-293 showed KRAS mutation-independent inhibition, with observed IC_{50} values of 11.5 ± 2.2 and 17.5 ± 3.0 nM for WT and G12C, respectively (Figure S6, Table S2). BI-2852, but not BI-2853, inhibited KRAS WT nucleotide exchange with the observed IC_{50} value of 2.8 ± 0.7 µM. ARS-853 and ARS-1620 inhibited KRAS G12C nucleotide exchange, giving IC_{50} values of 1.1 ± 0.1 and 0.21 ± 0.04 µM, respectively (Figure S6, Table S2). Based on these results, all inhibitors showed the expected function at the expected concentration range.

Next, thermal stabilization of KRAS G12C by covalent binders was investigated. As expected, both ARS-853 and ARS-1620 showed a significant concentration-dependent thermal stability increase over KRAS G12C alone (Figure 4A). With 50 nM KRAS G12C, saturated stabilization was observed at 5 µM ARS-853 and ARS-1620. At a concentration of 1.25 µM per compound, two thermal transitions could be observed, corresponding to free and covalently compound occupied KRAS G12C (Figures 4A and S6). We could further

confirm the specificity of ARS-853 and ARS-1620 towards KRAS G12C over WT when using SYPRO Orange (Figure S7). As expected, the SOS binding BAY-293 and the non-binding BI-2853 gave no response, but also with BI-2852 and KRAS G12C, G12D or WT the thermal stability effect was negligible (Figures S6 and S8). ARS-853 and ARS-1620 demonstrated the power of using the more sensitive Protein-Probe technique in comparison to SYPRO Orange, as it enables the estimation of inhibitor binding affinity. Due to the 200-fold lower KRAS G12C concentration in the Protein-Probe assay, 5 μM ARS-853 and ARS-1620 fully saturated the thermal stability increase, giving a ΔT_m of 16 to 18 °C, respectively, while with SYPRO Orange and 10 μM KRAS G12C, 20 μM ARS-853 and ARS-1620 still provided double transitions (Figures 4A and S6).

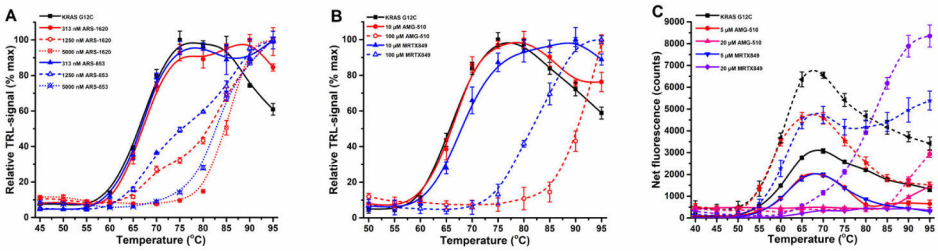

Figure 4. Covalent KRAS G12C inhibitors in the KRAS thermal stability assay. (**A**) 50 nM KRAS G12C (black) was stabilized in a concentration-dependent manner by both ARS-1620 (red) and ARS-853 (blue) inhibitors (313–5000 nM) in the Protein-Probe assay. (**B**) 50 nM KRAS G12C (black) was stabilized in a concentration-dependent manner by AMG-510 (red) and MRTX849 (blue) inhibitors in the Protein-Probe assay. (**C**) 6 μM KRAS G12C (black) was concentration-dependently stabilized by AMG-510 (red scale) and MRTX849 (blue scale) inhibitors in the SYPRO Orange (solid line) and ANS (dashed line) assays. No thermal shift was detected with 5 μM AMG-510, but the second transition was visible with the same concentration of MRTX849. An increase in AMG-510 concentration induced a significant signal quenching of both SYPRO Orange and ANS dyes. Data represent mean ± SD (n = 3).

We further continued the study by using two clinical stage KRAS G12C inhibitors, AMG-510 and MRTX849 [50]. In a nucleotide exchange assay with 15 nM KRAS G12C, both AMG-510 and MRTX849 showed very potent binding, giving IC_{50} values of 20.7 ± 1.2 and 6.9 ± 0.8 nM already after ~10 min incubation (Figure S9, Table S2). Next, we continued by studying KRAS G12C stability with the Protein-Probe (Figure 4B) and with SYPRO Orange and ANS (Figure 4C). With AMG-510, we observed significant signal quenching with ANS or SYPRO Orange, which also was quenched with MRTX849 (Figure 4B). However, this AMG-510-induced signal quenching was non-visible at nM concentrations already producing a maximal thermal stability increase in the Protein-Probe assay (Figure 4C). Even though the affinity for KRAS G12C was higher for MRTX849 than for AMG-510, the thermal stability increase in the Protein-Probe assay with AMG-510 was more pronounced than with MRTX849, giving ΔT_m values of 24.8 vs. 15.6 °C, respectively. The confirmed trend was the same with other dyes, and this is likely due to differences in the binding modes of these molecules, as both target the same KRAS pocket [50,51]. The effect on signal quenching seems to be indicative for binding, as the SYPRO Orange fluorescence was nearly preserved with the KRAS WT (Figure S8B). As the signal quenching does not occur directly through SYPRO Orange and AMG510, we cannot rule out the possibility that instead of quenching, AMG-510 shifts the thermal curve out from the measurement range. In our hands, the reliable measurement range ends at approximately 90 °C, and AMG-510 had a tendency to increase the signal at the high-end temperatures. In all cases, the improved sensitivity of the Protein-Probe avoids the complications faced with AMG-510 (Figure 4).

2.4. Protein Based Inhibitors Can Induce Covalent-Like Thermal Stability Increase

Biologics, typically proteins, are interesting alternatives, especially when the target does not allow the use of small molecule drugs. RAS has been a notoriously difficult target for small molecule drugs due to a lack of defined binding pockets, supporting the use of biologics that provide different modes of action. Thus, we decided to test Designed Ankyrin Repeat Proteins (DARPins). They are highly stable binding molecules selected from diverse synthetic libraries to bind specifically and with high affinity to the target of interest [52]. As they contain no cysteine and can fold in the cytoplasm, they have potential as intracellular inhibitors. For the study, three different DARPins, K27, K13, and K19, were tested to define their protein–protein interaction (PPI) effect on KRAS stability [53,54].

For DARPins K27, K13, and K19, IC_{50} values of 30.6 ± 4.2, 140 ± 23, and 125 ± 16 nM were observed, respectively, in a nucleotide exchange assay (Figure S10, Table S2). Next we utilized this information to monitor the DARPin-induced increase in thermal stability, which we previously reported with K27 and the Protein-Probe method [20]. To our surprise, K13 and K19 had no effect on KRAS thermal stability in any of the tested concentrations, while K27 showed the expected increase in KRAS thermal stability (Figure 5) [20]. K13 and K19 bind to the same position on KRAS, the allosteric lobe at the interface between helix α3/loop 7/helix α4 [54]. This area is distant from the area where K27 binds, namely the switch I area overlapping the SOS binding site [53]. Due to these differences, we continued to monitor the effect on SOS^{cat}-induced and intrinsic nucleotide exchange with these DARPins. All these DARPins blocked the SOS^{cat}-induced reaction (Figure S10), but only K27 also blocked the intrinsic nucleotide exchange activity of KRAS (Figure S11). This indicates that K27 potentially has a more significant effect on the KRAS structure in comparison to K13 and K19, acting mainly by blocking the KRAS interaction with SOS^{cat} [53,54]. By using KRAS WT and K27 as a control, we further tested if K27 would stabilize the G12D, G13D, Q61L, and Q61R mutants. Of these mutants, only KRAS Q61R was not stabilized by K27, further supporting a link between intrinsic KRAS nucleotide exchange activity and thermal stability (Figures 5B and S12).

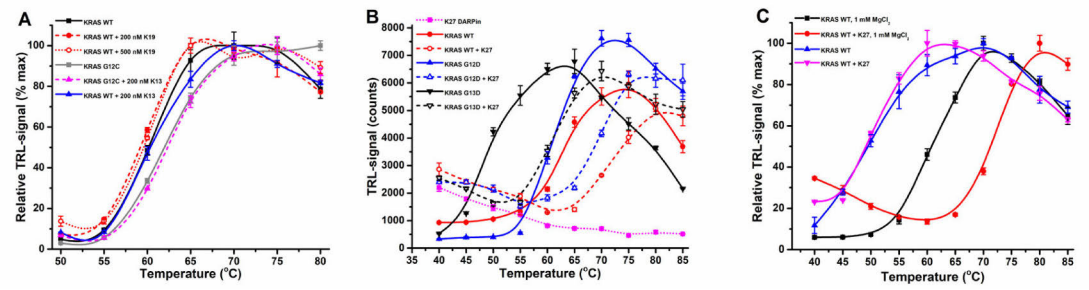

Figure 5. KRAS thermal stabilization by DARPins in the Protein-Probe assay. (**A**) Neither DARPin K13 nor K19 stabilized KRAS WT or G12C (50 nM). K19 (red) did not stabilize KRAS WT (black) at 200 (red dashed) or 500 nM (red dotted). Similarly 200 nM K13 had no effect on KRAS WT (black compared to blue solid lines) or KRAS G12C (gray solid line compared to magenta dashed line). (**B**) DARPin K27 (100 nM) showed a similar degree of stabilization with 50 nM KRAS WT (red), G12D (blue), and G13D (black). DARPin K27 (magenta) was responsible for the signal in the Protein-Probe assay at low temperatures. (**C**) DARPin K27 (100 nM)-induced thermal stabilization of KRAS WT (50 nM) was Mg^{2+}-dependent. In addition, 1 mM $MgCl_2$ stabilized KRAS (black compared to blue) and was also necessary for K27-induced stabilization (red compared to magenta). Data represent mean ± SD (n = 3).

Q61 is part of the Switch II region, which plays an essential role in effector interactions, GAP-mediated and intrinsic GTP hydrolysis, as well as nucleotide binding [38]. Thus, we next tested if the removal of Mg^{2+} has an effect on K27-induced KRAS stabilization. K27 is reported as a GDP-KRAS binder, and without Mg^{2+}, we detected no thermal stability

increase with K27 and KRAS WT (Figure 5C). Additionally, ARS-1620 also required Mg^{2+} to stabilize KRAS G12C (Figure S13). These results indicate that TSA results with KRAS might be biased toward those binders that cover the Switch I and II and/or that have an effect on nucleotide loading state. This is in line with the structural data showing no effect on these areas when KRAS is bound to K19 [54]. Unfortunately, this statement could not be confirmed by other TSA dyes, due to their lack of sensitivity and concentration restrictions. It is unlikely, however, that this finding would be only related to the Protein-Probe assay, but it needs to be considered prior to assay design, as assays run with or without Mg^{2+} are expected to produce differences in results.

2.5. Non-Observable Thermal Shifts Can Be Visualized Using a Competition Thermal Stability Protocol

Thermal stability changes cannot be used to visualize all KRAS binding inhibitors, as found, e.g., for DARPins K13 and K19. The binding area for K13 and K19 is known and their binding can be expected to affect, in turn, the binding of KRAS G12C to covalent inhibitors targeting the switch-II pocket. Therefore, MRTX849, AMG-510, ARS853, and ARS1620 were selected to investigate a competition-based protocol. We hypothesized that upon K13 or K19 binding, the large thermal stability increase induced by these covalent binders will be reduced or disappear, as the DARPin can block the binding of the covalent inhibitor either competitively or by changing the KRAS structure. We first tested this hypothesis by using 1:1 complex of KRAS (50 nM) and K13 (50 nM), and we found this to be true especially with AMG-510 and to lesser extent with MRTX849 (Figure 6). In the presence of K13, 100 nM AMG-510 had no effect on KRAS stability, but it was detected at higher AMG-510 concentrations (Figure 6A). Change from a single thermal transition curve with 900 nM AMG-510 to double transition curves in the presence of K13 is also a clear indication for competitive binding. On the other hand, the ΔT_m was only 3–7.4 °C with MRTX849, in comparison to ΔT_m values over 10 °C monitored with AMG-510 using the same protocol. These changes observed with either AMG-510 or MRTX849 may indicate slight differences in binding and conformational compatibility with the K19 DARPin-bound KRAS. With ARS853 and ARS1620, we also found the affinity-driven effect, and both inhibitors showed competitive behavior (Figure S14). In summary, by using a competitive protocol, one could potentially help to find compounds that target specific pockets on the target protein. However, affinity restrictions set by the TSA method used and chosen binders must be carefully considered.

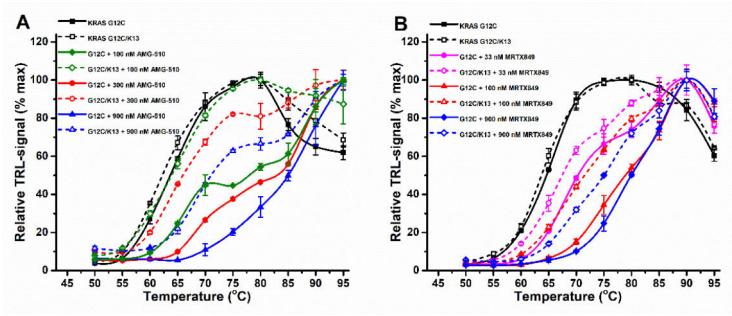

Figure 6. Competitive thermal shift assay for visualizing inhibitors having no direct effect on KRAS thermal stability. (**A**) In the absence of K13 (solid), 50 nM KRAS G12C (black) was significantly stabilized by 100 (green), 300 (red), or 900 nM (blue) AMG-510. In the presence of K13 (dashed), KRAS G12C was not affected, but the stabilizing effect of AMG-510 could be totally or partially reversed. (**B**) In the absence of K13 (solid), 50 nM KRAS G12C (black) was significantly stabilized by 33 (magenta), 100 (red), or 900 nM (blue) MRTX849. In the presence of K13 (dashed), KRAS G12C was not affected, but the stabilizing effect of MRTX849 could be partially reversed. Data represent mean ± SD (n = 3).

3. Materials and Methods

3.1. Protein-Probe Thermal Stability Assays

Detailed lists of materials and instrumentation as well as the production/purification of KRAS and related proteins are presented in the Supplementary Materials. In addition, detailed protocols for RAS nucleotide exchange assays and data analysis are presented there. All presented assays were performed in triplicate unless otherwise indicated.

All Protein-Probe assays were performed using a sample volume of 8 µL and a two-step assay protocol. Detection was performed at room temperature (RT) by adding 65 µL Protein-Probe solution: 4 µM HIDC (1,1,3,3,3′,3′-hexamethylindodicarbocyanine iodide) and 1–1.5 nM Eu^{3+}-labeled peptide probe (NH_2-EYEEEEEVEEEVEEE) [19]. Assays were performed in a sample buffer containing 10 mM HEPES (pH 7.5), 0.001% Triton X-100 and 20 mM NaCl and the buffer was supplemented with 0–10 mM $MgCl_2$, 0–1 mM $CaCl_2$, or 0–1 mM EDTA, depending on the assay. In all thermal stability assays, samples were preincubated at RT for 10 min (nucleotides) or 30 min (inhibitors) prior to thermal measurements. Depending on the studied protein, thermal ramping was performed up to 95 °C, using 5 °C intervals. At each temperature, samples were incubated for 3 min before the Protein-Probe solution was added, and the TRL-signals at 620 nm were monitored at RT.

3.2. Concentration and Buffer Composition–Related Effects on GTPase Stability

Melting curves of KRAS WT (50–1250 nM), GMPPNP-KRAS (50 nM), and mutants G13D (50–150 nM) and Q61R (50–1250 nM) were monitored in sample buffer with or without 1 mM $MgCl_2$ or 1 mM EDTA. In addition, KRAS WT was monitored in a sample buffer supplemented with 0–10 mM $MgCl_2$ or 0–1 mM $CaCl_2$. The melting curves for HRAS (1000–2000 nM), NRAS (500–2000 nM), Ac-KRAS (100–2000 nM), iMet-KRAS (100–1000 nM), RhoA (2 µM), Gαi (50 nM), and KRAS mutants Q61L (50–1250 nM), G12D (50–150 nM), G12C (10–1250 nM), and Q61R (50–150 nM) were monitored in the presence of 1 mM $MgCl_2$.

3.3. Nucleotide Concentration–Induced GTPase Stabilization

KRAS G13D (50 nM) was monitored in the presence of 0–900 nM GDP, and KRAS WT, G13D, G12D, and Q61R (50 nM) were monitored with 10 and/or 100 µM GDP, GTP, and ATP in buffer supplemented with 1 mM $MgCl_2$. KRAS WT (50 nM) was also monitored with 10 µM GDP in a buffer without $MgCl_2$ or supplemented with 0–1 mM $CaCl_2$ or 1 mM EDTA. HRAS (2 µM), NRAS (2 µM), RhoA (2 µM), and Gαi (50 nM) were monitored with 100 µM GDP, GTP, or ATP in buffers with or without 1 mM $MgCl_2$ and 1 mM EDTA. In addition, melting curves for KRAS WT (50 nM) were measured with GTP analogs GTPγS, GMPPNP, and GMPPCP (0–300 µM), and GMP (0–1000 µM) in the presence of 1 mM $MgCl_2$.

3.4. KRAS Thermal Stabilization Using Small Molecular Inhibitors

All inhibitor assays were performed with a buffer containing 1 mM $MgCl_2$. Thermal curves for KRAS G12C and WT (50 nM) were measured in the presence of ARS-853 (0–5000 nM), ARS-1620 (0–5000 nM), AMG-510 (0–900 nM), and MRTX849 (0–900 nM). KRAS WT, G12C, and G12D (50 nM) were also monitored with 10 µM BI-2852, BI-2853, and BAY-293. In addition, KRAS G12C (50 nM) was studied with ARS-1620 (1 µM) in a buffer without $MgCl_2$ and with 1 mM EDTA.

3.5. KRAS Thermal Stabilization Using Protein-Based Binders

Assays were performed using three DARPins alone or in combination with small molecular inhibitors. DARPins K13 (200 nM) and K19 (200 or 500 nM) were assayed with KRAS WT and G12C (50 nM) and DARPin K27 (100 nM) KRAS WT, G13D, G12D, Q61R, and Q61L (50 nM) in a buffer supplemented with 1 mM $MgCl_2$. KRAS WT (50 nM) was also assayed with DARPin K27 (50 nM) with 0–1 mM EDTA. Competitive thermal stability assays were performed by first combining KRAS G12C (50 nM) with DARPin K13 (50 nM) and after 10 min incubation by additionally adding AMG-510 (0–900 nM), MRTX849

(0–900 nM), ARS-853 (0–20 μM), or ARS-1620 (0–20 μM). The thermal curves were monitored after an additional 30 min incubation at RT.

3.6. SYPRO Orange and ANS Thermal Ramping Assays

SYPRO Orange and ANS assays were performed using a one-step protocol, where the samples (8 μL) and SYPRO Orange/ANS solution (12 μL) were combined prior to the first heating step. The samples were incubated for 3 min at each temperature, followed by fluorescence signal measurement. SYPRO Orange was used at 5× (stock 5000×) and ANS at 10 μM final concentration.

Thermal stability curves for KRAS WT, G12C, G13D, and Q61R (0–30 μM) were monitored both with SYPRO Orange and ANS in an assay buffer with or without 1 mM $MgCl_2$. In addition, HRAS, NRAS, KRAS V14I, RhoA, and Gαi were studied at 10 μM concentration. KRAS G13D (3 μM) was assayed with SYPRO Orange in thermal ramping in combination with 0–1000 μM GDP, 1000 μM GTP, and 1000 μM ATP in a buffer supplemented with 1 mM $MgCl_2$. Additionally, 10 μM HRAS, NRAS, KRAS V14I, Ac-KRAS iMet-KRAS, RhoA, and Gαi were studied without additional nucleotides or with 10 or 100 μM GDP/GTP in an assay buffer supplemented with 1 mM $MgCl_2$ or 1 mM EDTA.

KRAS WT, G12D, and G12C (3 μM) were monitored with 20 μM BI-2852, BI-2853, and BAY-293, and 10 μM KRAS WT and G12C were also measured in combination with 20 μM ARS-853 and ARS-1620. In addition, KRAS G12C (10 μM) was assayed with 0–20 μM AMG-510 and MRTX849 using both SYPRO Orange and ANS.

4. Conclusions

In this study, we investigated KRAS and additional small GTPases in terms of thermal stability to critically evaluate TSA suitability for inhibitor screening and validation. TSA is a widely used tool for protein stability monitoring, but some critical factors influence the assay. Based on our findings, in addition to buffer composition, the variables of free nucleotide, protein concentration, and inhibitor binding mode/area all affect the TSA data. Direct comparison with traditional nucleotide exchange assays showed that inhibitors blocking either intrinsic nucleotide exchange or binding covalently to the target GTPase showed significant thermal shifts. However, other inhibitors that are functional in a nucleotide exchange assay with SOS^{cat} showed only small or negligible thermal shifts. Nevertheless, we showed that some of these binders can be validated through a competitive TSA protocol, by using the Protein-Probe technique. This further proves that molecules can bind without evident target stabilization. TSA can be a valuable tool both for inhibitor screening and validation, but one must appreciate that not all interactions can be detected. In addition, the results might be biased for inhibitors functioning in a certain way, as we showed with KRAS in a buffer with or without $MgCl_2$. It is clear that data obtained with minor changes in buffer composition might be affected. Moreover, this should be taken into account especially in the case of studies using high protein concentrations, in which the carried storage buffer can also affect the results. These factors must all be considered carefully when designing a TSA screen so that their effect can be considered during data interpretation.

Supplementary Materials: The following supporting information can be downloaded at: https://www.mdpi.com/article/10.3390/ijms23137095/s1.

Author Contributions: K.K. and H.H. conceived the project. K.K., S.V., R.M. and N.H. designed, developed, and performed the assays. J.N.K., W.G., B.D., L.L., K.D.W. and A.P. contributed by providing materials and consultancy for design of the final assays together with K.K. The manuscript was written through contributions of all authors. All authors have read and agreed to the published version of the manuscript.

Funding: This work is supported by the Turku University Foundation (K.K.), Academy of Finland (323433/K.K. and 329012/K.K.), Emil Aaltonen Foundation (S.V.), Swiss Cancer Research foundation

KFS-5290-02-2021 (J.N.K. and A.P.), NIH/NCI R01 CA244341 (K.D.W.), NIH P30CA142543 (K.D.W.), and Cancer Prevention and Research Institute of Texas RP220145 (K.D.W.).

Institutional Review Board Statement: Study involves no animals or humans.

Informed Consent Statement: Not applicable.

Data Availability Statement: Data are available on request to the corresponding author.

Acknowledgments: The authors would like to thank Allison Champagne, Matt Drew, Peter Frank, Randy Gapud, José Sánchez Hernández, Jennifer Mehalko, Shelley Perkins, Nitya Ramakrishnan, Mukul Sherekar, Simon Messing, Troy Taylor, Vanessa Wall, and Tim Waybright for cloning, expression, purification, and QC of the used small GTPase proteins.

Conflicts of Interest: The authors declare the following competing financial interest: Kari Kopra has commercial interest through QRET Technologies Ltd. Harri Härmä has commercial interest through QRET Technologies Ltd. Ken Westover is a member of the SAB for Vibliome Therapeutics and Reactive Biosciences. The Westover lab receives or has received research funding from Astellas and Revolution Medicines. Other authors and Leidos Biomedical Research, Inc. have no commercial interest.

References

1. Huynh, K.; Partch, C.L. Analysis of protein stability and ligand interactions by thermal shift assay. *Curr. Protoc. Protein Sci.* **2015**, *79*, 28.9.1–28.9.14. [CrossRef] [PubMed]
2. Gao, K.; Oerlemans, R.; Groves, M.R. Theory and applications of differential scanning fluorimetry in early-stage drug discovery. *Biophys. Rev.* **2020**, *12*, 85–104. [CrossRef] [PubMed]
3. Senisterra, G.; Chau, I.; Vedadi, M. Thermal denaturation assays in chemical biology. *Assay Drug Dev. Technol.* **2012**, *10*, 128–136. [CrossRef] [PubMed]
4. Lang, B.E.; Cole, K.D. Differential scanning calorimetry and fluorimetry measurements of monoclonal antibodies and reference proteins: Effect of scanning rate and dye selection. *Biotechnol. Prog.* **2017**, *33*, 677–686. [CrossRef]
5. Leyva-Porras, C.; Cruz-Alcantar, P.; Espinosa-Solís, V.; Martínez-Guerra, E.; Piñón-Balderrama, C.I.; Martínez, I.C.; Saavedra-Leos, M.Z. Application of differential scanning calorimetry (DSC) and modulated differential scanning calorimetry (MDSC) in food and drug industries. *Polymers* **2020**, *12*, 5. [CrossRef]
6. Hinz, H.J.; Schwarz, F.P. Measurement and analysis of results obtained on biological substances with dsc. *J. Chem. Thermodyn.* **2001**, *33*, 1511–1525. [CrossRef]
7. Johnson, C.M. Differential scanning calorimetry as a tool for protein folding and stability. *Arch. Biochem. Biophys.* **2013**, *531*, 100–109. [CrossRef]
8. Wu, T.; Yu, J.; Gale-Day, Z.; Woo, A.; Suresh, A.; Hornsby, M.; Gestwicki, J.E. Three essential resources to improve differential scanning fluorimetry (DSF) experiments. *bioRxiv* **2020**. [CrossRef]
9. Shi, S.; Semple, A.; Cheung, J.; Shameem, M. DSF method optimization and its application in predicting protein thermal aggregation kinetics. *J. Pharm. Sci.* **2013**, *102*, 2471–2483. [CrossRef]
10. Kirley, T.L.; Norman, A.B.; Wetzel, H.N. A novel differential scanning fluorimetry analysis of a humanized anti-cocaine mAb and its ligand binding characteristics. *J. Immunol. Methods* **2020**, *476*, 112676. [CrossRef]
11. McClure, S.M.; Ahl, P.L.; Blue, J.F. High throughput differential scanning fluorimetry (DSF) formulation screening with complementary dyes to assess protein unfolding and aggregation in presence of surfactants. *Pharm. Res.* **2018**, *35*, 81. [CrossRef] [PubMed]
12. Oshinbolu, S.; Shah, R.; Finka, G.; Molloy, M.; Uden, M.; Bracewell, D.G. Evaluation of fluorescent dyes to measure protein aggregation within mammalian cell culture supernatants. *J. Chem. Technol. Biotechnol.* **2018**, *93*, 909–917. [CrossRef]
13. Bai, Y.; Wan, W.; Huang, Y.; Jin, W.; Lyu, H.; Xia, Q.; Dong, X.; Gao, Z.; Liu, Y. Quantitative interrogation of protein co-aggregation using multi-color fluorogenic protein aggregation sensors. *Chem. Sci.* **2021**, *12*, 8468–8476. [CrossRef] [PubMed]
14. Duy, C.; Fitter, J. How aggregation and conformational scrambling of unfolded states govern fluorescence emission spectra. *Biophys. J.* **2006**, *90*, 3704–3711. [CrossRef] [PubMed]
15. Alexander, C.G.; Wanner, R.; Johnson, C.M.; Breitsprecher, D.; Winter, G.; Duhr, S.; Baaske, P.; Ferguson, N. Novel microscale approaches for easy, rapid determination of protein stability in academic and commercial settings. *Biochem. Biophys. Acta* **2014**, *1844*, 2241–2250. [CrossRef]
16. Ablinger, E.; Leitgeb, S.; Zimmer, A. Differential scanning fluorescence approach using a fluorescent molecular rotor to detect thermostability of proteins in surfactant-containing formulations. *Int. J. Pharm.* **2013**, *441*, 255–260. [CrossRef]
17. Kroeger, T.; Frieg, B.; Zhang, T.; Hansen, F.K.; Marmann, A.; Proksch, P.; Nagel-Steger, L.; Groth, G.; Smits, S.H.J.; Gohlke, H. EDTA aggregates induce SYPRO orange-based fluorescence in thermal shift assay. *PLoS ONE* **2017**, *12*, e0177024. [CrossRef]
18. Simeonov, A.; Davis, M.I. Interference with Fluorescence and absorbance. In *Assay Guidance Manual*; Markossian, S., Grossman, A., Brimacombe, K., Arkin, M., Auld, D., Austin, C.P., Baell, J., Chung, T.D.Y., Coussens, N.P., Dahlin, J.L., et al., Eds.; Eli Lilly & Company: Indianapolis, IN, USA; National Center for Advancing Translational Sciences: Bethesda, MD, USA, 2004.

19. Vuorinen, E.; Valtonen, S.; Eskonen, V.; Kariniemi, T.; Jakovleva, J.; Kopra, K.; Härmä, H. Sensitive label-free thermal stability assay for protein denaturation and protein-ligand interaction studies. *Anal. Chem.* **2020**, *92*, 3512–3516. [CrossRef]
20. Valtonen, S.; Vuorinen, E.; Kariniemi, T.; Eskonen, V.; Le Quesne, J.; Bushell, M.; Härmä, H.; Kopra, K. Nanomolar protein-protein interaction monitoring with a label-free Protein-Probe technique. *Anal. Chem.* **2020**, *92*, 15781–15788. [CrossRef]
21. Vuorinen, E.; Valtonen, S.; Hassan, N.; Mahran, R.; Habib, H.; Malakoutikhah, M.; Kopra, K.; Härmä, H. Protease substrate-independent universal assay for monitoring digestion of native unmodified proteins. *Int. J. Mol. Sci.* **2021**, *22*, 6362. [CrossRef]
22. Valtonen, S.; Vuorinen, E.; Eskonen, V.; Malakoutikhah, M.; Kopra, K.; Härmä, H. Sensitive, homogeneous, and label-free protein-probe assay for antibody aggregation and thermal stability studies. *mAbs* **2021**, *13*, 1955810. [CrossRef] [PubMed]
23. Kopra, K.; Ligabue, A.; Wang, Q.; Syrjänpää, M.; Blaževitš, O.; Veltel, S.; van Adrichem, A.J.; Hänninen, P.; Abankwa, D.; Härmä, H. A homogeneous quenching resonance energy transfer assay for the kinetic analysis of the GTPase nucleotide exchange reaction. *Anal. Bioanal. Chem.* **2014**, *406*, 4147–4156. [CrossRef] [PubMed]
24. Kopra, K.; Rozwandowicz-Jansen, A.; Syrjänpää, M.; Blaževitš, O.; Ligabue, A.; Veltel, S.; Lamminmäki, U.; Abankwa, D.; Härmä, H. GTP-specific fab fragment-based GTPase activity assay. *Anal. Chem.* **2015**, *87*, 3527–3534. [CrossRef] [PubMed]
25. Kopra, K.; van Adrichem, A.J.; Salo-Ahen, O.M.H.; Peltonen, J.; Wennerberg, K.; Härmä, H. High-Throughput dual screening method for Ras activities and inhibitors. *Anal. Chem.* **2017**, *89*, 4508–4516. [CrossRef] [PubMed]
26. Kopra, K.; Vuorinen, E.; Abreu-Blanco, M.; Wang, Q.; Eskonen, V.; Gillette, W.; Pulliainen, A.T.; Holderfield, M.; Härmä, H. Homogeneous dual-parametric-coupled assay for simultaneous nucleotide exchange and KRAS/RAF-RBD interaction monitoring. *Anal. Chem.* **2020**, *92*, 4971–4979. [CrossRef]
27. Hunter, J.C.; Manandhar, A.; Carrasco, M.A.; Gurbani, D.; Gondi, S.; Westover, K.D. Biochemical and structural analysis of common cancer-associated KRAS mutations. *Mol. Cancer Res.* **2015**, *13*, 1325–1335. [CrossRef]
28. Pantsar, T. The current understanding of KRAS protein structure and dynamics. *Comput. Struct. Biotechnol. J.* **2019**, *26*, 189–198. [CrossRef]
29. Menyhárd, D.K.; Pálfy, G.; Orgován, Z.; Vida, I.; Keserű, G.M.; Perczel, A. Structural impact of GTP binding on downstream KRAS signaling. *Chem. Sci.* **2020**, *11*, 9272–9289. [CrossRef]
30. Haigis, K.M. KRAS alleles: The devil is in the detail. *Trends Cancer* **2017**, *3*, 686–697. [CrossRef]
31. Uprety, D.; Adjei, A.A. KRAS: From undruggable to a druggable cancer target. *Cancer Threat. Rev.* **2020**, *89*, 102070. [CrossRef]
32. Christensen, J.G.; Olson, P.; Briere, T.; Wiel, C.; Bergo, M.O. Targeting $Kras^{g12c}$-mutant cancer with a mutation-specific inhibitor. *J. Intern. Med.* **2020**, *288*, 183–191. [CrossRef] [PubMed]
33. Mustachio, L.M.; Chelariu-Raicu, A.; Szekvolgyi, L.; Roszik, J. Targeting KRAS in cancer: Promising therapeutic strategies. *Cancers* **2021**, *13*, 1204. [CrossRef] [PubMed]
34. Leshchiner, E.S.; Parkhitko, A.; Bird, G.H.; Luccarelli, J.; Bellairs, J.A.; Escudero, S.; Opoku-Nsiah, K.; Godes, M.; Perrimon, N.; Walensky, L.D. Direct inhibition of oncogenic KRAS by hydrocarbon-stapled SOS1 helices. *Proc. Natl. Acad. Sci. USA* **2015**, *112*, 1761–1766. [CrossRef] [PubMed]
35. Yin, G.; Kistler, S.; George, S.D.; Kuhlmann, N.; Garvey, L.; Huynh, M.; Bagni, R.K.; Lammers, M.; Der, C.J.; Campbell, S.L. A KRAS GTPase K104Q mutant retains downstream signaling by offsetting defects in regulation. *J. Biol. Chem.* **2017**, *292*, 4446–4456. [CrossRef]
36. Xu, K.; Park, D.; Magis, A.T.; Zhang, J.; Zhou, W.; Sica, G.L.; Ramalingam, S.S.; Curran, W.J.; Deng, X. Small molecule KRAS agonist for mutant KRAS cancer therapy. *Mol. Cancer* **2020**, *19*, 93. [CrossRef]
37. Kistler, S.K. Investigating the Role of Post-Translational Modifications in the Core RAS GTPase Domain. Ph.D. Thesis, University of North Carolina at Chapel Hill, Chapel Hill, NC, USA, 24 July 2019.
38. Cooke, A. Biochemical and Biological Characterization of KRAS Q61 Mutants. Master's Thesis, University of North Carolina at Chapel Hill, Chapel Hill, NC, USA, 5 December 2018.
39. Dharmaiah, S.; Tran, T.H.; Messing, S.; Agamasu, C.; Gillette, W.K.; Yan, W.; Waybright, T.; Alexander, P.; Esposito, D.; Nissley, D.V.; et al. Structures of N-terminally processed KRAS provide insight into the role of N-acetylation. *Sci. Rep.* **2019**, *9*, 10512. [CrossRef]
40. John, J.; Sohmen, R.; Feuerstein, J.; Linke, R.; Wittinghofer, A.; Goody, R.S. Kinetics of interaction of nucleotides with nucleotide-free H-ras p21. *Biochemistry* **1990**, *29*, 6058–6065. [CrossRef]
41. Hall, A.; Self, A.J. The effect of Mg^{2+} on the guanine nucleotide exchange rate of $p21^{N\text{-}ras}$. *J. Biol. Chem.* **1986**, *261*, 10963–10965. [CrossRef]
42. Mistou, M.Y.; Cool, R.H.; Parmeggiani, A. Effects of ions on the intrinsic activities of c-H-*ras* protein p21. A comparison with elongation factor Tu. *Eur. J. Biochem.* **1992**, *15*, 179–185. [CrossRef]
43. John, J.; Rensland, H.; Schlichting, I.; Vetter, I.; Borasio, G.D.; Goody, R.S.; Wittinghofer, A. Kinetic and structural analysis of the Mg(2+)-binding site of the guanine nucleotide-binding protein p21H-ras. *J. Biol. Chem.* **1993**, *268*, 923–929. [CrossRef]
44. Johnson, C.W.; Lin, Y.J.; Reid, D.; Parker, J.; Pavlopoulos, S.; Dischinger, P.; Graveel, C.; Aguirre, A.J.; Steensma, M.; Haigis, K.M.; et al. Isoform-specific destabilization of the active site reveals a molecular mechanism of intrinsic activation of KRas G13D. *Cell Rep.* **2019**, *28*, 1538–1550.e7. [CrossRef] [PubMed]
45. Killoran, R.C.; Smith, M.J. Conformational resolution of nucleotide cycling and effector interactions for multiple small GTPases determined in parallel. *J. Biol. Chem.* **2019**, *294*, 9937–9948. [CrossRef] [PubMed]

46. Buhrman, G.; Holzapfel, G.; Fetics, S.; Mattos, C. Allosteric modulation of Ras positions Q61 for a direct role in catalysis. *Proc. Natl. Acad. Sci. USA* **2010**, *107*, 4931–4936. [CrossRef] [PubMed]
47. O'Connor, C.; Kovrigin, E.L. Characterization of the second ion-binding site in the G domain of H-Ras. *Biochemistry* **2012**, *51*, 9638–9646. [CrossRef] [PubMed]
48. Zhang, B.; Zhang, Y.; Wang, Z.; Zheng, Y. The role of Mg^{2+} cofactor in the guanine nucleotide exchange and GTP hydrolysis reactions of Rho family GTP-binding proteins. *J. Biol. Chem.* **2000**, *275*, 25299–25307. [CrossRef]
49. Bera, A.K.; Lu, J.; Wales, T.E.; Gondi, S.; Gurbani, D.; Nelson, A.; Engen, J.R.; Westover, K.D. Structural basis of the atypical activation mechanism of $KRAS^{V14I}$. *J. Biol. Chem.* **2019**, *294*, 13964–13972. [CrossRef]
50. Moore, A.R.; Rosenberg, S.C.; McCormick, F.; Malek, S. RAS-targeted therapies: Is the undruggable drugged? *Nat. Rev. Drug Discov.* **2020**, *19*, 533–552. [CrossRef]
51. Zuberi, M.; Khan, I.; O'Bryan, J.P. Inhibition of RAS: Proven and potential vulnerabilities. *Biochem. Soc. Trans.* **2020**, *48*, 1831–1841. [CrossRef]
52. Plückthun, A. Designed ankyrin repeat proteins (DARPins): Binding proteins for research, diagnostics, and therapy. *Annu. Rev. Pharmacol. Toxicol.* **2015**, *55*, 489–511. [CrossRef]
53. Guillard, S.; Kolasinska-Zwierz, P.; Debreczeni, J.; Breed, J.; Zhang, J.; Bery, N.; Marwood, R.; Tart, J.; Overman, R.; Stocki, P.; et al. Structural and functional characterization of a DARPin which inhibits Ras nucleotide exchange. *Nat. Commun.* **2017**, *8*, 16111. [CrossRef]
54. Bery, N.; Legg, S.; Debreczeni, J.; Breed, J.; Embrey, K.; Stubbs, C.; Kolasinska-Zwierz, P.; Barrett, N.; Marwood, R.; Watson, J.; et al. KRAS-specific inhibition using a DARPin binding to a site in the allosteric lobe. *Nat. Commun.* **2019**, *10*, 2607. [CrossRef] [PubMed]

Mahran, R., Vello, N., Komulainen, A., Malakoutikhah, M., Härmä, H. and Kopra, K. (2023)
Isothermal chemical denaturation assay for monitoring protein stability and inhibitors interactions.
Journal of Scientific Reports 13:20066

III

scientific reports

Check for updates

OPEN

Isothermal chemical denaturation assay for monitoring protein stability and inhibitor interactions

Randa Mahran, Niklas Vello, Anita Komulainen, Morteza Malakoutikhah, Harri Härmä & Kari Kopra

Thermal shift assay (TSA) with altered temperature has been the most widely used method for monitoring protein stability for drug research. However, there is a pressing need for isothermal techniques as alternatives. This urgent demand arises from the limitations of TSA, which can sometimes provide misleading ranking of protein stability and fail to accurately reflect protein stability under physiological conditions. Although differential scanning fluorimetry has significantly improved throughput in comparison to differential scanning calorimetry and differential static light scattering throughput, all these methods exhibit moderate sensitivity. In contrast, current isothermal chemical denaturation (ICD) techniques may not offer the same throughput capabilities as TSA, but it provides more precise information about protein stability and interactions. Unfortunately, ICD also suffers from limited sensitivity, typically in micromolar range. We have developed a novel method to overcome these challenges, namely throughput and sensitivity. The novel Förster Resonance Energy Transfer (FRET)-Probe as an external probe is highly applicable to isothermal protein stability monitoring but also to conventional TSA. We have investigated ICD for multiple proteins with focus on KRAS^{G12C} with covalent inhibitors and three chemical denaturants performed at nanomolar protein concentration. Data showed corresponding inhibitor-induced stabilization of KRAS^{G12C} to those reported by nucleotide exchange assay.

Protein stability is critical to their correct function in cell, but also biologics and many in vitro assays utilizing the native protein structure and function. Protein stability is also fundamental for determination of optimum conditions for protein expression, purification, and storage[1]. Therefore, it is important to understand how various conditions such as solvent components and temperature affects the stability of different proteins.

Nowadays, thermal shift assays (TSAs) are the most used methods to assess protein stability[2]. This is due to simple TSA protocols, good throughput, and easy automation. These assays monitor protein stability during the temperature increase and can be used also in the presence of potential binding partners. Typically, all TSAs are based on fluorescence readout, in which the denaturation is seen as an increase in observed signal. On the other hand, protein–ligand interaction can be visualized as an increase in protein stability. In drug discovery, the shift in protein melting temperature ($\Delta\ T_m$) has become a popular parameter to identify potential protein binding ligands. However, the change in T_m values does not directly reflect the binding affinities or rank order of the ligands, as molecule binding to distinct parts of the target may have different effects on stability. In addition, an increase in temperature may cause differences not occurring at physiological temperature, therefore, $\Delta\ T_m$ may not accurately predict the efficacy of drug candidate under physiological conditions.

Fluorescence, differential scanning calorimetry (DSC) and circular dichroism (CD) spectroscopy are often used tools for monitoring thermal stability[3–8]. DSC is the recognized gold standard technique for measuring protein thermal stability, but it cannot give similar information about the exact structural changes in the studied protein as CD. Even valuable tools to study proteins, unfortunately, both methods share common limitations such low sensitivity and limited throughput[9,10]. This makes these methods material and time consuming especially when larger ligand panels are studied. To overcome these limitations, differential scanning fluorimetry (DSF) has become an increasingly practical and popular alternative to study protein thermal stability. DSF utilizes external dyes and thus it needs no target protein labeling, and assays can be executed employing relatively simple instrumentation. In DSF, many different external protein stability sensing dyes have been used and developed, but only few have gained wider popularity[11]. SYPRO Orange, which enables the direct use of qPCR equipment, is currently the most popular DSF dye. Independently of the exact probe structure and mechanism, all external probes

Department of Chemistry, University of Turku, Henrikinkatu 2, 20500 Turku, Finland. email: randa.r.mahran@utu.fi

target hydrophobic parts of the target proteins exposed during the protein unfolding, resulting in an increase in the fluorescence. However, as these probes sense their environment, dye structure and assay buffer selection may affect the assay functionality. In addition, properties of some assay buffer components itself, e.g., tris and histidine, are altered by heating[12]. These factors need to be considered to obtain reliable data using DSF[13,14]. To overcome these limitations, labelling of target proteins with fluorophore tags was recently introduced to DSF for better understanding of proteins unfolding in complex physiological systems[15–17]. While being a valuable technique, it cannot be universally applied since it needs to be customized for each specific protein being studied.

In addition to the use of external dyes, NanoDSF (nDSF) enables sensitive and precise method that determines protein unfolding by monitoring changes in the intrinsic fluorescence of the protein or by using fluorescently labeled protein[18]. In case of intrinsic protein fluorescence, denaturation of the protein causes change in the environmental surroundings of tyrosine and tryptophan amino acids leading to a shift in their fluorescence spectra and intensity, enabling also direct protein chemical stability monitoring[19]. In addition to nDSF, intrinsic Förster resonance energy transfer (iFRET), which is based on energy transfer from the tryptophan intrinsic fluorescence to a fluorescent labeled probe, can be used[20]. This technique, however, has been found problematic due to the high sensitivity of the tyrosine and tryptophan to the surrounding microenvironment, which might cause signal quenching or a spectral shift. Especially for chemical denaturation, addition of the chemical denaturant by itself might cause a shift in the fluorescence spectra, which is not actually related to the protein unfolding[18].

Even TSA is often used, monitoring protein stability at physiological temperature may give better view about ligand binding and its effect on protein stability[21,22]. In TSA, heating causes proteins to acquire more kinetic energy, which breaks down weak hydrogen bonds and disrupts protein tertiary structure, leading to structural unfolding of protein. In case of chemical denaturation, the mechanism of protein unfolding differs depending on the denaturing agent[23]. Alcohols are often used for protein precipitation and denaturation, and they function by disrupting the protein tertiary structure by making hydrogen bonds with the protein side chains[24]. Urea, on the other hand, causes protein unfolding either directly through interaction with protein hydrophobic parts and water molecules, or indirectly through alteration of the solvent composition.[25–27]. In addition, low and high pH can cause protein denaturation, by causing protonation or deprotonation depending on isoelectric point (PI) of the protein and used pH[28].

In case of isothermal chemical denaturation (ICD), mostly run in the presence of urea and guanidium chloride as denaturants, binding affinities can be simply obtained, which is not the case with TSA[21,29]. The downside in ICD is that these denaturants often require long incubation time to reach equilibrium in a denaturant titration, and high concentration of denaturant may also affect the affinity of the studied inhibitor. To overcome the limited throughput of ICD and relatively low sensitivity of both TSA and ICD, we have developed new member for the Protein-Probe family of techniques. The original Protein-Probe assay was based on protein stability sensing using a Eu^{3+}-chelate peptide-probe, a highly polar glutamic-acid-rich peptide. This negatively charged probe has low interaction with the native protein compared to the denatured form, as it is believed that the main interaction of Eu^{3+}-probe occurs through the protein hydrophobic core. However, the Protein-Probe method functionality rely on acidic pH, due to partial protonation of the peptide, and thus the assay must be performed in two steps, heating of the protein then addition of the detection solution, prior the monitoring of the time-resolved luminescence (TRL) signal. Even the method is highly sensitive, significantly improved sensitivity over the commercial reference methods, the need for low pH limits its use in single-step assay, typical for TSA and ICD[30–34]. Thus, we started to modify the system to enable protein thermal profiling at single-step and neutral pH, by changing the signal modulator to a more positive peptidic structure. However, by modifying only the modulator structure, we still end up two component system relying on electrostatic interactions, which might be more sensitive for unwanted responses in ICD. Thus, we developed here presented the single-peptide-probe for proteins stability studies, named as the FRET-Probe. In the FRET-Probe system, developed peptide-probe is labeled at both ends using Eu^{3+}-chelate and Cy5 fluorophore. In the assays, the structure of the dual-labeled FRET-Probe changes upon binding to denatured protein, reducing the distance between labels. This provides an increase in time-resolved Förster resonance energy transfer (TR-FRET) signal with denatured protein, as low TR-FRET is monitored with the native or ligand stabilized protein. With the used model proteins, the FRET-Probe was found suitable for both TSA and ICD principles, enabling sensitive monitoring of protein–ligand interactions (PLIs) at nanomolar protein concentrations.

Results and discussion

Overview of the FRET-Probe structure and functionality

Stability of native proteins is strictly attributed to a narrow range of conditions of the solvent components and thermodynamic parameters[26]. Protein unfolding can occur due to many external stimuli, either physical like heat and radiation, or chemical like pH and organic compounds. Current methodologies to study protein unfolding under these varying denaturation conditions are unfortunately restricted by their limited sensitivity. Previously, we have introduced the Protein-Probe method, working under specific modulation conditions as an endpoint TSA. The Protein-Probe technique was developed to overcome the sensitivity limitation of the existing TSA methods, and we obtained approx. 100-fold improved sensitivity using nanomolar protein concentration levels. However, the endpoint assay protocol makes the assay inconvenient for TSA, and thus this technique was found to be more useful for the detection of protein aggregates and protease activity of native unmodified proteins[30,32]. Thus, we designed a modified Protein-Probe family member called the FRET-Probe to overcome limitations related to the use of two detection components and low pH modulation condition, enabling real-time stability monitoring at neutral pH.

The FRET-Probe consists of N-terminal Eu^{3+}chelate donor and C-terminal Cy5-fluorophore as an acceptor conjugated to a peptide containing 24 amino acids (Fig. 1a). The peptide sequence of the FRET-Probe comprises

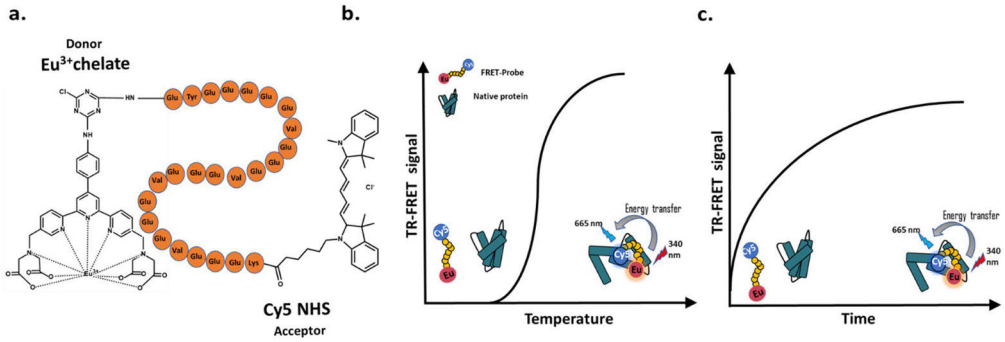

Figure 1. Structure and principle of the FRET-Probe. (**a**) The FRET-Probe is a peptide conjugated to Eu^{3+}-chelate at the N-terminus and Cy5 at the C-terminus of a highly polar glutamic-acid-rich peptide sequence. Binding with the unfolded protein decreases the distance between the labels, allowing energy transfer to occur and thus increasing the TR-FRET signal monitored with heating in the TSA (**b**) or with longer incubation of the protein with the chemical denaturant in the ICD assay (**c**). In ICD assays, IC_{50} values are calculated at RT from the sigmoidal curve formed of the TR-FRET signal obtained in presence of a titration of the inhibitor concentration during the chemical denaturation of proteins at a specific time point.

four repeating units formed of three glutamic acids and one valine, with an additional three glutamic acids and one tyrosine at the N-terminus and three glutamic acids and one lysine at the C-terminus. By using two peptide conjugated labels, the system enables the use of a single detection component, unlike in other Protein-Probe-type assay platforms that have separate Eu^{3+}-probe and Cy5-containing modulator. This additionally leads to monitoring of TR-FRET signal, unlike in other Protein-Probe-type assays, in which the Eu^{3+}-chelate TRL-signal is monitored. Even the exact binding mechanism of the FRET-Probe, as also previously reported Eu^{3+}-probe is still partly unknown, the interaction with the denatured protein increases the observed TR-FRET signal, as the signal with native protein is negligible. Both in the case of heat or chemically induced denaturation, binding of the FRET-Probe leads to a decrease in the donor and acceptor dye distance and increase in TR-FRET signal (Fig. 1). Interaction between the FRET-Probe and unfolded protein also protects the labels from their surroundings indicating that not only the probe sequence, but also fluorescent labels play a role in the detection of the denaturation event. As the FRET-Probe works independently of the denaturation method, we studied its functionality for PLIs in the ICD assay, previously not possible with the other Protein-Probe techniques (Fig. S1). As there is no TR-FRET applicable qPCR device, we systematically studied the FRET-Probe with a single denaturant concentration in a time-dependent manner, in a way enabling single concentration ligand library screening (Fig. 1c).

FRET-Probe as a tool for protein thermal stability monitoring

As the FRET-Probe is functionally and structurally distinct from our previous Eu^{3+}-probe-based systems, we first validated it in a TSA format. Assays were performed utilizing three proteins, Son of Sevenless catalytic domain (SOS^{cat}, 10 nM), trastuzumab (25 nM), and malate dehydrogenase (MDH, 20 nM) (Fig. 2a, Table S1). The assay was performed in a single step fashion, and data clearly showed the functionality of the FRET-Probe assay. T_m values measured for SOS^{cat}, MDH and trastuzumab were 42.3 ± 1.6, 46.2 ± 0.4, and 75.4 ± 0.1 °C, respectively (Fig. 2a). These values were similar to the reported values, 45, 50 and 75 °C measured using Protein-Probe, fluorescence spectroscopy, and DSF, respectively[32,35,36]. All proteins gave high signal-to-background ratio and due to the atypical stepwise heating with 5 °C interval, a sharp transition curve was observed.

Next, we compared the FRET-Probe performance alongside the two-component and two-step Protein-Probe assay as both methods work in the same protein concentration range. The comparison was carried out using $KRAS^{WT}$ and two mutants ($KRAS^{G13D}$ and $KRAS^{Q61R}$) as target proteins (Fig. 2b, Table S1). These mutants were selected due to their different intrinsic nucleotide exchange activity leading to different stability profiles[34]. T_m values of 57.2 ± 0.2, 49.9 ± 0.2 and 64.1 ± 0.2 °C were measured with the Protein-Probe assay, respectively. T_m values with the FRET-Probe assay, 53.6 ± 0.4, 44.7 ± 0.1 and 59.2 ± 0.3 °C, were downshifted, but the rank order of the T_m values was the same in both assays (Fig. 2b). $KRAS^{G13D}$ was the least stable protein with ΔT_m 7.3 for Protein-Probe and 8.9 °C for FRET-Probe compared to $KRAS^{WT}$, while $KRAS^{Q61R}$ was the most stable with ΔT_m 6.9 for Protein-Probe and 5.6 °C for FRET-Probe (Fig. 2b). These small differences in the observed T_m values can be attributed to the varying assay conditions, as the assays are performed in different buffers and with different protocols. In Protein-Probe, KRAS is heated in 8 µL volume in which the concentration was 150 nM, but the detection is performed by adding 65 µL of detection, thus diluting the sample for the detection. On the other hand, the FRET-Probe method was performed in a 25 µL final volume using a single step protocol.

From these KRAS proteins we selected $KRAS^{Q61R}$, as it was less protein and Mg^{2+} concentration dependent and tested it with two commercial DSF methods: GloMelt and SYPRO Orange (Fig. S2). This selection was made as it is known that T_m is affected by protein concentration. In addition, KRAS is affected by Mg^{2+} concentration, thus, protein *Tm* values cannot be easily compared with different techniques that were run at varying

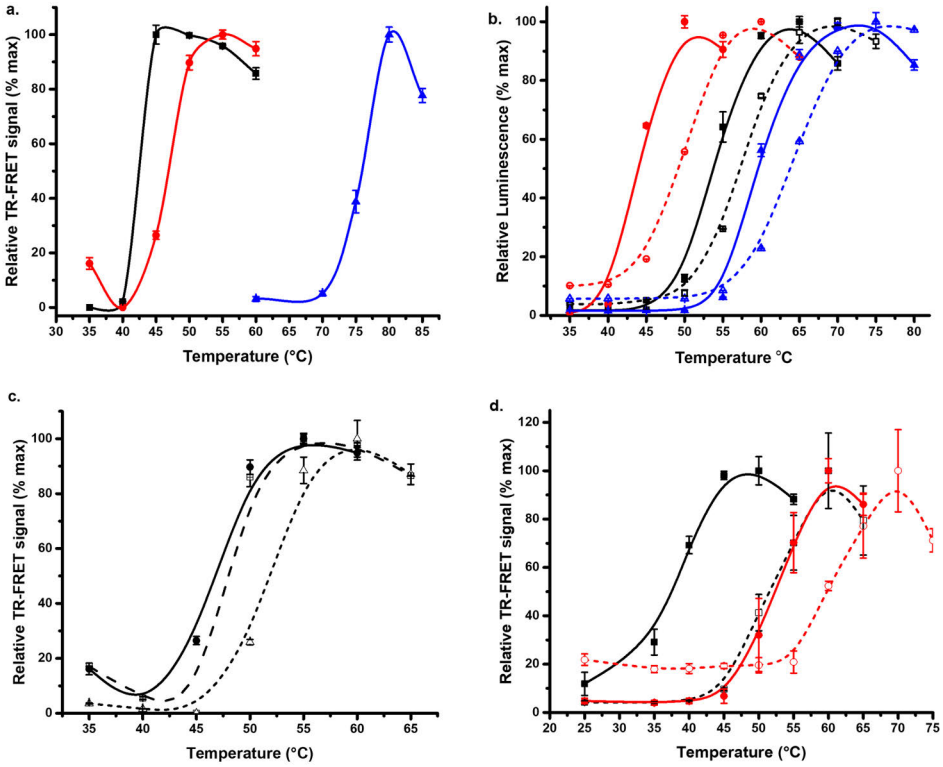

Figure 2. Protein thermal stability and protein ligand interaction (PLI) monitoring. (**a**) Thermal stability of SOS^{cat} (10 nM, black), MDH (25 nM, red), and trastuzumab (20 nM, blue) using the single-step FRET-Probe assay, T_m values were, 42.3 ± 1.6, 46.2 ± 0.4, and 75.4 ± 0.1 °C respectively. (**b**) Comparison of the FRET-Probe (solid) and Protein-Probe (dashed) assays for 150 nM $KRAS^{WT}$ (black), $KRAS^{G13D}$ (red), and $KRAS^{Q61R}$ (blue), FRET-Probe T_m values were 53.6 ± 0.4, 44.7 ± 0.1 and 59.2 ± 0.3 °C, whereas Protein-Probe T_m values were, 57.2 ± 0.2, 49.9 ± 0.2 and 64.1 ± 0.19 °C respectively. (**c**) Thermal stability of 25 nM MDH (solid) with 5 (dashed) and 50 µM (dotted) NADH, T_m values were 46.7 ± 0.9, 47.9 ± 0.6 and 51.7 ± 0.2 °C respectively. (**d**) Thermal stability of 25 nM $KRAS^{G12C}$ with (red) and without (black) 30 min preincubated adagrasib (250 nM), in the absence of Mg^{2+} (solid), T_m values were 38.5 ± 0.4 and 53.2 ± 1.2 °C respectively, whereas in presence (dashed) of Mg^{2+} (200 µM), T_m values were 53.5 ± 0.4 and 62.2 ± 0.9 °C respectively. Data represents mean ± SD (n = 3).

assay setup.[34,37]. With the commercial dye, 5 µM $KRAS^{Q61R}$ was used, as the FRET-Probe assay was performed using 0.15 µM, still significantly higher than the lowest usable concentration for KRAS with the FRET-Probe. All methods efficiently measured the thermal stability of $KRAS^{Q61R}$, having highly similar T_m values 59.5 ± 0.2, 61.2 ± 0.4 and 61.8 ± 0.3 °C using FRET-Probe, GloMelt, and SYPRO Orange, respectively (Fig. S2). Similar T_m values indicate that the FRET-Probe monitors the protein denaturation equally to GloMelt, and SYPRO Orange, but with increased sensitivity.

To further study the FRET-Probe, model PLI assays were next conducted for MDH with reduced nicotinamide adenine dinucleotide (NADH), and $KRAS^{G12C}$ with its covalent inhibitor adagrasib[39,40]. To ensure that the results are solely attributable to the effect of the ligands, the FRET-Probe method was performed initially by incubating the protein and the ligand in plate, to enable interaction, before the FRET-Probe addition and the heating cycle. Additionally, each assay included a positive (protein only) and a negative (buffer only) control. It is known that many ligands stabilize native protein structure when bound, due to change of the unfolding-dissociation equilibrium[38,39]. As a first model, we chose MDH/NADH due to its low affinity interaction (K_D = 3.8 µM)[40]. Using 5 µM NADH concentration, MDH was only partially loaded with the ligand and thermal shift was moderate Δ T_m = 1.2 °C (Fig. 2c). By increasing the MDH loading to 50 µM NADH, MDH thermal shift was more pronounced Δ T_m = 5.0 °C. Thereafter, we studied high affinity interaction with $KRAS^{G12C}$ and adagrasib. Adagrasib is known to interact with GDP-bound form of $KRAS^{G12C}$ with nanomolar affinity, forming a covalent bond with the cysteine. Assay was performed in a buffer without and with 200 µM Mg^{2+}, as Mg^{2+} is needed to preserve GDP loading, and using $KRAS^{G12V}$ as a negative control[41]. For 25 nM KRAS, a typical Mg^{2+} induced effect on $KRAS^{G12V}$ and $KRAS^{G12C}$ stability was observed (Fig. 2d and S1). In the absence of Mg^{2+}, T_m values of 38.3 ± 0.2 and 38.5 ± 0.4 °C were monitored, respectively. In the presence of Mg^{2+}, $KRAS^{G12V}$ and $KRAS^{G12C}$ were both

stabilized, and the T_m values of 53.2 ± 0.4 and 53.5 ± 0.4 °C were measured, respectively. As expected, 250 nM adagrasib did not have any ligand-induced stabilization for $KRAS^{G12V}$ in presence or absence of Mg^{2+} (Fig. S3). However, significant $KRAS^{G12C}$ stabilization was found with adagrasib, both in the absence (Δ T_m 14.7 °C) and presence (Δ T_m 8.7 °C) of Mg^{2+}. Obtained data indicates that as low as 1.25 μM Mg^{2+}, originated from KRAS storage buffer, is sufficient to preserve $KRAS^{G12C}$ GDP-loading, and to induce stabilization of $KRAS^{G12C}$ with adagrasib (Fig. 2d).

Denaturation through protonation at low pH

As the FRET-Probe showed promising functionality in the TSA, we continued to study FRET-Probe in the ICD context. TSA requires heating and subsequent rapid or continuous reading during the heating cycle. As no real-time TR-FRET reader with temperature ramping exists, the interest for isothermal detection became obvious. Typically, ICD assays involve subjecting the target protein to a prolonged incubation with an increasing concentration of the chemical denaturant until equilibrium is achieved. This process can be accelerated by a mild isothermal heating, still preserving physiological or near physiological conditions[42,43]. Although ICD provides a distinct advantage over TSA, as it measures stability at ambient temperature, assay format with long incubation and multiple denaturant concentrations for each sample makes ICD somewhat impractical especially for PLI assays due to the lowered throughput compared to TSA[44,45]. Thus, we hypothesized that by combination of the nanomolar FRET-Probe sensitivity, high throughput properties of TSA, and positive aspects related to ICD, such as preserved protein structure and function[29,42,46], reliable data can be obtained especially for PLIs. To this end, we developed a novel approach for ICD monitoring at room temperature (RT) by selecting a single denaturant condition and monitoring the denaturation over time (Fig. 1c and S1). The most crucial step was to select an appropriate denaturant with correct concentration, and thus, several known mild denaturants were scanned to study the real-time protein stability and interactions utilizing the FRET-Probe. In all of the ICD assays, we tracked the time-dependent TR-FRET signal at multiple intervals over a 150-min incubation period.

Buffer pH is known to have a significant effect on protein stability, which needs to be additionally considered in all assay designs. In the original Protein-Probe platform, low pH was one of the key elements to modulate the assay function. Thus, low pH was first studied to evaluate the FRET-Probe ICD functionality[47]. For the TSA, neutral or slightly alkaline pH was used for our two main model proteins, MDH (25 nM) and KRAS (50 nM)[48,49], as for the ICD assay, several acidic conditions were screened. Based on the preliminary testing, pH 5 was the mildest condition inducing denaturation of these model proteins in reasonable time window. At pH 5, MDH denaturates slowly with a 30-min lag-phase before the onset of the measurable denaturation process (Fig. 3a). When tested in PLI, using 5 and 50 μM NADH, a clear ligand-induced stabilization was observed showing also that lowered pH is compatible for the PLI monitoring. These results are comparable to those observed in TSA, indicating correct FRET-Probe function in the pH driven ICD setting (Fig. 3a). We further titrated MDH with several NADH concentrations and measured the signals multiple times at different time points. Based on the results obtained after 90 min incubation, we obtained an EC_{50} value of 4.7 ± 0.8 μM, which is well in line with that reported previously (Fig. 3b)[40].

KRAS (50 nM) was shown to be more sensitive to acidic pH in comparison to MDH, as there was no lag phase when assayed at pH 5 (Fig. 3c). To test another PLI assay, $KRAS^{G12V}$ was tested with guanosine-5'-triphosphate (GTP) as a ligand. GTP is essential for $KRAS^{G12V}$ stabilization as it keeps $KRAS^{G12V}$ in the nucleotide loaded state, and its affinity is very high even though the interaction in non-covalent. Addition of excess of GTP clearly stabilizes $KRAS^{G12V}$, by preventing apo-KRAS formation. Surprisingly, our results showed that $KRAS^{G12V}$ was stabilized already at nanomolar GTP concentration, much lower than previously measured with TSA (Fig. 3c)[34]. To confirm that the reduction in signal is related to GTP binding induced stabilization, a similar test was performed with ATP. As expected, TR-FRET signal level for the protein alone was in the same range as with ATP, even up to 10 μM concentration, confirming that GTP binding was the stabilizing factor (Fig. 3c and S4). To further study the PLI with GTP, TR-FRET signals for GTP titration were monitored at multiple time points. Longer incubation time increased the observed S/B ratio from 2.7 to 5.9, but no major change in the EC_{50} values of 4.5 ± 1.9, 2.6 ± 0.7, 3.5 ± 0.1 and 4.6 ± 0.3 nM, was observed at the four studied time points 30, 60, 90, and 120 min, respectively (Fig. 3d).

MDH and $KRAS^{G12V}$ exhibit different molecular weights and clearly also their stability differs (Fig. 2a and Fig. 3)[50,51]. However, these both proteins are quite unstable and thus pH 5 was already destabilizing the structure enough to enable assays with the FRET-Probe. This is not the case with all proteins, some highly stable in acidic conditions, and thus pH as a denaturant is not expected to be suitable for all proteins. In addition, pH might also affect the negatively charged FRET-Probe or its labels, even Eu^{3+}-chelate and Cy5 are rather stable. Thus, the method is expected to function only in rather mildly acidic conditions, which are unable to unfold stable proteins.

Denaturation by altering protein tertiary structure using alcohols

Alcohols such as ethanol, methanol, propanol, and butanol have been proposed for chemical denaturation of proteins due to their high content of hydrocarbon and water miscibility, facilitating the unfolding of native structure at a relatively low dose[24,52]. We selected ethanol and 1-propanol for FRET-Probe based protein denaturation testing at RT. In case of $KRAS^{G12V}$ (50 nM), a relatively high alcohol concentration was required for full denaturation, 1-propanol being more efficient than ethanol. Interestingly, 1-propanol also gave an improved concentration dependency in comparison to ethanol for $KRAS^{G12V}$ denaturation when 20, 25 and 30% alcohol were compared (Fig. 4a, Fig. S5a). Data for 1-propanol is shown at optimal 40 min time point as it demonstrates the best separation among the different alcohol concentrations tested. In 20% and 25% 1-propanol, maximal signal was reached after 40 min incubation, whereas in the 30% 1-propanol, maximal signal was monitored at 60 min (Fig. 4a). EDTA is expected to destabilize KRAS by chelating the Mg^{2+} required to preserve nucleotide loading,

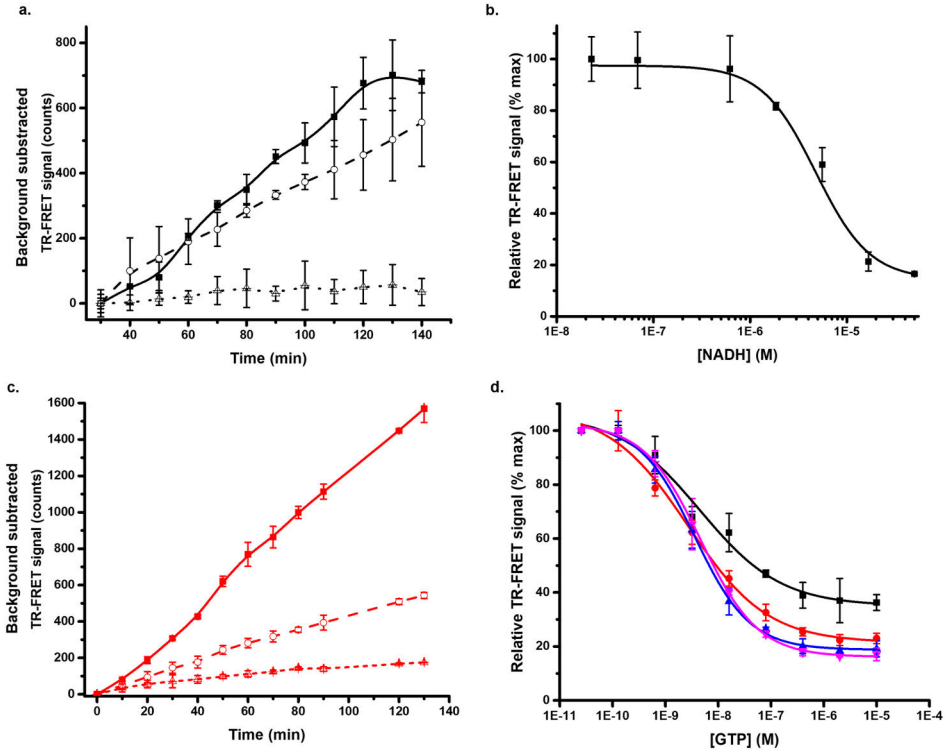

Figure 3. pH driven denaturation of $KRAS^{G12V}$ and MDH. (**a**) Time-dependent pH 5 induced denaturation of 25 nM MDH (solid) with 5 (dashed) and 50 µM (dotted) NADH monitored at RT using the FRET-Probe. (**b**) NADH titration in the presence of constant MDH (25 nM) concentration in pH 5 denaturation buffer, EC_{50} value was 4.7 ± 0.8 µM. (**c**) pH 5 induced denaturation of 50 nM $KRAS^{G12V}$ (solid) with 15 (dashed) and 2000 nM GTP (dotted) in a real-time FRET-Probe denaturation assay. (**d**) GTP titration in pH 5 denaturation buffer with constant $KRAS^{G12V}$ (50 nM) concentration monitored at 30 (black), 60 (red), 90 (blue) and 120 (magenta) min time points, EC_{50} values were 4.5 ± 1.9, 2.6 ± 0.7, 3.5 ± 0.1, 4.6 ± 0.3 respectively. Data represents mean ± SD (n = 3).

therefore, the assay was conducted in the presence of EDTA (0.2 mM) to examine its impact on denaturation rate (Fig. S5, Fig. S6a). With both alcohols, EDTA accelerated the denaturation rate and increased the overall TR-FRET signal compared to assays without EDTA. However, EDTA had basically no effect on optimal ethanol concentration (30%) (Fig. S5), but there was a significant effect on the optimal 1-propanol concentration, 20% in the absence and 4% in the presence of EDTA (Fig. S6a). When EDTA was tested with adagrasib and $KRAS^{G12C}$, IC_{50} values obtained after 60 min incubation were similar with 30% ethanol, 4% 1-propanol + EDTA, and 20% propanol after 60 min incubation, 18.1 ± 0.1, 26.6 ± 2.3, and 19.2 ± 1.8 nM, respectively (Fig. S6b). To test the EDTA effect on a non-covalent KRAS binder, GTP titration was conducted in the presence of 20% 1-propanol (Fig. 4b). Similar to the pH denaturation assay, we titrated GTP and measured TR-FRET signals at different time points from 30 to 120 min. We observed that the monitoring duration during alcohol denaturation had no effect on the EC_{50} values of GTP (3.5–5.2 nM), and only moderate effect on the S/B ratio.

MDH was more tolerant to pH than $KRAS^{G12V}$, and therefore, the alcohol denaturation experiments were tested with a wider range of alcohol concentrations. In a preliminary test, ~ 50% ethanol was sufficient for MDH denaturation. We demonstrated with $KRAS^{G12V}$ that ethanol is a milder denaturant than 1-propanol, and thus, we proceeded to test 1-propanol concentrations below 40%. MDH did not show any response at 20%, but denaturation was seen at 40% concentration (Fig. 4c). Based on this data we further tested 1-propanol at concentrations between 30 and 50% in a PLI assay with NADH. Interestingly, MDH was denatured at 30% 1-propanol with higher S/B than that obtained at 40% and 50% concentration of 1-propanol. This decrease in the S/B ratio might be attributed to protein aggregation or interference with the FRET-Probe binding at high alcohol concentration (Fig. 4d)[53]. Moreover, NADH stabilizing effect remained consistent across all tested alcohol concentrations with EC_{50} values at 60 min incubation of 29–38 µM (Fig. 4d). These results indicate that the high 1-propanol concentration does not affect the FRET-Probe binding, at least by affecting the EC_{50} values monitored.

Both tested alcohols are FRET-Probe compatible, but as in case of pH, target protein stability affects the needed optimal concentration. Based on the results, stable proteins cannot be efficiently used as over 50% alcohol

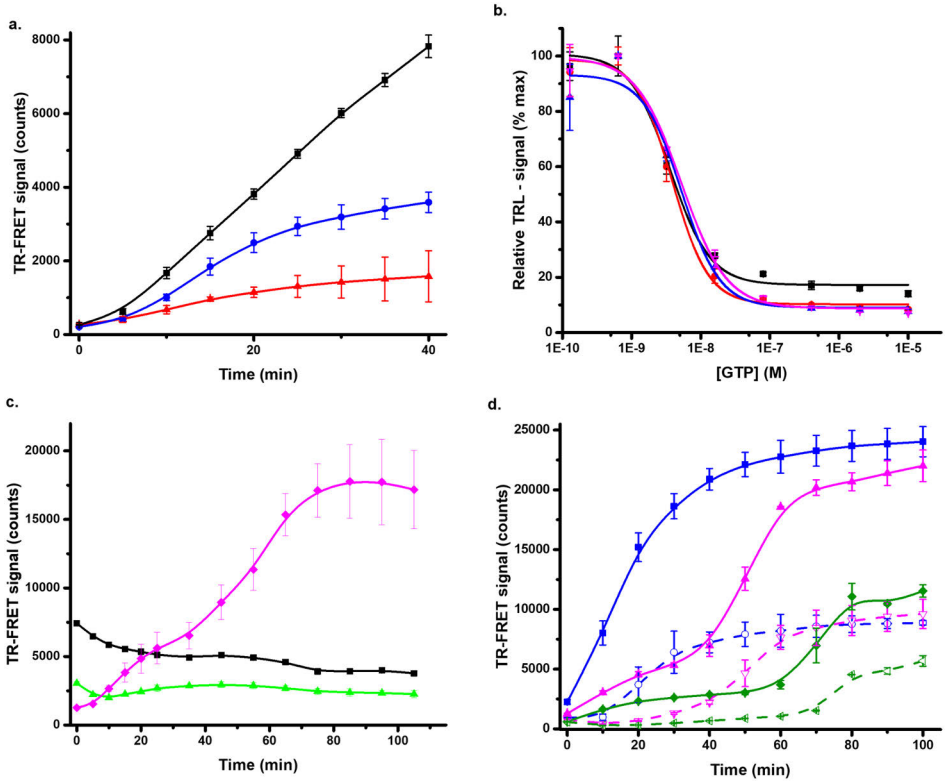

Figure 4. 1-propanol induced denaturation of $KRAS^{G12V}$ and MDH monitored with the FRET-Probe at RT. (**a**) Destabilization of $KRAS^{G12V}$ (50 nM) was observed with 20 (red), 25 (blue) and 30% (black) 1-propanol at RT. (**b**) GTP titration in 20% 1-propanol monitored at 30 (black), 60 (red), 90 (blue) and 120 (magenta) min, EC_{50} values were 3.6 ± 0.5, 3.8 ± 0.4, 5.2 ± 1.2 and 5.2 ± 0.7 respectively. (**c**) MDH 25 nM (black) denaturation with 20% (green) and 40% (magenta) 1-propanol. (**d**) Propanol denaturation of 25 nM MDH (solid) with 30 (blue), 40 (magenta) and 50% (green) in presence of NADH 50 µM (dashed), higher S/B was obtained at lower alcohol concentration. Data represents mean ± SD (n = 3).

concentrations are not easily usable, even no interference to FRET-Probe functionality was seen. In addition, evaporation starts to play a role when high alcohol concentration and long incubation times are used. Mild heating could induce alcohol effects, but this would increase the evaporation related variation. Interestingly, alcohol as a denaturant seems to increase the observed TR-FRET signal those observed in TSA, as lowered pH had opposite effect.

Denaturation by altering protein hydration using urea

Urea is one of the most used chemical denaturants, and it was selected as a third chemical denaturant to study the FRET-Probe[54]. Again, MDH and $KRAS^{G12V}$ were first investigated to assess the optimum urea concentration (0–5 M). Based on the preliminary tests, MDH denaturation was not measurable, as urea concentrations above 3 M had a negative effect on the FRET-Probe function (data not shown). Based on previous reports, MDH is relatively stable in urea, and denatures at 5–6 M urea concentration[55,56]. Therefore, we focused on $KRAS^{G12V}$ showing a clear response at low 1–3 M urea concentration (data not shown). When the urea concentration was studied further, incubation time was found to have an influence on the optimal urea concentration (Fig. 5a). This can be highlighted in an assay with 50 nM $KRAS^{G12V}$ monitored in the absence and presence of GTP (1 µM) and using 1, 1.5, and 2 M urea. The rank order of different urea concentrations was changed over time, as in the highest urea concentration (2 M) the observed TR-FRET signal saturated after 30 min, much faster than with the other two lower concentrations (Fig. 5b). No saturation was reached with either 1 or 1.5 M urea during the 60 min incubation. As in the previous tests with other denaturants, $KRAS^{G12V}$ stability also increased in the urea assay in the presence of GTP (Fig. 5b). When $KRAS^{G12V}$ denaturation reactions with and without GTP were compared at optimal 60 min time point, high S/B ratios of 15.1 and 20.3 were monitored with 1.5 and 2 M urea, respectively (Fig. 5b). Urea is typically used at high 5 to 8 M solutions and it is known that some proteins can tolerate these even these conditions for several hour[26,55–57]. However, we selected not to study protein denaturation with

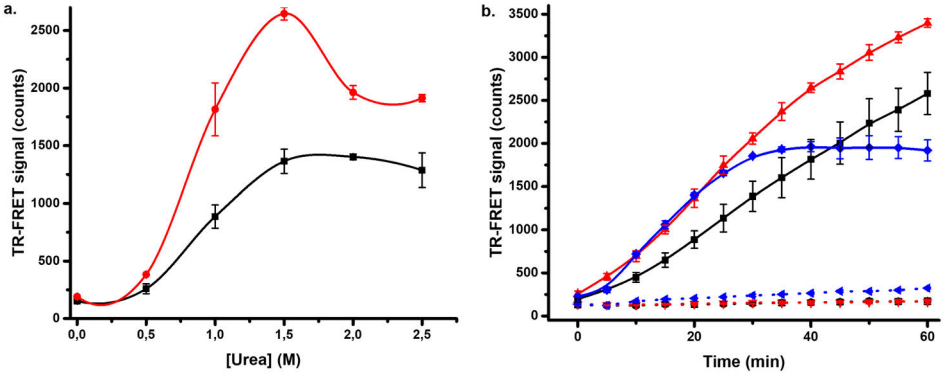

Figure 5. Urea induced denaturation of KRAS^{G12V}. (**a**) 0–2.5 M urea was titrated with 50 nM KRAS^{G12V} and monitored after 20 (black) and 40 min (red) of incubation at RT to examine the impact of incubation time on the optimal urea concentration. (**b**) The time dependence of KRAS^{G12V} 50 nM (solid) and stabilizing effect of 1 µM GTP (dashed) was observed with 1 (black), 1.5 (red) and 2 M (blue) urea, when KRAS^{G12V} denaturation was monitored with and without GTP after 60 min incubation in 1 and 1.5 M urea, S/B ratios of 15.1 and 20.3 were recorded, respectively. Data represents mean ± SD (n = 3).

extended period of time, but rather keep the assay time short. Urea denaturation can also be combined with heating, lowering the concentration demand, but to keep assay simple, we performed all assays at room temperature.

Comparison of denaturants using covalent KRAS^{G12C} inhibitors

Due to the different functionalities of the different denaturants with different proteins, it is important to optimize the assay for the selected target. Our results consistently demonstrated that alcohol denaturation occurs in concentration dependent manner and is dependent on the used alcohol. Also with mildly acidic pH, chosen model proteins were efficiently denatured in few hours. On the other hand, urea denaturation with KRAS showed consistent results and high S/B ratio with low variation, but on the other hand, MDH could not be denatured. As KRAS^{G12V} denaturation was visible with all denaturants, we next compared the conditions with several KRAS^{G12C} covalent inhibitors.

For the inhibitor testing, two early generation KRAS^{G12C} inhibitors (ARS1620 and ARS853) having high nM to low µM binding affinity were selected[58,59], together with two recently FDA approved nanomolar binders AMG510 (sotorasib) and MRTX849 (adagrasib)[60]. These covalent inhibitors bind to the GDP-loaded KRAS^{G12C} at the switch II pocket, interfering SOS binding and nucleotide exchange keeping RAS in its inactive form[61]. We analyzed these four inhibitors first by using SOS^{cat} catalyzed nucleotide exchange assay, which is based on quenching resonance energy transfer (QRET). In the assay, Eu^{3+}-GTP binds to KRAS^{G12C} giving high TRL-signal in the absence of inhibitor, whereas TRL-signal is low in the presence of nucleotide exchange inhibitor[34,62,63], All inhibitors showed expected stabilizing effect on KRAS^{G12C} structure and blocking of KRAS^{G12C} nucleotide exchange in the control experiments (Fig. 6, Fig. S7). The IC_{50} values with QRET nucleotide exchange for ARS853 and ARS1620 were 353 ± 50 nM, and 240 ± 36, respectively (Fig. 6a), and for adagrasib and sotorasib were 18.9 ± 0.7 nM, and 35.0 ± 7.1 nM, respectively (Fig. 6b).

Thereafter, we tested ARS853 and ARS1620 using pH 5 buffer for denaturation. IC_{50} values were calculated after 60 min incubation at RT and those were 1017 ± 383 and 123 ± 35 nM for ARS853 and ARS1620, respectively (Fig. S7a). Sotorasib and adagrasib were also tested under the same conditions, and IC_{50} values of 25.0 ± 3.3 and 25.0 ± 4.6 nM were observed, respectively (data not shown). IC_{50} values are protein concentration dependent in nature, and thus, inhibitors with binding affinity below half of the protein concentration will not yield accurate IC_{50} value, but rather monitors protein concentration. In these experiments, KRAS^{G12C} concentration was 50 nM, and thus, IC_{50} values observed might not be completely accurate. However, these values are highly similar to those reported earlier[60], but this highlights the importance of maintaining a low protein concentration in the assay, a distinctive aspect of our FRET-Probe methodology. Next, ARS1620 and ARS853 titration was conducted using 15–25% 1-propanol. We observed that the selected 1-propanol concentration influenced the monitored IC_{50} value calculated after 60 min incubation at RT (Fig. S7b). IC_{50} values for ARS853 and ARS1620 were 312 ± 23, 197 ± 62 and 1279 ± 98 nM and 40.1 ± 1.3, 54.0 ± 2.7, and 414 ± 8 nM in 15, 20, and 25% 1-propanol, respectively. The data clearly shows that the change in protein structure upon exposure to alcohol, is primarily dependent on the concentration of alcohol, but also that the used condition must be carefully selected, and values obtained in varying conditions might not be directly comparable[52].

Next, urea-induced denaturation was tested for KRAS^{G12C} with ARS853 or ARS1620 using the same 60 min incubation time as with other denaturants. The IC_{50} values with urea for ARS853 and ARS1620 were 1104 ± 126 and 289 ± 55, respectively (Fig. 6a). The data with urea is in line with those observed with pH 5 ICD and QRET nucleotide exchange, and interestingly, data obtained with 25% 1-propanol is also comparable. However, lower isopropanol concentration had a tendency to lower the obtained IC_{50} values obtained. When adagrasib and

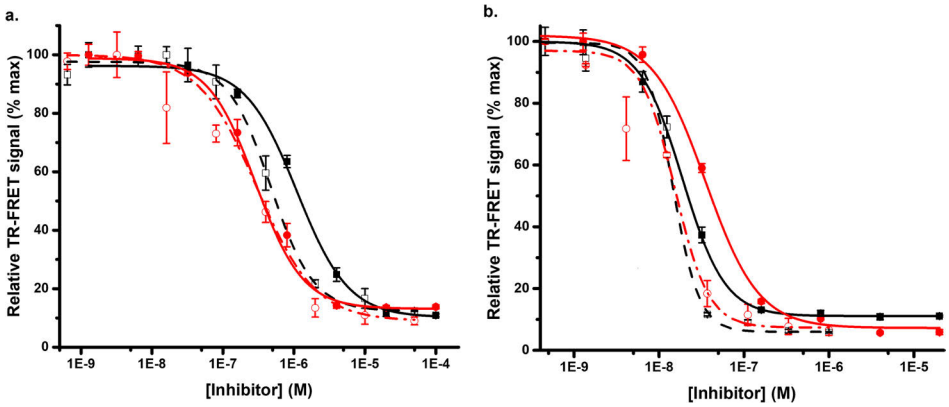

Figure 6. Urea denaturation monitoring with different KRAS^{G12C} covalent inhibitors using the FRET-Probe. (**a**) ARS853 (black) and ARS1620 (red) inhibitor titration for 50 nM KRAS^{G12C} with urea (dashed) in comparison to QRET nucleotide exchange assay data (solid). The IC_{50} values after 60 min with urea and QRET nucleotide exchange for ARS853 were 1104 ± 126 and 353 ± 50 nM, and for ARS1620 were 289 ± 55 and 240 ± 36 respectively. (**b**) Adagrasib (black) and sotorasib (red) inhibition of 50 nM KRAS^{G12C} with urea (dashed) in comparison to nucleotide exchange (solid). IC_{50} with urea and nucleotide exchange assay for adagrasib were 14.5 ± 1.1 and 18.9 ± 0.7 nM, and for sotorasib, 15.4 ± 1.2 and 35 ± 7.1 nM, respectively. Data represents mean ± SD (n = 3).

sotorasib were monitored with urea, similar highly comparable results were measured with the FRET-Probe in urea and pH 5 ICD assays, and in the nucleotide exchange, IC_{50} with urea were 14.5 ± 1.1 and 15.4 ± 1.2 for adagrasib and sotorasib, respectively (Fig. 6b).

In this study, we introduce the FRET-Probe method enabling denaturation studies both using heating and chemical denaturants. We selected two distinct model proteins, KRAS and MDH exhibiting contrasting characteristics with regards to size and structure, and used these proteins to analyze functionality of different denaturation conditions. Following a comprehensive study of the model proteins with three chemical denaturants, each having a unique mechanism of action, our data showed that MDH, was more tolerant to all three denaturants than KRAS, even both proteins are relatively unstable. MDH cannot be denatured in used urea concentrations in a used incubation time at RT. In contrast, KRAS was measurable with all denaturants and its stability can be easily further adjusted by using varying Mg^{2+} concentrations or EDTA. As an opposite of MDH, urea denaturation was preferred over alcohols and pH with KRAS, in terms of S/B, reproducibility, and kinetics. As the FRET-Probe method using single denaturant concentration at RT is mainly targeted to PLI analysis, ligand binding studies were performed to compare the functionality. Importantly, IC_{50} values obtained using varying ICD conditions were comparable and also in line with values in literature and reference methods. As an exception, low alcohol concentrations had a tendency to provide lower IC_{50} values with KRAS^{G12C} inhibitors than other methods. Therefore, it is clear that method selection is dependent on the studied protein. KRAS^{G12C} inhibitor studies also showed the importance of assay sensitivity, as the FRET-Probe could monitor IC_{50} values also for nanomolar binders. This is not possible with other label-free stability assays, as their limited sensitivity forces the use of micromolar level target protein concentrations.

Methods

The detailed list of materials and instrumentation, synthesis, and purification of proteins and Eu^{3+} conjugates are presented in the (supplementary data).

Thermal shift assays

All FRET-Probe TSA were conducted in triplicates using a single-step protocol, by adding the sample protein in 5 µL and FRET-Probe (0.5 nM) in 20 µL volumes. All concentrations are reported in a 25 µL final volume. Assays were performed in an assay buffer containing 10 mM HEPES (pH 7.5) supplemented with 0.001% (v/v) Triton X-100. Trastuzumab (20 nM), SOS^{cat} (10 nM), MDH (25 nM), and KRAS (25–150 nM) were all assayed between 35–90 °C using 5 °C steps and heating the sample 2 min at each step prior TR-FRET measurement. Additionally, MDH was assayed in the presence of NADH (0–50 µM) and KRAS^{G12C} with adagrasib (0–0.25 µM) in a buffer with or without additional $MgCl_2$ (0.2 mM).

TSA control assays were performed using the Protein-Probe. Assay in conducted using two step protocol, in which protein concentration was calculated in 8 µL volume used for sample heating. Samples were heated 3 min at each temperature followed by addition of 65 µL of Protein-Probe detection solution and TRL-signal monitoring. KRAS^{WT}, KRAS^{G13D} and KRAS^{Q61R} (150 nM) were added in sample buffer (10 mM HEPES, (v/v) 0.001% Triton X-100) and Protein-Probe detection solution containing citrate–phosphate buffer (7.7 mM Na_2HPO_4 and 6.1 mM citric acid, pH 4) supplemented with 0.01% (v/v) Triton X-100, 3.5 µM HIDC, and 1 nM Eu^{3+}-probe.

SYPRO Orange and GloMelt assays were performed by a one-step protocol using 5 µM $KRAS^{Q61R}$ in buffer (20 mM HEPES (pH 7.5), 100 mM NaCl, 5% glycerol). Samples (16 µL) and SYPRO Orange/GloMelt solution (4 µL) were combined prior to the first heating step in a white 96-well plate (BioRad). The samples were incubated for 1.5 min at each temperature, followed by fluorescence signal measurement every 2 °C. SYPRO Orange was used at 5 × (stock 5000 ×) and GloMelt at 1 × final concentration (stock 200x). Signals were monitored using 460 and 485 nm excitation and 510 and 590 nm emission wavelengths for SYPRO Orange and GloMelt, respectively.

FRET-Probe isothermal chemical denaturation assays

All isothermal chemical denaturation (ICD) assays were conducted in triplicates at RT using a single-step protocol with 25 µL final volume. Sample protein and ligand were added in 5 µL in a buffer (10 mM HEPES (pH 7.5), 10 mM NaCl, (v/v) 0.01% Brij 30) without denaturant. FRET-Probe (0.5 nM) was added to the assay buffer supplemented with chemical denaturant, urea (0–5 M), ethanol (0–30%) or 1-propanol (0–50%). Additionally, 0.2 mM EDTA was used in combination with alcohols. Acid denaturation was performed in citrate phosphate buffer (10.3 mM Na_2HPO_4 and 4.85 mM citric acid, pH 5) supplemented with 0.01% (v/v) Brij 30.

In all ICD protein assays, time-resolved Förster resonance energy transfer (TR-FRET) signal was monitored kinetically at multiple time points during 150 min incubation. In all assays with protein binding ligands, 30 min preincubation prior denaturant addition was performed. In acid induced denaturation assay, GTP (0–2 µM) and NADH (0–50 µM) were titrated with $KRAS^{G12V}$ and MDH, respectively. 1-propanol (30–50%) ICD assays were also performed for MDH in the presence of NADH (0–50 µM) and (20%) for $KRAS^{G12V}$ using GTP (0–10 µM). Ethanol (30%) and 1-propanol (4 & 20%) were tested with $KRAS^{G12C}$ using adagrasib (2 µM) single concentration or in a titration (0–10 µM). ARS1620 and ARS853 (0–50 µM) or adagrasib and sotorasib (0–2 µM) titrations were performed with $KRAS^{G12C}$ using pH 5, 1-propanol (15–25%) and urea (1 M) as a denaturant. Additionally, urea was tested with 1 µM GTP with $KRAS^{G12V}$.

Nucleotide exchange assay

The nucleotide exchange was performed by incubating $KRAS^{G12C}$ (50 nM) with the covalent inhibitor, sotorasib and adagrasib (0–1 µM) or ARS1620 and ARS853 (0–50 µM) for 30 min in 10 µL volume. Thereafter, 5 µL of detection solution (3 µM Q14, 10 nM Eu^{3+}-GTP) was added and reaction was initiated with 10 nM SOS^{cat}. TRL-signals were monitored multiple times during 60 min incubation. Assays were performed in a buffer containing 20 mM HEPES (pH 7.5) 1 mM $MgCl_2$, 10 mM NaCl, 0.01% Triton X-100. The assay was performed using triplicate reactions.

Data analysis

In all assays, the signal-to-background ratio (S/B) was calculated as μ_{max}/μ_{min} and coefficient of variation (CV%) (σ/μ) *100, where µ is the mean value and σ is the standard deviation. T_m values, EC_{50}, and IC_{50} values were obtained using standard sigmoidal fitting functions with fitting equation, y = A2 + (A1-A2)/(1 + (x/ × 0)^p). Data were analyzed using Origin 2016 software (Origin Lab, Northampton, MA).

Conclusion

Protein denaturation by heating (TSA) is the most often used method to study protein stability and especially PLIs. Although ICD is often proposed to provide biologically more relevant and accurate information, fluorescence-based TSA assays are simpler and faster to perform especially with a panel of ligands[21,22]. This study demonstrates that the novel FRET-Probe assay design is high throughput compatible, and both heat and temperature can be equally used for protein denaturation. The FRET-Probe assay allows assays with nanomolar sensitivity independently of the denaturation condition, and also PLI studies using single-step protocol. This is a remarkable improvement to our previously developed Protein-Probe family of assays and compared to current commercial methods typically working at micromolar protein concentrations. Assay sensitivity not only saves materials, but also enables accurate binding studies also for nanomolar binders. This makes the FRET-Probe assay design a powerful tool especially for high throughput ligand screening without a need for special instrument but using a standard plate reader under isothermal condition. However, the exact binding mechanism of the FRET-Probe is unknown, and the universality of the method for different types of proteins is yet to be unraveled. It is likely that not all proteins can be studied at low nanomolar concentrations and that mild denaturation conditions used in the study are not equally suitable for all proteins. However, as ICD can be easily combined with mild heating, some of the more stable proteins might also be studied with the ICD method. It also remains unknown if harsher denaturation conditions could be used with an increased FRET-Probe concentration or with varying buffer composition. For this, more research to understand the FRET-Probe binding mechanism is needed.

Data availability

Data for this article will be made available from the corresponding author upon reasonable request.

Received: 27 July 2023; Accepted: 3 November 2023
Published online: 16 November 2023

References

1. Deller, M. C., Kong, L. & Rupp, B. Protein stability: A crystallographer's perspective. *Acta Crystallogr. F Struct. Biol. Commun.* **72**, 72–95 (2016).
2. Moreau, M. J. J., Morin, I. & Schaeffer, P. M. Quantitative determination of protein stability and ligand binding using a green fluorescent protein reporter system. *Mol. Biosyst.* **6**, 1285–1292 (2010).

3. Brandts, J. F. & Lin, N. Study of strong to ultralight protein interactions using differential scanning calorimetry1-A second major advantage of the DSC method over equi-&copy. *Biochemistry* **29**, 6927–6940 (1990).
4. Pantoliano, M. W. *et al.* High-density miniaturized thermal shift assays as a general strategy for drug discovery. *SLAS Discov.* **6**, 429–440 (2001).
5. Matulis, D., Kranz, J. K., Salemme, F. R. & Todd, M. J. Thermodynamic stability of carbonic anhydrase: measurements of binding affinity and stoichiometry using thermofluor. *Biochemistry* **44**, 5258–5266 (2005).
6. Lo, M. C. *et al.* Evaluation of fluorescence-based thermal shift assays for hit identification in drug discovery. *Anal Biochem* **332**, 153–159 (2004).
7. Miles, A. J. & Wallace, B. A. Circular dichroism spectroscopy of membrane proteins. *Chem Soc Rev* **45**, 4859–4872 (2016).
8. Ireland, S. M., Sula, A. & Wallace, B. A. Thermal melt circular dichroism spectroscopic studies for identifying stabilising amphipathic molecules for the voltage-gated sodium channel NavMs. *Biopolymers* **109**, e23067 (2018).
9. Johnson, C. M. Differential scanning calorimetry as a tool for protein folding and stability. *Arch Biochem Biophys* **531**, 100–109 (2013).
10. Fiedler, S., Cole, L. & Keller, S. Automated circular dichroism spectroscopy for medium-throughput analysis of protein conformation. *Anal Chem* **85**, 1868–1872 (2013).
11. Malik, K., Matejtschuk, P., Thelwell, C. & Burns, C. J. Differential scanning fluorimetry: rapid screening of formulations that promote the stability of reference preparations. *J Pharm Biomed Anal* **77**, 163–166 (2013).
12. Zbacnik, T. J. *et al.* Role of buffers in protein formulations. *J Pharm Sci* **106**, 713–733 (2017).
13. Hawe, A., Sutter, M. & Jiskoot, W. Expert review extrinsic fluorescent dyes as tools for protein characterization. *Pharm. Res.* **25**, 1487–1499 (2008).
14. Mcclure, S. M., Ahl, P. L. & Blue, J. T. High throughput differential scanning fluorimetry (DSF) formulation screening with complementary dyes to assess protein unfolding and aggregation in presence of surfactants. *Pharm. Res.* **35**, 1–10 (2018).
15. Dart, M. L. *et al.* Homogeneous assay for target engagement utilizing bioluminescent thermal shift. *ACS Med. Chem. Lett.* **9**, 546–551 (2018).
16. Sorenson, A. E. & Schaeffer, P. M. High-throughput differential scanning fluorimetry of GFP-tagged proteins. In *Targeting enzymes for pharmaceutical development: methods and protocols* (ed. Labrou, N.) 69–85 (Humana Press, 2020). https://doi.org/10.1007/978-1-0716-0163-1_5.
17. Ronzetti, M. H. *et al.* Application of temperature-responsive HIS-tag fluorophores to differential scanning fluorimetry screening of small molecule libraries. *Front. Pharmacol.* **13**, 1040039 (2022).
18. Lasagna, M., Gratton, E., Jameson, D. M. & Brunet, J. E. Apohorseradish peroxidase unfolding and refolding: Intrinsic tryptophan fluorescence studies. *Biophys. J.* **76**, 443–450 (1999).
19. Wen, J., Lord, H., Knutson, N. & Wikström, M. Nano differential scanning fluorimetry for comparability studies of therapeutic proteins. *Anal. Biochem.* **593**, 113581 (2020).
20. Ghisaidoobe, A. B. T. & Chung, S. J. Intrinsic tryptophan fluorescence in the detection and analysis of proteins: a focus on förster resonance energy transfer techniques. *Int. J. Mol. Sci.* **15**, 22518–22538 (2014).
21. Schön, A., Brown, R. K., Hutchins, B. M. & Freire, E. Ligand binding analysis and screening by chemical denaturation shift. *Anal. Biochem.* **443**, 52–57 (2013).
22. Svilenov, H., Markoja, U. & Winter, G. Isothermal chemical denaturation as a complementary tool to overcome limitations of thermal differential scanning fluorimetry in predicting physical stability of protein formulations. *Eur. J. Pharm. Biopharm.* **125**, 106–113 (2018).
23. Jackson, S. E. How do small single-domain proteins fold?. *Fold Des.* **3**, 81–91. https://doi.org/10.1016/S1359-0278(98)00033-9 (1998).
24. Herskovits, T. T., Gadegbeku, B. & Jaillet, H. On the structural stability and solvent denaturation of proteins: I. Denaturation by the alcohols and glycols. *J. Biol. Chem.* **245**, 2588–2598 (1970).
25. Rossky, P. J. Protein denaturation by urea: Slash and bond. *Proc. Natl. Acad. Sci. U.S.A.* **105**, 16825–16826 (2008).
26. Das, A. & Mukhopadhyay, C. Urea-mediated protein denaturation: A consensus view. *J. Phys. Chem. B* **113**, 12816–12824 (2009).
27. Hua, L., Zhou, R., Thirumalai, C. D. & Berne, B. J. Urea denaturation by stronger dispersion interactions with proteins than water implies a 2-stage unfolding. *Proc. Natl. Acad. Sci. U.S.A.* **105**, 16928–16933 (2008).
28. Talley, K. & Alexov, E. On the pH-optimum of activity and stability of proteins. *Proteins Struct. Funct. Bioinform.* **78**, 2699–2706 (2010).
29. Rizzo, J. M. *et al.* Application of a high-throughput relative chemical stability assay to screen therapeutic protein formulations by assessment of conformational stability and correlation to aggregation propensity. *J. Pharm. Sci.* **104**, 1632–1640 (2015).
30. Valtonen, S. *et al.* Sensitive, homogeneous, and label-free protein-probe assay for antibody aggregation and thermal stability studies. *MAbs* **13**, 1955810 (2021).
31. Vuorinen, E. *et al.* Sensitive label-free thermal stability assay for protein denaturation and protein-ligand interaction studies. *Anal. Chem.* **92**, 3512–3516 (2020).
32. Vuorinen, E. *et al.* Protease substrate-independent universal assay for monitoring digestion of native unmodified proteins. *Int. J. Mol. Sci.* **22**, 6362 (2021).
33. Valtonen, S. *et al.* Nanomolar protein–protein interaction monitoring with a label-free protein-probe technique. *Anal. Chem.* **92**, 15781–15788 (2020).
34. Kopra, K. *et al.* Thermal shift assay for small GTPase stability screening: evaluation and suitability. *Int. J. Mol. Sci.* **23**, 7095 (2022).
35. Lourenço, E. C. Synthesis of new enzyme stabilisers inspired by compatible solutes of hyperthermophilic microorganisms (Doctoral dissertation, Universidade NOVA de Lisboa (Portugal)) (2013).
36. Pérez, L. M. *et al.* Conformational characterization of a novel anti-HER2 candidate antibody. *PLoS ONE* **14**, e0215442 (2019).
37. Yavşan, E. & Uzunlar, S. K. Fluorescence-based thermal stability screening is concentration-dependent and varies with protein size. *Front. Life Sci. RT* **4**, 62–67 (2023).
38. Fukadas, H., Sturtevantq, J. M. & Quiocho, F. A. Thermodynamics of the binding of L-arabinose the L-arabinose-binding protein of Escherichia and of D-galactose to coli. *J. Biol. Chem.* **258**, 13193–13198 (1983).
39. Cimmperman, P. *et al.* A quantitative model of thermal stabilization and destabilization of proteins by ligands. *Biophys. J.* **95**, 3222–3231 (2008).
40. Shore, J. D., Evans, S. A., Holbrook, J. J. & Parker, D. M. NADH binding to porcine mitochondrial malate dehydrogenase. *J. Biol. Chem.* **254**, 9059–9062 (1979).
41. Rudack, T., Xia, F., Schlitter, J., Kötting, C. & Gerwert, K. The role of magnesium for geometry and charge in GTP hydrolysis, revealed by quantum mechanics/Molecular mechanics simulations. *Biophys. J.* **103**, 293–302 (2012).
42. Freire, E., Schön, A., Hutchins, B. M. & Brown, R. K. Chemical denaturation as a tool in the formulation optimization of biologics. *Drug. Discov. Today* **18**, 1007–1013 (2013).
43. Lazar, K. L., Patapoff, T. W. & Sharma, V. K. Cold denaturation of monoclonal antibodies. *MAbs* **2**, 42–52 (2010).
44. Duy, C. & Fitter, J. How aggregation and conformational scrambling of unfolded states govern fluorescence emission spectra. *Biophys. J.* **90**, 3704–3711 (2006).
45. Gao, K., Oerlemans, R. & Groves, M. R. Theory and applications of differential scanning fluorimetry in early-stage drug discovery. *Biophys. Rev.* **2**, 85–104 (2020).

46. Wafer, L., Kloczewiak, M., Polleck, S. M. & Luo, Y. Isothermal chemical denaturation of large proteins: Path-dependence and irreversibility. *Anal. Biochem.* **539**, 60–69 (2017).
47. Mok, Y. K., De Prat Gay, G., Butler, P. J. & Bycroft, M. Equilibrium dissociation and unfolding of the dimeric human papillomavirus strain-16 E2 DNA-binding domain. *Protein Sci.* **5**, 310–319 (1996).
48. Huynh, M. V. *et al.* Oncogenic KRAS G12C: Kinetic and redox characterization of covalent inhibition. *J Biol Chem* **298**, 102186 (2022).
49. Han, X. *et al.* Enzymatic activity analysis and catalytic essential residues identification of brucella abortus malate dehydrogenase. *Sci. World J.* https://doi.org/10.1155/2014/973751 (2014).
50. Li, Q., Scholl, Z. N. & Marszalek, P. E. Unraveling the mechanical unfolding pathways of a multidomain protein: Phosphoglycerate kinase. *Biophys. J.* **115**, 46–58 (2018).
51. Vishwanath, S., De Brevern, A. G. & Srinivasan, N. Same but not alike: structure, flexibility and energetics of domains in multi-domain proteins are influenced by the presence of other domains. *PLoS Comput. Biol.* **14**, e1006008 (2018).
52. Bull, H. B. & Breese, K. Interaction of alcohols with proteins. *Biopolymers* **17**, 2121–2131 (1978).
53. Giugliarelli, A., Sassi, P., Paolantoni, M., Onori, G. & Cametti, C. Heat-denatured lysozyme aggregation and gelation as revealed by combined dielectric relaxation spectroscopy and light scattering measurements. *J. Phys. Chem. B* **116**, 10779–10785 (2012).
54. England, J. L. & Haran, G. Role of solvation effects in protein denaturation: From thermodynamics to single molecules and back. *Annu. Rev. Phys. Chem.* **62**, 257–277 (2011).
55. Diamant, S., Eliahu, N., Rosenthal, D. & Goloubinoff, P. Chemical chaperones regulate molecular chaperones in vitro and in cells under combined salt and heat stresses. *J. Biol. Chem.* **276**, 39586–39591 (2001).
56. Wang, G. F., Cao, Z. F., Zhou, H. M. & Zhao, Y. F. Comparison of inactivation and unfolding of methanol dehydrogenase during denaturation in guanidine hydrochloride and urea. *Int. J. Biochem. Cell Biol.* **32**, 873–878 (2000).
57. Bennion, B. J. & Daggett, V. The molecular basis for the chemical denaturation of proteins by urea. *PNAS* **100**, 5142–5147 (2003).
58. Janes, M. R. *et al.* Targeting KRAS mutant cancers with a covalent G12C-specific inhibitor. *Cell* **172**, 578–589 (2018).
59. Lito, P., Solomon, M., Li, L. S., Hansen, R. & Rosen, N. Cancer therapeutics: Allele-specific inhibitors inactivate mutant KRAS G12C by a trapping mechanism. *Science* **351**, 604–608 (2016).
60. Kwan, A. K., Piazza, G. A., Keeton, A. B. & Leite, C. A. The path to the clinic: a comprehensive review on direct KRAS G12C inhibitors. *J. Exp. Clin. Cancer Res.* **41**, 27 (2021).
61. Pagba, C. V. *et al.* KRAS Inhibitor that simultaneously inhibits nucleotide exchange activity and effector engagement. *Cite This ACS Bio. Med. Chem. Au.* **2022**, 617–626 (2022).
62. Kopra, K. *et al.* Homogeneous dual-parametric-coupled assay for simultaneous nucleotide exchange and KRAS/RAF-RBD interaction monitoring. *Anal. Chem.* **92**, 4971 (2020).
63. Kopra, K. *et al.* High-throughput dual screening method for RAS activities and inhibitors. *Anal. Chem.* **89**, 4508–4516 (2017).

Acknowledgements

This work was supported by the Academy of Finland (323433/K.K., 329012/K.K., and 353324/K.K.), Otto A. Malm foundation and Finnish Academy of Science and Letters (foundation of Vilho, Yrjö, and Kalle Väisälä). We thank Dr. William Gillette and his team from Leidos Biomedical Research, Inc. and Frederick National Laboratory for Cancer Research for providing us with KRAS and the related proteins.

Author contributions

R.M. contributed to data acquisition, figures preparation and writing original manuscript, N.V. contributed to data acquisition, A.K. contributed to data acquisition, M.M. contributed to validation and reviewing, H.H. contributed to supervision, reviewing & editing and funding acquisition. K.K. contributed to conceptualization, design, data interpretation, writing, reviewing and editing.

Competing interests

The authors declare the following competing financial interest(s): K.K. and H.H. have commercial interest through QRET Technologies. All the remaining authors have no competing interests.

Additional information

Supplementary Information The online version contains supplementary material available at https://doi.org/10.1038/s41598-023-46720-w.

Correspondence and requests for materials should be addressed to R.M.

Mahran, R., Kapp, J., Valtonen, S., Plückthun, A., Härmä, H., Pantsar, T. and Kopra, K.
Beyond KRAS(G12C): biochemical and computational characterization of sotorasib and adagrasib binding specificity and the critical role of H95 and Y96.

IV

Beyond KRAS(G12C): biochemical and computational characterization of sotorasib and adagrasib binding specificity and the critical role of H95 and Y96

Randa Mahran,[a,#] Jonas Kapp,[b,#] Salla Valtonen,[a] Allison Champagne,[c] Jinying Ning,[d] William Gillette,[c] Andrew G. Stephen,[c] Feng Hao,[d] Andreas Plückthun,[b] Harri Härmä,[a] Tatu Pantsar,[e,1] and Kari Kopra[a,1]

[a] Department of Chemistry, University of Turku, Henrikinkatu 2, 20500 Turku, Finland
[b] Department of Biochemistry, University of Zurich, Winterthurerstrasse 190, 8057 Zurich, Switzerland
[c] Leidos Biomedical Research, Inc., Frederick National Laboratory for Cancer Research, 8560 Progress Dr., Frederick, MD 21702, USA
[d] KYinno Biotechnology Co., Ltd, Yizhuang Biomedical Park, No.88, Kechuang Six Street, BDA, Beijing, China, 101111
[e] School of Pharmacy, Faculty of Health Sciences, University of Eastern Finland, Yliopistonrinne 3, 70210 Kuopio, Finland

Mutated KRAS proteins are frequently expressed in some of the most lethal cancers, and it has been a target of active drug discovery efforts for decades. Lately, KRAS(G12C) switch-II pocket targeting covalent small molecule inhibitors have finally reached clinical practice. Sotorasib (AMG-510), was the first FDA approved covalent inhibitor to treat KRAS(G12C) positive non–small cell lung cancer (NSCLC), followed soon by adagrasib (MRTX849). Both drugs target the GDP-bound KRAS(G12C), exploiting the strong nucleophilicity of the acquired cysteine. Here we evaluate the similarities and differences between sotorasib and adagrasib in their RAS switch-II pocket binding by applying both biochemical, cellular, and computational methods. The exact knowledge on switch-II pocket binding enables targeting of this site by other non-covalent inhibitors for KRAS mutants beyond G12C. We show that adagrasib is strictly KRAS, but not KRAS(G12C) specific, due to the strong and unreplaceable H95 interaction. Unlike adagrasib, sotorasib is not that dependent on H95 for its binding, while its RAS isoform agnostic interactions to Y96 are more profound. Our results emphasize that the switch-II pocket is accessible beyond oncogenic G12C and aid in understanding of the molecular mechanism behind the clinically observed drug resistance related to the secondary mutations on KRAS H95 and Y96.

Keywords: GTPases, RAS, adagrasib, sotorasib, thermal stability, molecular dynamics simulations

Significance

When KRAS(G12C) covalent inhibitors adagrasib and sotorasib reached the clinics, it created new hope to target also other mutated KRAS oncogenes beyond G12C. For this targeting the switch-II pocket, which is also targeted by both adagrasib and sotorasib, has been the most promising approach. Non-covalent mechanisms behind these successful KRAS(G12C) inhibitors have already provided valuable information to covalently target also other KRAS mutants. Our biochemical assays revealed that sotorasib have weak binding to all RAS isoforms, while adagrasib interacts only with KRAS. Molecular dynamics simulations and mutation analysis suggest that the KRAS specificity of adagrasib is created through His-95, as sotorasib is dependent on Tyr-96, conserved in all RAS isoforms. This rationalizes the clinical finding revealing adagrasib tolerance of an acquired secondary mutation at Tyr-96. Additionally, these findings can be used to support ongoing development of KRAS or pan-RAS drugs also for oncogenic RAS lacking a cysteine residue.

Author contributions: T.P. and K.K. designed research; R.M., J.K., S.V., A.C., J.N, T.P., and K.K. performed research; R.M., J.K., S.V., A.C., J.N, W.G., A.G.S., F.H., T.P., and K.K. analyzed data; and R.M., J.K., A.P., H.H., T.P., and K.K. wrote the paper.

The authors declare the following competing financial interest(s): Kari Kopra and Harri Härmä have commercial interest through QRET Technologies Ltd. Jinying Ning and Feng Hao have commercial interest through KYinno Biotechnology Co., Ltd.

Data deposition: The molecular dynamics simulations trajectories are freely available at https://doi.org/10.5281/zenodo.XXXXXX.

[#] These authors corresponded equally in this work

[1]To whom correspondence may be addressed. Email: tatu.pantsar@uef.fi (molecular dynamics simulations) and kari.kopra@utu.fi (wet laboratory experiments).

This article contains supporting information online at

Introduction

KRAS is frequently mutated in cancer, and RAS oncogenes have been reported in almost 30% of all malignant tumors.[1] Most commonly mutated RAS oncogenes are found in solid tumors, including pancreatic adenocarcinomas, colorectal cancers, and melanoma, creating RAS a potential target for a novel anti-cancer drug.[2–5] Mutations promote RAS to occur mainly in the GTP-bound active state, due to their diminished intrinsic GTPase activity, insensitivity to GTPase activating protein (GAPs) or elevated nucleotide exchange.[6,7] These changes are associated to tumorigenesis as a result of the constantly active RAS pathways and RAS effectors, promoting uncontrolled cell division and epithelial invasion. More than 85% of HRAS and 95% of both KRAS and NRAS mutations occur at the so called ''hotspot'' codons, G12, G13 and Q61.[8] In case of KRAS, G12 mutations are the most frequent, and for example in case of non–small cell lung cancer (NSCLC), this mutation is found in 40% of all cases.[9] RAS was found to be a difficult drug target, and before success with the covalent G12C inhibitors, it was even considered as an ''undruggable'' target.[1,10–13]

Covalent inhibitors have the advantage of prolonged target engagement and they have already proved their capabilities in clinical trials, also in the context of KRAS(G12C).[14–16] Two covalent KRAS(G12C) inhibitors engaging the cryptic switch-II pocket,[17,18] sotorasib (AMG-510; Lumakras) and adagrasib (MRTX849; Krazati), have been recently approved by FDA for the treatment of non-small cell lung cancer (NSCLC). Both inhibitors target namely the GDP-bound state of KRAS(G12C) trapping the protein into this inactive state, thus, inhibiting the overactive KRAS downstream signaling. Successful targeting of KRAS(G12C) rely not only on the unique cysteine, which enables the covalent bond formation, but also on the intrinsic GTPase activity of KRAS(G12C).[19–21] This feature enables targeting of GDP-bound state of KRAS(G12C), which is considered unviable for some other oncogenic KRAS alleles (e.g. G12R and Q61R) that are mainly found at GTP-bound active state.[22,23]

Switch-II pocket (SII-P) has been under heavy investigation, and due to its dynamic nature, many of the designed peptides and small molecule ligands exploit this cryptic pocket for their binding to RAS.[24–30] The same pocket was also targeted with the early covalent inhibitors such as ARS-1620, which binding properties, however, are significantly compromised in comparison to the clinically approved sotorasib and adagrasib.[31,32] These two inhibitors have demonstrated efficacy in clinical trials as a monotherapy and they are tested in combination with other treatment modalities. Recently, resistance and reactivation of RAS pathways after inhibitor treatment was reported occurring mainly through acquired secondary mutation in KRAS(G12C) SII-P.[32–40] The detailed information about the binding specificities and interactions of these compounds towards RAS mutants is unfortunately still incomplete.

Recently, SII-P engagement was studied for the first time in a systematic fashion by using especially sotorasib, but also adagrasib as model compounds.[18] Shokat *et al.* highlighted that the SII-P is accessible also for noncovalent ligands in case of other KRAS mutants beyond G12C. In this study, we determine the detailed binding mechanism of sotorasib and adagrasib and reasoned how tolerance through mutation at H95 and Y96 occurs. Using ultra-sensitive

thermal stability assay (TSA)[41–43] and nucleotide exchange assays[44–47] with HRAS, NRAS and multiple KRAS mutants including H95L and Y96D, we demonstrate specificity profiles for sotorasib and adagrasib. These biochemical results are supported by cell-based assays, and molecular dynamics (MD) simulations, providing mechanistic atomic level insights in their non-covalent binding specificities and suggest an undisclosed resistance mechanism of Y96D. Both biochemical and computational data reveals the unreplaceable nature of H95 and Y96 for sotorasib and adagrasib, but also how direct target engagement of non-G12C oncogenic KRAS mutants might occur through the switch-II pocket, and how KRAS specificity over NRAS and HRAS through H95 can be exploited. Together, data also revealed that as adagrasib is KRAS specific, sotorasib can equally target not only KRAS(G12C), but also NRAS and HRAS(G12C), potentially bringing new possibilities for cancer treatment.

Results

Adagrasib interacts specifically with KRAS as sotorasib equally targets all RAS(G12C) forms

Sotorasib and adagrasib are clinically validated KRAS(G12C) inhibitors occupying the same SII-P and rely on covalent binding to Cys-12 in an inactive GDP-bound KRAS (Figure 1A).[20,48,49] To understand similarities and dissimilarities between these binders, we started by determining the biochemical binding of sotorasib and adagrasib for RAS beyond KRAS(G12C).[46,50–52] In a nucleotide exchange assay with KRAS(G12C), IC_{50} values of sotorasib and adagrasib were 20.2 ± 1.9 and 4.3 ± 0.6 nM, respectively (Figure S1A). These values are in expected range, as both inhibitors are known to have low nanomolar KRAS(G12C) binding affinity.[41,50,53] In TSA, performed by two external probes for differential scanning fluorimetry (DSF), Protein-Probe (PP) and 8-anilinonaphthalene-1-sulfonic acid (ANS), the binding is equally monitored (Figure S1B). With both techniques, sotorasib induced slightly higher increase in KRAS(G12C) thermal stability (ΔT_m PP; 26.4 °C, ANS; 25.8 °C) over adagrasib (ΔT_m PP; 17.4 °C, ANS; 19.9 °C).

When the same binding analyses were performed with KRAS(WT), especially adagrasib showed an effect (Figure 1B, S2A, and S3). In a QRET nucleotide exchange assay with Eu^{3+}-GTP for KRAS(WT), IC_{50} value of 200 ± 20 nM for adagrasib was monitored (Figure 1B), and the result was confirmed (IC_{50} = 303 ± 51 nM) with a TR-FRET assay using AF647-GTP (Figure S3). For sotorasib, observed effect was clearly diminished with KRAS(WT), as IC_{50} of 3.5 ± 0.8 µM and >10 µM were monitored using QRET or TR-FRET, respectively (Figure 1B and S3). In TSA, both adagrasib (ΔT_m = 6.6 °C) and sotorasib (ΔT_m = 10.4 °C) stabilize KRAS(WT) at high concentration. As in these assays sotorasib showed a clear luminescence quenching already at low micromolar concentrations, we further confirmed these results using surface plasmon resonance (SPR) (Figure 1C and S4). SPR showed a concentration-dependent adagrasib response with KRAS(WT), as no measurable response was monitored with sotorasib. The K_d observed for adagrasib with KRAS(WT) was 0.78 ± 0.05 µM, in line with those observed using nucleotide exchange assays. To verify the *in vitro* results in a cellular system, we measured RAS-GTP levels of the KRAS(WT) and KRAS(G12C), and performed cell viability assays with wild-type KRAS, HRAS, and NRAS (Figure 1D, and S5). RAS-GTP levels were measured in starvation and in the presence of adagrasib and sotorasib, followed by

mitogenic stimulation. Condition was selected to mimic the performed nucleotide exchange assays *in cellulo*. Clear inhibition of KRAS(G12C) activation was monitored with both adagrasib (IC_{50} = 145 ± 12 nM) and sotorasib (IC_{50} = 137 ± 68 nM), which are in line with the reported values.[49,50,53] Next, we confirmed the cross reactivity of adagrasib on KRAS(WT), and response was monitored at concentrations > 1 µM, while sotorasib did not show any effect at the tested concentrations (Figure 1D). However, as adagrasib started to show KRAS independent toxicity already at low micromolar concentrations in these conditions, we next performed cell viability assay with adagrasib and sotorasib to further confirm these results. Assay was performed using stable Ba/F3 cells expressing human KRAS(G12C) as a control, and with wild-type KRAS, NRAS, and HRAS expressing cells to study non-covalent binding of these inhibitors (Figure S5). With KRAS(G12C) expressing cells, adagrasib and sotorasib both lowered the cell viability already at low nanomolar concentrations having IC_{50} values of 7.6 ± 0.6 and 55.7 ± 5.3 nM, respectively. In the case of K/N/HRAS(WT) expressing cells, RAS independent toxicity (IC_{50} values 0.76 – 1.49 µM) was detected with adagrasib. With sotorasib, only minor effect in cell viability was monitored, enabling IC_{50} value determination (3.5 ± 1.8 µM) only with NRAS(WT) (Figure S5).

As effect of sotorasib on WT-proteins is much weaker than that for adagrasib, we next tested if KRAS mutations in positions G12, G13, and Q61, the most common hotspot mutations in cancer, will alter the accessibility of these sotorasib or adagrasib (Figure S6). In a nucleotide exchange assay, KRAS mutations G13D (IC_{50} = 401 ± 89 nM) and Q61L (IC_{50} = 432 ± 52 nM) had no significant effect on adagrasib function over KRAS(WT), as G12D and G12V mutations increased the IC_{50} value approximately 10-fold in comparison to KRAS(WT). This was confirmed by the thermal stability assay, in which adagrasib stabilization was more pronounced with KRAS(G13D) and KRAS(Q61L) (ΔT_m = 6.6 and 4.7 °C), as for the KRAS(G12V) (ΔT_m = 1.9 °C) (Figure S7). The weak effect on hindering the nucleotide exchange observed using sotorasib and KRAS(WT) was preserved in case of all four tested KRAS mutants (IC_{50} 4.3-8.2 µM), indicating low affinity against all non-G12C KRAS proteins (Figure S6). However, at high sotorasib concentration (100 µM) clear stabilization for KRAS(G12V), KRAS(Q61L), and KRAS(G13D), providing ΔT_m values of 13.2, 10.2, and 3.9 °C, was monitored, respectively (Figure S7).

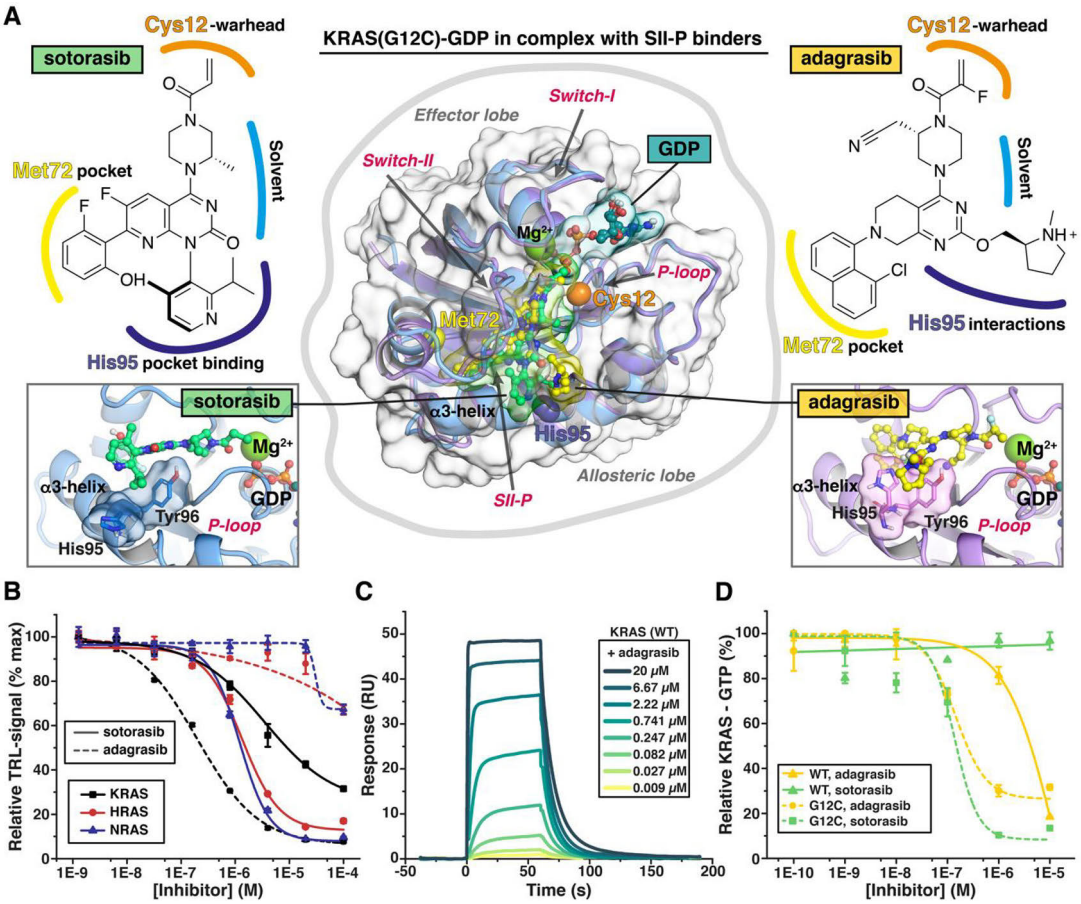

Fig. 1. Adagrasib is KRAS specific while sotorasib binds equally to NRAS and HRAS. (**A**) Structures of sotorasib and adagrasib and their binding modes in KRAS switch-II pocket (SII-P). Superimposed KRAS(G12C) co-crystal structures are shown in the middle (PDB IDs: 6OIM, 6UT0 [49,50]). A key-difference in their binding mode appears on KRAS-specific α3-helix residue H95, which is in out-conformation with adagrasib and in-conformation with adagrasib (zoom-in illustrations). Sotorasib is shown in green ball and sticks model, with protein highlighted with blue cartoon; adagrasib is shown in yellow ball and sticks model, with protein highlighted with purple cartoon. GDP is illustrated in ball and stick model with teal carbons. Mg^{2+}-ion is shown as green sphere; Cα-atoms of C12, M67, and H95 as orange, yellow, and blue spheres, respectively. (**B**) Concentration-dependent inhibition of SOS^{cat}-mediated guanine nucleotide exchange of 100 nM RAS after 30 min preincubation with sotorasib and adagrasib at RT (mean ± SD, n = 3). (**C**) Adagrasib surface plasmon resonance sensogram showing concentration-dependent binding to KRAS(WT) (mean ± SD, n = 3). (**D**) G-LISA Ras activation assay using starved cell incubated with adagrasib and sotorasib followed by mitogenic stimulation and monitoring of RAS-GTP levels of the KRAS(WT) and KRAS(G12C) (mean ± SD, n = 3).

Adagrasib showed no measurable binding with HRAS(WT) or NRAS(WT) in QRET nucleotide exchange assays (IC_{50} >15 µM) (Figure 1B). Sotorasib, on the contrary, displayed IC_{50} values of 1.3 ± 0.2 µM and 1.2 ± 0.2 µM for HRAS(WT) and NRAS(WT), respectively (Figure 1B). Also, TR-FRET nucleotide exchange assay and cell viability assay indicate that sotorasib interaction might be improved with NRAS(WT) in comparison to KRAS(WT)

(Figure S3 and S5). Thermal stability analysis with NRAS(WT) also indicates interaction with sotorasib but not with KRAS specific adagrasib (Figure 2A and S2). Together these data suggest that sotorasib might be equally useful with NRAS(G12C) and HRAS(G12C) mutants as with KRAS(G12C). To assess the potential relevance of targeting NRAS(G12C) and/or HRAS(G12C) mutant harboring cancers we explored the Catalogue of Somatic Mutations in Cancer (COSMIC v98).[54] In case of KRAS, the number of G12C mutation is 11.6%. From all NRAS and HRAS missense mutations in the database, 2.8% and 1.7% are G12C mutations. Nearly half of all NRAS(G12C) mutations are found from haematopoietic and lymphoid tissue, as the top 2 for HRAS(G12C) are skin and urinary track. Even the number is small, these searches confirmed the existence of patients carry non-KRAS(G12C) mutations. These patients might benefit from treatment with sotorasib, whether these mutations can be considered disease relevant drivers.

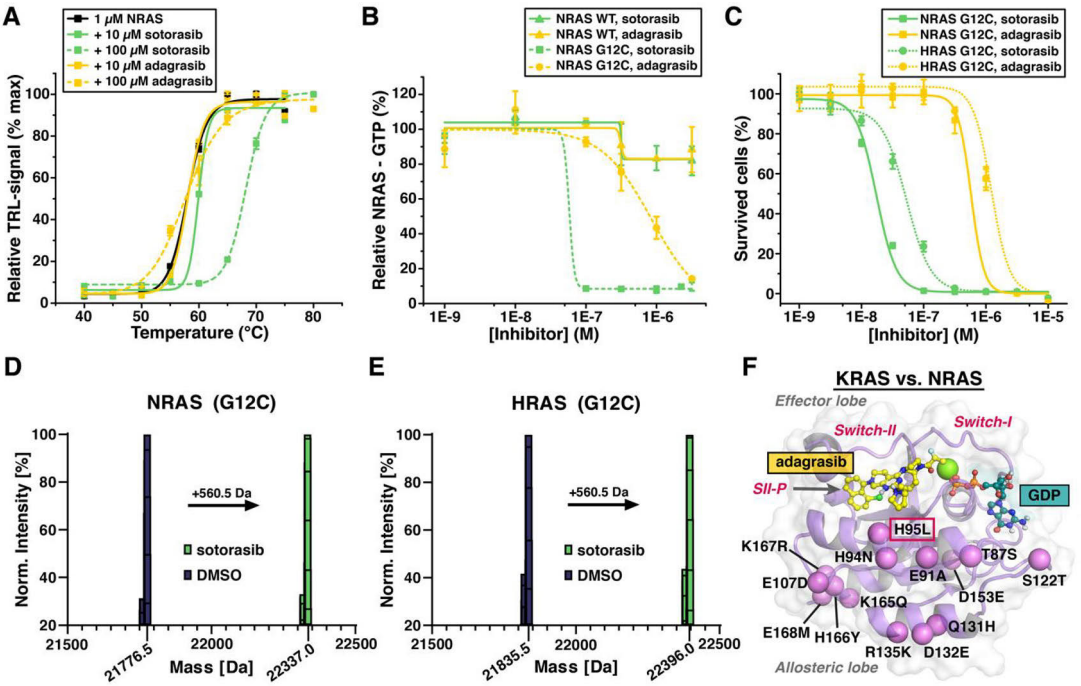

Fig. 2. Sotorasib binds covalently to G12C mutants of KRAS, NRAS, and HRAS. (**A**) Concentration-dependent thermal stabilization of 1 µM NRAS after 30 min preincubation with sotorasib and adagrasib at RT (mean ± SD, n = 3). (B) G-LISA Ras activation assay using starved cell incubated with adagrasib and sotorasib followed by mitogenic stimulation and monitoring of RAS-GTP levels of the NRAS(WT) and NRAS(G12C) (mean ± SD, n = 3). (**C**) Cell viability assay with adagrasib and sotorasib using stable Ba/F3 cells expressing human NRAS and HRAS(G12C) (mean ± SD, n = 3). (**D**) Mass spectrometric analysis of sotorasib binding to NRAS(G12C) and (**E**) HRAS(G12C). (**F**) Structural differences between NRAS and KRAS. The only discrepancy in SII-P residues is observed at position 95.

To further prove the non RAS isoform discriminating behavior of sotorasib, we performed a panel of assays also to explore the mechanism enabling binding. Cellular RAS-GTP assay confirmed that NRAS(G12C) (IC_{50} =58.0 ± 6.7 nM) is similarly targeted by sotorasib as the KRAS(G12C) (IC_{50} = 137 ± 68 nM), but that adagrasib inhibition is more KRAS-specific

(Figure 1D and 2B). Cell viability assays confirmed these results, as IC_{50} values of 17.4 ± 1.9 and 53.0 ± 6.4 nM for sotorasib with stable Ba/F3 cells expressing human NRAS and HRAS(G12C) were monitored, respectively (Figure 2C). We confirmed the covalent attachment of sotorasib to NRAS(G12C) and HRAS(G12C) by liquid chromatography–mass spectrometry (LC–MS) approach (Figure S8). The highest peak (12.2 min) from the separation, was analyzed by MS (Figure S9), and in case of both NRAS(G12C) (Figure 2E) and HRAS(G12C) (Figure 2F), 560.5 g/mol increase in molecular weight (MW) was observed in the presence of sotorasib ($C_{30}H_{30}F_2N_6O$). This increase is equal to expected MW for sotorasib (560.59 g/mol), proving the covalent attachment to both NRAS and HRAS(G12C) (Figure 2E, 2F, and S9). The only residue that differs between the isoforms within the SII-P is found in position 95, which is His, Leu or Gln in case of KRAS, NRAS, and HRAS, respectively (Figure 2F and S10).

KRAS specificity of adagrasib occurs through His-95

To rationalize our findings related to the WT isoform binding and specificity of the two inhibitors, we conducted molecular dynamics (MD) simulations with non-covalently bound adagrasib and sotorasib in SII-P with KRAS(WT), NRAS(WT), and HRAS(WT). These simulations, which describe a stable binding of the inhibitors in the WT SII-Ps, suggest that with sotorasib the observed key-interactions appear mainly isoform-agnostic while with adagrasib this is not the case (Figure S11). A huge discrepancy between the inhibitors exists with observed position 95 interactions in MD simulations (Figure 3A-E and S11). With adagrasib, its various interactions to KRAS H95 (total of 156% interaction frequency) are dramatically diminished with NRAS L95 (8%) (Figure 3A). In contrast, L95 introduces hydrophobic contacts with sotorasib, resulting in slightly increased interaction frequency of the inhibitor to the residue in this position with NRAS. These observed KRAS H95 interactions of both inhibitors are consistent throughout the conducted simulations (Figure 3B). Moreover, adagrasib, which exhibits tighter contact to H95 than sotorasib, displays clear instability in this location when in complex with NRAS, as demonstrated by the increased distance to this residue (Figure 3C–E). With sotorasib this distance to the position 95 remains unaltered regardless of the RAS isoform (Figure 3C, 3E). Also, in simulations the root-mean-square deviation (RMSD) of adagrasib is elevated when in complex with NRAS, indicating instability (Figure S12). Overall, these simulation results suggests that the interactions to H95 with adagrasib are deterministic for its KRAS(WT) binding and selectivity over other RAS(WT) isoforms, while H95 interactions are not in the key-role with sotorasib, offering higher tolerance for amino acid variation in this position.

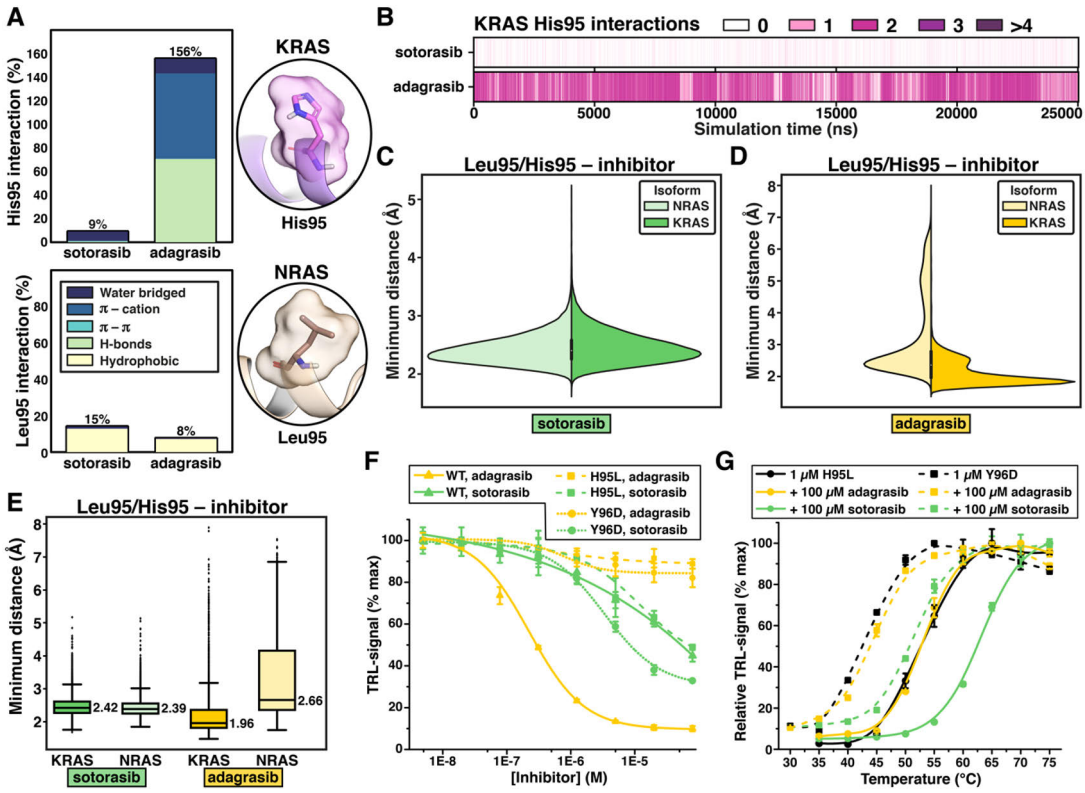

Fig. 3. Adagrasib RAS isoform specificity is determined by His-95 of KRAS. (**A**) Adagrasib displays strong interactions with His-95 (KRAS) with high frequency but not with Leu-95 (NRAS) in MD simulations. For sotorasib the interactions to His-95 are not in the key-role and the interaction frequency appears slightly elevated with Leu-95. (**B**) KRAS His-95 interactions in the MD simulations with sotorasib and adagrasib are consistent throughout the simulations, as demonstrated by the observed interactions in time-specific plot of the concatenated trajectories (five individual 5 μs simulations). (**C**) Isoform specific mininum distance of sotorasib to position 95 shown with violinplot. (**D**) Isoform specific minimum distance of adagrasib to position 95 shown with violinplot. (**E**) Data of C and D is shown here with boxplots, with their median values. The black horizontal line in the box represents the median, the box displays the quartiles of the dataset (25–75%) and whiskers the rest of the data with maximum 1.5 IQR. Outliers are indicated with black diamonds. Data shown in A–E of each system (25 μs) was analyzed by each ns. (**F**) Concentration-dependent inhibition of SOS^{cat}-mediated guanine nucleotide exchange of 100 nM KRAS(WT), KRAS(H95L), and KRAS (Y96D) after 30 min preincubation with sotorasib and adagrasib at RT (mean ± SD, n = 3). (**G**) Concentration-dependent thermal stabilization of 1 μM KRAS(WT), KRAS(H95L), and KRAS (Y96D) after 30 min preincubation with sotorasib and adagrasib at RT (mean ± SD, n = 3).

MD simulations suggested the irreplaceable role of H95 with adagrasib, and both inhibitors display interactions to Y96 with high frequency (Figure S13). To further validate the importance of KRAS H95 and Y96, a second mutation clinically reported to cause resistance,[17,31,34] we performed a set of assays with sotorasib and adagrasib with various KRAS mutants. We created two single mutant constructs, KRAS(H95L) reflecting the native switch-II pocket present in NRAS(WT), and KRAS(Y96D) linked to the formation of resistance with

G12C targeting inhibitors.[34] During the characterization of these mutants, we found KRAS(Y96D) to have negative impact on SOS^{cat} induced nucleotide exchange, but more importantly KRAS(Y96D) thermal stability (T_m = 42.6 ± 0.6 °C) appeared significantly reduced in comparison to KRAS(G12C) (T_m = 53.4 ± 0.3 °C) used as a control (Figure S14). SYPRO Orange (SO) TSA data confirmed the lowered KRAS(Y96D) stability (48.9 ± 0.2 °C), as with KRAS(H95L), more typical KRAS stability (PP; 51.9 ± 0.9 °C, SO; 59.8 ± 0.2 °C) was observed (Figure S14B and S15). In the nucleotide exchange assay, we observed comparable weak inhibition with sotorasib using both KRAS(H95L) and KRAS(Y96D) as with KRAS (WT) (Figure 2F). In case of adagrasib, however, both mutants were resistant to nucleotide exchange inhibition, indicating non-existing binding at the used concentrations. Observations from the PP thermal stability assay are in line with these findings, as 100 µM sotorasib displayed ΔT_m of 11.8 °C and 9.6 °C with KRAS(H95L) and KRAS(Y96D), respectively (Figure 2G). These are equal to the ones monitored with the KRAS(WT) (Figure S2). On the other hand, adagrasib (at 100 µM concentration) exhibited negligible stabilization. Thus, the results from biochemical assays are in line with the MD simulation data.

KRAS(G12C) secondary mutations on His-95 and Tyr-96 disrupts sotorasib and adagrasib binding

In order to obtain more biologically relevant data, we created two new double mutants, KRAS(G12C/H95L) and KRAS(G12C/Y96D). When characterized, KRAS(G12C/H95L) showed kinetically slightly faster SOS^{cat} induced nucleotide exchange than KRAS(G12C), and also KRAS(G12C/Y96D) nucleotide exchange activity was rescued in comparison to KRAS(Y96D) (Figure S14A). Y96D effect is potentially due to KRAS R68 interaction with SOS E1002 in its "active" conformation, and thus D96–R68 may reduce the KRAS–SOS interaction.[55] KRAS(G12C/H95L) (PP; 56.2 ± 0.2 °C, SO; 63.0 ± 0.2 °C) and KRAS(G12C/Y96D) (PP; 48.8 ± 0.8 °C, SO; 52.7 ± 0.2 °C) also showed increased stability over their single mutant forms, even KRAS(G12C/Y96D) stability was still reduced in comparison to KRAS(G12C) (PP; 52.0 ± 1.0 °C, SO; 61.7 ± 0.2 °C) (Figure S14B and S15).

The effect of these mutations was also evident in a nucleotide exchange assay with sotorasib and adagrasib. The IC_{50} values with sotorasib for KRAS(G12C/H95L) and KRAS(G12C/Y96D) in the used conditions were 0.17 ± 0.04 and 1.6 ± 0.1 µM, respectively (Figure 4A). These values are higher in comparison to the ones with KRAS(G12C), reflecting significantly compromised inhibition. Adagrasib showed negligible inhibition with KRAS(G12C/Y96D), but surprisingly with KRAS(G12C/H95L) the inhibition (IC_{50} value of 0.94 ± 0.07 µM) was observed (Figure 4A). Using the mutant KRAS(G12C/H95L), also the observed thermal stability increased with both 10 µM and 100 µM sotorasib (ΔT_m = 5.4 °C and 14.4 °C), as adagrasib only modestly increased the stability of this mutant (ΔT_m = 1.5 °C and 4.1 °C) (Figure 4B). With KRAS(G12C/Y96D), only 100 µM sotorasib gave measurable increase in thermal stability (ΔT_m = 7.7 °C) (Figure S16). As the nucleotide exchange and thermal stability results differ especially with KRAS(G12C/H95L), we studied the nucleotide exchange kinetics of this mutant in more details. The control experiment with KRAS(G12C)

showed that adagrasib blocks the nucleotide exchange slightly faster than sotorasib, but in both cases, KRAS(G12C) is locked to its GDP-loaded state (Figure S17). This indicates that adagrasib and sotorasib will bind covalently to KRAS(G12C) immediately when it has reached the GDP-loaded state. Response with KRAS(WT) occurs only with adagrasib, but without the covalent bond, KRAS(WT) is not locked to its GDP-loaded state permanently. Sotorasib, on the other hand, blocks KRAS(G12C/H95L) nucleotide exchange similar to KRAS(G12C), as adagrasib is nearly unresponsive (Figure S17). Together this data indicates that sotarasib binds covalently to KRAS(G12C/H95L), but that the slightly weakened binding due to the H95L mutation is causing a multiplying effect in the thermal assay.

By monitoring active KRAS(G12C/H95L) population, we could confirm that indeed sotorasib function is not compromised by additional H95 mutation (IC_{50} = 122 ± 23 nM) in comparison to KRAS(G12C) (IC_{50} = 137 ± 68 nM), as on the other hand, adagrasib function is nearly abolished (Figure 1D and 4C). Cell viability assay results in stable Ba/F3 cells expressing human KRAS(G12C/H95Q) and KRAS(G12C/Y96D) are equally in line with the previous findings (Figure 4D). The observed sotorasib IC_{50} values for KRAS(G12C/H95Q), double mutant used in this experiment, and KRAS(G12C) were similar (73.3 ± 6.9 nM vs. 55.7 ± 5.3 nM), as the effect on KRAS(G12C/Y96D) was negligible. On the other hand, adagrasib results follows the non-RAS driven decrease in cell viability, and no specific response to either KRAS(G12C/H95Q) or KRAS(G12C/Y96D) were monitored (Figure 4D and S5B).

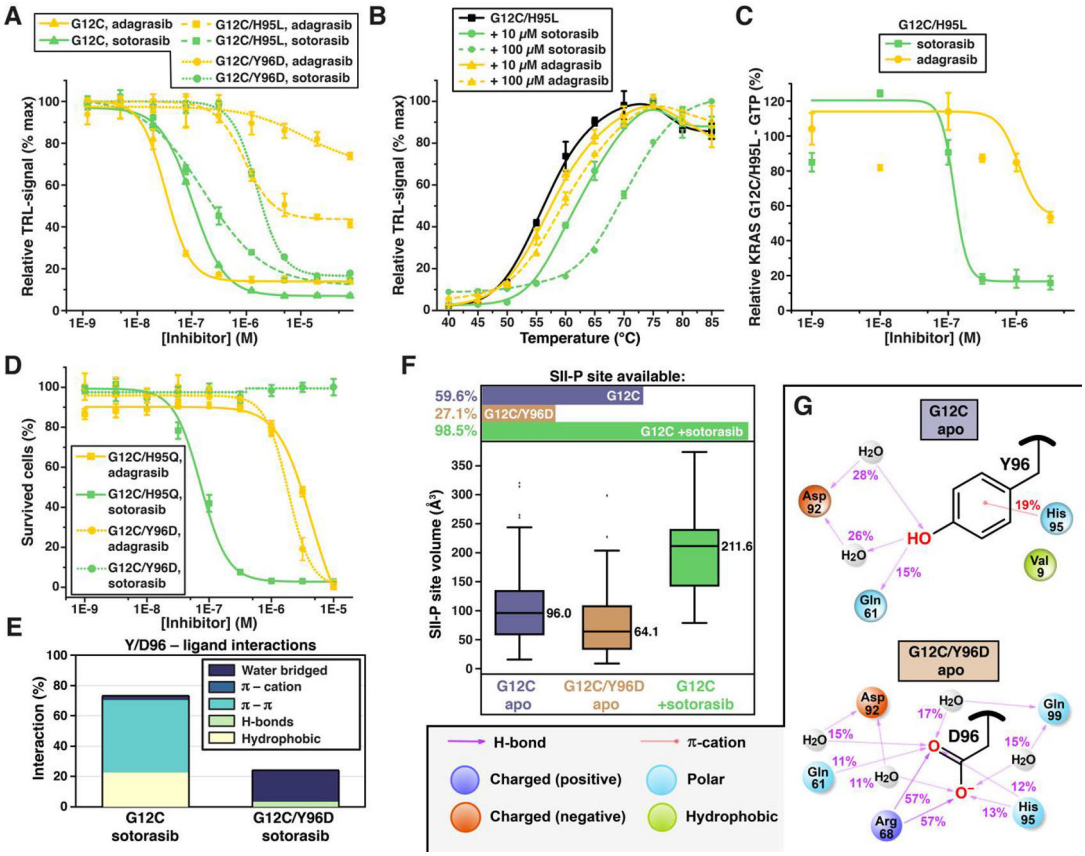

Fig. 4. Adagrasib RAS isoform specificity is determined by His-95 of KRAS. (**A**) Concentration-dependent inhibition of SOS^{cat}-mediated guanine nucleotide exchange of 100 nM KRAS(G12C), KRAS(G12C/H95L), and KRAS(G12C/Y96D) after 30 min preincubation with sotorasib and adagrasib at RT (mean ± SD, n = 3). (**B**) Concentration-dependent thermal stabilization of 1 µM KRAS(G12C/H95L) after 30 min preincubation with sotorasib and adagrasib at RT (mean ± SD, n = 3). (**C**) G-LISA Ras activation assay using starved cell incubated with adagrasib and sotorasib followed by mitogenic stimulation and monitoring of RAS-GTP levels of the KRAS(G12C/H95L) (mean ± SD, n = 3). (**D**) Cell viability assay with adagrasib and sotorasib using stable Ba/F3 cells expressing human KRAS(G12C/H95Q) and (G12C/Y96D) (mean ± SD, n = 3). (**E**) Observed Y96 and Y96D interactions of non-covalently bound sotorasib in MD simulations of KRAS(G12C) and KRAS(G12C/Y96D) systems. (**F**) Observed SII-P availability and volume in (GDP-bound) apo simulations of KRAS(G12C) and KRAS(G12C/Y96D), and with KRAS(G12C) with non-covalently bound sotorasib. Pocket availability and size for the 20 µs simulation data of each system was analyzed for each 50 ns with SiteMap. Boxplots consist of 239, 109 and 395 (of 401) data points for KRAS(G12C) apo, KRAS(G12C/Y96D) apo, and KRAS(G12C) + sotorasib simulations, respectively. (**G**) Interaction profile of the position 96 residues in the simulations without SII-P ligand. Interactions with >10% frequency are shown. Total of 20 µs data for both systems.

To provide more insights into the role of the secondary mutation Y96D and its negative impact on sotorasib binding, we conducted MD simulations of G12C and G12C/Y96D with non-covalently bound sotorasib in the SII-P. These simulations provide insight into the stability of

the inhibitor in the binding site before the covalent reaction takes place with the C12. As was observed with the KRAS(WT), also with KRAS(G12C) Tyr-96 forms highly frequent interactions to sotorasib, including π–π and hydrophobic interactions (Figure 4E and S18). These key-interactions are abolished by Y96D mutation, which leads to the instability of sotorasib in the binding site. In fact, in one of our simulation replicas we observed a total dissociation of sotorasib from the switch-II pocket at 2000 ns of the simulation (Figure S19). Furthermore, we conducted additional simulations of both G12C and G12C/Y96D without the SII-P binding ligand, to observe if the mutation itself has any impact on the binding pocket conformational behavior (Figure S20). Indeed, the resistant secondary mutation Y96D appears to constrict the SII-P compared to KRAS(G12C) (Figure 4F). The SII-P with G12C/Y96D is less available (SiteMap site available only in 27.1% of the analyzed frames) and when the pocket is present it is associated with smaller volume (median of 64.1Å^3) when compared to G12C (found in 59.6%; median volume of 96.0Å^3). With sotorasib in the SII-P, the pocket volume median is 211.6Å^3. While the native Y96 displays no interactions to R68 (for which sotorasib displays interactions with high frequency in G12C), the mutated Y96D promotes a salt-bridge interaction between these two residues (Figure 4G). This secondary mutation introduces a possibility for a novel intraprotein interaction, influencing the size and accessibility of the SII-P, putatively hindering the inhibitor binding, suggesting an additional mechanism on the inhibitor resistance via this clinically observed secondary mutation. In addition to secondary mutation R68, Q99 mutation has been also found clinically relevant.[33,36,40] We could confirm the importance of R68 for sotorasib, when tested with KRAS(G12C/R68M) expressing Ba/F3 cells (Figure S21). In a cell viability assay, IC_{50} values for sotorasib and adagrasib were 1073 ± 22 and 94.2 ± 29.9 nM, respectively. On the other hand, IC_{50} values for sotorasib and adagrasib with KRAS(G12C/Q99L) expressing cells were 75.8 ± 1.0 and 175.1 ± 13.3 nM, respectively. Thus, the secondary Q99 mutation seems to have no effect on sotorasib and clear effect on adagrasib in comparison to viability assays using KRAS(G12C) expressing cells with sotorasib (55.7 ± 5.3 nM) and adagrasib (7.5 ± 0.8 nM), respectively (Figure S21 and S5). Together, results are in line with clinical observations that R68M, and Y96D/S mutations are highly resistant to sotorasib, whereas Y96D/S and Q99L conferred strong resistance to adagrasib.[40] MD simulations gave no clear reason how Q99L affects to adagrasib binding, but it indicates that it is through H95 position rather than directly (Figure S22).

Conclusions

Sotorasib and adagrasib are the first FDA approved drugs for RAS.[39,40,56] Both inhibitors occupy the same SII-P, but due to interaction differences, their specificity profile varies. Thus, unsurprisingly, reported secondary mutations inducing resistance for these inhibitors also vary. KRAS(Y96D) was one of the first of these secondary mutations reported for adagrasib resistance, and the same mutation was found to confer resistance to multiple KRAS(G12C) inhibitors currently in clinical trials.[34] Later, KRAS alterations outside the ‘’hotspot’’ area, have been reported especially in R68, H95, and Y96.[33] H95 has been counted as adagrasib-specific resistance mutation, as sotorasib tolerates H95 mutations, but either of these inhibitors tolerates R68 or Y96 mutations in cell viability assays.[33] We have now studied both sotorasib and adagrasib binding and relation to these clinically reported secondary mutations causing

resistance. Our data obtained both from biochemical and cell-based assays clearly indicate that adagrasib specificity is created through His-95, as sotorasib is dependent on Tyr-96, conserved in all RAS isoforms. MD simulations further underpin this observation, which also indicates that sotorasib could be potentially useful for patients having HRAS(G12C) and NRAS(G12C) mutation. Together, presented results can support ongoing development of KRAS or pan-RAS drugs also for RAS lacking a cysteine covalently targeted cysteine. Results also highlight how a panel of different methods can unravel functionalities and support each other, when inhibitors are studied *in vitro*.

Data Availability Statement: Data generated during the study is available upon request. The original MD simulation Desmond raw trajectories, generated and analyzed in the study have been deposited in the Zenodo repository and are freely available at: https://doi.org/10.5281/zenodo.xxxxxxx; https://doi.org/10.5281/zenodo.XXXXXXX

Methods

Protein Expression and Purification. Detailed list of materials and instrumentation are provided in SI Appendix. Details for SOS^{cat} (564-1048), RAS(WT) proteins (HRAS (1-189), KRAS(2-188), and NRAS(1-189)), and for full length KRAS mutants (G12C, G12D, G12V, G13D, and Q61L) has been described previously.[41–43,45–47,57] Avi-KRAS (1-188) production and purification has been also described elsewhere, and Avi-HRAS and Avi-NRAS were created accordingly.[41] Protein expression and purification of KRAS(H95L), KRAS(Y96D), KRAS(G12C/H95L), and KRAS(G12C/Y96D) are provided in SI Appendix.

Nucleotide Exchange Assay. All concentrations are given in final volume. Endpoint assays using QRET and TR-FRET, were performed in 15 µL and 10 µL final volume in an assay buffer (20 mM HEPES (pH 7.5), 1 mM $MgCl_2$, 10 mM NaCl, 0.01% Triton X-100, and 0.005% γ-globulins), respectively.[45–47,58] In QRET, 3 µL of sotorasib (0-100 µM) and adagrasib (0-100 µM) were mixed in 384-well with equal volume of RAS (10-100 nM), and incubated for 15 min. After the incubation, 6 µL of the detection solution (10 nM Eu^{3+}-GTP and 2.5 µM MT2) was added and TRL-signal was monitored using Tecan Spark 20M with excitation and emission wavelengths of 340 and 620 nm. Reaction was initiated with 3 µL of SOS^{cat} (5-10 nM) and TRL-signal was monitored at several time points during 60 min incubation. TR-FRET assays were performed using similar protocol, as an exception that detection (50 nM AF647-GTP and 5 nM SA-Eu^{3+}) and SOS^{cat} were both added in 2 µL volume. TR-FRET signal was monitored at several time points using excitation and emission wavelengths of 340 and 665 nm. Kinetic assays were all performed with Eu^{3+}-GDP. Assays without inhibitors were performed using 100 nM of RAS and detection solution with 10 nM Eu^{3+}-GDP and 3 µM of MT2, added in 9 and 10 µL volume, respectively. Reaction was initiated with 10 nM SOS^{cat} (1 µL) and TRL-signal was monitored for 30 min at 30-s intervals. KRAS(WT), KRAS(G12C), and KRAS(G12C/H95L) were further assayed with GDP (5 µM), sotorasib (5 µM), and adagrasib (5 µM). These assays were performed also with 100 nM KRAS (8 µL), modified detection (50 nM Eu^{3+}-GDP and 4.5 µM MT2). Reaction was initiated with 20 nM SOS^{cat} (1 µL) and TRL-signal was monitored for 15 min at 60-s intervals, before blockers (GDP, sotorasib, and adagrasib) were added in 1 µL, and TRL-signal monitoring was continued for 60 min at 60-s intervals.

Thermal Stability Assays. All RAS thermal stability assays were performed in 96-well plate mainly by using two-step Protein-Probe assay with 50-1000 nM RAS concentration (8 µL).[43,59]

Two DSF dyes (ANS and SYPRO Orange), used as a control, were performed with one-step protocol and 10 µM RAS (20 µL) concentration.[41,43,52] In the Protein-Probe, RAS (4 µL) and inhibitor (4 µL) were added in assay buffer (10 mM HEPES (pH 7.5), 0.001% Triton X-100 and 20 mM NaCl) and incubated for 30 min before heating for 3 min at each temperature (25-95 °C) using 5 °C interval. Sotorasib and adagrasib were mainly used at 10 or 100 µM concentration (at 8 µL), except assays with KRAS(G12C), KRAS(G12C/H95L), and KRASG12C(Y96D), which were also assayed using 0-1 µM inhibitor concentration. After heating RAS at each temperature, detection solution (citrate-phosphate buffer (pH 4), 0.01% Triton X-100, 3.5 µM 1,1,3,3,3′,3′-hexamethylindodicarbocyanine iodide, and 1 nM Eu^{3+}-probe) was added in 65 µL, before TRL-signal monitoring at RT. With ANS and SYPRO Orange, RAS (10 µM) and inhibitors (20 µM) were added in assay buffer (10 mM HEPES (pH 7.5), 0.001% Triton X-100 and 20 mM NaCl) and incubated for 30 min in 8 µL volume, prior the addition of the DSF dye (10 µM ANS and 5 x SYPRO Orange, final) at 12 µL. Samples were incubated for 3 min at each temperature, followed by fluorescence signal measurement (ANS; 350/490 nm and SYPRO Orange; 485/590 nm).

Ras-GTP assays. HEK293T cells were maintained at 37 °C with 5% CO_2. Cells were grown in DMEM supplemented with 10% fetal calf serum (FCS) and 1% penicillin/streptomycin. HEK293T cells were seeded at 5 x 10^5 cells / well in 6-well plates and incubated for 24 h. Cells were transfected with 1.25 µg plasmid DNA and by using 3.75 µL TransIT-293 (Mirus, MIR 2700) per well. Medium was exchanged to DMEM containing 0.5% FCS 48 h post-transfection, and the indicated concentration of either adagrasib, sotorasib or DMSO were added. 64 h post-transfection the cells were stimulated by adding 10% FCS, 4 min prior transferred on ice. Cells were washed twice with ice-cold 1 x PBS (phosphate buffered saline) and lysed subsequently.

Quantification of RAS-GTP was performed using the absorbance-based G-LISA Ras Activation Kit (Cytoskeleton, BK131). After cell lysis with the supplied buffer, the samples protein content was determined by the supplied protein assay. Depending on the transfected construct, 6 to 22 µg of whole-cell lysate was used in duplicates for the RAS-GTP assay. To ensure that only the transfected RAS isoform or mutant is detected, we replaced the supplied primary and secondary detections with a mouse anti-HA antibody (Sigma, H9658) and a goat anti-mouse HRP antibody (Pierce, 31438).

Cell viability assays. Assays were performed using mouse Ba/F3 cell lines stably expressing exogenous KRAS(WT) or KRAS bearing amino acid mutation studied (G12C, G12C/H95Q, G12C/Y96D, and G12C/Q99L) (Kyinno biotechnology, Peking, China). Additionally, Ba/F3 cell lines expressing exogenous HRAS(WT) and HRAS(G12C) or NRAS(WT) and NRAS(G12C) were used. Cell culture and assays using sotorasib and adagrasib (10 μM) were performed according to manufacturer's instructions. Shortly, cells were cultured in 10% FBS supplemented RPMI-1640 medium and seeded in 96-well plate (3000 cells/well). Cells were cultured overnight prior sotorasib (0-10 μM) and adagrasib (0-10 μM) addition, and plates were further incubated for 72 h. Cell viability was measured using CellTiter-Glo assay according to manufactures instruction by measuring the luminescence using PerkinElmer Envision (PerkinElmer, Waltham, MA).

LC-MS binding studies. Recombinant NRAS (G12C, 1-169) and HRAS (G12C, 1-169) were incubated with either 0.1 % DMSO or 10 μM sotorasib for 1h at RT and subsequently submitted to the LC-MS service at the Functional Genomics Center Zurich (FGCZ). Full protocol is provided in SI Appendix.

Molecular modeling. Molecular modeling was conducted with Maestro (Schrödinger release 2020-2, Schrödinger LLC, New York, NY) using OPLS3e force field [60,61]

Molecular dynamics simulations

PDB ID: 6OIM [50]

Reverse mutated the engineered residues back to native: S51 to C51 and L80 to C80

Initiator methionine was deleted and T2 was acetylated.

Missing residues added.

PDB ID: 6UT0 [49]

Reverse mutated the engineered residues back to native: S118 to C118

We removed the covalent linkage from the inhibitor to C12, which

Protein Preparation Wizard [62]

To acquire a comparable WT NRAS system with a similar starting configuration for the simulations, we mutated the KRAS residues to the native NRAS ones (T87S; E91A; H94N; H95L; E107D; S122T; Q131H; D132E; R135K; D153E; K165Q; H166Y; K167R; E168M), which was prepared, and energy minimized with the Protein Preparation Wizard as above.

Simulations were conducted with Desmond D engine.[63] Systems were then solvated in a 15 Å cubic box with TIP3P water with 150 mM K^+ and Cl^- salt (adjusted to a neutral net charge).[64] The final systems comprised ~35–38k atoms. Prior to the production simulations, the default Desmond relaxation was applied for both systems. The production simulations were run in NpT ensemble (p = 1.01325 bar; T = 310 K) with settings as in previous report.[65]

Simulations of the mutant KRAS(G12C) and KRAS(G12C/Y96D) systems with and without non-covalently bound sotorasib were generated from the above KRAS(WT)-sotorasib system, by mutating G12 to C12 and Y96 to D96 (for the G12C/Y96D), and in the case of the apo systems sotorasib was deleted. Simulation settings were as above. Five replicas for each system were simulated for 4 μs, except for one replica of the KRAS(G12C/Y96D)-sotorasib systems the simulation was terminated already at 3 μs while the ligand dissociated at 2000 ns.

Computational analysis of binding sites. Analysis of switch-II pocket volume was conducted with trajectory_binding_site_volumes.py script (Schrödinger LLC). Trajectories were analyzed for every 50th frame (50 ns intervals).

ACKNOWLEDGMENTS.

This work was supported by Academy of Finland (323433/K.K., 329012/K.K., and 353324/K.K). The authors would like to thank Matt Drew, Peter Frank, Randy Gapud, José Sánchez Hernández, Jennifer Mehalko, Shelley Perkins, Nitya Ramakrishnan, Mukul Sherekar, Simon Messing, Troy Taylor, Vanessa Wall, and Tim Waybright for cloning, expression, purification, and QC of the used small GTPase proteins. The authors wish to acknowledge CSC—IT Center for Science, Finland, for computational resources.

References:

1. Moore, A. R., Rosenberg, S. C., McCormick, F. & Malek, S. RAS-targeted therapies: is the undruggable drugged? *Nat Rev Drug Discov* **19**, 533–552 (2020).

2. Raphael, B. J. *et al.* Integrated Genomic Characterization of Pancreatic Ductal Adenocarcinoma. *Cancer Cell* **32**, 185-203.e13 (2017).

3. Muzny, D. M. *et al.* Comprehensive molecular characterization of human colon and rectal cancer. *Nature* **487**, 330 (2012).

4. Akbani, R. *et al.* Genomic Classification of Cutaneous Melanoma. *Cell* **161**, 1681–1696 (2015).

5. Cancer Genome Atlas Research Network, T. ARTICLE Comprehensive molecular profiling of lung adenocarcinoma. *Nature* (2014) doi:10.1038/nature13385.

6. Lu, S., Jang, H., Nussinov, R. & Zhang, J. The Structural Basis of Oncogenic Mutations G12, G13 and Q61 in Small GTPase K-Ras4B. *Scientific Reports 2016 6:1* **6**, 1–15 (2016).

7. Kim, D., Xue, J. Y. & Lito, P. Targeting KRAS(G12C): From Inhibitory Mechanism to Modulation of Antitumor Effects in Patients. *Cell* **183**, 850–859 (2020).

8. Murugan, A. K., Grieco, M. & Tsuchida, N. RAS mutations in human cancers: Roles in precision medicine. *Semin Cancer Biol* **59**, 23–35 (2019).

9. Dogan, S. *et al.* Molecular Epidemiology of EGFR and KRAS Mutations in 3026 Lung Adenocarcinomas: Higher Susceptibility of Women to Smoking-related KRAS-mutant Cancers. *Clin Cancer Res* **18**, 6169 (2012).

10. Cox, A. D., Fesik, S. W., Kimmelman, A. C., Luo, J. & Der, C. J. Drugging the undruggable RAS: Mission Possible? *Nat Rev Drug Discov* **13**, 828–851 (2014).

11. Khan, I., Rhett, J. M. & O'Bryan, J. P. Therapeutic targeting of RAS: New hope for drugging the "undruggable". *Biochimica et Biophysica Acta (BBA) - Molecular Cell Research* **1867**, 118570 (2020).

12. Uprety, D. & Adjei, A. A. KRAS: From undruggable to a druggable Cancer Target. *Cancer Treat Rev* **89**, 102070 (2020).

13. Molina-Arcas, M., Samani, A. & Downward, J. Drugging the Undruggable: Advances on RAS Targeting in Cancer. *Genes (Basel)* **12**, (2021).

14. McCormick, F. Sticking it to KRAS: Covalent Inhibitors Enter the Clinic. *Cancer Cell* **37**, 3–4 (2020).

15. Li, H., Qi, W., Wang, Y. & Meng, L. Covalent inhibitor targets KRasG12C: a new paradigm for drugging the undruggable and challenges ahead. *Genes Dis* (2021) doi:10.1016/J.GENDIS.2021.08.011.

16. Boike, L., Henning, N. J. & Nomura, D. K. Advances in covalent drug discovery. doi:10.1038/s41573-022-00542-z.

17. Pantsar, T. KRAS(G12C)–AMG 510 interaction dynamics revealed by all-atom molecular dynamics simulations. *Sci Rep* **10**, (2020).

18. Vasta, J. D. *et al.* KRAS is vulnerable to reversible switch-II pocket engagement in cells. *bioRxiv* 2021.10.15.464544 (2021) doi:10.1101/2021.10.15.464544.

19. Nagasaka, M. *et al.* KRAS G12C Game of Thrones, which direct KRAS inhibitor will claim the iron throne? *Cancer Treat Rev* **84**, 101974 (2020).

20. Ostrem, J. M., Peters, U., Sos, M. L., Wells, J. A. & Shokat, K. M. K-Ras(G12C) inhibitors allosterically control GTP affinity and effector interactions. *Nature* **503**, 548–551 (2013).

21. Lito, P., Solomon, M., Li, L. S., Hansen, R. & Rosen, N. Allele-specific inhibitors inactivate mutant KRAS G12C by a trapping mechanism. *Science* **351**, 604–608 (2016).

22. Zhang, Z., Morstein, J., Ecker, A. K., Guiley, K. Z. & Shokat, K. M. Chemoselective Covalent Modification of K-Ras(G12R) with a Small Molecule Electrophile. (2022) doi:10.1021/jacs.2c05377.

23. Burd, C. E. *et al.* Mutation-Specific RAS Oncogenicity Explains NRAS Codon 61 Selection in Melanoma. *Cancer Discov* **4**, 1418–1447 (2014).

24. Ostrem, J. M. L. & Shokat, K. M. Direct small-molecule inhibitors of KRAS: from structural insights to mechanism-based design. *Nat Rev Drug Discov* **15**, 771–785 (2016).

25. Patricelli, M. P. *et al.* Selective Inhibition of Oncogenic KRAS Output with Small Molecules Targeting the Inactive State. *Cancer Discov* **6**, 316–329 (2016).

26. Janes, M. R. *et al.* Targeting KRAS Mutant Cancers with a Covalent G12C-Specific Inhibitor. *Cell* **172**, 578-589.e17 (2018).

27. Zhang, Z. *et al.* GTP-State-Selective Cyclic Peptide Ligands of K-Ras(G12D) Block Its Interaction with Raf. *Cite This: ACS Cent. Sci* **2020**, 1753–1761 (2020).

28. Sogabe, S. *et al.* Crystal Structure of a Human K-Ras G12D Mutant in Complex with GDP and the Cyclic Inhibitory Peptide KRpep-2d. (2017) doi:10.1021/acsmedchemlett.7b00128.

29. Sakamoto, K., Masutani, T. & Hirokawa, T. Generation of KS-58 as the first K-Ras(G12D)-inhibitory peptide presenting anti-cancer activity in vivo. *Scientific Reports 2020 10:1* **10**, 1–16 (2020).

30. Drosten, M. & Barbacid, M. KRAS inhibitors: going noncovalent. *Mol Oncol* **16**, 3911–3915 (2022).

31. Kwan, A. K., Piazza, G. A., Keeton, A. B. & Leite, C. A. The path to the clinic: a comprehensive review on direct KRAS G12C inhibitors. *Journal of Experimental & Clinical Cancer Research* **41**, 27 (2021).

32. Ning, W., Yang, Z., Kocher, G. J., Dorn, P. & Peng, R. W. A Breakthrough Brought about by Targeting KRAS G12C: Nonconformity Is Punished. *Cancers (Basel)* **14**, (2022).

33. Awad, M. M. *et al.* Acquired Resistance to KRAS G12C Inhibition in Cancer . *New England Journal of Medicine* **384**, 2382–2393 (2021).

34. Tanaka, N. *et al.* Clinical Acquired Resistance to KRASG12C Inhibition through a Novel KRAS Switch-II Pocket Mutation and Polyclonal Alterations Converging on RAS–MAPK Reactivation. *Cancer Discov* **11**, 1913–1922 (2021).

35. Ryan, M. B. *et al.* KRAS G12C-independent feedback activation of wild-type RAS constrains KRAS G12C inhibitor efficacy. doi:10.1016/j.celrep.2022.110993.

36. Feng, S. *et al.* A saturation mutagenesis screen uncovers resistant and sensitizing secondary KRAS mutations to clinical KRASG12C inhibitors. *Proc Natl Acad Sci U S A* **119**, (2022).

37. Jiao, D. & Yang, S. Overcoming Resistance to Drugs Targeting KRASG12C Mutation. *The Innovation* **1**, 100035 (2020).

38. Addeo, A., Banna, G. L. & Friedlaender, A. KRAS G12C Mutations in NSCLC: From Target to Resistance. *Cancers (Basel)* **13**, (2021).

39. Liu, J., Kang, R. & Tang, D. The KRAS-G12C inhibitor: activity and resistance. *Cancer Gene Therapy 2021* 1–4 (2021) doi:10.1038/s41417-021-00383-9.

40. Koga, T. *et al.* KRAS Secondary Mutations That Confer Acquired Resistance to KRAS G12C Inhibitors, Sotorasib and Adagrasib, and Overcoming Strategies: Insights From In Vitro Experiments. *Journal of Thoracic Oncology* **16**, 1321–1332 (2021).

41. Kopra, K. *et al.* Thermal Shift Assay for Small GTPase Stability Screening: Evaluation and Suitability. *Int J Mol Sci* **23**, 7095 (2022).

42. E, V. *et al.* Sensitive Label-Free Thermal Stability Assay for Protein Denaturation and Protein-Ligand Interaction Studies. *Anal Chem* **92**, 3512–3516 (2020).

43. Valtonen, S. *et al.* Nanomolar Protein–Protein Interaction Monitoring with a Label-Free Protein-Probe Technique. *Anal Chem* **92**, 15781–15788 (2020).

44. Kopra, K. *et al.* Homogeneous Dual-Parametric-Coupled Assay for Simultaneous Nucleotide Exchange and KRAS/RAF-RBD Interaction Monitoring. *Cite This: Anal. Chem* **92**, 4971–4979 (2020).

45. Kopra, K. *et al.* A homogeneous quenching resonance energy transfer assay for the kinetic analysis of the GTPase nucleotide exchange reaction. *Anal Bioanal Chem* **406**, 4147–4156 (2014).

46. Kopra, K. *et al.* High-Throughput Dual Screening Method for Ras Activities and Inhibitors. *Anal Chem* **89**, 4508–4516 (2017).

47. Kopra, K. & Härmä, H. Methods to Monitor Ras Activation State. *Methods in Molecular Biology* **2262**, 137–167 (2021).

48. Lanman, B. A. *et al.* Discovery of a Covalent Inhibitor of KRASG12C (AMG 510) for the Treatment of Solid Tumors. *J Med Chem* **63**, 52–65 (2019).

49. Fell, J. B. *et al.* Identification of the Clinical Development Candidate MRTX849, a Covalent KRAS G12C Inhibitor for the Treatment of Cancer. *Cite This: J. Med. Chem* **63**, 6679–6693 (2020).

50. Canon, J. *et al.* The clinical KRAS(G12C) inhibitor AMG 510 drives anti-tumour immunity. *Nature 2019 575:7781* **575**, 217–223 (2019).

51. Mortison, J. D. *et al.* Rapid Evaluation of Small Molecule Cellular Target Engagement with a Luminescent Thermal Shift Assay. *Cite This: ACS Med. Chem. Lett. 2021* **12**, 1288–1294 (2021).

52. Valtonen, S. *et al.* Sensitive, homogeneous, and label-free protein-probe assay for antibody aggregation and thermal stability studies. *MAbs* **13**, (2021).

53. Hallin, J. *et al.* The KRASG12C inhibitor MRTX849 provides insight toward therapeutic susceptibility of KRAS-mutant cancers in mouse models and patients. *Cancer Discov* **10**, 54–71 (2020).

54. Tate, J. G. *et al.* COSMIC: the Catalogue Of Somatic Mutations In Cancer. *Nucleic Acids Res* **47**, D941–D947 (2019).

55. Ann Boriack-Sjodin, P., Margarit, S. M., Bar-Sagi, D. & Kuriyan, J. *The structural basis of the activation of Ras by Sos*. *NATURE* vol. 394 (1998).

56. Blaquier, J. B., Cardona, A. F. & Recondo, G. Resistance to KRASG12C Inhibitors in Non-Small Cell Lung Cancer. *Front Oncol* **11**, 5551 (2021).

57. Kopra, K. *et al.* Homogeneous Dual-Parametric-Coupled Assay for Simultaneous Nucleotide Exchange and KRAS/RAF-RBD Interaction Monitoring. *Anal Chem* **92**, 4971 (2020).

58. Syrjänpää, M. *et al.* QTR-FRET: Efficient background reduction technology in time-resolved förster resonance energy transfer assays. *Anal Chim Acta* **1092**, 93–101 (2019).

59. Vuorinen, E. *et al.* Protease substrate-independent universal assay for monitoring digestion of native unmodified proteins. *Int J Mol Sci* **22**, (2021).

60. Harder, E. *et al.* OPLS3: A Force Field Providing Broad Coverage of Drug-like Small Molecules and Proteins. (2015) doi:10.1021/acs.jctc.5b00864.

61. Roos, K. *et al.* OPLS3e: Extending Force Field Coverage for Drug-Like Small Molecules. (2019) doi:10.1021/acs.jctc.8b01026.

62. Madhavi Sastry, G., Adzhigirey, M., Day, T., Annabhimoju, R. & Sherman, W. Protein and ligand preparation: parameters, protocols, and influence on virtual screening enrichments. doi:10.1007/s10822-013-9644-8.

63. Bowers, K. J. *et al.* Scalable algorithms for molecular dynamics simulations on commodity clusters. *Proceedings of the 2006 ACM/IEEE Conference on Supercomputing, SC'06* (2006) doi:10.1145/1188455.1188544.

64. Jorgensen, W. L., Chandrasekhar, J., Madura, J. D., Impey, R. W. & Klein, M. L. Comparison of simple potential functions for simulating liquid water. *J Chem Phys* **79**, 926 (1998).

65. Pantsar, T. *et al.* Decisive role of water and protein dynamics in residence time of p38α MAP kinase inhibitors. doi:10.1038/s41467-022-28164-4.

TURUN
YLIOPISTO
UNIVERSITY
OF TURKU

Painosalama Oy, Turku, Finland 2023

ISBN 978-951-29-9614-8 (PRINT)
ISBN 978-951-29-9615-5 (PDF)
ISSN 0082-7002 (Print)
ISSN 2343-3175 (Online)